Chemical upgrading of biowaste and bio-sourced molecules through catalysis, green extraction and functional nanomaterials synthesis.

Chiara Bersani

A thesis submitted in fulfilment of the requirements for the degree of Joint Doctor of Philosophy.

Faculty of Science
The University of Sydney

in Cotutelle agreement (Joint PhD) with
The University of Trieste and Ca' Foscari University of Venice.

February 2026

Research conducted in this thesis was supported by the award of a University of Sydney International Scholarship to the PhD candidate.

Student Declaration

This is to certify that the content of this thesis is my own work and that all assistance received in preparing this thesis and all sources have been acknowledged. This thesis has not been submitted to any institution for the award of a degree. No generative AI was used at any stage of the completion of this thesis, including research, writing, or editing.

X _____

Chiara Bersani
PhD candidate

Acknowledgements

I'm grateful to God, who gave me strength every time I did not have it myself.

My endless thanks go to my two supervisors, Professor Selva and Professor Maschmeyer, who, with their wisdom and support, guided me, mentored me, and shaped me over these three years – not an easy task, considering my stubborn head. Today I know every choice was made for my own good. I will always be grateful to them for allowing me to live the most beautiful year of my life *down under*.

A special thank you goes to Professor Masters, for the daily visits to the lab, the stimulating questions, and the joke always ready at the right moment. In the same way, I thank Professor Perosa for bringing lightness into difficult moments and for his approach that helped me see "problems" from a more balanced perspective.

Thank you to all the wonderful people of the GOST group at Ca' Foscari, past and present. Especially to Ilaria, with whom I am happy to have started (and finished) this adventure. I am grateful to Daily for the support and help, and even for giving me a place to stay when I needed it, and to Nicola, always ready to share a good glass of wine and a few laughs. Then Giulia, Gianky, Matteo, Francesco, Paolina, Oscar, Ing. Nicoletti, Riccardo and Enrico – with you I shared many lunch breaks, but above all the most intense moments of this PhD rollercoaster. Thank you for giving me so many moments of lightness.

A heartfelt thank you to everyone in the Advanced Catalysis for Sustainability laboratory of the University of Sydney. I am deeply indebted to my tutor, Alex Major, for often sharing his endless knowledge on just about any topic – but especially for making me taste the entire Arnott's biscuit catalogue. Thank you to Chris, for supporting me with his brilliant mind, for helping me countless times, and for teaching me how to solder – a skill that may always come in handy. To my fume-hood neighbour, Alex Minor, I am grateful for the lab companionship and for the pleasant chats in Italian. And then Michael, Jack, Tom, Henrik, Jess, and Zach – you will all always have a sweet place in my memories.

I'm thankful to Stefano, who has always been there, no matter whether the kilometres between us were 300 or 16000. Thank you for the conversations, the scientific tips, and the music advice (almost) always appreciated.

A special thank you to Sam and Sahira – you have been a blessing and truly wonderful housemates. I cannot wait to come back and hug you.

Thank you to my favourite chemists, Pippo, Annina, Marta, and Erika, for the support and the countless times you brought me a breath of happiness, as we enjoyed Venice together and many spritz.

Even though it will never be enough, a heartfelt and necessary thank you goes to Francesco, for the thousands of kilometres travelled by train – and by plane – and for all the sacrifices of these three years. Above all, thank you for never stopping believing in me, not even for a single day, and for often doing it for both of us.

I am grateful to my nonna for always filling me with good food every time I came back home. Finally, and more importantly, thank you to my mum and dad. I tried my best to make you proud of me.

This Thesis is the result of three years of hard work, but it is also the result of all the people I met, the places I saw, and the experiences I lived. For all of this, I will always be grateful.

Part of this research was conducted on Gadigal Country. I would therefore like to acknowledge the Gadigal people of the Eora Nation as the Traditional Custodians of the land on which this research was carried out. I recognise and pay respect to the Elders and communities – past, present, and emerging – of the land on which the University of Sydney's campus stands, and I extend that respect to all Aboriginal and Torres Strait Islander people today. For thousands of years, they have shared and exchanged knowledge across innumerable generations for the benefit of all.

Abstract

Global challenges such as climate change and our deep reliance on finite resources force us to newly evaluate our approach to energy and material use. Facing these issues requires not only a massive reduction of waste and emissions generated but also rethinking how value can be created from what is conventionally considered waste, according to a circular economy perspective. In this framework, the present work focuses on the design of sustainable catalytic systems and biomass valorisation strategies.

For instance, due to their low toxicity, cost-effectiveness and chemical robustness molybdenum catalysts can represent excellent non-noble metal alternatives to more conventional noble metal catalysts. As one of the core topics of this thesis, a multiphase heterogeneous catalytic system that exploits the potential of molybdenum supported on a bio-based carbon. This system was developed for the selective oxidation of bio-sourced alcohols into aldehydes, taking advantage of air as a green oxidant and methyltrioctyl ammonium chloride as a hydrophobic ionic liquid phase designated for catalyst confinement. This approach enabled quantitative conversions and selectivities up to 99%, while showing remarkable resilience over time and ensuring efficient catalyst reuse over multiple consecutive cycles.

A different kind of investigation was conducted with the aim to optimise an environmentally friendly protocol for the isolation of a functional biopolymer, chitin, directly from fishery biowaste using water-compatible ionic liquids, such as ammonium formate. The optimised pulping method yielded high-quality chitin with physicochemical properties (DA>94%, MW 6.6×10^5 g/mol) comparable to the commercial counterpart, while significantly reducing the environmental impact compared to conventional chemical extraction.

Finally, a consistent part of this work was focused on the optimisation of a synthetic protocol for the preparation of nitrogen-doped carbon nanomaterials from bio-based precursors, including chitin and chitinous biowaste, which were subsequently investigated as non-toxic and cost-effective additives in aqueous zinc-ion batteries. These nanomaterials proved effective in preventing zinc dendrite formation and promoting uniform metal deposition, enabling electrode stabilisation even at high current densities and proving efficient during consecutive zinc plating/stripping cycles.

List of publications

- C. Bersani, D. Rodríguez-Padrón, D. Ballesteros, E. Rodríguez-Castellón, A. Perosa, M. Selva, Selective Multiphase-Assisted Oxidation of Bio-Sourced Primary Alcohols over Ru- and Mo- Carbon Supported Catalysts, *ChemSusChem* **2024**, e202400888;
- C. Bersani, A. Perosa, D. Rodríguez-Padrón, M. Selva, Unlocking the Potential of Liquid Multiphase Systems for Metal-Catalysed Reactions, *ChemCatChem* **2024**, 16, e202400060, and Front Cover, *ChemCatChem* **2024**, 16, e202481401.
- C. Campalani, I. Bertuol, C. Bersani, R. Calmanti, S. Filonenko, D. Rodríguez-Padrón, M. Selva, A. Perosa, Green extraction of chitin from hard spider crab shells, *Carbohydrate Polymers* **2024**, 345, 122565.
- C. Bersani, T. Ellis, M.T. Aida, A. Masters, M. Selva, T. Maschmeyer, Bio-sourced Nitrogen-doped Carbon Quantum Dots (N-CQDs) as Additives for Near Dendrite-free Zn Batteries. Manuscript in preparation.

Authorship Attribution Statement

Section 2.1 of this thesis has been published as a Review Article in: C. Bersani, A. Perosa, D. Rodríguez-Padrón, M. Selva, *ChemCatChem* (**2024**), 16, 14. The Author of this thesis equally contributed with the other Authors of the article to the selection and discussion of the papers described.

The results described in Section 2.2 of this thesis have been published as a Research Article in: C. Bersani, D. Rodríguez-Padrón, D. Ballesteros, E. Rodríguez-Castellón, A. Perosa, M. Selva, *ChemSusChem* (**2025**), 18, e202400888. Most of the work was performed by the Author of this thesis, who contributed to the optimisation, execution, and interpretation of the multiphase reaction conditions, the investigation of catalytic activity, and part of the characterisation of the catalytic samples.

Significant parts of Chapter 3 of this thesis have been published as a Research Article in: C. Campalani, I. Bertuol, C. Bersani, R. Calmanti, S. Filonenko, D. Rodríguez-Padrón, M. Selva, A. Perosa, *Carbohydrate Polymers* (**2024**), 345, 122565. The author contributed to the design and execution of the extraction tests, and to part of the characterisation of the extracts.

In addition to the authorship attribution statements above, in cases where I am not the corresponding author of a published item, permission to include the published material has been granted by the corresponding author.

X

Chiara Bersani
PhD candidate

As supervisor for the candidature upon which this thesis is based, I can confirm that the authorship attribution statements above are correct.

X

Prof. Maurizio Selva
Supervisor

X

Prof. Thomas Maschmeyer
Supervisor

List of reprinted images

The list of the following images in this thesis contain parts of the work of others and have been reproduced with permission from the relevant Authors and/or content owners:

- **Scheme 1.5.** Reprinted with permission from: *Angew.Chem Int.* **52**, 12492, (2013).
- **Figure 2.2.** Reprinted with permission from: *ACS Catal.* **10**, 6463–6472 (2020).
- **Figure 2.14.** Reprinted with permission from: *Green Chem.* **17**, 1949–1950 (2015), and *ACS Sustain. Chem. Eng.* **7**, 18434–18443 (2019).
- **Figure 3.3.** Reprinted with permission from: Poly(Vinyl Chloride) Based Composites and Nanocomposites, Engineering Materials, 117–128 (2024).
- **Figure 3.4.** Reprinted with permission from: *Acta Mater.* **53**, 4281–4292 (2005).
- **Figure 3.9.** Reprinted with permission from: *Carbohydr. Polym.* **287**, 119349 (2022).
- **Figure 4.3.** Reprinted with permission from: *Adv. Energy Mater.* **12**, 2200665 (2022).

Table of Contents

Abbreviations

AA	Acetic acid
AF	Ammonium formate
AZIBs	Aqueous Zinc Ion Batteries
BnOH	Benzyl alcohol
CEP	Conventional extraction process
CNDs	Carbon Nano Dots
CPDs	Carbon Polymer Dots
CQDs	Carbon Quantum Dots
CRB-CDs	Crab-derived carbon dots
CTN-CDs	Chitin-derived carbon dots
CV	Cyclic Voltammetry
DA	Degree of acetylation
DES	Deep Eutectic Solvents
DETA	Diethylenetriamine
DFT	Density Functional Theory
ESI-MS	Electro-spray Ionisation Mass Spectrometry
FAO	Food and Agriculture Organisation
FLW	Food Loss and Waste
FT-IR	Fourier Transform Infrared (Spectroscopy)
GC	Gas Chromatography
GHG	Greenhouse Gas
gQDs	graphene Quantum Dots
GTP	Global Temperature change Potential
GWP	Global Warming Potential
HAM	Hydroaminomethylation
HBA	Hydrogen Bond Acceptor
HBD	Hydrogen Bon Donor
HER	Hydrogen Evolution Reaction
HOMO	Highest Occupied Molecular Orbital

HRTEM	High-Resolution Transmission Electron Microscopy
HT	Hydrothermal
ICP-MS	Inductively Coupled Plasma – Mass Spectrometry
ICP-OES	Inductively Coupled Plasma – Optical Emission Spectroscopy
IL	Ionic liquid
LCA	Life Cycle Assessment
LiCl-NMP	Lithium chloride *N*-methyl Pyrrolidone
LUMO	Lowest Unoccupied Molecular Orbital
MPS	Multiphase system
MWCO	Molecular Weight Cutoff
NADEs	Natural Deep Eutectic Solvents
n-BuOH	normal Butanol
N-CDs	Nitrogen-doped Carbon Dots
NMR	Nuclear Magnetic Resonance
OER	Oxygen Evolution Reaction
ORR	Oxygen Reduction Reaction
PhCHO	Benzaldehyde
PhCOOH	Benzoic acid
PMI	Process Mass Intensity
SEM	Scanning-Electron Microscopy
TGA	Thermogravimetric Analysis
TOF	Turnover Frequency
TON	Turnover Number
UNFCC	United Nations Framework Convention on Climate Change
WHO	World Health Organization
XPS	X-ray Photoelectron Spectroscopy
XRD	X-ray Diffraction

1. Introduction

1.1 The growth paradigm between climate change and global challenges

Since the dawn of the Industrial Revolution in the late 18th century, fossil fuels have empowered the development of the humankind and driven our society through extraordinary transformations: coal, oil, and natural gas became the backbone of industrial manufacture, transportation, electricity production and domestic life, giving birth to globalisation and leading to the development of the tertiary sector, an unprecedented economic expansion and the exponential growth of the world's population.[1] This can be illustrated by the fact that over the approximately 250 years since the onset of industrialisation, the abundance of resources extracted and converted into goods and services has driven the global population to expand from about 1 to 8 billion people, primarily due by a marked decline in infant mortality rates from 50% to 4%,[2,3] and a substantial increase in lifespan at all ages, which globally reached 73.3 years in 2024.[4,5] However, the cost of this energetic conquest, along with a brakeless resource consumption, has become increasingly visible with serious long-term consequences in the form of environmental degradation, global warming and climate change.[6]

In 1824 Jean-Baptiste Joseph Fourier was the first to articulate the concept later termed the "greenhouse effect" as part of his attempt to explain the mechanisms by which the Earth maintains sufficient warmth to support the development and persistence of life.[7] During the XIX century, other scientists – including Eunice N. Foote in 1856,[8] John Tyndall in 1873,[9] and Svante Arrhenius in 1896[10] – demonstrated that specific atmospheric gases possess the capacity to absorb infrared radiations and established the first qualitative connections between anthropogenic emissions of greenhouse gases (GHGs) and the progressive warming of the Earth's atmosphere. Solar electromagnetic radiations that penetrate the atmosphere and reach the Earth's surface are only partially absorbed by land, oceans, and vegetation and partially re-emitted as infrared radiation. Under normal conditions, some of this heat get back into space. However, GHGs, including carbon dioxide (CO_2), methane (CH_4), nitrous oxide (N_2O), ozone (O_3), and water vapor, interact with this infrared radiation, absorbing and re-radiating energy back towards the Earth's surface, trapping heat in the lower atmosphere.[11] While this effect is indeed natural and necessary to some extent to sustain life, it becomes problematic when excessive amounts of these gases are released in the atmosphere through human activities, causing a planetary energy imbalance[12] that

leads to global temperature rise, altered precipitation patterns, and more frequent extreme weather events such as droughts and floods.[13]

Although the overall impact of an excess of GHGs in the Earth's biosphere is unequivocally negative, not all these contaminants exert the same climatic influence. The Global Warming Potential (GWP) express the radiative forcing of a specific amount of a gas relative to the same amount of CO_2 over a defined time horizon, accounting for its radiative efficiency and atmospheric lifetime. The Global Temperature change Potential (GTP) instead estimates the resulting change in global mean temperature at a specific future time after a pulse emission, also relative to CO_2. Together, GWP and GTP translate the effects of various GHGs into CO_2-equivalent fluxes, enabling consistent comparison of their impact (**Table 1.1**).[14,15]

Table 1.1. Lifetime, Radiative efficiency, GWP and GTP values for 100 years standardised on CO_2-equivalent.

Name and formula	Lifetime (years)	Radiative efficiency ($Wm^{-2}ppb^{-1}$)	GWP 100-years	GTP 100-years
Carbon dioxide (CO_2)	*	$1.37 \cdot 10^{-5}$	1	1
Methane (CH_4)	12.4	$3.63 \cdot 10^{-4}$	28	4
Fossil methane (CH_4)	12.4	$3.63 \cdot 10^{-4}$	30	6
Nitrous oxide (N_2O)	121	$3.00 \cdot 10^{-3}$	265	234
HCFC-22 ($CHClF_2$)	11.9	0.21	1,760	262
CFC-11 (CCl_3F)	45	$1.72 \cdot 10^{-10}$	4,660	2,340
CFC-12 (CCl_2F_2)	100	$2.69 \cdot 10^{-10}$	10,200	8,450

e.g., a GWP = 28 and a GTP = 4 over 100 years means that a ton of CH_4 is 28 times more effective in absorbing cumulative heat than a ton of CO_2, while the temperature increase from that emission is 4 times larger in comparison to CO_2. *No single lifetime can be given for CO_2.[15]

Among GHGs, the case of CO_2 is emblematic, being by far the most abundant GHG emitted through human activities and, as a result, the dominant driver of global surface temperature increase. Unlike many others, it is not destroyed but redistributed across multiple Earth system reservoirs, with fractions persisting in the atmosphere over very different timescales, ranging from decades to millennia. Consequently, its warming effect is long-term and cumulative, making CO_2 a defining challenge of our contemporary era.

Although living organism breathing, oceanic outgassing, soil respiration and volcanic activity contribute in large volume to natural CO_2 emission, estimated at 550-848 billion tons per year,[16] these are mostly balanced by natural sinks like oceans and forests, which act like carbon reservoirs by absorbing more CO_2 than they emit.[17] What disrupt this equilibrium is the anthropogenic component: an additional 25-41 billion tons of CO_2 per year are released by human activities connected to fossil fuel combustion, food production, industries and deforestation, following a trend which has kept growing since 1990. This fraction, which might seem small in comparison to the total CO_2 emissions, has a significant cumulative impact, creating a dangerous and persistent surplus that natural systems are no longer able to fully absorb.

Atmospheric CO_2 concentration, which was around 280 ppm before the industrialisation advent, is now approaching 430 ppm,[18] a level not seen in over three million years, far preceding the evolution of *Homo sapiens*. Projections from the 2021 Report of the IPCC suggest that this level could potentially reach 550 ppm by 2050.[19] This atmospheric carbon increase is depicted with exceptional accuracy by the Keeling Curve, which records CO_2 concentrations at the Mauna Loa Observatory in Hawaii and reconstructs their temporal trend with remarkable precision (**Figure 1.1**).

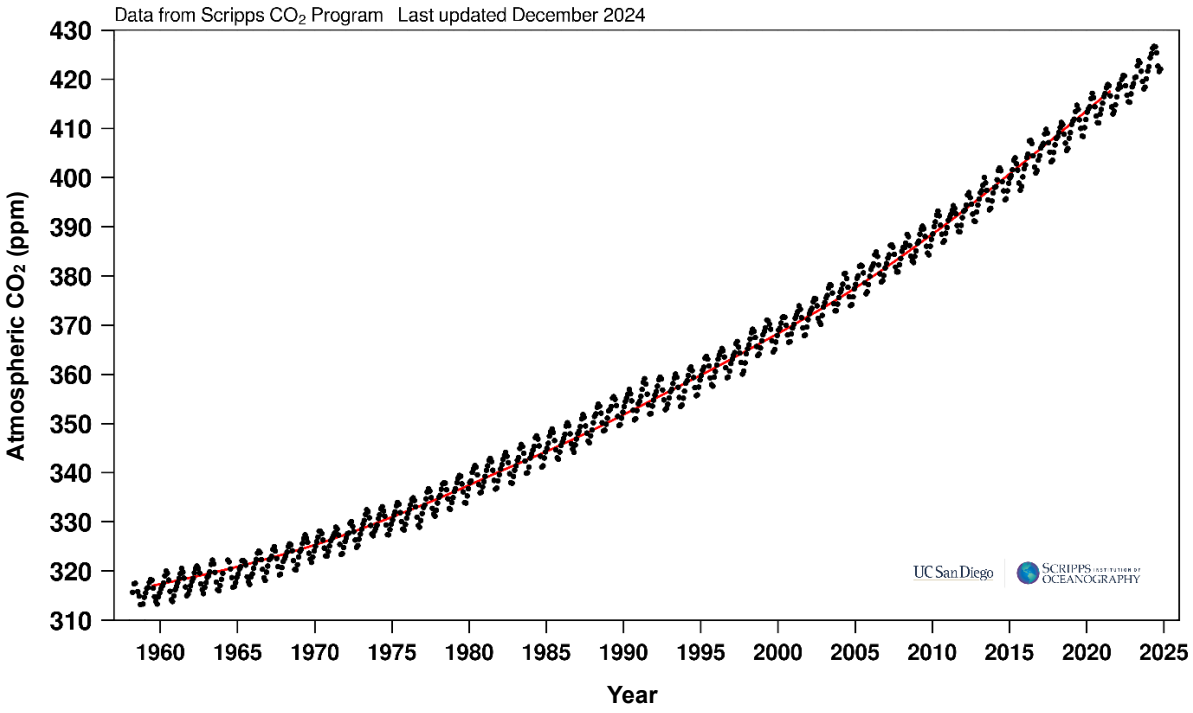

Figure 1.1. The Keeling Curve. The black dotted curve represents the monthly average atmospheric CO_2 concentration over time, while the red curve shows a fixed fraction (57%) of cumulative industrial CO_2 emissions from fossil fuel combustion and cement production. Reproduced from [20] under the terms of the Creative Commons CC BY license.

Developed in 1958 by Professor Charles David Keeling of the Scripps Institution of Oceanography, this dataset highlights both the natural seasonal fluctuations and the constant rise due to human emissions.[18] What's most concerning isn't just that the line keeps rising, but that it's getting steeper, suggesting that human activities are intensifying, pushing us further into the climate crisis.

The 2021 Report of the IPCC also confirms with high confidence the near-linear correlation between cumulative anthropogenic CO_2 emissions and global temperatures rise.[19] For every 1000 billion tons of emitted CO_2, the planet is likely to warm by about 0.27-0.63 °C (**Figure 1.2**). This relationship, known as the *Transient Climate Response to cumulative CO_2 Emissions* (TCRE), means that a net-zero CO_2 emission is required to stop temperatures from rising, or, more practically, a "carbon budget" must be stuck as the total CO_2 amount that cannot be exceeded to stay below a specific warming limit.

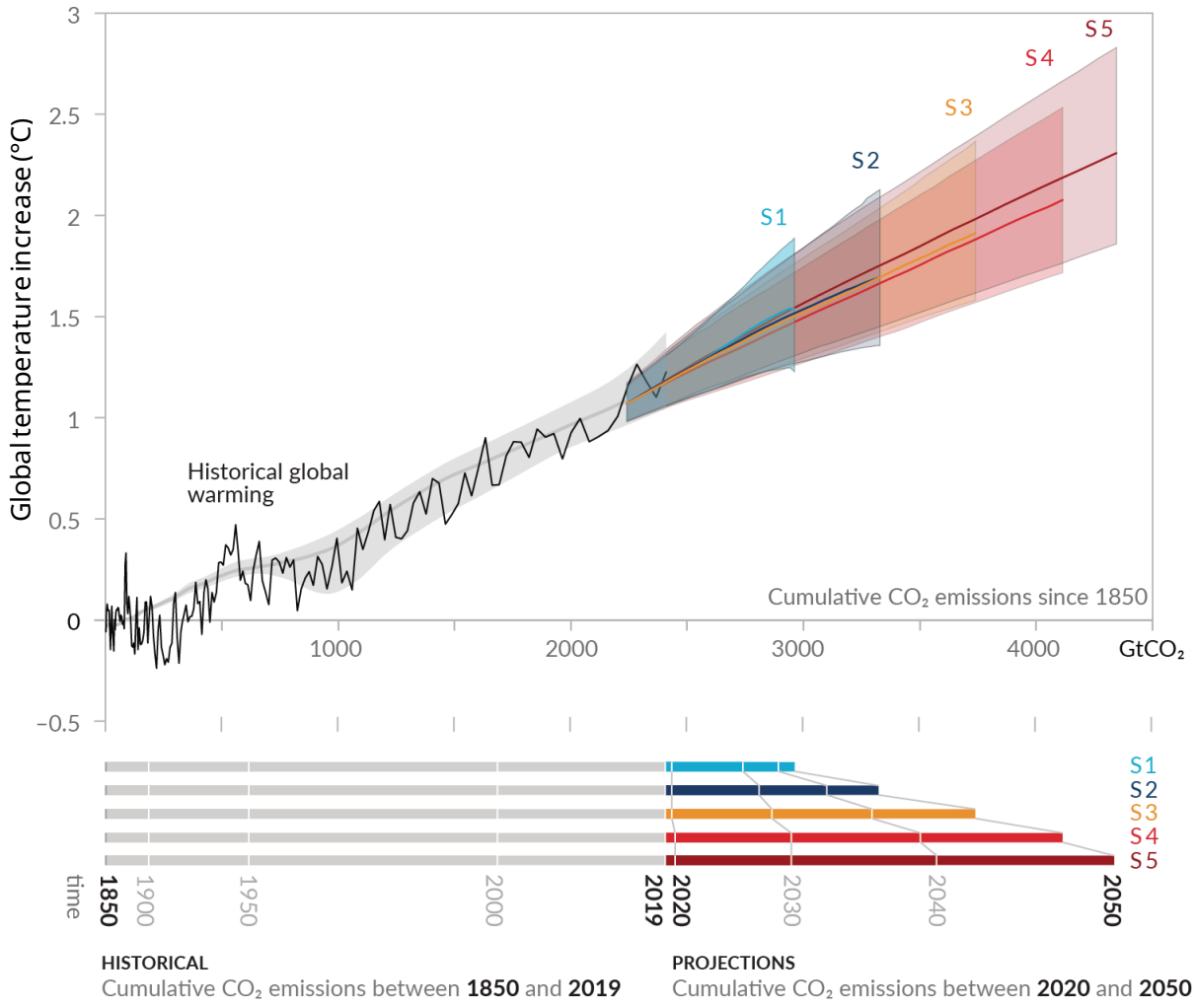

Figure 1.2. The near-linear relationship between the cumulative CO_2 emissions (in $GtCO_2$) and the global temperatures increase for five illustrative scenarios covering possible futures until 2050. Adapted from [19].

Other GHGs such as CH_4 and N_2O, though less abundant than CO_2, are potent contributors to the climatic temperature shift. Methane's global warming potential is about 28-30 times that of CO_2, and mainly originates from livestock production, organic waste management, and fossil gas extraction. Nitrous oxide, with a global warming potential 265 times greater than CO_2, is largely emitted using fertilizer and during industrial processes. Together, CH_4 and N_2O account for nearly 26% of total GHGs emissions, a share that continues to rise alongside population growth, intensified food production and industrialisation.[11] Today, fossil fuel combustion alone is responsible for over 75% of the worldwide GHG emissions.[21]

It is important to highlight that the overall rise in atmospheric GHGs is not solely the result of rising emissions, but also of the declining capacity of natural systems to absorb them. Among anthropogenic drivers, deforestation has played a critical role in shaping the current total atmospheric GHGs balance.[11] Large-scale deforestation began roughly 8000 years ago, when the expansion of agriculture and livestock farming lead to the first significant human-induced transformation of terrestrial ecosystems. Since then, the amount of habitable land covered by forests has diminished from about 57% (roughly 6 billion hectares) to the current 38% (around 4 billion hectares), with a total loss of nearly one-third of global forested area due to human activities. However, around half of this loss has occurred since the beginning of the XX century, when industrialisation accelerated deforestation. Although the pace has slowed in recent decades, it has never fully ceased, continuing to weaken one of our most important natural carbon sinks.

The effects of this carbon legacy are increasingly evident: rising global temperatures have already begun to reshape our ecosystems and economies. Since 1900, Earth's average temperature has increased by 1.1 °C, with a yearly warming rate which has speed up from 0.06 °C to 0.20 °C over the past 30 years. Anthropogenic surface temperature increase is estimated between 0.8 °C and 1.3 °C from the pre-industrial age, with the most likely value around 1.07 °C. In 2024, global temperatures ranked as the hottest ever recorded, with +1.35 °C above pre-industrial levels, while the past decade includes the ten warmest years ever recorded.[22] Extreme heat events are becoming more frequent and more intense, with the ratio of record high to record cold temperatures doubling by 2009.[23] Projections also suggest a ratio of 20 to 1 by mid-century and as high as 50 to 1 by the end of the century, implying that we're going to have many more unsustainably hot days in the future.

This warming trend is vividly captured in climate visualisations such as the "Show Your Stripes" graphic[24] (**Figure 1.3**), developed in 2016 by Professor Ed Hawkins, a climate scientist of the University of Reading (UK) in collaboration with the IPCC.

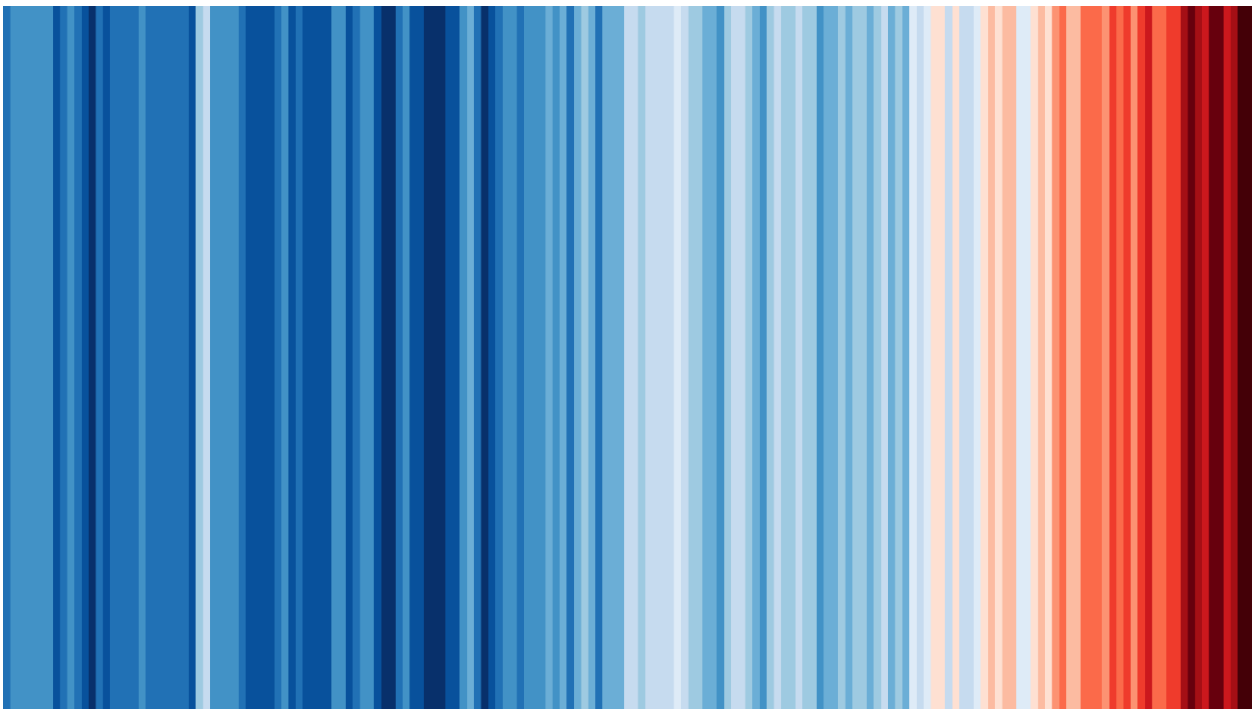

Figure 1.3. The *Show Your Stripes* graphic illustrates the progressive global warming trend (from left to right) from 1850 to 2024. Data sources: Berkeley Earth & ERA5-Land, NOAA (USA), UK Met Office, MeteoSwiss, DWD (Germany), SMHI (Sweden), University of Reading (UK) & ZAMG (Austria). Reprinted from [24].

Each vertical stripe represents one year of global temperature data over the past 150 years, with colours ranging from cool blues to intense reds symbolising the progression from cooler historical conditions to the pronounced warming of recent decades. This striking simplicity allows for immediate comprehension of complex climate data, making it a widely recognised visual tool for communicating the reality of anthropogenic climate change.

Another deeply concerning aspect is that the social and health implications of climate change are profoundly unequal: the countries suffering the most are often those with limited resources and low industrial development, who contribute the least to global pollution. Regions already vulnerable due to rain-fed agriculture, weak infrastructure, and fragile economies, are disproportionally affected by these changes, which can even hinder crop growth and reduce nutrient content under elevated CO_2 levels, worsening malnutrition and food insecurity.[25] Even in wealthier areas, marginalised and economically disadvantaged communities often bear the burden of climate-related pressures. During extreme heatwaves,

many people may lack access to air conditioning or cannot afford the electricity to use it. Elevated CO_2 levels may also affect human health, contributing to hypertension, blood acidosis, systemic inflammation, and even affecting cognitive function and bone health. As global temperatures rise, so does the risk of heat stress, respiratory illness, and mortality, with elderly being especially vulnerable.[26] 1.4 million people in China, as well as 650,000 in India and 180,000 in the EU die every year because of air pollution.[27,28] According to the WHO, current emission trends could potentially cause 250,000 additional deaths per year from 2030-2050 due to heat stress, undernutrition, malaria, and diarrheal diseases.[29]

As climate change exacerbates many environmental injustices,[30] the concept of "climate justice" has come to birth with the aim to frame climate change not only as an environmental issue, but also as a matter of ethics, equity, and human rights.[31] Climate justice calls for policies that prioritise the needs of the most affected communities, address structural inequalities rooted in poverty and colonial legacies, and ensure that climate solutions are fair and inclusive. This also means wealthier nations supporting more vulnerable ones with resources, technology, and shared decision-making, so the path to a sustainable future is built on justice as well as ambition.[30,32]

Further to this point, the evolution of the global climate action has been driven by growing scientific consensus and increasing public awareness, bringing to the gradual development of international agreements.[33] Beginning with the 1979 World Climate Conference in Geneva, early recognition of climate risks led to the formation in 1988 of the IPCC, a UN organ tasked with assessing scientific knowledge related to climate change. Since its birth, the IPCC has played a central role in investigating human impact on global warming, publishing regularly updated reports and informing policymaking. A major milestone followed in 1994 with the United Nations Framework Convention on Climate Change (UNFCCC) committing 198 nations to emission reductions and support for developing countries through financial aid and technology transfer. The subsequent 1997 Kyoto Protocol was built on this foundation, establishing legally binding emission targets and requiring regular reporting.[34]

However, the most comprehensive and inclusive accord to date is the Paris Agreement, adopted at the 21st Conference of the Parties of the UNFCCC in 2015, where all the 195 countries involved here were required to submit Nationally Determined Contributions (NDCs) and emphasizes transparency, adaptive capacity, and a program of financial investments on the climate agenda. Its core objective is to limit global warming to "well below" 2 °C above pre-industrial levels, with efforts to keep it under 1.5 °C.[35]

Unfortunately, further projections in the meantime revealed that many of the current national pledges, even if fully implemented, remain insufficient (**Figure 1.4**), likely resulting in a temperature rise closer to 2.6-3.1°C by 2100.[36]

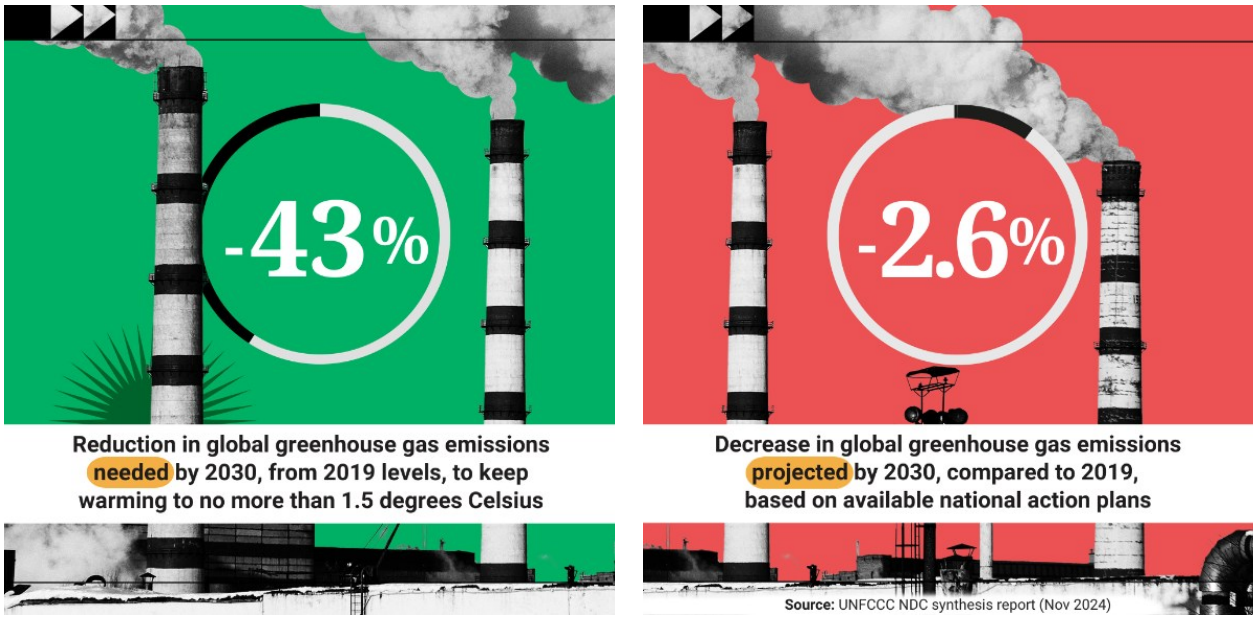

Figure 1.4. The gap between ambition and action: current national climate pledges would only cut global emissions of 2.6% by 2030 compared to 2019 levels, while a 43% reduction is needed to stay on track for the 1.5°C goal of the Paris Agreement. Reprinted from [37].

In order not to compromise our future more than it has been already done, government policies must be accompanied by concrete facts to follow scientific progress in the fight against climate change. Sustainability, therefore, cannot be treated as a peripheral issue but must be understood as central theme to the stability of ecological systems, human health, economic security, and intergenerational justice.

This introduction chapter aims to explore this topic further, examining how sustainability together with science, and more specifically chemistry, must be redefined and reshaped to meet the demands of a rapidly changing world.

1.2 The double role of Chemistry: from problem to solution

During the past century, chemistry has been one of the driving forces in achieving incredible progresses in many fields, such as health, pharmaceuticals, materials, and technology.[38]

Among many others, one of the most significant milestones was the discovery of the antibacterial properties of penicillin by Alexander Fleming in 1928, followed by its large-scale production started at the Merck & Co.'s pilot plant in the 1940s.[39] Penicillin saved millions of lives from infections that had previously been fatal, such as pneumonia, particularly during the Second World War.

In parallel, the development of synthetic anaesthetics, such as halothane,[40] revolutionised surgery practices by making them safer and less painful, while the introduction of strict hygienic standards and the use of antiseptic substances, such as phenol, drastically reduced postoperative infections.[41] The adoption of water chlorination made urban water supplies safer, keeping under control epidemics of typhoid fever and cholera.[42] Vaccines also played a decisive role: from Edward Jenner's pioneering work on smallpox in 1796 to global immunisation programs that, after an estimated 300-500 million deaths in the XX century alone, led to its eradication in 1979.[43,44] Widespread vaccination against diphtheria, tetanus, and pertussis, within the same years, has since saved hundreds of millions of lives worldwide. World Health Organisation estimates that vaccines have saved over 150 million lives over the past 50 years.[45]

Chemistry also transformed agriculture through the Haber-Bosch process (1908-1913) for the industrial synthesis of ammonia at BASF (Germany) from atmospheric nitrogen and hydrogen under pressure above 100 bar and temperature up to 400-500 °C. This innovation provided a reliable supply of nitrogen-based fertilizers on global scale: today, over 150 million tonnes of ammonia are produced annually, about 85% of which is used for fertilizer, supporting the nutrition of approximately one-third of the world's population.[46,47] Combined with high-yield crop breeding, pesticides, and mechanisation, this innovation fuelled the Green Revolution, which began in Mexico and soon spread around the world, reshaping much of global agricultures between the 1940s and the 1970s.[48]

In industry, synthetic polymers reshaped material culture. Bakelite, developed in 1907 by Leo Baekeland, was the first fully synthetic thermosetting plastic[49], followed by polyethylene in 1933, nylon in 1938, polyethylene terephthalate in 1941, and the isotactic polypropylene pioneered by Giulio Natta in 1957. By the 1950s-1960s, plastics became omnipresent in household goods, packaging, electronics, construction materials, and sterile single-use

medical devices.[50] Global plastic production grew from 2 to 380 million tonnes between 1950 and 2015, irreversibly altering modern economies and societies.[51]

From life-saving drugs and clean water to versatile plastics and fuels, chemistry has transformed our society and improved quality of life. But these advances relied heavily on synthetic chemicals, fossil fuels and non-renewable resources. By the 1970s, the dark side of unhindered chemical innovation was already evident due to issues like dioxin toxicity, DDT bioaccumulation, acidic rain, chlorofluorocarbons-related ozone layer depletion, and microplastic poisoning affecting both marine and terrestrial ecosystems, contributing to biodiversity loss, global pollution and climate crisis.[52] For instance, in 2021 microplastics started to be detected in human placental tissue.[53]

In response to an increasing environmental awareness, entire new research fields emerged during the last 45 years, with the aim of rethinking how to make, use and manage chemical substances in a more responsible way, turning chemistry from driver of the climate crisis into a key part of the solution. Green chemistry appeared in the 1980s proposing a proactive approach towards the design of chemical syntheses and processes aimed to pollution prevention and waste minimisation.[54] To guide chemists through one of the most transformative periods in history, a wide range of metrics and assessment tools have emerged. The first mass-based indicators introduced in the 1990s include atom economy (AE), process mass intensity (PMI), and the E-factor (EF), which correlate process efficiency to waste reduction.[55]

Then, in 1998 the 12 Principles of Green Chemistry (**Figure 1.5**) were introduced by Paul Anastas and John Warner,[56] emphasising energy efficiency, renewable feedstocks, waste prevention, and inherently less hazardous syntheses procedures. These principles became the backbone of a more environmentally conscious chemical innovation. However, it soon became clear that green chemistry alone could not capture the full complexity of sustainability.[57] While following its principles can lower the environmental footprint of a single process, it does not address broader drivers of GHG emissions such as energy infrastructure, industrial policies, or economic factors, which may shift environmental or social problems elsewhere.[58] To address these limitations, sustainable chemistry came into existence,[52] focusing not only on *how*, but also *why* and *whether* certain processes should exist at all, considering the full lifecycle of materials and energy flows, from resource extraction to production, use, and final disposal, other than the impact across environmental, social, and economic areas.

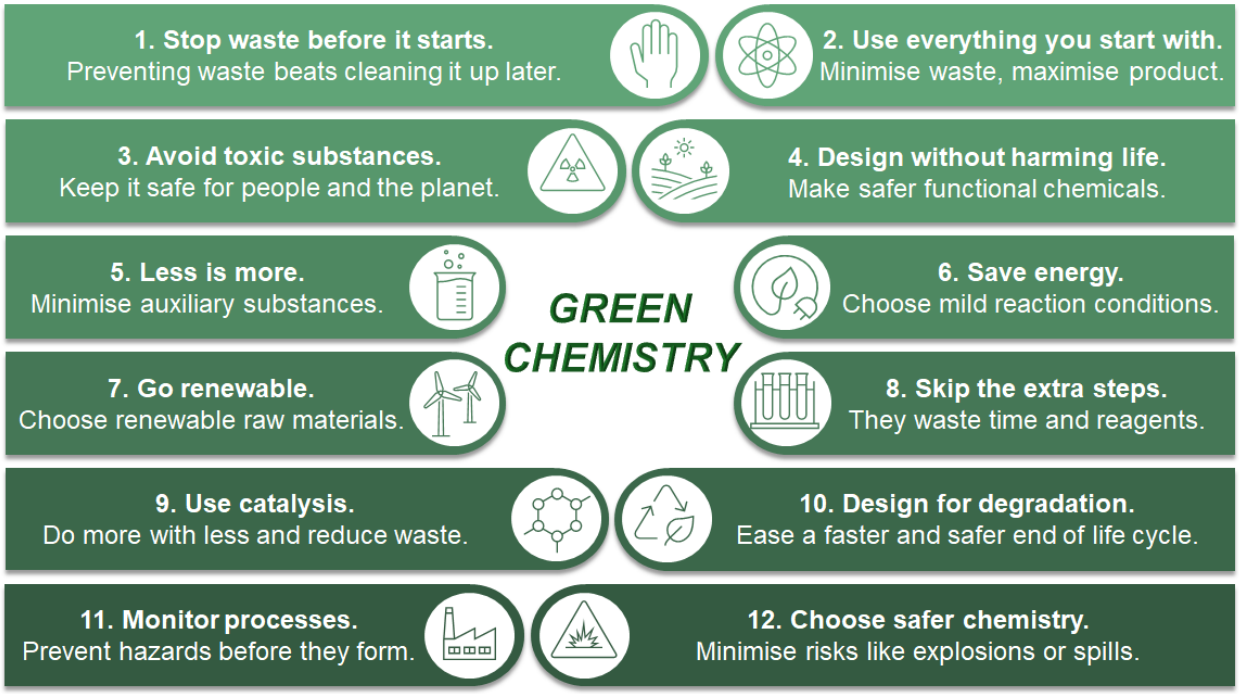

Figure 1.5. Illustration of the 12 Principles of Green Chemistry as a guide for innovation that balances scientific progress with environmental responsibility.

Green and sustainable chemistry, however, are not always aligned: a green process might use benign reagents and avoid hazardous byproducts but still rely on rare or non-renewable feedstocks, or consume excessive energy, thereby failing some of the sustainability criteria. Conversely, a process deemed sustainable for its net-zero carbon balance might involve intermediates or catalysts that violate principles of toxicity reduction or waste minimisation.

To better capture this interchange, life-cycle assessment (LCA) became an essential tool. By evaluating impacts "from cradle to grave", LCA provides a holistic picture of sustainability, covering climate impacts, human health aspects, and ecosystem effects. For instance, applying LCA to plastic production has shown that simply shifting to bio-based feedstocks is insufficient to meet sustainability thresholds, unless paired with high recycling rates of at least 75% and CO_2 capture-utilisation.[59] Aside of LCA, more than 70 distinct sustainability metrics and over 600 quantifiable parameters have been proposed up to date, ranging from reaction-level measures to global indicators grounded in the concept of planetary boundaries[60], in line with an increasingly consolidated international policy framework.

In 2015, alongside the Paris Agreement, all the 193 United Nations Member States adopted the 2030 Agenda for Sustainable Development (**Figure 1.6**).[61] The Agenda outlines 17 Sustainable Development Goals (SDGs) ranging from environment protection, poverty

eradication, health, education, and gender equality to climate change mitigation.[62] Several of the SDGs are highly relevant to chemistry and directly connected to the conscious and sustainable use of chemical processes. SDG 3 ("Good Health and Well-being") calls for limiting toxic substances and reducing air and water pollution. SDG 6 ("Clean Water and Sanitation") promotes safer solvents and advanced purification technologies. SDG 7 ("Affordable and Clean Energy") highlights catalysis for renewable energy, sustainable fuels, and batteries, while SDG 9 ("Industry, Innovation and Infrastructure") stresses sustainable industrial processes. SDG 12 ("Responsible Consumption and Production") focuses on resource efficiency, waste reduction, and circular chemistry. In parallel, SDG 13 ("Climate Action") targets GHG emissions reduction and chemical processes decarbonisation. SDG 14 ("Life Below Water") calls for reducing marine pollutants, such as plastics and solvents, while promoting valorisation of fishery byproducts - another central theme of this Thesis. Finally, SDG 15 ("Life on Land") emphasises reducing pesticides and contaminants to protect terrestrial ecosystems. Overall, chemistry plays a pivotal role in at least 8 of the 17 SDGs, underscoring its central importance in the global transition towards sustainability.

Figure 1.6. Illustration of the 17 Sustainable Development Goals of the 2030 Agenda. Reprinted from [61].

1.3 From fossil to bio: the evolution of Carbon

Carbon has been embedded into our planet's structure in a wide variety of chemical state and atomic arrangements, from allotropes as graphite and diamond, to fossil hydrocarbons deposits, and in living systems, in the molecular backbone of biomolecules as carbohydrates, proteins, lipids, and nucleic acids.[63]

Over the course of geological eras, organic matter including both plants and organisms buried underground were transformed by heat and pressure into carbon-rich substances such as coal, petroleum, and natural gas, possessing an astonishing ability to store chemical energy in their bonds, which can be released by combustion in the presence of oxygen:

$$C_xH_y + (x+y/4)O_2 \rightarrow xCO_2 + (y/2)H_2O + \text{Energy}$$

This high energy density coupled to ease of storage and transportability, led to a massive preparation and use of fossil fuels that became a pillar of industrial development, and undeniably contributing to the technological advancement and economic growth of modern societies. Fossil resources (coal, natural gas and petroleum) were also fundamental to the birth of the modern industrial organic chemistry, for the productions of thousands of chemicals and materials that are at the basis of our daily life. [64]

The petrochemical industry, indeed, emerged as a natural evolution of the petroleum and fossil fuels industry, driven by the will to use these raw materials not only as simple fossil fuels for combustion, but also as chemical feedstock. Catalytic cracking and reforming processes significantly marked this transition, making available a wide variety of low-cost olefinic and aromatic building blocks on a large scale, such as ethylene, propylene, methanol, benzene, toluene, and xylene. In 1921, the Union Carbide company set up in West Virginia the first petrochemical industrial plant in the world, manufacturing ethylene glycol and ethylene chlorohydrin as antifreeze for automotive. Two decades later, Dow Chemical emerged as the next major producer of ethylene, beginning in 1941.[65] Since then, the global production capacity of ethylene increased up to 227.6 million metric tons between by 2023, accounting for around 150 million tons of CO_2 emissions annually and making it one of the most significant building block from petrochemicals (**Scheme 1.1**) for both value and environmental impact.[66]

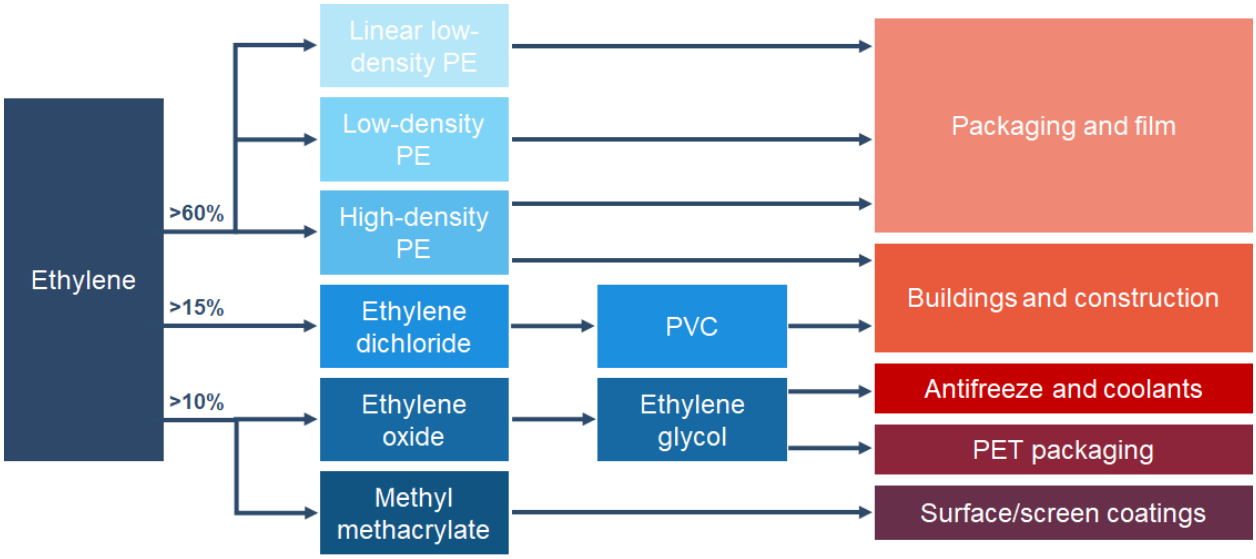

Scheme 1.1. The estimated global market flow of ethylene which shows the five main intermediate chemical products derived from ethylene. Adapted from [67].

Several other processes within the petrochemical industry soon emerged, defining the chemical industrial landscape of the XX century. Among the earliest, the first large-scale production of methanol from syngas - a mixture of carbon monoxide (CO) and hydrogen (H_2) in various ratios, generally obtained by the gasification of coal or natural gas - was pioneered by BASF in 1923 at Leuna, Germany, employing zinc/chromium oxide catalysts under quite harsh conditions: up to 300-400 °C of temperatures and 250-350 atm of pressure.[68] It was at this plant where methanol production reached 100,000 tonnes per year in 1936 and 200,000 tonnes per year during World War II.[69] A few decades later, in 1966, significant improvements to the process were introduced by Imperial Chemical Industries (ICI) at Billingham, UK, where the methanol was synthesised operating with Cu/ZnO catalysts at milder conditions of 300 °C and 100 atm, reducing the energy required. Many further implementations have been carried out through time and more industrial plants have been opened to meet the production needs, which almost doubled in the last decades and reached 98 million tons per year in 2023, 69% of which is used to produce many other important chemicals, including formaldehyde, acetic acid, polyethylene and polypropylene.[70,71] Latest projections estimate that this number might reach 500 million tons per year by 2050, generating 1.5 billion tons CO_2 emissions if produced exclusively from fossil fuels.[71]

In parallel, one of the most influential processes of the XX century emerged, establishing for the first time a catalytic route to synthetic fuels from coal-derived syngas: the Fischer-

Tropsch process (**Scheme 1.2**). Developed in 1926 by Franz Fischer and Hans Tropsch at the Kaiser Wilhelm Institut for Coal Research in Mülheim, Germany, in collaboration with the Ruhrchemie Company, this process demonstrated the feasibility of transforming the CO + H_2 mixture into liquid hydrocarbons. The reaction proceeds in the presence of transition-metal catalysts, such as iron, cobalt, nickel or ruthenium, typically under conditions of 200-350 °C and pressures of tens of bars.[72]

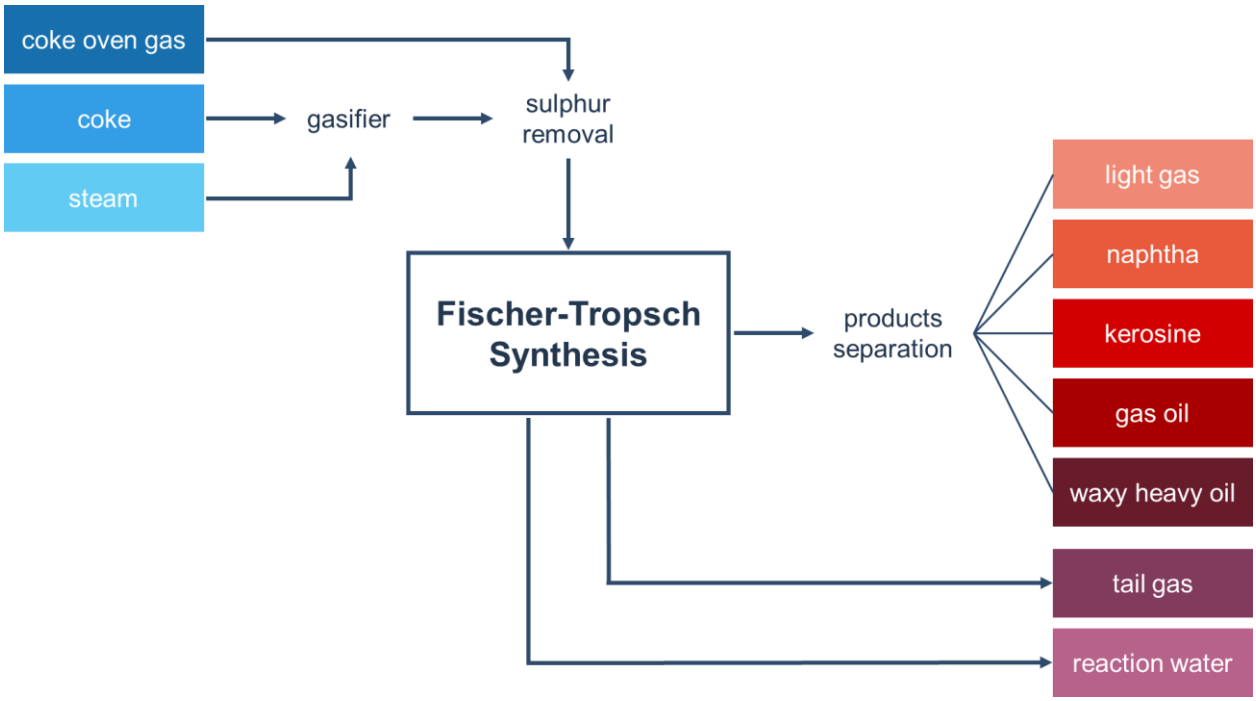

Scheme 1.2. The original Fischer-Tropsch process scheme from U.S. Naval Technical Mission in Europe Technical Report No. 248−45 The synthesis of hydrocarbons and chemicals from CO and H_2 (1945).

By 1938 a large-scale application of the Fischer-Tropsch process was represented by several plants already in full operation, and by 1945 their combined capacity reached approximately 600,000 tons per year, primarily aimed at meeting the energy demands of wartime Germany.[73,74] During the 1940s, Fischer-Tropsch hydrocarbons also started to be subjected to controlled oxidation with air, giving rise to mixtures of alcohols, ketones, esters and carboxylic acids. At the same time, investigations about the addition of ethylene during the process led to the synthesis of aldehydes and the discovery of the effectiveness of cobalt-based catalysts, such as $HCo(CO)_4$, in the hydroformylation process.

Thus, in 1938 Otto Roelen discovered the Oxo process “for the preparation of oxygen-containing compounds in which unsaturated hydrocarbons (e.g., olefinic hydrocarbons) are

treated at elevated pressure and temperatures up to approximately 200 °C with water gas or other gas mixtures containing carbon monoxide and hydrogen".[75]

The process was industrialized by Ruhrchemie/Rhône-Poulenc, establishing the synthesis of aldehydes from syngas and olefins. Subsequent work later demonstrated that tributyl phosphines (PBu_3) were more effective ligands for improving the selectivity of aldehydes obtained from cobalt-catalysed processes. From the 1970s onward, cobalt catalysts were replaced by more effective rhodium-based catalysts, that would later evolve into multiphase catalysis,[76] to be described in more detail in the following section and in Chapter 2. The hydroformylation process still represent today one of the most important examples of homogeneous catalysis application in industry, accounting more than 12 million tons of oxo products synthesised every year.[77]

The race for bulk chemical production in the last century was accompanied by other significant innovations and developments, such as the olefin metathesis reaction in the 1960s[78] - still applied today in several industrial processes, including the Shell Higher Olefin Process (SHOP) for the production of linear α-olefins and the Phillips Triolefin Process for the production of propylene[79] - a discovery that earned Yves Chauvin, Robert Grubbs, and Richard Schrock the Nobel Prize in Chemistry in 2005.

Major breakthroughs in polymerisation chemistry also market the second half of the XX century, most notably with the advent of the titanium-based Ziegler-Natta catalysts, which enabled the stereoselective synthesis of isotactic polypropylene in 1957.[80] Polypropylene soon became popular due to its outstanding mechanical properties and versatility, and today is the second most abundant global plastic product after polyethylene, accounting for the 17% of the total plastic produced.[81] Along with polyethylene (24%), polyethylene terephthalate (17%), polyvinyl chloride (11%), polyurethane (5%), polystyrene (5%), and other key styrene-based plastics (2%) such as styrene-acrylonitrile and acrylonitrile-butadiene-styrene, these materials together account for about 80% of global primary plastics production from fossil resources (**Figure 1.7**).[82]

Global plastic production, which reached a total of 460 million tonnes in 2019, is one of the major sources of GHGs emissions, accounting alone for roughly 2.24 billion tonnes of CO_2-equivalent emissions in 2019 and 5.3% of the world's total emission for that year,[82] with future projection estimating these numbers potentially tripling by 2060.[83]

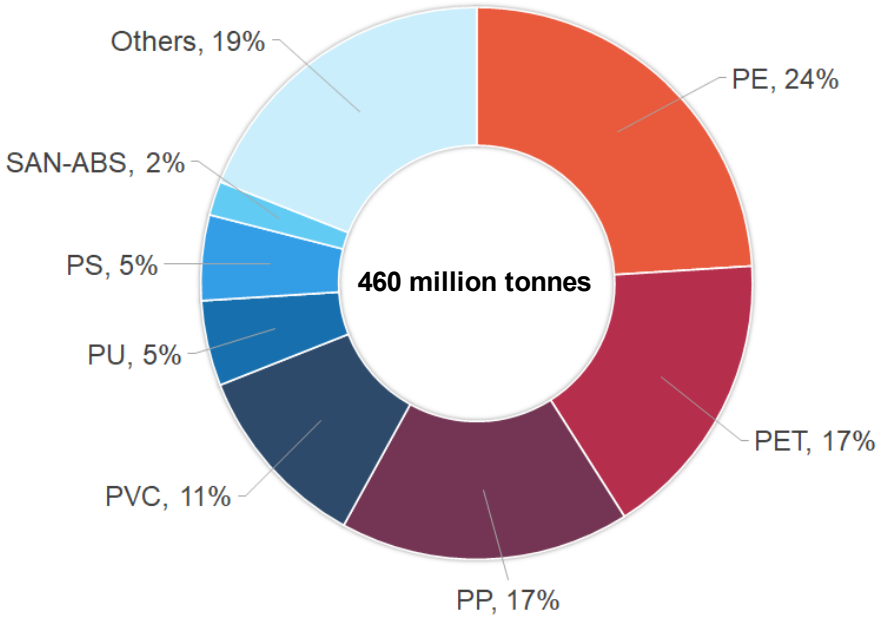

Figure 1.7. Distribution of global primary plastic production from fossil resources in 2019. Adapted from [82].

Unfortunately, the versatility and extended use that made fossil resources such effective energy carriers and building blocks for chemistry and material science were also the major responsible for their environmental impact throughout history. Alongside climate issues, another spread critical concern is the depletion of fossil carbon resources. Extraction and use of fossil materials, formed in a finite amount over geological timescales, raise questions about their long-term availability, with all the geopolitical vulnerabilities associated with their supply chain.[84]

Although fossil resource estimates rely on very well-established classification methods, they remain subject to several and significant uncertainties. These do not concern only physical or technical aspects, but also economic, socio-political, and sustainability dimensions. Fossil resources are generally divided into different categories - such as already produced, economically recoverable, potentially recoverable, and yet-to-be-discovered - each one associated with a different degree of uncertainty in both economical evaluation and physical quantification.[85] Even with the aid of advanced extraction technologies, a complete knowledge of underground deposits remains often difficult to reach, and in any case the share considered “economically recoverable” depends strongly on market prices. Moreover, climate targets set by the 2015 Paris Agreement require a substantial portion of known reserves to remain unextracted to stay below the +1.5 °C carbon budget. This would imply leaving in the ground roughly 60% of global oil and fossil methane gas reserves, and more

than 90% of coal.[86] In reality, the immediate risk is not that fossil fuels will be physically exhausted in the short term – they are expected to still last several decades[69] – but rather that burning all currently classified "recoverable" reserves would far exceed climate target limits, with catastrophic consequences for our planet.

The global energy demand (**Figure 1.8**) grew by 2.2% in 2024, a notably faster rate than the annual average of 1.3% seen between 2013 and 2023, reaching 650 exajoule of energy (about 15,500 million tonnes of oil equivalent). Although global energy systems and the production of chemicals and materials remain overwhelmingly dependent on fossil-derived feedstocks, growing attention and investment have been directed towards hydroelectric, solar, wind, hydrogen, and biomass as alternative renewable energy sources.[87] Global oil demand growth, indeed, slowed in 2024, rising by 0.8%, after increasing by 1.9% in 2023, while other non-fossil fuel energy sources (including nuclear and renewables, bioenergy and waste) grew by over 5% in 2024, and made up nearly half the total growth in global energy demand in the year.[88,89]

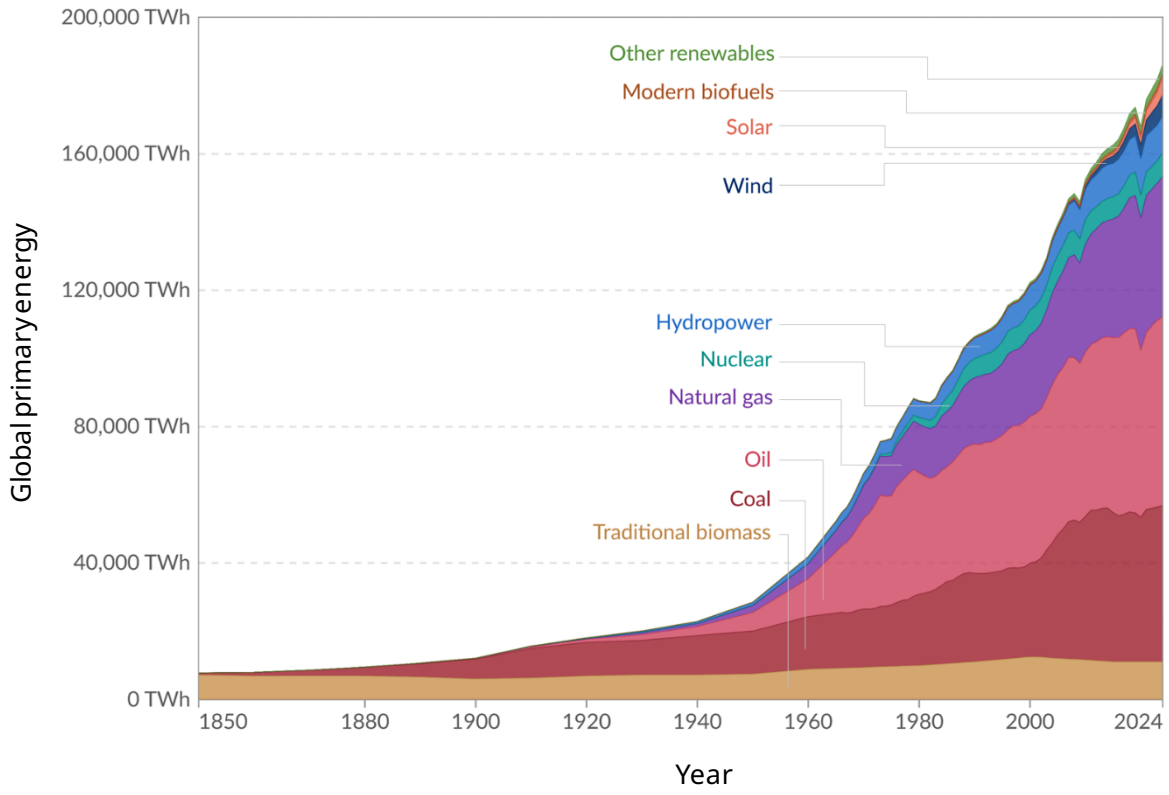

Figure 1.8. Global primary energy (available as resources, before it has been burned) consumption by source, over time (1850-2024). Energy values are expressed in Terawatt-hours (TWh; 1 Watt-hour is equivalent to 3600 joules of energy) and are adjusted for efficiency losses (substitution method).[90] Adapted from [91].

Biomass is already part of the natural carbon cycle, and when managed under sustainable frameworks, its use can limit additional net CO_2 emissions, while simultaneously reducing fossil resources dependency.

The concept of biorefinery started to emerge in the early 2000s.[92] Just like a petroleum refinery, a biorefinery integrates conversion processes for the production of fuels, energy, and valuable chemicals, where, instead of crude oil, the feedstocks are renewable resources such as agricultural residues, forestry byproducts, and organic waste, minimising the waste stream and enhance the overall environmental beneath of bio-based industries.

First-generation biofuels come from sugar, starch, and oil crops that are also used for food, e.g., bioethanol from sugarcane or corn, and biodiesel from rapeseed or soybean. Global bioethanol production reached about 51 billion litres in 2006, with the United States (19.8 billion litres) and Brazil (17.8 billion litres) as the leading producers, while the European Union contributed approximately 3.4 billion litres.[93] Although these biofuels demonstrated measurable reductions in GHGs emissions[94] compared with conventional fossil fuels, they also raise concerns about their long-term sustainability because they compete with food production and rely on land, fertilizer, and water reserve. To overcome these limitations, since 2008 second-generation biofuels have been developed from non-food sources, especially lignocellulosic biomass such as agricultural residues, forestry byproducts, and dedicated non-food energy crops.[95] Whitin this feedstock, the carbohydrate fractions (cellulose and hemicellulose) can be hydrolysed into fermentable sugars and converted into bioethanol or biomethanol, while lignin can be valorised as a precursor for high value biochemicals.[96]

This way, and unlike first-generation processes which only use a fraction of the above-ground biomass (like seeds or grains), second-generation technologies are able to exploit the whole plant, improving efficiency.[97] The climate benefits of these fuels depend heavily on the feedstock and the production pathway, with biomass supply generally varying on availability and productivity of land, accessibility of residues and waste.[85]

Today biorefinery offers clear advantages by producing both energy carriers and a wide spectrum of bio-based chemicals, with major outputs including bioethanol, biomethanol, biodiesel and biomethane, as well as glycerol, sorbitol, lactic acid, furan dicarboxylic acid, succinic acid, and levulinic acid, among many others.[98] These represent valuable building blocks for bioplastics, solvents, and pharmaceuticals. Future projections indicate that

renewable fuels, particularly biomass-derived fuels, are expected to play a growing role, with estimates suggesting they could replace up to 27% of petroleum-based fuels by 2050.[99]

After nearly a century since its development, even the Fischer-Tropsch process has been reframed within the context of green chemistry and global decarbonization targets, with the development of the BtL (Biomass to Liquid) technology, a process which consists of gasification of the biomass to produce syngas, followed by Fischer-Tropsch synthesis and, finally, distillation of the liquid hydrocarbons, enabling the production of environmentally friendly synthetic fuels and bulk chemicals from biomass.[100]

More recently, research has increasingly focused on the use of industrial off-gases and even captured CO_2 as alternative carbon sources their own,[97] or in combination with bioenergy to achieve negative emissions (**Scheme 1.3**).[101]

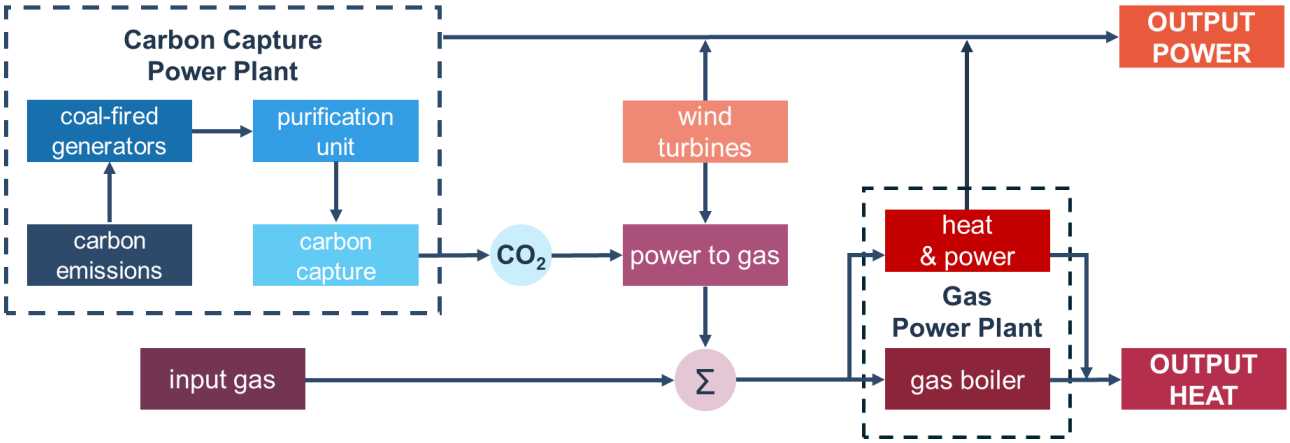

Scheme 1.3. Energy flow diagram of integrated energy system with CCUS technology. Adapted from [102].

The prevailing idea is, indeed, to develop integrated production systems - whether for energy, chemicals, or materials production - where different technologies are synergistically combined to enhance efficiency, sustainability, and added value. A transition to a low-carbon future cannot rely on a single technological route, but requires integrated approaches that orchestrate multiple, complementary strategies for carbon management. Biomass represents only one component of the renewable energy landscape and, on its own, cannot deliver the scale of emission reductions required, especially when land-use impacts and feedstock fluctuations are considered. For this reason, integration with other measures, such as energy storage systems[103] and energy recovery from industrial by-products[104] is increasingly promoted within the framework of a circular carbon economy.

Waste CO_2 itself, indeed, could become an excellent source of carbon. For example, CCUS (carbon capture, utilization, and storage) is becoming a technological pillar in the fight against climate change.[105] This approach involves extracting CO_2 emissions from industrial processes, transporting the gas, and either storing it in geological formations or using it to produce new products. CCUS is widely recognized as a necessary bridge technology, especially in those sectors hard to decarbonize, like heavy industry and transport. Research into new materials and membranes, such as carbon molecular sieve membranes, has shown promise in improving the efficiency and cost-effectiveness of CO_2 separation. Major challenges, however, remain the scaling up of these technologies, the minimization of energy inputs, and the long-term stability of CO_2 storage.[101]

Scientists, engineers, policymakers, and, especially, an informed public must engage in shared efforts to develop, adopt, and adapt solutions towards the carbon neutrality.[105] In this context, an emblematic case is the ARC Centre of Excellence for Carbon Science and Innovation in Australia, which represents a strategic measure for the growing need for advanced carbon-based technologies. Supported by the Australian government, this centre conducts pioneering research on carbon-based materials derived from renewable sources, emphasizing sustainable approaches to energy storage, advanced carbon catalysis, and functional materials.[106] Its mission reflects a broader global transformation, that not only addresses environmental challenges but also entails cultural, social, and economic change, requiring a fundamental rethinking of how resources, materials, and waste are evaluated and, where possible, reused, as will be discussed in greater detail in the following sections.

1.4 Sustainable carbon-based materials for catalysis and beyond

As a natural extension of the expansion of a variety of sustainable carbon management strategies, recent years have seen a growing demand for the development of carbon-based technologies, in which the remarkable versatility of carbon, particularly when obtained from renewable sources, represents a key element for the transition towards the production of low-impact energy and materials. Inspired by nature, materials scientists and engineers have made significant progress in developing advanced carbon materials, such as activated carbons and carbon aerogels, using carbon from renewable sources like biomass or directly from CO_2.[107,108] Owing to their low density, high porosity, and tuneable texture, these materials are increasingly finding applications not only in modern industry but also in a wide range of sectors of everyday life, such as water treatment and heavy metals removal, air purification and capture of toxic gases, catalysis or as catalyst supports, additives, food processing and sustainable/biodegradable packaging solutions as alternatives to conventional plastics.[109–112]

A striking number of studies have focused on synthesising activated carbons from biowaste, showing that by precisely controlling experimental parameters is possible to tune the surface area, pore volume, and pore-size distribution to achieve highly specific properties.[113,114] Within these processes, the initial waste material is usually subjected to an activation step, which can be either physical (direct carbonisation at high temperature, up to about 1000 °C, using oxidizing gases such as steam, CO_2 or N_2), chemical (typically carried out by mixing chemical activating agents, such as acids, bases, oxidants or dehydrants, with the biomass through an impregnation step before carbonisation), sometimes physiochemical (which combines the aforementioned two), or even microwave-assisted (**Scheme 1.4**).[107,114]

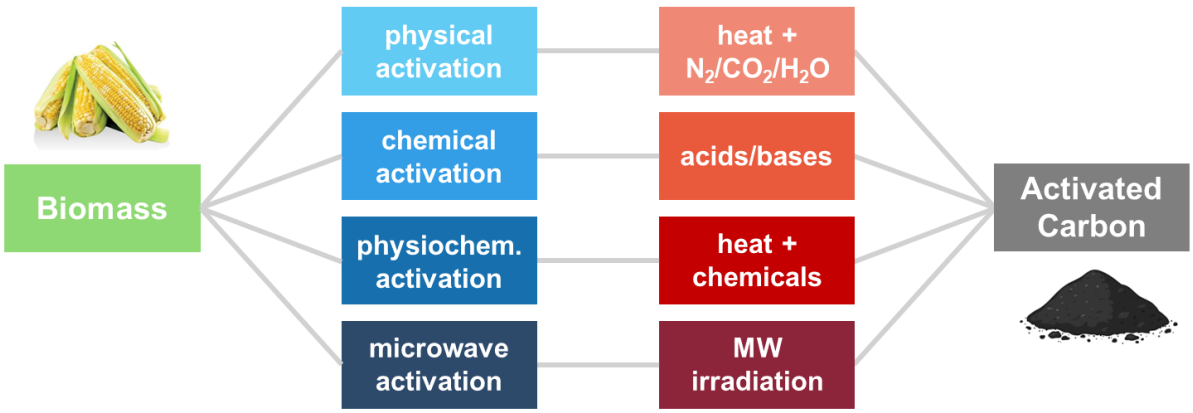

Scheme 1.4. Synthesis of activated carbon through different physical/chemical activating methods.

Materials obtained through these approaches can differ significantly, exhibiting a wide range of properties suitable for diverse applications. For example, gas adsorption capacity can vary considerably: CO_2 uptake in many materials is in the range of 2-7 mmol/g, strongly depending on pressure, temperature and pore size (with micropores, typically < 2 nm, being especially effective for CO_2 uptake at low pressures).[113,115,116]

These materials can be produced from a wide variety of starting substrates, such as wood, agricultural residues like rice husk or corn cob, fruit stones, nut shells, grape stalks, pomegranate seeds, oil-palm stones, and many others (**Figure 1.9**).[117]

Figure 1.9. Different substrates for biomass valorisation in activated carbon synthesis.

However, the porosity of activated carbons is not only essential for adsorption but also has a huge potential in catalysis. Within this context, the well-developed pore network of activated carbons offers a perfect support for catalytic materials. This structures, indeed, provide multiple anchoring sites for highly dispersed metal nanoparticles, maximizing the number of accessible active sites and, in turn, enhancing the catalytic efficiency.[117–119] Moreover, beyond their textural properties and the obvious sustainability benefits, biomass-derived activated carbons exhibit an astonishing chemical versatility, as their surface can

result into a highly functionalised latticework with oxygen-, nitrogen-, or sulphur-containing groups of which the starting biomass was rich, that tailor metal-support interactions and enhance selectivity.

This unique combination of structural and chemical features makes them ideal candidates for heterogeneous catalysis, a field that plays a preeminent role in sustainable chemistry, mostly due to ease of synthesis, recyclability and industrial scalability of heterogenous systems, which make them not only economically attractive but also instrumental in reducing the carbon footprint of chemical processes.[120]

Shifting from homogeneous to heterogeneous catalysis can lower the overall environmental impact by orders of magnitude, especially when using metals supported on renewable materials.[121,122] LCA analyses have highlighted an emblematic case in the palladium-catalysed Sonogashira reaction. Cross-coupling reactions (which earned the scientists Richard Heck, Ei-ichi Negishi, and Akira Suzuki the Nobel Prize in 2010) play a central role in the synthesis of chemical building blocks, yet they are largely dominated by homogeneous catalysis with soluble complexes of precious metals.[123] It has been demonstrated that an appropriately designed heterogeneous palladium single-atom catalyst (SAC) supported on nitrogen-doped carbon can drastically lower the environmental impact of the reaction in terms of GWP (60 times lower al second catalytic cycle in comparison to the homogeneous counterpart), impacts on human health, ecosystem quality, and resource use.[124]

Bio-based carbon-supported metal catalysts are widely employed in diverse heterogeneous catalytic processes, mostly including hydrogenation of organic compounds, selective oxidation of alcohols and biomass-derived molecules, and degradation of environmental pollutants. Thanks to their properties, bio-based carbons have emerged as indispensable scaffolds for next-generation catalytic systems, effectively bridging industrial efficiency with environmental awareness.[125–130]

A remarkable sustainability concerns in metal-based catalytic systems remains the reliance on precious and rare elements such as palladium, platinum, rhodium, and iridium. These metals are associated with high costs, geopolitical supply risks, significant environmental burdens during their extraction and refinement, and are proven endangered with risks of shortage in the medium/long term.[85]

The EuChemS Periodic Table of Element Scarcity (**Figure 1.10**), first released in 2019, provides a clear and explicative overview of the general scarcity of elements resulting from excessive and uncontrolled human-driven overexploitation. The most recent 2023 version

introduced a new deep shade of red for carbon, nitrogen, and phosphorous to highlight elements that humans are using in such a way that they are causing irreversible environmental damage. This colour emphasizes the disruption of the biogeochemical cycles with repercussions on the biosphere. Lithium's colour also has changed, from yellow to orange, reflecting an increased risk of shortage due to the fabrication of batteries.[131]

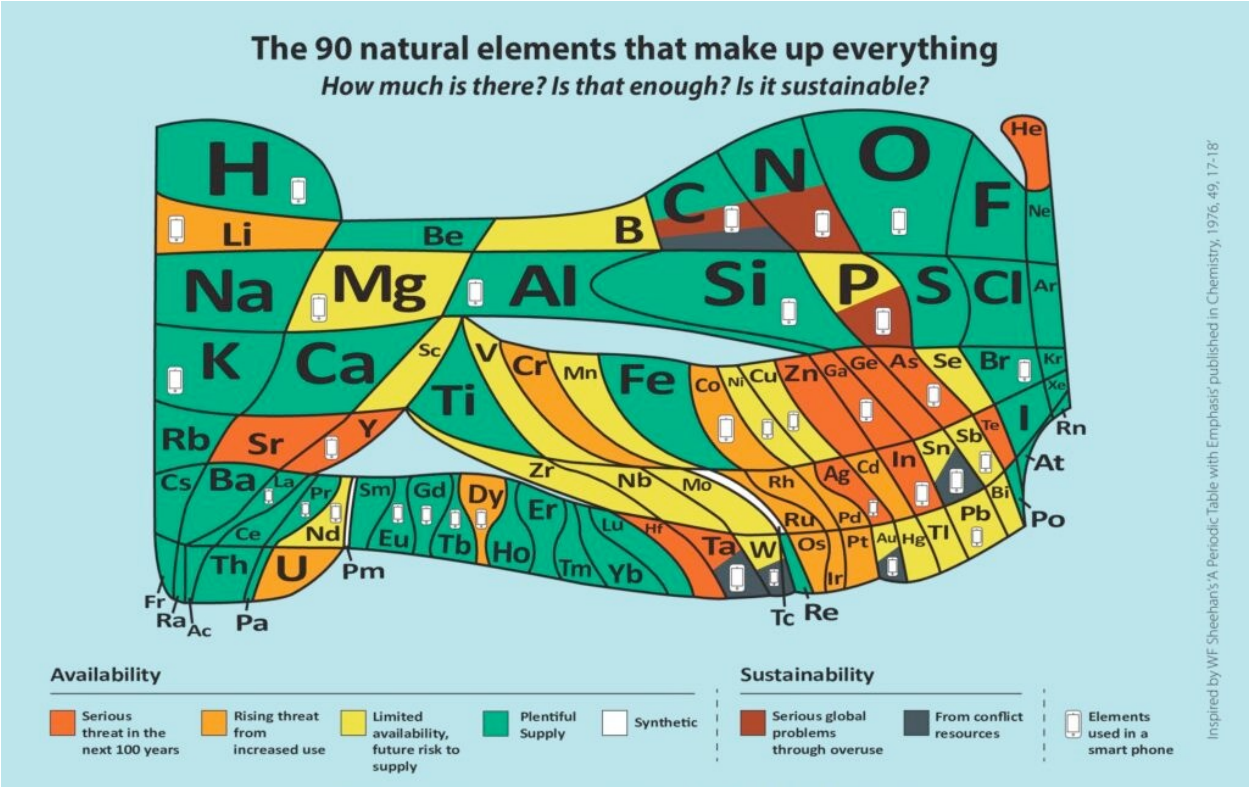

Figure 1.10. *The 90 natural elements that make up everything* has been drawn so that the area occupied by each element gives an indication of the amount (numbers of atoms on a logarithmic scale) of that element in the Earth's crust and atmosphere.[131]

Beyond policies and educational measures aimed at raising awareness about the sustainability of elements crucial to research in catalysis, the scientific community has increasingly embraced the importance of addressing this issue. Current literature highlights a growing amount of works focused on replacing precious metals with more abundant, less toxic, and more sustainable alternatives based on earth-abundant metals like iron, manganese, nickel, and molybdenum.[132–138]

Yet, this transition is not without issues, and it requires not only a re-design of the catalyst, but very often, also of the reactors and reaction conditions. Remarkable advances within this field have been reported by introducing aqueous/organic multiphase environments where phase separation is used to isolate products or recover catalysts or both.

This topic, briefly discussed below, is one of the core issues of this Thesis and will therefore be explored further in Chapter 2.

The concept of multiphasic catalysis basically relies on the possibility of confining a catalyst into a separate and immiscible phase with respect to that where both reagent(s) and product(s) are dissolved. In line with the principles of green and sustainable chemistry,[139] this configuration has offered significant advantages in terms of both reducing solvents required for the extraction and purification steps and enabling recycling techniques for the catalytic system.

Developed in 1968, the Shell Higher Olefin Process (SHOP) was one of the first examples of biphasic catalysis for oligomerisation of ethylene into α-olefins (**Scheme 1.5**). With more than one million tonnes of alpha-olefins produced every year, the SHOP process is still one of the most significant industrial processes based on homogeneous transition-metal catalysis.[139,140]

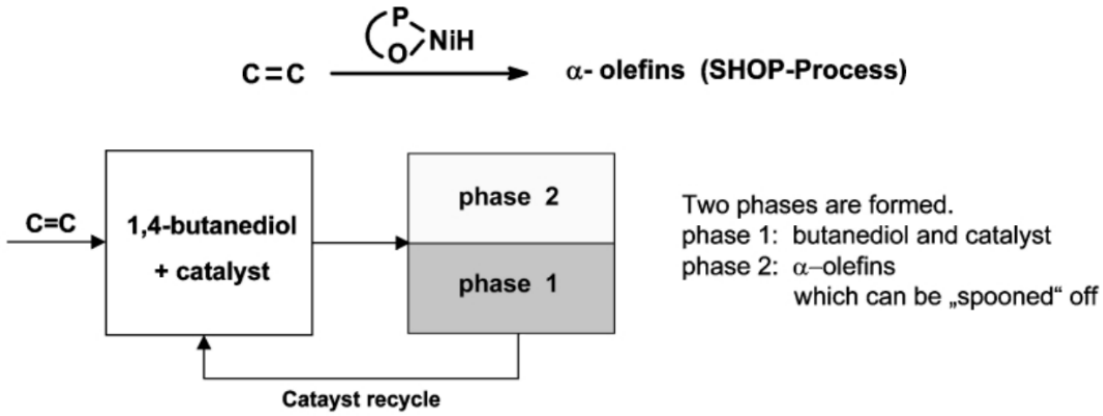

Scheme 1.5. Schematic representation of the SHOP process for oligomerisation of ethylene into α-olefins catalysed by square planar PO-chelate-Ni-complexes. Reprinted from [139] with permission.

From this case on, a myriad of other metal-catalysed processes has been successfully reported under multiphase conditions for both homogeneous and heterogeneous systems, including hydrogenation[141] and hydroformylation[142] processes, C-C and C-X bonds formation,[143] alcohols oxidation,[144] tandem reactions,[145] as well as chemical upgrading of biomass.[146,147] In particular, multiphasic systems using heterogeneous catalysts have long been recognized as versatile platforms for batch and continuous-flow reactions for their ability to integrate the reaction step, separation, and recycling to reduce both the energy demand and environmental challenges.[148–150]

The choice of immiscible phases (both the reaction solvent and the catalyst(s) segregating medium) represents one the most critical parameters in the design of such systems, as it influences mass transfer, phase behaviour, and catalyst stability.[151,152] Besides traditional organic solvents, water, the quintessential green medium has often been introduced as an immiscible polar phase to facilitating product separation and catalyst recycling.[153]

An increasing attention has been directed also at non-traditional media, including ionic liquids (ILs), supercritical fluids (like supercritical CO_2) and deep eutectic solvents (DES). These alternatives offer tuneable properties and, in many cases, a reduced environmental impact. Among them, ILs represent an emblematic case. As per their definition, ILs are organic salts that are liquids in the proximity of ambient conditions, and they offer several advantages over conventional solvents, such as non-volatility, thermal stability, and highly customizable properties to improve extraction/reaction selectivity, that made them favourable in terms of energy demand and reduced footprint.[154]

One of their key features is the ability to create systems in which (mostly) a heterogeneous catalyst can be segregated in an ionic liquid phase where it can:

i) promote a reaction occurring in a different (aqueous or organic) medium; and

ii) be recycled virtually indefinitely without loss of catalytic activity, while never being removed from the reaction vessel.

Interfacial phenomena between different immiscible phases have often resulted in surprising rate accelerations and/or unique selectivity. This concept/configuration has been intensively investigated also by our group. One example is the regioselective Ru/C-assisted catalytic oxidation of HMF (5-hydroxymethyl-furfurale) into DFF (2,5-diformylfuran), HMFCA (5-hydroxymethyl-2-furancarboxylic acid), FFCA (2,5-formylfurancarboxylic acid), and FDCA (2,5-furandicarboxylic acid) obtained with complete conversion and high selectivity under three different multiphase configurations and mild temperature (90-130 °C): a combination of water/isooctane was effective in synthesising FDCA (91% isolated yield), whereas the same system added of $[N_{8881}][Cl]$ (methyl trioctylammonium chloride) as an ionic liquid third phase provided FFCA (89% yield); once FFCA was obtained, a simple one-pot two-step protocol under hydrogen-assisted reductive conditions was effective in obtaining HMFCA (85% yield), and finally, a different combination of acetonitrile/isooctane allowed the synthesis of DDF (96% isolated yield).[155]

Among other applications, it was found that in a multiphase system comprised of water, isooctane, and [N_{8881}][Cl] (methyl trioctylammonium chloride) as an ionic liquid, the oxidation of benzyl alcohol to benzaldehyde occurred with a very high selectivity (up to 99%, at a conversion >95%), by replacing costly and endangered Ru/C with much cheaper and available bio-based Mo/C,[156] a catalytic process that will be further detailed in Chapter 2.

Albeit highly versatile, the multiphase catalysis either IL-assisted or not, requires specific requisites for the catalysts; in particular, heterogenous catalysts must be very often supported on carbon-based materials of moderate hydrophobicity and surface acidity to grant phase segregation in an ionic liquid or a hydrocarbon medium.[157] These characteristics have proved interesting in stimulating studies aimed at the fabrication of catalytic supports based on innovative carbon materials such as, for example, bio-based materials. Interestingly, a recent work of our group has demonstrated that a N-doped carbon support derived from a natural biopolymer as chitin, was excellent to immobilize Pd-nanoparticles active to catalyse hydrogenation reactions: in this case, cinnamaldehyde was exclusively converted to hydrocinnamaldehyde in a triphasic (liquid-liquid-liquid) batch reactor where the catalyst was compartmentalized in an ionic liquid layer. No carbonyl reduction was observed. p-Type dopants like nitrogen, were assumed to induce more negatively charged supports, causing palladium to display more electropositive behaviour[158] Noteworthy, by changing the catalysts and the multiphase environment, other Authors observed a different reaction: in the presence of a Pt/C catalyst, in a (liquid-liquid) biphase of an aqueous alkaline solution and toluene, cinnamyl alcohol was the sole product.[141] However, materials science research on bio-sourced functional carbon-based materials is not just about catalysts and their supports. The transition towards greener chemical processes extend to a range of advanced technologies based on safe, efficient, and sustainable materials, including fullerenes, nanotubes, nanoparticles and graphene, and more, that are key players for energy storage systems, photovoltaic devices, and fuel cells, among others. Nanomaterials, typically identified by having at least one spatial dimension measuring less than 100 nm, possess physical and chemical behaviour which often differ dramatically from those of the bulk material. Based on how many dimensions fall within this range, nanomaterials are categorized as nanoplates (one nanoscale dimension), nanofibers (two), or nanoparticles, in which all three dimensions are below 100 nm. Because of their high surface/volume ratios and quantum or surface-driven phenomena, they can exhibit peculiar optical properties or changes in thermal and electrical properties, but also enhanced reactivity, conductivity, and mechanical strength.

Over the years, carbon-based nanomaterials (**Figure 1.11**) have attracted major scientific attention and recognition, including several prestigious awards such as the 1996 Nobel Prize in Chemistry, awarded to Robert Curl, Richard Smalley, and Harold Kroto for the discovery of fullerenes, and the 2010 Nobel Prize in Physics, jointly awarded to Andre Geim and Konstantin Novoselov for their pioneering work on graphene, a one-atom-thick, two-dimensional lattice of carbon atoms.

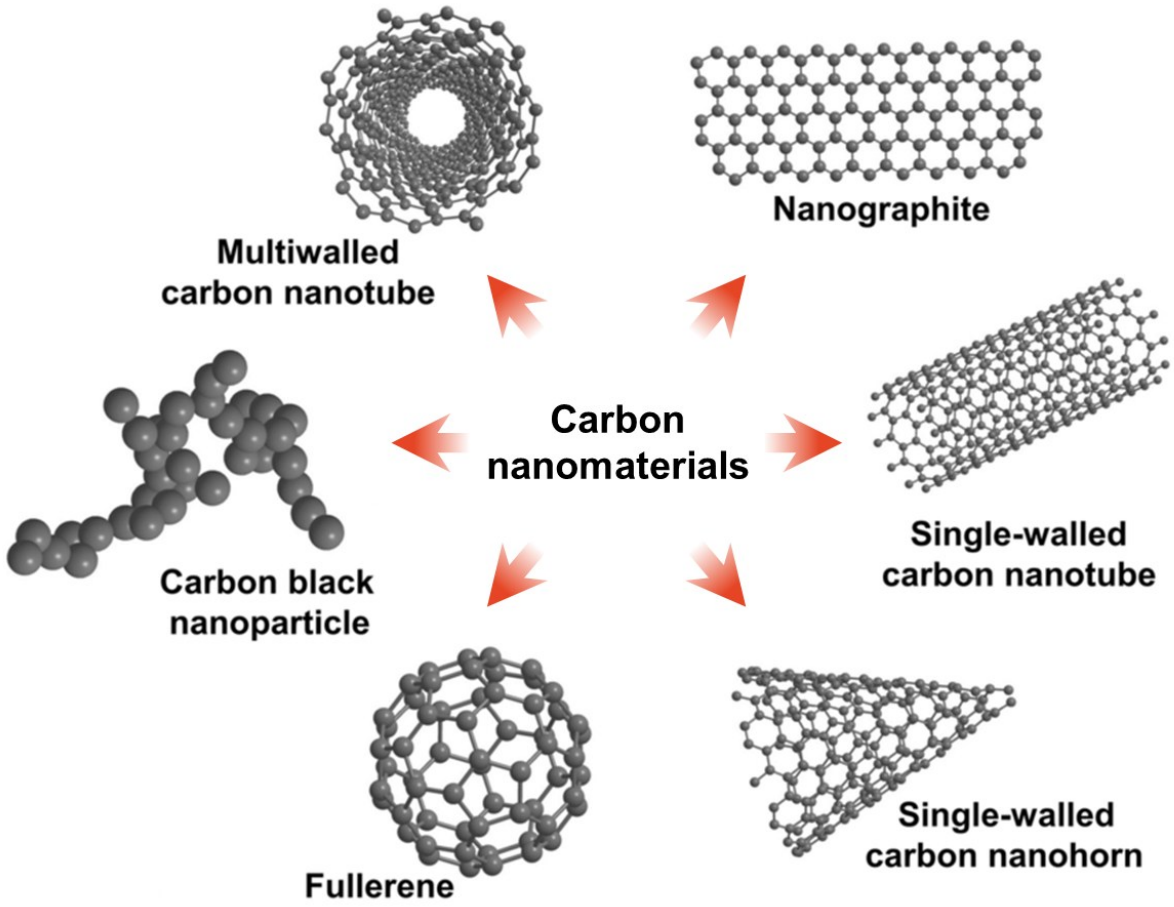

Figure 1.11. Pictorial representation of common carbon-based nanomaterials and their applications.

The current interest in these functional materials relies not only on the range of applications they may be designed for, but also on the preparation methods and customization opportunities that increasingly align with the principles of sustainability. These materials are generally synthesized using two complementary strategies: top-down and bottom-up approaches, both of which can directly influences the size, shape, and properties of the resulting products. Top-down approach involves breaking down the size of a bulk structure to the nanoscale and the bottom-up approach involves build-up of nanostructures from even smaller components, like molecules and atoms.[159]

An exciting category of such carbon-based nanomaterials is represented by carbon quantum dots (CQDs), also simply known as carbon dots. Carbon dots are tiny carbon-based particles with special photoluminescent properties, being able to efficiently absorb light and then re-emit it at different wavelengths. Their fluorescence is not only beautiful but also useful in many applications such as bioimaging, sensing, photocatalysis, batteries, and electronics.[160]

An attractive features of carbon dots is that they can be synthesised from a very wide range of carbon-rich substrates: among them inexpensive natural or waste-derived feedstocks as agricultural residues, by-products from the food industry, biowaste from fisheries, and other biomass sources, are increasingly being used as sustainable starting materials, with the double aim of reducing cost and environmental impact while enabling surface functionalisation with useful heteroatoms-rich functional groups.[161,162]

A striking application of carbon dots is their use as additives or interfacial layers in aqueous zinc-ion batteries (AZIBs). This topic is explored in more detail in the following section as it has been part of the research carried out in this doctoral thesis. As an example, carbon dots with abundant zincophilic functional groups such as –CHO or –C≡N, when employed as an artificially formed interface layer on Zn anodes, have been shown to markedly reduce the nucleation barrier for Zn^{2+}, achieve more uniform zinc deposition, suppress parasitic side reactions (including hydrogen evolution reaction, HER), and prolong cell life.[163]

N-doped Carbon Quantum Dots (N-CQDs) have been recently synthesised from bio-sources such as chitin and chitinous-containing fishery biowaste and used as an electrolyte additive in AZIBs. This study demonstrated remarkable improvements in suppressing Zinc dendrite formation and promoted uniform zinc deposition at current densities up to 20 mA/cm^2 for 4 hours of plating, with performances linked to their specific chemical and physical properties. This topic will be examined in more depth in Chapter 4, where the synthesis of carbon dots from chitin, crustacean shells, or other fishery waste will be explored, together with their integration in zinc battery systems.

1.5 Circular economy: a revised concept of waste

The linear economy based on "take–make–use–dispose" has deeply dominated our society during the industrialisation process. Within this traditional model, raw materials are extracted from nature, used to make products, and then these products thrown away once no longer needed (**Figure 1.12**).[164]

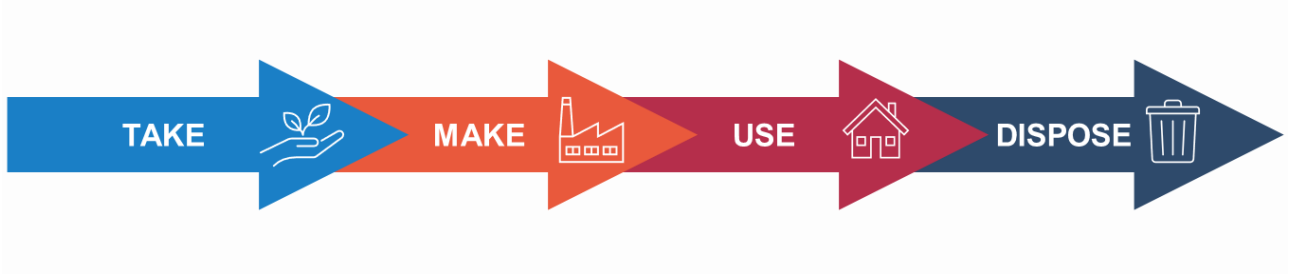

Figure 1.12. Pictorial illustration of the linear economy traditional model of "take–make–use–dispose".

Despite having helped economies to grow quickly for almost 200 years, the linear model is intrinsically unsustainable on our planet, bringing to the production of large amounts of waste, environmental pollution, and the depletion of limited natural resources. Global warming, microplastic dispersion, ocean acidification, and escalating material scarcity across industrial value chains, that have longed been ignored, are becoming increasingly visible by now, and will only become more pronounced in light of a global population that is expected to reach 9.7 billion individuals by 2050,[165] along with the demand for raw materials and energy.

In 1989, David W. Pearce and R. Kerry Turner first introduced the term “circular economy” to describe an economic system that mimic natural ecosystems, where nothing is wasted, and everything could become input for another process, encouraging this way recycling, reusing, repairing, and remanufacturing, instead of throwing things away.[166] The concept of the circular economy has then re-emerged in recent decades as a response to pressing global challenges related to environmental degradation and climate change, with its popularity growing significantly after the raising awareness efforts made by the sailor and philanthropist Ellen MacArthur. In 2005, while completing her solo sailing trip around the globe, she experienced first-hand the need to manage limited on-board resources with care and efficiency – an insight that inspired her to argue that humanity should adopt a similar mindset in managing Earth’s finite resources.

"The linear system, which depletes natural resources and generates waste, is deeply flawed and can be productively replaced by a model in which waste does not exist as such but is only food for the next cycle" – Ellen MacArthur

Inspired by this vision, researchers, policymakers and many others began to rethink how design, use, and reuse materials and resources in a more responsible and sustainable way. The circular approach is based on a continuous loop in which materials are used more efficiently, pollution is reduced, and products are designed for longer use and reuse, turning a traditionally considered waste into a resource for future value creation (**Figure 1.13**).

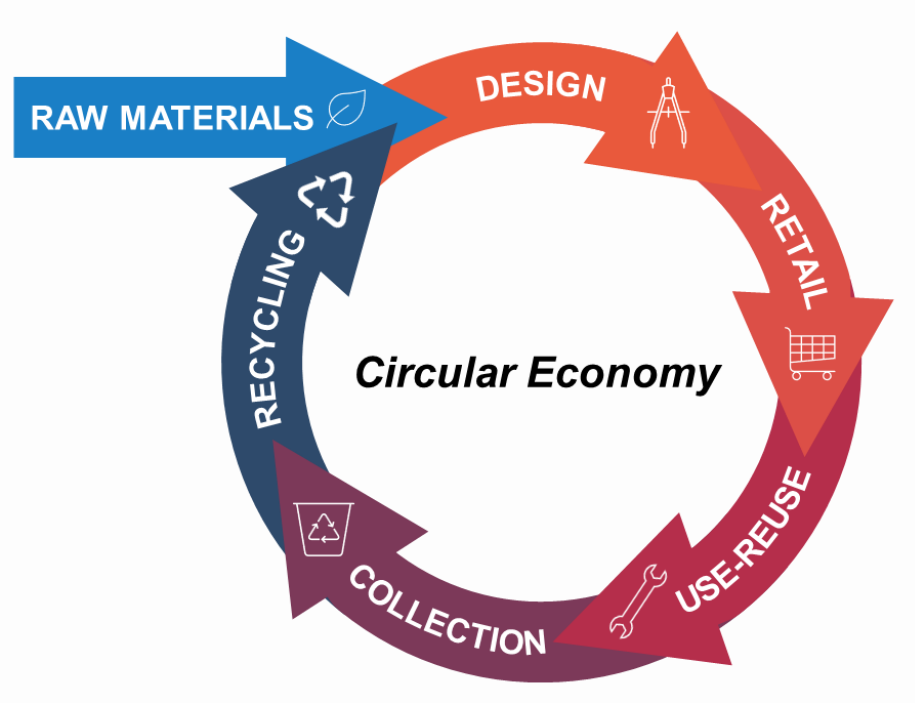

Figure 1.13. Pictorial illustration of the circular economy closed loop, represented as a regenerative system in which materials are specifically designed to sustainably remain in circulation through up-grading recycling.

Across Europe in particular, the recognition that manufactured goods and the use we make of them can have a significant impact on our environment, led the introduction of the Ecodesign for Sustainable Products Regulation (ESPR), which came into effect in mid-2024 to make products on the EU market more sustainable by boosting their circularity, energy efficiency, recyclability, and durability. Other Countries are moving in the same direction, with France (Anti-Waste and Circular Economy Law, 2022), Scotland (Circular Economy Act, 2024), and Australia (Product Lifecycle Responsibility Act of NSW, 2025) launching their national legislation to support this transition and holding manufacturers accountable for the

lifespan of their products, "*from cradle to grave*", aligning with the Sustainable Development Goals of the 2030 Agenda.

Chemistry plays a crucial role in this context, accounting for a large portion of industrial production (and waste generated), and is therefore central to implementing circular economy. In chemical research and material science, this circular model translates into the development of processes and technologies for waste valorisation and recovery of valuable compounds and polymers (waste-to-chemicals, waste-to-energy).

Among global waste streams, biowaste represents a significant and underutilised fraction. It refers to any biodegradable waste from food, agriculture, forestry, fisheries, and organic industrial by-products, including plant trimmings, shells, bones, offal, and sludge, often undervalued, despite its rich composition of bioactive compounds, nutrients, and structurally valuable polymers.[167,168] Hydrothermal carbonisation and pyrolysis of lignocellulosic residues are few of the most common strategies of biowaste valorisation for the production of carbon-rich materials such as hydrochar/biochar, biooils and platform chemicals.[169] Through anaerobic digestion, biomass can be transformed into biomethane.[170,171] Fermentation of carbohydrate-rich residues enables the generation of bio-based chemicals, such as organic acids and ethanol,[172] whereas food waste composting results effective to produce organic fertilizers (**Figure 1.14**).[173]

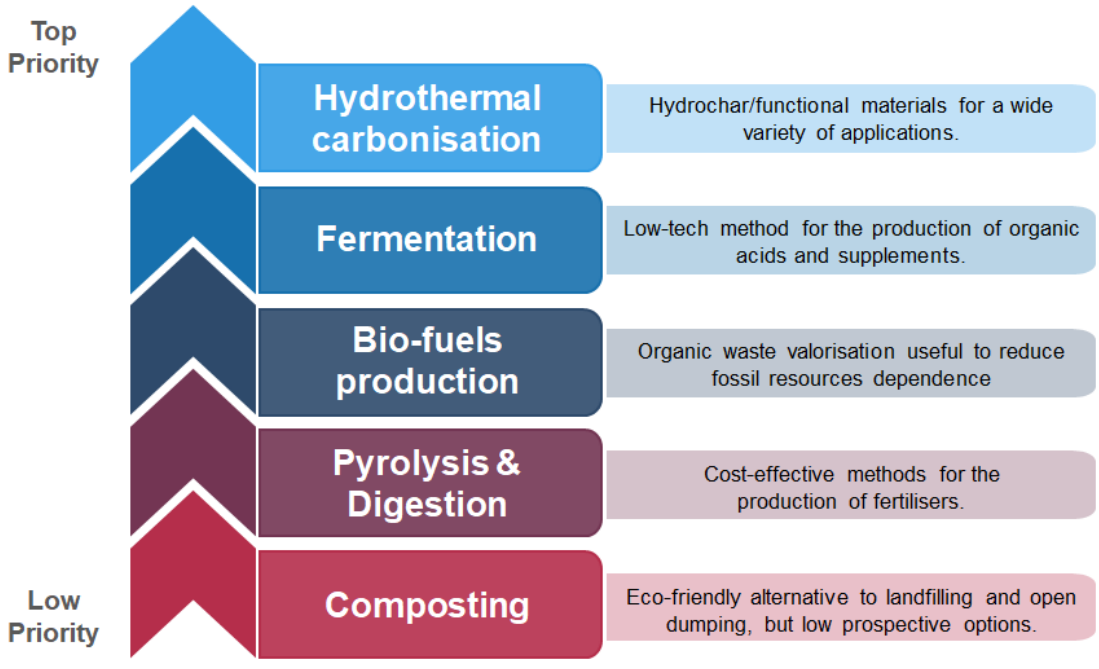

Figure 1.14. Example of biowaste valorisation strategies from low (bottom) to high (top) priority.

Other high-value routes of biowaste valorisation, especially those enabling the recovery of bioactive compounds, such as antioxidants, polyphenols and structurally valuable biopolymers, include the development and use of green extraction techniques, which seek to reduce energy input, avoid toxic chemicals, and maintain the structural integrity of sensitive biomolecules.[174]

Cutting-edge methods include several fast, energy-efficient techniques, as supercritical fluid extraction (SFE), ultrasound-assisted extraction (UAE), and microwave-assisted extraction (MAE), useful to isolate compounds suitable for nutraceutical and food applications.[175] Enzymatic hydrolysis and subcritical water extraction (SWE) are further methods interesting for their sustainability, scalability and versatility.[176]

Within this context, deep eutectic solvents (DESs) and ionic liquids (ILs) recently gained attention as a class of green extraction solvents.[177–180] Both lipophilic species such as omega-3 fatty acids,[181] carotenoids,[182] and essential oils,[183] and more polar derivatives like phenols, antioxidants, or proteins can be selectively extracted with high yields and preserved bioactivity.[184,185] ILs such as [Ch][Lys] (choline lysine), for instance, have demonstrated astonishing capability to selectively extract lignin (up to 60 wt.% yield) from rice straw and other lignocellulosic waste. and at the same time, they can be reused across several cycles, up to 5, without significant decrease in delignification efficiency.[186–188]

An ILs-assisted green extraction approach for chitin recovery from biowaste, specifically crab shells, has recently been developed within our research group.[189] In particular, high-quality chitin was isolated almost quantitatively by synthesising formate-based ILs in a one-pot sustainable process. This topic, together with the valorisation of fishery waste, represents a central theme of this thesis and will be further discussed in the following sections and in Chapter 3.

Overall, these technologies, albeit offering a lot of opportunities, are not without challenges. Scalability, cost-efficiency, and biodegradability (especially for ILs), still represent issues to be addressed to close the loop in resource use.

1.6 Fishery waste valorisation

Aquatic foods like fish, shellfish, and seaweeds, are among the most nutrient-dense sources available, providing omega-3 fatty acids, essential micronutrients and high-quality protein, being especially important in areas where food insecurity is widespread.[190] Global seafood production (**Figure 1.15**) has reached over 200 million tonnes per year and a value of $472 billion in 2022, with much of this growth coming from aquaculture.[191] Alongside this impressive production, however, comes a significant amount of waste. In a 2025 report, the Food and Agriculture Organization (FAO) of the UN outlined that the global edible aquatic Food Loss and Waste (FLW) reached 23.8 million tonnes in 2021, representing the 15% of the total aquatic food produced that year.[192] This trend reflects many inefficiencies throughout the entire value chain, from production and processing to distribution and end use, and pose serious environmental and ethical challenges.

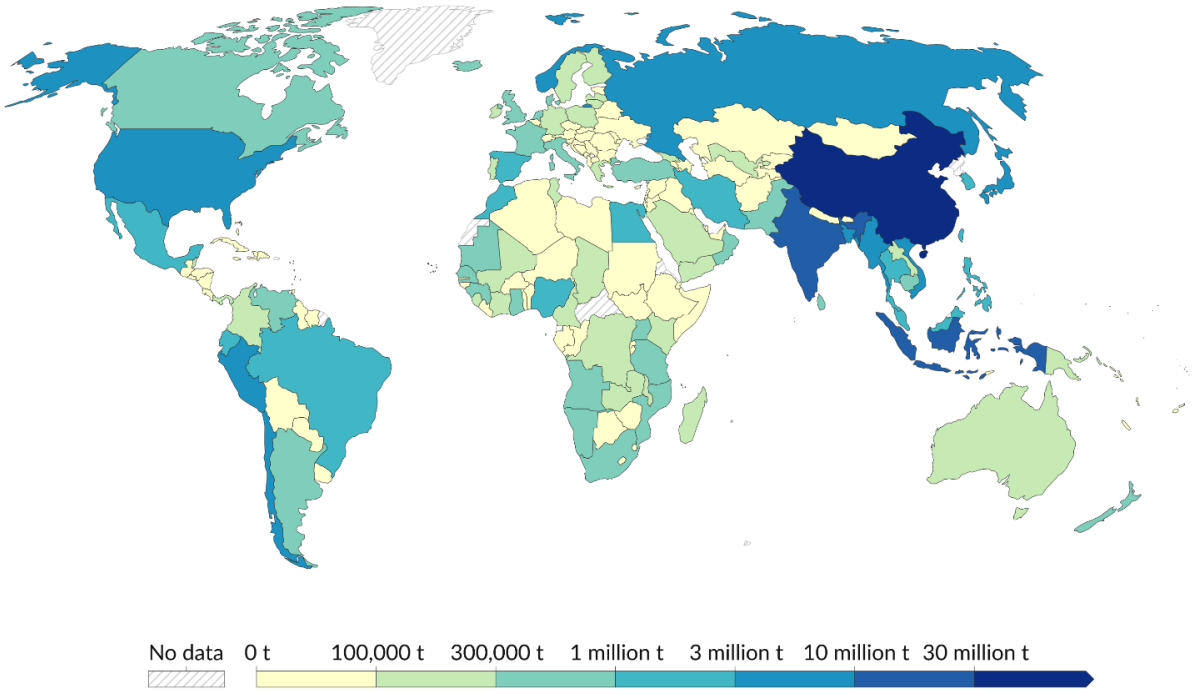

Figure 1.15. Fish and seafood production (2022) around the World, as sum of fish from aquaculture and wild fish catching.[193] Adapted from [194].

On the other hand, fishery waste from the seafood industry represents an excellent source for valorisation.[195] This biowaste contains approximately 58 ± 5% proteins, 19 ± 6% fats, 1 ± 1% fibre, 22 ± 3% ash, and mineral elements (including Ca, P, K, Na, Mg, Fe, Zn, Mn, and Cu), in a variable composition according to fish species, sex, age, nutritional status, season,

and health conditions. The extent and nature of food loss and waste in aquatic supply chains vary considerably across regions, species, and stages of production and distribution.[196] In low- and middle-income countries, losses can reach up to 40% and tend to occur shortly after harvest, largely due to lack of cold storage, poor handling, and inefficient transport.[197] By contrast, in higher-income countries, most losses occur at retail and consumer levels, frequently driven by consumer expectations for appearance and market standards, over-purchasing, and misunderstanding of labelling terms like “best before”.[198] In addition, another issue is the edible biomass lost in the sea due to unintentional capture of non-target species, known as bycatching, which is responsible for the discard of fish that are either undersized, unmarketable, or caught in excess. These losses not only reduce food for human consumption but also raise sustainability and social concerns in terms of inefficient use of resources and energy.

An issue with fishery waste valorisation is the perishability and the short shelf life of aquatic species that make them vulnerable to spoilage. Indeed, fish spoilage quickly occurs after death due to proteolytic enzymes that initiate the breakdown of adenosine 5′-triphosphate (ATP). These leads to the sequential formation of ADP, AMP, IMP, inosine, and hypoxanthine, and weakens muscle structure and reducing water-holding capacity. Simultaneously, microbial populations proliferate in the flesh, metabolizing nitrogen-rich substrates such as free amino acids and peptides. This activity generates many volatile compounds, including biogenic amines (histamine, cadaverine, putrescine), trimethylamine (TMA), ammonia (NH_3), organic acids, sulphides, alcohols, aldehydes, and ketones, which are responsible for unpleasant taste and smell.[199]

As in general for biowaste, valorisation of fishery waste can involve several high-impact strategies (**Figure 1.16**). One of the most prominent is the extraction of nitrogen-rich bioactive compounds, including collagen, chitin, gelatine, and peptides, which find a lot of applications in food supplements, nutraceuticals, cosmetics, biomedical, and pharmaceuticals fields.[200] An interesting perspective is the so-called shell biorefinery for the processing of crustacean shells enabling the supply of chitin, calcium carbonate, and proteins for the market of bio-commodities and biomaterials. By contrast, low-tech approaches, such as the production of fishmeal through drying or cooking, remain common in remote regions lacking suitable infrastructure, but generate mainly low-value products for feed and fertilizers.

It should be mentioned, however, that fish oil generated as a by-product of fishmeal, although often unsuitable for food use, may find uses in the co-generation of energy as an in-house or regional fuel. In this case, fish oil obtained after hard boiling of fish residues is subjected to catalytic transesterification with both methanol and ethanol to get a mixture of fatty acid methyl or ethyl esters (FAMEs or FAEEs) that must fulfil standard biodiesel specifications (ASTM D6751).[201]

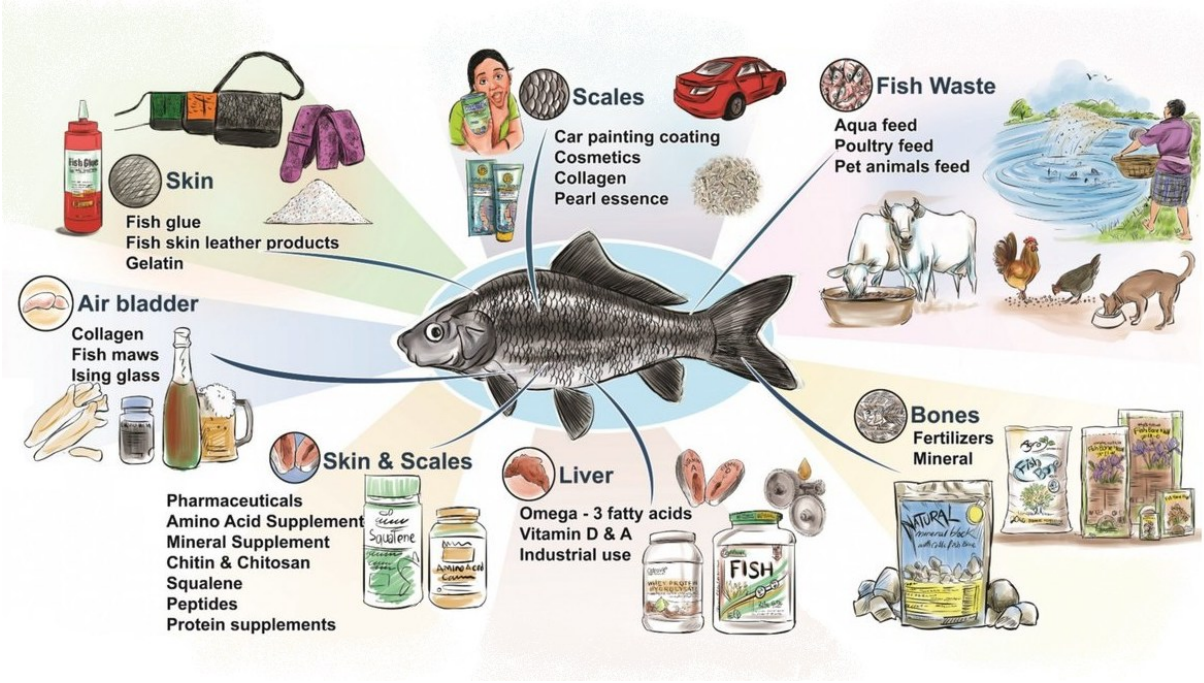

Figure 1.16. Fishery waste valorisation strategies. Adapted from [202].

These valorisation strategies directly contribute to the UN 2030 Agenda for Sustainable Development, particularly SDG 2 on “Zero Hunger”, SDG 12 on “Responsible Consumption and Production” and SDG 14 on “Life Below Water”. Despite a lot of work is still needed to overcome some critical technical limitations, valorisation of fishery by-products shows strong potential and with supportive policies and investments, can become a strategic tool towards the transition to a global circular economy. A particular focus on this topic will find place in Chapter 3, by investigating innovative IL-mediated techniques for the extraction of chitin from crab shells.

1.7 Aim and structure of the Thesis

This Thesis work was carried out as part of a Cotutelle PhD program between Università Ca' Foscari Venezia, Italia, and The University of Sydney, Australia. Approximately two-thirds of the entire research period were spent in Venice within the Green Organic Synthesis Team (GOST) under the supervision of Professor Maurizio Selva, and about one-third at the Laboratory of Advanced Catalysis for Sustainability under the supervision of Professor Thomas Maschmeyer. Although not all members of these two groups are listed among the authors of the experimental works presented in this Thesis, each of them provided an essential contribution – either intellectual or moral support – to the completion of the projects here described, which results will be illustrated in the following Chapters.

The contribution to the advancement of sustainable and circular approaches in chemistry was the leitmotiv of this doctoral research, with particular emphasis on the optimisation of greener synthetic and extraction protocols, as well as on the valorisation of biowaste for the development of advanced functional materials. In particular, the research was conducted pursuing the following objectives:

i) the conceptualisation and optimisation of a sustainable multiphasic catalytic system.

As previously mentioned in Section 1.4, multiphasic catalytic systems offer significant advantages in controlling the reactivity of chemical species through the confinement of reagents, products and catalyst in different phases. The mechanisms underlying this configuration were investigated through extensive bibliographical research among literature, which led to the publication of a review article on this topic and provided the necessary consciousness for developing a multiphasic catalytic system based on a non-noble metal catalyst and air as an oxidant for the selective oxidation of primary alcohols (both benzylic and aliphatic). An additional advantage of multiphase systems lies in the ease of product recovery and catalyst recycling, often enabled by the use of a catalyst-philic phase, such as an ionic liquid, which segregates the catalyst. This aspect was explored in detail by testing the resilience of the system for multiple consecutive catalytic cycles and extensively discussed in Chapter 2.

ii) the development of an environmentally friendly protocol for chitin extraction from fishery biowaste through the employment of ionic liquids.

This project involved several collaborators. The author's main contribution focused on optimising the extraction parameters, such as biomass loading, pulping temperature and duration, along with an extensive characterisation of the so obtained products, with the aim of establishing an effective one-pot process to achieve both demineralisation and deproteinisation of the starting organic matrix (Spider crab shells). The proposed environmentally benign pulping method successfully yielded high-quality chitin, demonstrating that the route to making some industrial processes more sustainable is viable, despite some efforts still need to be made. This topic is discussed in Chapter 3.

iii) the design and optimisation of a synthetic procedure for the preparation of advanced nanomaterials to be used as non-toxic, water-stable, and cost-effective additives for improving the performance of zinc aqueous batteries.

Building on the knowledge gained from biowaste valorisation studies, this research project – mainly carried out at The University of Sydney – explored the use of chitin and crab waste as precursors for the synthesis of nitrogen-doped carbon dots. Chapter 4 examines in depth the critical role played by heteroatoms, incorporated into the carbon matrix during the hydrothermal treatment, which promote Zn^{2+} coordination in aqueous electrolytes, thus enhancing the performance of aqueous zinc-ion batteries in terms of dendrite suppression and electrochemical stability.

Through these interconnected studies, the thesis aims to bridge the gap between the conceptual principles of sustainable chemistry and their practical implementation, demonstrating how circular valorisation of organic waste can lead to concrete advances in materials science and green technology.

Bibliography

1. Daniel Scholten. *Handbook on the Geopolitics of the Energy Transition*. (Edward Elgar Publishing, 2023). doi:10.4337/9781800370432.
2. Volk, A. A. & Atkinson, J. A. Infant and child death in the human environment of evolutionary adaptation. *Evol. Hum. Behav.* **34**, 182–192 (2013).
3. World Health Organization (WHO), the United Nations Children's Fund (UNICEF), the United Nations Population Fund (UNFPA), the W. & Division, B. and the U. N. P. *World Population Prospects: The 2024 Revision*. (2024).
4. *A Companion to Global Environmental History*. (Wiley, 2025). doi:10.1002/9781119988229.
5. Goldewijk, K. K. Three Centuries of Global Population Growth: A Spatial Referenced Population (Density) Database for 1700–2000. *Popul. Environ.* **26**, 343–367 (2005).
6. Soeder, D. J. *Energy Futures*. (Springer Nature Switzerland, Cham, 2025). doi:10.1007/978-3-031-83603-9.
7. Fourier, J. Remarques générales sur les températures du globe terrestre et des espaces planétaires. *Ann. Chem. Phys.* **27**, 136–167 (1824).
8. Foot, E. Circumstances affecting the heat of the sun's rays. ART. XXXI. *Am. J. Sci. Arts* **22**, 382 (1856).
9. Tyndall, J. *Heat Considered as a Mode of Motion.* (D. Appleton and Company, New York, 1875).
10. Arrhenius, S. XXXI. On the influence of carbonic acid in the air upon the temperature of the ground. *Lond. Edinb. Dublin Philos. Mag. J. Sci.* **41**, 237–276 (1896).
11. Filonchyk, M., Peterson, M. P., Zhang, L., Hurynovich, V. & He, Y. Greenhouse gases emissions and global climate change: Examining the influence of CO2, CH4, and N2O. *Sci. Total Environ.* **935**, 173359 (2024).
12. YUE, X.-L. & GAO, Q.-X. Contributions of natural systems and human activity to greenhouse gas emissions. *Adv. Clim. Change Res.* **9**, 243–252 (2018).
13. Rogers, J. S., Maneta, M. P., Sain, S. R., Madaus, L. E. & Hacker, J. P. The role of climate and population change in global flood exposure and vulnerability. *Nat. Commun.* **16**, 1287 (2025).
14. Neubauer, S. C. Global Warming Potential Is Not an Ecosystem Property. *Ecosystems* **24**, 2079–2089 (2021).

15. Intergovernmental Panel on Climate Change (IPCC). Anthropogenic and Natural Radiative Forcing. in *Climate Change 2013 – The Physical Science Basis* 659–740 (Cambridge University Press, 2014). doi:10.1017/CBO9781107415324.018.
16. Yurak, V. V. & Fedorov, S. A. Review of natural and anthropogenic emissions of carbon dioxide into the earth's atmosphere. *Int. J. Environ. Sci. Technol.* **22**, 2719–2736 (2025).
17. Le Quéré, C. *et al.* Trends in the sources and sinks of carbon dioxide. *Nat. Geosci.* **2**, 831–836 (2009).
18. Trends in Atmospheric Carbon Dioxide (CO2). https://gml.noaa.gov/ccgg/trends/.
19. Intergovernmental Panel on Climate Change (IPCC). Summary for Policymakers. in *Climate Change 2021 – The Physical Science Basis* 3–32 (Cambridge University Press, 2021). doi:10.1017/9781009157896.001.
20. Mauna Loa Fossil Fuel Trend - Scripps CO2 Program. https://scrippsco2.ucsd.edu/graphics_gallery/mauna_loa_record/mauna_loa_fossil_fuel_trend.html.
21. United Nation Climate Action. Causes and Effects of Climate Change. https://www.un.org/en/climatechange/science/causes-effects-climate-change.
22. NOAA Climate.gov. Climate change: global temperature. https://www.climate.gov/news-features/understanding-climate/climate-change-global-temperature (2025).
23. Meehl, G. A., Tebaldi, C., Walton, G., Easterling, D. & McDaniel, L. Relative increase of record high maximum temperatures compared to record low minimum temperatures in the U.S. *Geophys. Res. Lett.* **36**, (2009).
24. Ed Hawkins. Show Your Stripes. https://showyourstripes.info/.
25. Kidane, B. *et al.* Nutritional challenges of staple crops due to increasing atmospheric carbon dioxide levels: Case of Sub-Saharan Africa. *J. Agric. Food Res.* **19**, 101592 (2025).
26. Jacobson, T. A. *et al.* Direct human health risks of increased atmospheric carbon dioxide. *Nat. Sustain.* **2**, 691–701 (2019).
27. Lelieveld, J., Evans, J. S., Fnais, M., Giannadaki, D. & Pozzer, A. The contribution of outdoor air pollution sources to premature mortality on a global scale. *Nature* **525**, 367–371 (2015).
28. Max-Planck-Gesellschaft. More deaths due to air pollution. www.mpg.de/9405012/mortality-air-pollution (2015).

29. United Nation Climate Action. Taking action for the health of people and the planet. https://www.un.org/en/climatechange/science/climate-issues/health#:~:text=Between 2030 and 2050%2C climate change is,stress%2C according to the World Health Organization.
30. Lane, M. K. M. *et al.* Green chemistry as just chemistry. *Nat. Sustain.* **6**, 502–512 (2023).
31. *Routledge Handbook of Climate Justice*. (Routledge, 2018). doi:10.4324/9781315537689.
32. Jafry, T. & Platje, J. (Joost). Climate justice – a new narrative informing development and climate policy. *Int. J. Clim. Change Strateg. Manag.* **8**, 474–476 (2016).
33. Fawzy, S., Osman, A. I., Doran, J. & Rooney, D. W. Strategies for mitigation of climate change: a review. *Environ. Chem. Lett.* **18**, 2069–2094 (2020).
34. Almeida, P., González Márquez, L. R. & Fonsah, E. The forms of climate action. *Sociol. Compass* **18**, (2024).
35. FALKNER, R. The Paris Agreement and the new logic of international climate politics. *Int. Aff.* **92**, 1107–1125 (2016).
36. United Nations Environment Programme. *We Are All in This Together - Annual Report 2024*. (2025).
37. United Nation Climate Action. Net-zero commitments must be backed by credible action. https://www.un.org/sw/node/134483.
38. Dietz, T., Shwom, R. L. & Whitley, C. T. Climate Change and Society. *Annu. Rev. Sociol.* **46**, 135–158 (2020).
39. Ligon, B. L. Penicillin: its discovery and early development. *Semin. Pediatr. Infect. Dis.* **15**, 52–57 (2004).
40. Ray, D. C., Drummond, G. B. Halothane hepatitis. *Br. J. Anaesth.* **67**, 84–99 (1991).
41. McDonnell, G. & Russell, A. D. Antiseptics and Disinfectants: Activity, Action, and Resistance. *Clin. Microbiol. Rev.* **12**, 147–179 (1999).
42. Taylor, D. L., Kahawita, T. M., Cairncross, S. & Ensink, J. H. J. The Impact of Water, Sanitation and Hygiene Interventions to Control Cholera: A Systematic Review. *PLOS ONE* **10**, e0135676 (2015).
43. Taube, J. C., Rest, E. C., Lloyd-Smith, J. O. & Bansal, S. The global landscape of smallpox vaccination history and implications for current and future orthopoxvirus susceptibility: a modelling study. *Lancet Infect. Dis.* **23**, 454–462 (2023).

44. Esparza, J., Nitsche, A. & Damaso, C. R. Beyond the myths: Novel findings for old paradigms in the history of the smallpox vaccine. *PLOS Pathog.* **14**, e1007082 (2018).
45. World Health Organization (WHO). Global immunization efforts have saved at least 154 million lives over the past 50 years. https://www.who.int/news/item/24-04-2024-global-immunization-efforts-have-saved-at-least-154-million-lives-over-the-past-50-years (2024).
46. Smith, C., Hill, A. K. & Torrente-Murciano, L. Current and future role of Haber–Bosch ammonia in a carbon-free energy landscape. *Energy Environ. Sci.* **13**, 331–344 (2020).
47. Wang, M. *et al.* Can sustainable ammonia synthesis pathways compete with fossil-fuel based Haber–Bosch processes? *Energy Environ. Sci.* **14**, 2535–2548 (2021).
48. Ameen, A. & Raza, S. Green Revolution: A Review. *Int. J. Adv. Sci. Res.* **3**, 129 (2018).
49. Baker, I. Bakelite. in *Fifty Materials That Make the World* 15–17 (Springer International Publishing, Cham, 2018). doi:10.1007/978-3-319-78766-4_4.
50. Feldman, D. Polymer History. *Des. Monomers Polym.* **11**, 1–15 (2008).
51. Geyer, R., Jambeck, J. R. & Law, K. L. Production, use, and fate of all plastics ever made. *Sci. Adv.* **3**, (2017).
52. Horváth, I. T. Introduction: Sustainable Chemistry. *Chem. Rev.* **118**, 369–371 (2018).
53. Ragusa, A. *et al.* Plasticenta: First evidence of microplastics in human placenta. *Environ. Int.* **146**, 106274 (2021).
54. Anastas, P. T. & Warner, J. C. What is green chemistry? in *Green Chemistry* 11–20 (Oxford University PressOxford, 2000). doi:10.1093/oso/9780198506980.003.0002.
55. Sheldon, R. A. The E factor at 30: a passion for pollution prevention. *Green Chem.* **25**, 1704–1728 (2023).
56. Anastas, P. T. & Warner, J. C. *Green Chemistry: Theory and Practice*. (Oxford University Press, 2000). doi:10.1093/oso/9780198506980.001.0001.
57. Zuin, V. G., Eilks, I., Elschami, M. & Kümmerer, K. Education in green chemistry and in sustainable chemistry: perspectives towards sustainability. *Green Chem.* **23**, 1594–1608 (2021).
58. Shakhashiri, B. Z. & Bell, J. A. Climate change and our responsibilities as chemists. *Arab. J. Chem.* **7**, 5–9 (2014).
59. Bachmann, M. *et al.* Towards circular plastics within planetary boundaries. *Nat. Sustain.* **6**, 599–610 (2023).

60. Mitchell, S., Martín, A. J., Guillén-Gosálbez, G. & Pérez-Ramírez, J. The Future of Chemical Sciences is Sustainable. *Angew. Chem. Int. Ed.* **63**, (2024).
61. United Nations. 17 Goals to Transform Our World. https://www.un.org/sustainabledevelopment/ (2015).
62. Fuso Nerini, F. *et al.* Connecting climate action with other Sustainable Development Goals. *Nat. Sustain.* **2**, 674–680 (2019).
63. Aversa, R., Petrescu, V., Apicella, A. & Petrescu, I. T. The Basic Elements of Life's. *Am. J. Eng. Appl. Sci.* **9**, 1189–1197 (2016).
64. Simon Pirani. *Burning Up - A Global History of Fossil Fuel Consumption*. (Pluto Press, 2018).
65. Dimitra Papadovasilaki & Federico Guerrero & Rattaphon Wuthisatian & Bhraman Gulati. The 1920s technological revolution and the crash of 1929: the role of RCA, DuPont, General Motors, and Union Carbide. *SN Bus. Econ.* **2**, 1–22 (2022).
66. Chauhan, R., Sartape, R., Minocha, N., Goyal, I. & Singh, M. R. Advancements in Environmentally Sustainable Technologies for Ethylene Production. *Energy Fuels* **37**, 12589–12622 (2023).
67. Leung, J. J., Goult, P. & Min, G. *Manufacturing Ethylene: Facts, Impacts, and Pathways*. (2025).
68. Bozzano, G. & Manenti, F. Efficient methanol synthesis: Perspectives, technologies and optimization strategies. *Prog. Energy Combust. Sci.* **56**, 71–105 (2016).
69. *Methanol: The Basic Chemical and Energy Feedstock of the Future: Asinger's Vision Today*. (Springer Berlin Heidelberg, Berlin, Heidelberg, 2014). doi:10.1007/978-3-642-39709-7.
70. Dalena, F. *et al.* Methanol Production and Applications: An Overview. in *Methanol* 3–28 (Elsevier, 2018). doi:10.1016/B978-0-444-63903-5.00001-7.
71. Tabibian, S. S. & Sharifzadeh, M. Statistical and analytical investigation of methanol applications, production technologies, value-chain and economy with a special focus on renewable methanol. *Renew. Sustain. Energy Rev.* **179**, 113281 (2023).
72. Leckel, D. Diesel Production from Fischer−Tropsch: The Past, the Present, and New Concepts. *Energy Fuels* **23**, 2342–2358 (2009).
73. Schulz, H. Short history and present trends of Fischer–Tropsch synthesis. *Appl. Catal. Gen.* **186**, 3–12 (1999).
74. Dry, M. E. The Fischer–Tropsch process: 1950–2000. *Catal. Today* **71**, 227–241 (2002).

75. Cornils, B., Herrmann, W. A. & Rasch, M. Otto Roelen, Pioneer in Industrial Homogeneous Catalysis. *Angew. Chem. Int. Ed. Engl.* **33**, 2144–2163 (1994).
76. Kohlpaintner, C. W., Fischer, R. W. & Cornils, B. Aqueous biphasic catalysis: Ruhrchemie/Rhône-Poulenc oxo process. *Appl. Catal. Gen.* **221**, 219–225 (2001).
77. Tao, S. *et al.* Single-atom catalysts for hydroformylation of olefins. *iScience* **26**, 106183 (2023).
78. Grubbs, R. H. Olefin metathesis. *Tetrahedron* **60**, 7117–7140 (2004).
79. Mol, J. Industrial applications of olefin metathesis. *J. Mol. Catal. Chem.* **213**, 39–45 (2004).
80. Hossain, Md. T. *et al.* Research and application of polypropylene: a review. *Discov. Nano* **19**, 2 (2024).
81. Alsabri, A., Tahir, F. & Al-Ghamdi, S. G. Environmental impacts of polypropylene (PP) production and prospects of its recycling in the GCC region. *Mater. Today Proc.* **56**, 2245–2251 (2022).
82. Karali, N., Khanna, N. & Shah, N. *Climate Impact of Primary Plastic Production*. https://escholarship.org/uc/item/6cc1g99q (2024).
83. United Nations Climate Action. Plastics – fueling oil demand, climate change and pollution. https://www.un.org/en/climatechange/science/climate-issues/plastics#:~:text=Plastics%20generated%201.8%20billion%20tonnes,expected%20to%20triple%20by%202060.
84. Wang, J. & Azam, W. Natural resource scarcity, fossil fuel energy consumption, and total greenhouse gas emissions in top emitting countries. *Geoscience Frontiers* https://linkinghub.elsevier.com/retrieve/pii/S1674987123002244 (2024).
85. Speirs, J., McGlade, C. & Slade, R. Uncertainty in the availability of natural resources: Fossil fuels, critical metals and biomass. *Energy Policy* **87**, 654–664 (2015).
86. Welsby, D., Price, J., Pye, S. & Ekins, P. Unextractable fossil fuels in a 1.5 °C world. *Nature* **597**, 230–234 (2021).
87. Abbass, K. *et al.* A review of the global climate change impacts, adaptation, and sustainable mitigation measures. *Environ. Sci. Pollut. Res.* **29**, 42539–42559 (2022).
88. IEA - International Energy Agency. Global Energy Review 2025 - Energy demand accelerates, with electricity leading the way. https://www.iea.org/reports/global-energy-review-2025/global-trends.

89. Ahmad, T. & Zhang, D. A critical review of comparative global historical energy consumption and future demand: The story told so far. *Energy Rep.* **6**, 1973–1991 (2020).
90. Energy Institute - Statistical Review of World Energy. Primary energy from other renewables. (2025).
91. Our World in Data. Global Primary Energy Consumption by Source - dataset with major processing by Our World in Data. https://ourworldindata.org/energy-production-consumption.
92. Ohara, H. Biorefinery. *Appl. Microbiol. Biotechnol.* **62**, 474–477 (2003).
93. Balat, M., Balat, H. & Öz, C. Progress in bioethanol processing. *Prog. Energy Combust. Sci.* **34**, 551–573 (2008).
94. Rehfeldt, M., Worrell, E., Eichhammer, W. & Fleiter, T. A review of the emission reduction potential of fuel switch towards biomass and electricity in European basic materials industry until 2030. *Renew. Sustain. Energy Rev.* **120**, 109672 (2020).
95. United Nations Trade & Development. *Second-Generation Biofuel Markets: State of Play, Trade and Developing Country Perspectives*. https://unctad.org/publication/second-generation-biofuel-markets-state-play-trade-and-developing-country-perspectives (2016).
96. Ragauskas, A. J. *et al.* Lignin Valorization: Improving Lignin Processing in the Biorefinery. *Science* **344**, 1246843 (2014).
97. Cherubini, F. The biorefinery concept: Using biomass instead of oil for producing energy and chemicals. *Energy Convers. Manag.* **51**, 1412–1421 (2010).
98. Werpy, T. & Petersen, G. *Top Value Added Chemicals from Biomass: Volume I -- Results of Screening for Potential Candidates from Sugars and Synthesis Gas*. DOE/GO-102004-1992, 15008859 http://www.osti.gov/servlets/purl/15008859/ (2004) doi:10.2172/15008859.
99. Pandey, A. & Sharma, Y. C. Advancements in biomass valorization in integrated biorefinery systems. *Biofuels Bioprod. Biorefining* **18**, 2078–2090 (2024).
100. Rauch, R., Kiennemann, A. & Sauciuc, A. Fischer-Tropsch Synthesis to Biofuels (BtL Process). in *The Role of Catalysis for the Sustainable Production of Bio-fuels and Bio-chemicals* 397–443 (Elsevier, 2013). doi:10.1016/B978-0-444-56330-9.00012-7.
101. Makepa, D. C. & Chihobo, C. H. Sustainable pathways for biomass production and utilization in carbon capture and storage—a review. *Biomass Convers. Biorefinery* **15**, 11397–11419 (2025).

102. Wang, R., Wen, X., Wang, X., Fu, Y. & Zhang, Y. Low carbon optimal operation of integrated energy system based on carbon capture technology, LCA carbon emissions and ladder-type carbon trading. *Appl. Energy* **311**, 118664 (2022).
103. Wang, W., Yuan, B., Sun, Q. & Wennersten, R. Application of energy storage in integrated energy systems — A solution to fluctuation and uncertainty of renewable energy. *J. Energy Storage* **52**, 104812 (2022).
104. Berjawi, A. E. H., Walker, S. L., Patsios, C. & Hosseini, S. H. R. An evaluation framework for future integrated energy systems: A whole energy systems approach. *Renew. Sustain. Energy Rev.* **145**, 111163 (2021).
105. Chen, S., Liu, J., Zhang, Q., Teng, F. & McLellan, B. C. A critical review on deployment planning and risk analysis of carbon capture, utilization, and storage (CCUS) toward carbon neutrality. *Renew. Sustain. Energy Rev.* **167**, 112537 (2022).
106. ARC Centre of Excellence for Carbon Science and Innovation (COE-CSI). Transforming Carbon Science and Innovation for a clean and sustainable future. https://www.carboncentre.org.au/.
107. Ao, W. *et al.* Microwave assisted preparation of activated carbon from biomass: A review. *Renew. Sustain. Energy Rev.* **92**, 958–979 (2018).
108. Tay, T., Ucar, S. & Karagöz, S. Preparation and characterization of activated carbon from waste biomass. *J. Hazard. Mater.* **165**, 481–485 (2009).
109. Jjagwe, J., Olupot, P. W., Menya, E. & Kalibbala, H. M. Synthesis and Application of Granular Activated Carbon from Biomass Waste Materials for Water Treatment: A Review. *J. Bioresour. Bioprod.* **6**, 292–322 (2021).
110. Shi, J. *et al.* Advances in multifunctional biomass-derived nanocomposite films for active and sustainable food packaging. *Carbohydr. Polym.* **301**, 120323 (2023).
111. Mu, Y. *et al.* Recent advances in research on biomass-based food packaging film materials. *Compr. Rev. Food Sci. Food Saf.* **24**, e70093 (2025).
112. Reza, M. S. *et al.* Preparation of activated carbon from biomass and its' applications in water and gas purification, a review. *Arab J. Basic Appl. Sci.* **27**, 208–238 (2020).
113. Blankenship, L. S. & Mokaya, R. Modulating the porosity of carbons for improved adsorption of hydrogen, carbon dioxide, and methane: a review. *Mater. Adv.* **3**, 1905–1930 (2022).
114. Gayathiri, M., Pulingam, T., Lee, K. T. & Sudesh, K. Activated carbon from biomass waste precursors: Factors affecting production and adsorption mechanism. *Chemosphere* **294**, 133764 (2022).

115. Asrafali, S. P., Periyasamy, T. & Bari, G. A. K. M. R. Advances in Carbon-Based Aerogels for CO2 Capture: Fundamental Design Strategies and Technological Progress. *Gels* **11**, 361 (2025).
116. Jha, M. K. *et al.* Surface Modified Activated Carbons: Sustainable Bio-Based Materials for Environmental Remediation. *Nanomaterials* **11**, 3140 (2021).
117. Iwanow, M., Gärtner, T., Sieber, V. & König, B. Activated carbon as catalyst support: precursors, preparation, modification and characterization. *Beilstein J. Org. Chem.* **16**, 1188–1202 (2020).
118. Alam, M. M. *et al.* The Potentiality of Rice Husk-Derived Activated Carbon: From Synthesis to Application. *Processes* **8**, 203 (2020).
119. Yang, J. *et al.* Iron doped effects on active sites formation over activated carbon supported Mn-Ce oxide catalysts for low-temperature SCR of NO. *Chem. Eng. J.* **379**, 122398 (2020).
120. Sheldon, R. A. & Downing, R. S. Heterogeneous catalytic transformations for environmentally friendly production. *Appl. Catal. Gen.* **189**, 163–183 (1999).
121. Poier, D. *et al.* Reaction Environment Design for Multigram Synthesis via Sonogashira Coupling over Heterogeneous Palladium Single-Atom Catalysts. *ACS Sustain. Chem. Eng.* **11**, 16935–16945 (2023).
122. Hai, X. *et al.* Geminal-atom catalysis for cross-coupling. *Nature* **622**, 754–760 (2023).
123. Osorio-Tejada, J. L., Ferlin, F., Vaccaro, L. & Hessel, V. The sustainability impact of Nobel Prize Chemistry: life cycle assessment of C–C cross-coupling reactions. *Green Chem.* **25**, 9760–9778 (2023).
124. Faust Akl, D. *et al.* Assessing the environmental benefit of palladium-based single-atom heterogeneous catalysts for Sonogashira coupling. *Green Chem.* **24**, 6879–6888 (2022).
125. Liu, J. *et al.* Heterogeneous catalysis for the environment. *Innov. Mater.* **2**, 100090 (2024).
126. Trentin, O. *et al.* Upcycling of Chitin to Cross-Coupling Catalysts: Tailored Supports and Opportunities in Mechanochemistry. *ChemSusChem* **18**, e202401255 (2025).
127. Zorzetto, F. *et al.* Orthogonal assisted tandem reactions for the upgrading of bio-based aromatic alcohols using chitin derived mono and bimetallic catalysts. *Green Chem.* **26**, 5221–5238 (2024).

128. Trentin, O. *et al.* Mechanochemistry through Extrusion: Opportunities for Nanomaterials Design and Catalysis in the Continuous Mode. *Chemistry* **5**, 1760–1769 (2023).
129. Polidoro, D., Perosa, A., Selva, M. & Rodríguez-Padrón, D. Metal-Free Carbonaceous Catalytic Materials: Biomass Feedstocks for a Greener Future. *ChemCatChem* **15**, e202300415 (2023).
130. Polidoro, D., Rodriguez-Padron, D., Perosa, A., Luque, R. & Selva, M. Chitin-Derived Nanocatalysts for Reductive Amination Reactions. *Materials* **16**, 575 (2023).
131. EuChemS - European Chemical Society. Element Scarcity – EuChemS Periodic Table. https://www.euchems.eu/euchems-periodic-table/ (2023).
132. Schrock, R. R. & Hoveyda, A. H. Molybdenum and Tungsten Imido Alkylidene Complexes as Efficient Olefin-Metathesis Catalysts. *Angew. Chem. Int. Ed.* **42**, 4592–4633 (2003).
133. Ge, H., Kuwahara, Y. & Yamashita, H. Development of defective molybdenum oxides for photocatalysis, thermal catalysis, and photothermal catalysis. *Chem. Commun.* **58**, 8466–8479 (2022).
134. Pisk, J. & Agustin, D. Molybdenum, Vanadium, and Tungsten-Based Catalysts for Sustainable (ep)Oxidation. *Molecules* **27**, 6011 (2022).
135. Ji, J., Bao, Y., Liu, X., Zhang, J. & Xing, M. Molybdenum-based heterogeneous catalysts for the control of environmental pollutants. *EcoMat* **3**, e12155 (2021).
136. Zhang, W. *et al.* Biodiesel production by transesterification of waste cooking oil in the presence of graphitic carbon nitride supported molybdenum catalyst. *Fuel* **332**, 126309 (2023).
137. Yan, J., Liu, P., Li, J., Huang, H. & Song, W. Effect of valence state on electrochemical nitrate reduction to ammonia in molybdenum catalysts. *Chem. Eng. J.* **459**, 141601 (2023).
138. Tang, C. *et al.* Coordination Tunes Selectivity: Two-Electron Oxygen Reduction on High-Loading Molybdenum Single-Atom Catalysts. *Angew. Chem.* **132**, 9256–9261 (2020).
139. Keim, W. Multiphase catalysis and its potential in catalytic processes: the story of biphasic homogeneous catalysisThis work was presented at the Green Solvents for Catalysis Meeting held in Bruchsal, Germany, 13–16th October 2002. *Green Chem.* **5**, 105–111 (2003).

140. Keim, W. Oligomerization of Ethylene to α-Olefins: Discovery and Development of the Shell Higher Olefin Process (SHOP). *Angew. Chem. Int. Ed.* **52**, 12492–12496 (2013).
141. Khan, M. Y., Joshi, S. S. & Ranade, V. V. Continuous Hydrogenation of Cinnamaldehyde: Gas–Liquid–Liquid–Solid Helical Coil Reactor. *Ind. Eng. Chem. Res.* acs.iecr.3c00841 (2023) doi:10.1021/acs.iecr.3c00841.
142. Vossen, J. T., Leitner, W. & Vorholt, A. J. Exploring the Hurdles in Thermomorphic Multicomponent Systems in the Rhodium-Catalyzed Multiphase Hydroformylation. *ACS Sustain. Chem. Eng.* **11**, 10462–10470 (2023).
143. Kim, S., Noda, S., Hayashi, K. & Chiba, K. An Oxidative Carbon−Carbon Bond Formation System in Cycloalkane-Based Thermomorphic Multiphase Solution. *Org. Lett.* **10**, 1827–1829 (2008).
144. Homma, T. & Kitaoka, T. Multiphase catalytic oxidation of alcohols over paper-structured catalysts with micrometer-size pores. *Appl. Catal. Gen.* **486**, 201–209 (2014).
145. Strohmann, M., Vossen, J. T., Vorholt, A. J. & Leitner, W. Recycling of two molecular catalysts in the hydroformylation/aldol condensation tandem reaction using one multiphase system. *Green Chem.* **22**, 8444–8451 (2020).
146. Wei, H., Wang, Z. & Li, H. Sustainable biomass hydrodeoxygenation in biphasic systems. *Green Chem.* **24**, 1930–1950 (2022).
147. Hommes, A., Heeres, H. J. & Yue, J. Catalytic Transformation of Biomass Derivatives to Value-Added Chemicals and Fuels in Continuous Flow Microreactors. *ChemCatChem* **11**, 4671–4708 (2019).
148. Yang, F. *et al.* Reductive C−N Coupling of Nitroarenes: Heterogenization of MoO_3 Catalyst by Confinement in Silica. *ChemSusChem* **14**, 3413–3421 (2021).
149. Dong, X. *et al.* Enabling room-temperature reductive C–N coupling of nitroarenes: combining homogeneous and heterogeneous synergetic catalyses mediated by light. *Green Chem.* **24**, 4012–4025 (2022).
150. Liu, M. *et al.* Enhancing reductive C–N coupling of nitrocompounds through interfacial engineering of MoO_2 in thin carbon layers. *Chem. Commun.* **59**, 12443–12446 (2023).
151. Alder, C. M. *et al.* Updating and further expanding GSK's solvent sustainability guide. *Green Chem.* **18**, 3879–3890 (2016).
152. Byrne, F. P. *et al.* Tools and techniques for solvent selection: green solvent selection guides. *Sustain. Chem. Process.* **4**, 7 (2016).

153. Chen, L., Zhang, S., Liu, X. & Ge, X. Recent advances in water-mediated multiphase catalysis. *Curr. Opin. Colloid Interface Sci.* **65**, 101691 (2023).
154. Nasirpour, N., Mohammadpourfard, M. & Zeinali Heris, S. Ionic liquids: Promising compounds for sustainable chemical processes and applications. *Chem. Eng. Res. Des.* **160**, 264–300 (2020).
155. Polidoro, D., Perosa, A. & Selva, M. Tunable Multi-Phase System for Highly Chemo-Selective Oxidation of Hydroxymethyl-Furfural. *ChemSusChem* **15**, e202201059 (2022).
156. Bersani, C. *et al.* Selective Multiphase-Assisted Oxidation of Bio-Sourced Primary Alcohols over Ru- and Mo- Carbon Supported Catalysts. *ChemSusChem* **18**, e202400888 (2025).
157. Bellè, A. *et al.* A Multiphase Protocol for Selective Hydrogenation and Reductive Amination of Levulinic Acid with Integrated Catalyst Recovery. *ChemSusChem* **12**, 3343–3354 (2019).
158. Polidoro, D. *et al.* Pd-N-doped carbons for chemoselective hydrogenation of cinnamaldehyde: Unravelling the influence of particle size and support in multiphase batch and continuous-flow systems. *Appl. Catal. Gen.* **685**, 119864 (2024).
159. Choudhary, F., Mudgal, P., Parvez, A., Sharma, P. & Farooqi, H. A review on synthesis, properties and prospective applications of carbon nanomaterials. *Nano-Struct. Nano-Objects* **38**, 101186 (2024).
160. Ozyurt, D., Kobaisi, M. A., Hocking, R. K. & Fox, B. Properties, synthesis, and applications of carbon dots: A review. *Carbon Trends* **12**, 100276 (2023).
161. Atchudan, R. *et al.* Tunable fluorescent carbon dots from biowaste as fluorescence ink and imaging human normal and cancer cells. *Environ. Res.* **204**, 112365 (2022).
162. Ng, H. K. M., Lim, G. K. & Leo, C. P. Comparison between hydrothermal and microwave-assisted synthesis of carbon dots from biowaste and chemical for heavy metal detection: A review. *Microchem. J.* **165**, 106116 (2021).
163. Yi, M. *et al.* Recent Developments of Carbon Dots for Advanced Zinc-Based Batteries: A Review. *Adv. Funct. Mater.* **34**, 2400001 (2024).
164. Rashid, S. & Malik, S. H. Transition from a Linear to a Circular Economy. in *Renewable Energy in Circular Economy* (eds Bandh, S. A., Malla, F. A. & Hoang, A. T.) 1–20 (Springer International Publishing, Cham, 2023). doi:10.1007/978-3-031-42220-1_1.
165. United Nations - Department of Economic and Social Affairs. *World Population Prospects 2019: Highlights*. https://population.un.org/wpp/ (2019).

166. Pearce, D. W. & Turner, R. K. *Economics of Natural Resources and the Environment*. (Johns Hopkins University Press, Baltimore, 1990).
167. Alan, H. & Köker, A. R. Analyzing and mapping agricultural waste recycling research: An integrative review for conceptual framework and future directions. *Resour. Policy* **85**, 103987 (2023).
168. *Biomass Valorization: A Sustainable Approach towards Carbon Neutrality and Circular Economy*. (Springer Nature Singapore, Singapore, 2024). doi:10.1007/978-981-97-8557-5.
169. Nicolae, S. A. *et al.* Recent advances in hydrothermal carbonisation: from tailored carbon materials and biochemicals to applications and bioenergy. *Green Chem.* **22**, 4747–4800 (2020).
170. Markou, G. *et al.* Methane production through anaerobic digestion of residual microalgal biomass after the extraction of valuable compounds. *Biomass Convers. Biorefinery* **12**, 419–426 (2022).
171. Manyi-Loh, C. E. & Lues, R. Anaerobic Digestion of Lignocellulosic Biomass: Substrate Characteristics (Challenge) and Innovation. *Fermentation* **9**, 755 (2023).
172. Matsakas, L., Gao, Q., Jansson, S., Rova, U. & Christakopoulos, P. Green conversion of municipal solid wastes into fuels and chemicals. *Electron. J. Biotechnol.* **26**, 69–83 (2017).
173. Palaniveloo, K. *et al.* Food Waste Composting and Microbial Community Structure Profiling. *Processes* **8**, 723 (2020).
174. Awad, A. M. *et al.* Green Extraction of Bioactive Compounds from Plant Biomass and Their Application in Meat as Natural Antioxidant. *Antioxidants* **10**, 1465 (2021).
175. Sebastian, J., Rouissi, T., Brar, S. K., Hegde, K. & Verma, M. Microwave-assisted extraction of chitosan from Rhizopus oryzae NRRL 1526 biomass. *Carbohydr. Polym.* **219**, 431–440 (2019).
176. *Food Waste Valorization: Green Techniques in Sustainable Management*. (Springer US, New York, NY, 2025). doi:10.1007/978-1-0716-4646-5.
177. Husanu, E. *et al.* Exploiting Deep Eutectic Solvents and Ionic Liquids for the Valorization of Chestnut Shell Waste. *ACS Sustain. Chem. Eng.* **8**, 18386–18399 (2020).
178. Wang, W. & Lee, D.-J. Lignocellulosic biomass pretreatment by deep eutectic solvents on lignin extraction and saccharification enhancement: A review. *Bioresour. Technol.* **339**, 125587 (2021).

179. Ling, J. K. U. & Hadinoto, K. Deep Eutectic Solvent as Green Solvent in Extraction of Biological Macromolecules: A Review. *Int. J. Mol. Sci.* **23**, 3381 (2022).
180. Mamilla, J. L. K., Novak, U., Grilc, M. & Likozar, B. Natural deep eutectic solvents (DES) for fractionation of waste lignocellulosic biomass and its cascade conversion to value-added bio-based chemicals. *Biomass Bioenergy* **120**, 417–425 (2019).
181. Fu, H., Li, M., Ni, R. & Lo, Y. M. Enzymatic catalysis for sustainable production of high omega-3 triglyceride oil using imidazolium-based ionic liquids. *Food Sci. Nutr.* **6**, 2020–2027 (2018).
182. Murador, D. C., Braga, A. R. C., Martins, P. L. G., Mercadante, A. Z. & De Rosso, V. V. Ionic liquid associated with ultrasonic-assisted extraction: A new approach to obtain carotenoids from orange peel. *Food Res. Int.* **126**, 108653 (2019).
183. Ullah, H., Wilfred, C. D. & Shaharun, M. S. Comparative assessment of various extraction approaches for the isolation of essential oil from polygonum minus using ionic liquids. *J. King Saud Univ. - Sci.* **31**, 230–239 (2019).
184. Ullah, H., Wilfred, C. D. & Shaharun, M. S. Ionic liquid-based extraction and separation trends of bioactive compounds from plant biomass. *Sep. Sci. Technol.* **54**, 559–579 (2019).
185. Lim, J. R., Chua, L. S. & Mustaffa, A. A. Ionic liquids as green solvent and their applications in bioactive compounds extraction from plants. *Process Biochem.* **122**, 292–306 (2022).
186. Fu, D., Mazza, G. & Tamaki, Y. Lignin Extraction from Straw by Ionic Liquids and Enzymatic Hydrolysis of the Cellulosic Residues. *J. Agric. Food Chem.* **58**, 2915–2922 (2010).
187. Chambon, C. L., Chen, M., Fennell, P. S. & Hallett, J. P. Efficient Fractionation of Lignin- and Ash-Rich Agricultural Residues Following Treatment With a Low-Cost Protic Ionic Liquid. *Front. Chem.* **7**, 246 (2019).
188. Hou, X., Smith, T. J., Li, N. & Zong, M. Novel renewable ionic liquids as highly effective solvents for pretreatment of rice straw biomass by selective removal of lignin. *Biotechnol. Bioeng.* **109**, 2484–2493 (2012).
189. Campalani, C. *et al.* Green extraction of chitin from hard spider crab shells. *Carbohydr. Polym.* **345**, 122565 (2024).
190. Charlton, K. E. *et al.* Fish, food security and health in Pacific Island countries and territories: a systematic literature review. *BMC Public Health* **16**, 285 (2016).

191. Food and Agriculture Organization (FAO) of the United Nations. *The State of World Fisheries and Aquaculture 2024*. (FAO, 2024). doi:10.4060/cd0683en.
192. Food and Agriculture Organization (FAO) of the United Nations. Food loss and waste in aquatic value chains session at the UN Ocean Conference 2025. https://www.fao.org/index.php?id=121813 (2025).
193. Food and Agriculture Organization (FAO) of the United Nations. Food Balances (old methodology and population).
194. Our World in Data. Fish and Seafood Production - graph processed by Our World in Data. https://ourworldindata.org/grapher/fish-seafood-production (2025).
195. Nawaz, A. *et al.* Valorization of fisheries by-products: Challenges and technical concerns to food industry. *Trends Food Sci. Technol.* **99**, 34–43 (2020).
196. Maschmeyer, T., Luque, R. & Selva, M. Upgrading of marine (fish and crustaceans) biowaste for high added-value molecules and bio(nano)-materials. *Chem. Soc. Rev.* **49**, 4527–4563 (2020).
197. Maulu, S., Hasimuna, O. J., Monde, C. & Mweemba, M. An assessment of post-harvest fish losses and preservation practices in Siavonga district, Southern Zambia. *Fish. Aquat. Sci.* **23**, 25 (2020).
198. EFSA - European Food Safety Authority. Food date labelling. https://www.efsa.europa.eu/en/safe2eat/food-date-labelling (2025).
199. Tavares, J. *et al.* Fresh Fish Degradation and Advances in Preservation Using Physical Emerging Technologies. *Foods* **10**, 780 (2021).
200. Zhang, J., Akyol, Ç. & Meers, E. Nutrient recovery and recycling from fishery waste and by-products. *J. Environ. Manage.* **348**, 119266 (2023).
201. Fadhil, A. B., Ahmed, A. I. & Salih, H. A. Production of liquid fuels and activated carbons from fish waste. *Fuel* **187**, 435–445 (2017).
202. NATIONAL FISHERIES DEVELOPMENT BOARD - Department of Fisheries, Indian Gov. Wealth from Fish Waste. *@nfdbindia on X* https://x.com/nfdbindia/status/1637823313472012289 (2023).

Chapter 2. Multiphasic Catalytic Systems

Chapter 2 is dedicated to delving into catalytic multiphase systems (MPS), which have been one of the core topics of this Thesis. As outlined in Section 1.4, the relevance and advantages of MPS are closely connected to ongoing efforts on reducing the environmental impact of chemical processes by developing more sustainable catalytic strategies.

Section 2.1 provides a critical overview of the state of the art in this field, along with the essential tools necessary to approach multiphase catalysis, while understanding the opportunities and the challenges. Gaining knowledge in this area has been essential for a deeper insight into the role that each phase can play in the overall mechanism of multiphase-assisted catalytic reactions. Moreover, this study allowed us to develop to design an innovative multiphasic catalytic system for the selective oxidation of primary alcohols, which will be discussed in detail in Section 2.2.

2.1 State of the art: Unlocking the Potential of Liquid Multiphase Systems for Metal-Catalysed Reactions

This section is part of the extended work of literature analysis on MPS carried out in this Thesis work. The following paragraph is largely based on the published Review Article: **C. Bersani**, A. Perosa, D. Rodríguez-Padrón, M. Selva, *ChemCatChem* (**2024**), 16, 14. The Author of the Thesis equally contributed to other Authors of the article in the selection and discussion of the papers described below.

Multiphase systems (MPS) literally permeate the world of chemical synthesis and catalysis with thousands of examples describing transformations where mixtures of gases, liquids and/or solid phases are involved. Just to name a few typical MPS of tremendous impact on industry and everyday life, these include:

i) reactions between gases and solids (G–S) as the control of the exhaust emission in catalytic converters of combustion engines,[1] the catalytic oxidation of VOCs (volatile organic compounds),[2] and the synthesis of ammonia;[3]

ii) reactions between gases and liquids (G–L) as homogeneously catalysed processes of hydroformylation, hydrogenation, oxidation, carbonylation, etc.[4]

iii) When it comes to heterogeneous catalysis, biphasic liquid-solid (L–S) or triphasic gas-liquid-solid (G–L–S) systems are well-recognised for the implementation of

both batch and continuous-flow processes.[5–8] Some widely employed G–L–S technologies include the synthesis of hydrogen peroxide, the production of heavy oil and synthetic crude from coal, the production of methanol and polyethylene, the flue gas desulphurisation, etc.[9]

iv) Solid-solid (S–S) mechanochemical reactions also deserve attention for their potential in the design of sustainable protocols aimed to reduce or eliminate the need of solvents.[10–12]

Liquid-liquid (L–L) MPS comprised of mixtures of immiscible solvents, offer another powerful perspective for reactions in both homogeneous and heterogeneous catalytic environments. In this case, the partitioning of reactants and catalyst in different phases implies liquid-liquid interfacial reactions that often open unique possibilities in terms of controlling either the kinetics and/or the products distribution.

The built-in separation of reagents/products/catalyst that characterise these systems, not only facilitate downstream operations for the products purification and avoid metal/organic cross-contamination but also allow an *in-situ* reuse of the catalyst though a semicontinuous mode. This approach improves sustainability through process intensification, increases steps economy while minimising waste and energy/mass consumption.

In the past 15 years, a variety of such liquid-liquid MPS have been proposed, mostly comprised of binary and tertiary mixtures of conventional organic solvents, but also of polar media as water and high-molecular weight liquids as polyethylene glycols and ionic liquids. Due to the vast body of literature on the subject and the specific focus of this Thesis, here the recent advances of catalytic liquid–liquid MPS will be delved with particular emphasis on L–L–L systems, where a homogeneous catalyst is dissolved into one of the liquid components of a ternary mixture, and L–L–S and L–L–L–S systems, where one of the liquids acts as catalyst-philic phase that confines a heterogeneous catalyst. These systems offer the opportunity to explore in greater depth the mechanisms of catalyst-solvent interactions and their effect on the reaction outcome, aspects that are crucial for introducing the topic of selective alcohol oxidation in multiphase conditions discussed in Section 2.2.

2.1.1 Multiphase Systems in Homogeneous Catalysis

Conventional conditions for homogeneous catalysis are based on a monophase system where catalysts, reactants and products are fully miscible. This molecular-level uniformity facilitates efficient and selective catalytic transformations since the catalyst's potential is exploited to the fullest through a complete and direct interaction with the substrates. Common examples of homogeneous catalysts include transition metal complexes, organometallic compounds, and a variety of metal-containing enzymes. Key to the success of such systems relies on their ability to undergo multiple catalytic cycles by reversible transformations, a feature which is further enhanced by tuning reaction conditions, especially temperature and pressure.

Albeit homogeneous catalysis is at the forefront for the design of innovative solutions in the synthesis of pharmaceuticals, fine chemicals, and advanced materials,[13–15] major drawbacks of these strategies are recognised in the demand of copious amounts of solvents, multistep purification processes, and the difficult, whenever possible, recovery and recycling of the catalysts.[16]

Several attempts to promote the heterogenisation of homogeneous catalysis have been conducted by supporting the catalyst on different materials to improve its reusability and recyclability. Unfortunately, in most cases they resulted in a decreasing catalytic activity due to the occlusion of the active sites and the scalability to industrial processes has never been fully accomplished.[17,18] Other alternative routes, such as the use of scavengers, biphasic systems, magnetically recoverable catalyst, thermoregulated catalysts, micellar media, and organic solvent nanofiltrations, have been covered in attempt to recover and recycle the catalytic material, still with several limitations.[19,20] These aspects not only impact on the overall costs of the production processes but may result in metal contamination in the final products, which is particularly undesirable in pharma synthesis, where there is an issue in controlling highly toxic metals at health concerning levels.[21]

The analysis of Keim dated back to 2003 offered one of the first overviews on the application of two-phase liquid-liquid systems and their potential towards a greener and sustainable use of homogeneous catalysis.[22] The strategy illustrated in **Figure 2.1**, is based on immobilising or heterogenising a homogeneous catalyst within a liquid phase that is immiscible either with the reactant solution or with the product phase that forms and self-separates as the reaction proceeds. This configuration allows the reuse of the catalyst without altering its performance

over time and aligns with the green chemistry principles by minimising solvent use for both catalysis and product isolation, thus avoiding loss/handling of the catalyst phase.

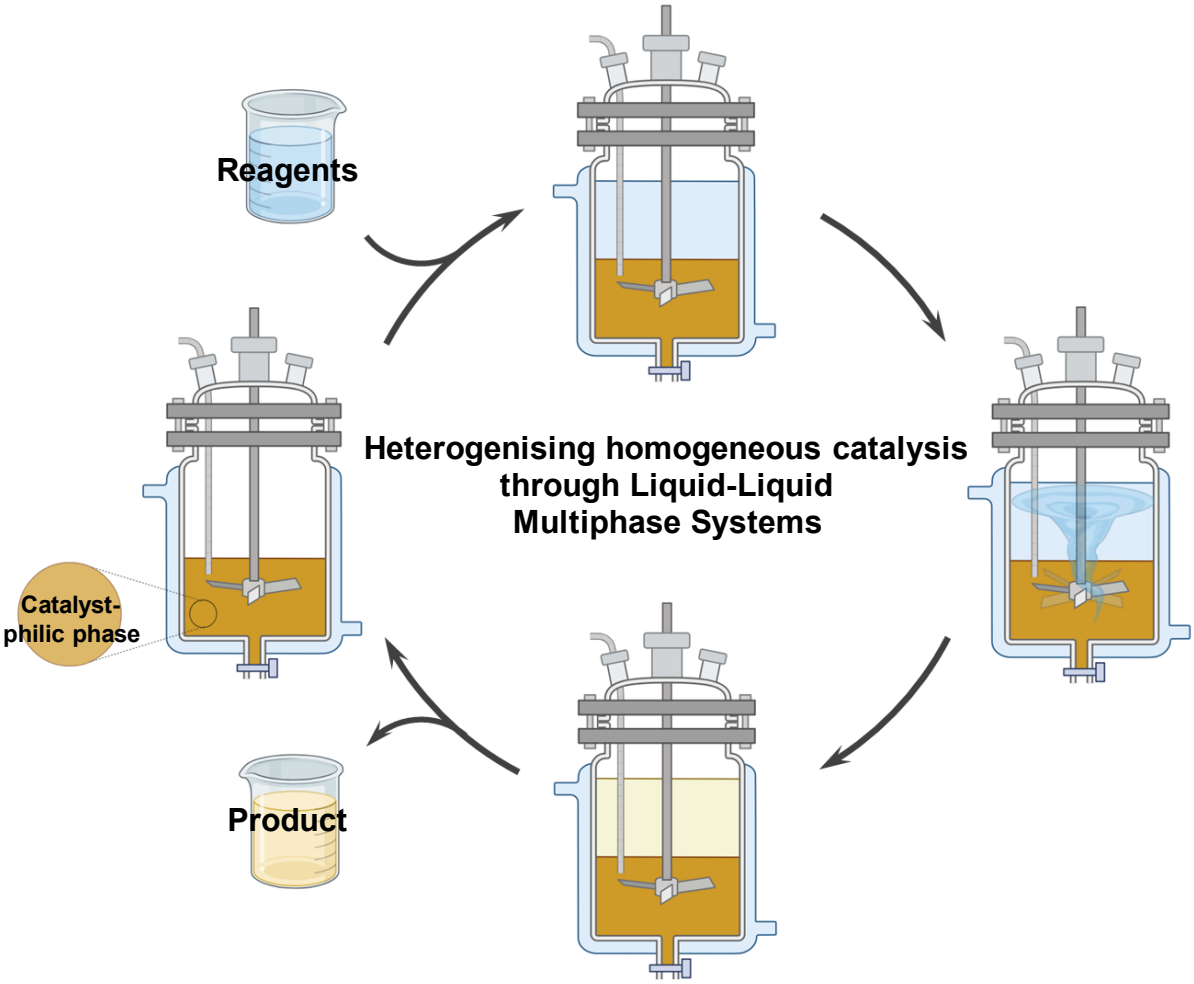

Figure 2.1. Schematic representation of homogeneous catalysis in a L–L MPS, with built-in catalyst separation.

As previously noted in Sections 1.3 and 1.4, the SHOP process, developed in 1968 to produce linear α-olefins via ethylene oligomerisation and olefin metathesis, stands as a forerunner in the development of multiphasic systems for commercial applications. The oligomerisation was carried out in a polar solvent (1,4-butanediol) during the first production step, while the homogeneous Ni-based catalyst was recirculated in a second step via phase separation from α-olefins.[23]

Another remarkable study to valorise this approach, has been described using catalytic MPS to the set-up of tandem reactions. Tandem reactions refer to two or more consecutive reactions performed without isolation of any intermediates or further additional work-up except for the final one. Notwithstanding the indisputable advantages of these synthetic

sequences in terms of step efficiency and minimisation of solvents/waste, challenges associated with tandem reactions, especially in the process monitoring, the reactor design, the purification of products and the recycling of the catalyst, are far from negligible. Bianga and co-workers proposed an outstanding example of a homogeneously catalysed auto-tandem hydroaminomethylation (HAM) reaction.[24] Discovered by Walter Reppe in 1949 at BASF laboratories, the transition metal- catalysed HAM reaction is a one-pot tandem hydroformylation-reductive amination sequence.[25] This reaction offers a highly efficient and atom-economical strategy to synthesise nitrogen-containing organic compounds from readily available starting materials (**Figure 2.2A**). The process developed by Bianga and co-workers, comprising the hydroformylation of 1-decene to the corresponding aldehyde and followed by its reductive amination, was performed in a liquid-liquid thermomorphic MPS (**Figure 2.2B**) by which higher aliphatic amines were obtained in a continuous flow mode.

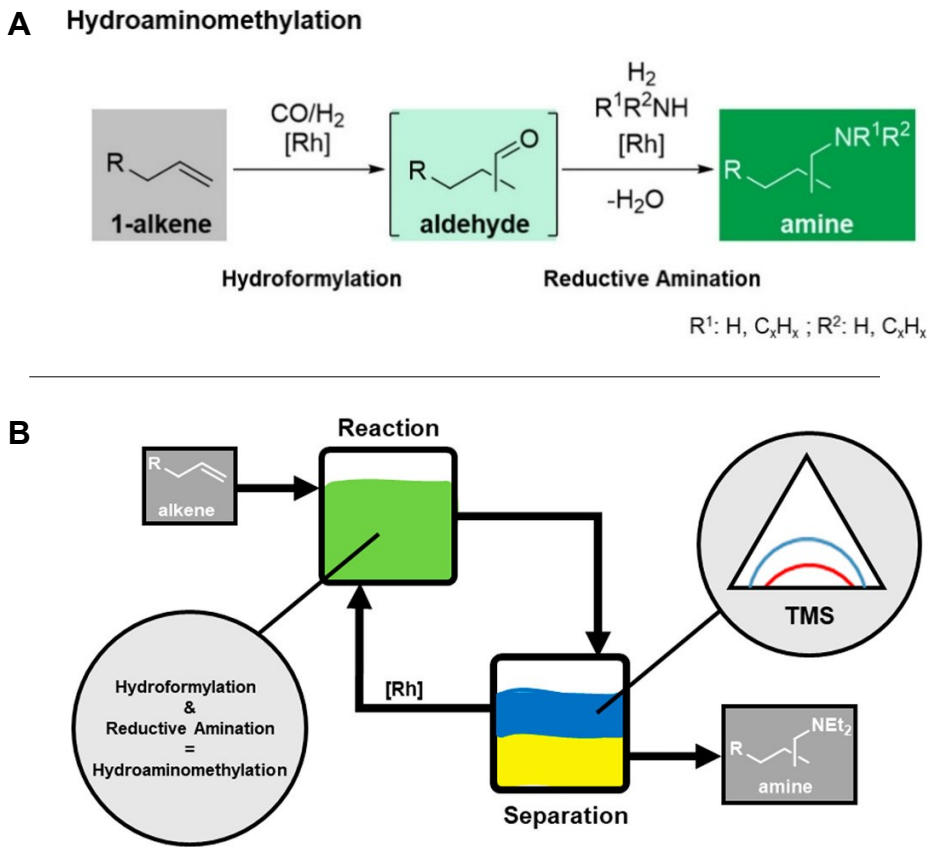

Figure 2.2. Schematic representations of **A**: tandem HAM reaction starting from 1-alkene; **B**: homogeneously catalysed tandem HAM in thermomorphic MPS. Reproduced from [24] with permission.

Notably, water is the sole byproduct of this reaction. Methanol and *n*-dodecane acted as a polar and a non-polar component of the biphasic liquid system, respectively, whose thermomorphic behaviour allowed reversible phase transition in response to changes in temperature. A monophasic mixture was reached at 125°C (pCO/H_2=36 bar, CO/H_2=1/2) to ensure the full operativity of the catalyst under homogeneous reaction conditions, while phases separation occurred upon cooling close to ambient temperature. This facilitated the isolation of pure products (alkyl amines) in the apolar solvent and the recovery/recycle of the catalyst, a Rhodium/SulfoXantphos system. Albeit the production of water was an advantage from the safety standpoint, its accumulation into the polar phase during the reaction induced an adverse effect on both the reaction selectivity and the thermomorphic behaviour of the biphasic environment. It was confirmed that undesirable byproducts of aldol condensations could be achieved in up to 8% due to water. Nonetheless, conditions were found to ensure a steady catalytic activity over six subsequent runs in the batch mode, with yields above 73% for linear amines and turnover frequencies up to 2400 h^{-1}. The total Rh leaching was <6% (on a total of 125 ppm of Rh in solution), while the total P leaching was <8%. Moreover, in the continuous-flow mode, an average product yield of 61% was achieved for over 60 h with a metal leaching of 0.1%/h.[24]

Substantial efforts have been made over the years to improve the regioselectivity of the hydroformylation step and the overall chemoselectivity of the HAM reaction towards the desired amines, emphasising in particular the potential of multiphasic systems.[26] An apparently similar but conceptually different approach was proposed through the design of an orthogonal tandem sequence, wherein multiple catalytic species rather than a single catalyst, were employed.[27] In this case, 1-pentene was firstly hydroformylated to *n*-hexanal, which then underwent self-aldol condensation to form the desired product 4- butyloctenal (**Figure 2.3**).

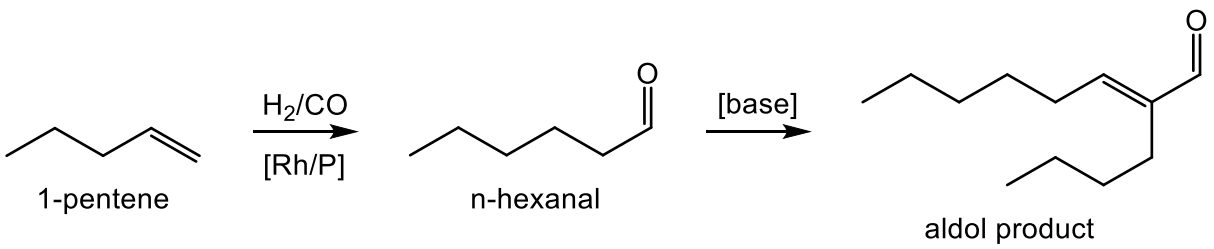

Figure 2.3. Orthogonal tandem sequence hydroformylation and aldol condensation. Adapted from [27].

The catalytic system that consisted of Rhodium/SulfoXantphos and basic NaOH as a hydroformylation catalyst and an aldol condensation initiator, respectively, was immobilised in a polyethylene glycol selected as a green polar phase for multiphase catalysis. During the reaction, the product phase spontaneously separated from the catalyst phase which was then extracted with pentane and treated under vacuum for further purification. Experiments carried out for 16 h at 120 °C, pH_2=25 bar, pCO=25 bar, showed a 97% conversion of the starting alkene to hexanal, which in the second step of the tandem reaction, was transformed in the aldol product with a 69% selectivity. Lowering the temperature to 100 °C allowed to enhance the selectivity towards the aldol product up to 80%. After nine consecutive runs, no significant loss of activity was observed with an overall Turnover Number (TON) of 8700 regarding the rhodium catalyst. The metal leaching was of only 0.07% per run.

The same Rhodium/SulfoXantphos catalytic system was used by the same research group to develop a different strategy as well, in which the potential of a thermomorphic MPS was exploited to induce the crystallisation of the catalyst.[28] Particularly, the hydroformylation of 1-octene to nonanal was investigated using solvents with a melting point just above room temperature, such as ethylene carbonate, which acted also as a solidifying agent at room temperature able to separate and recycle the catalyst (**Figure 2.4**).

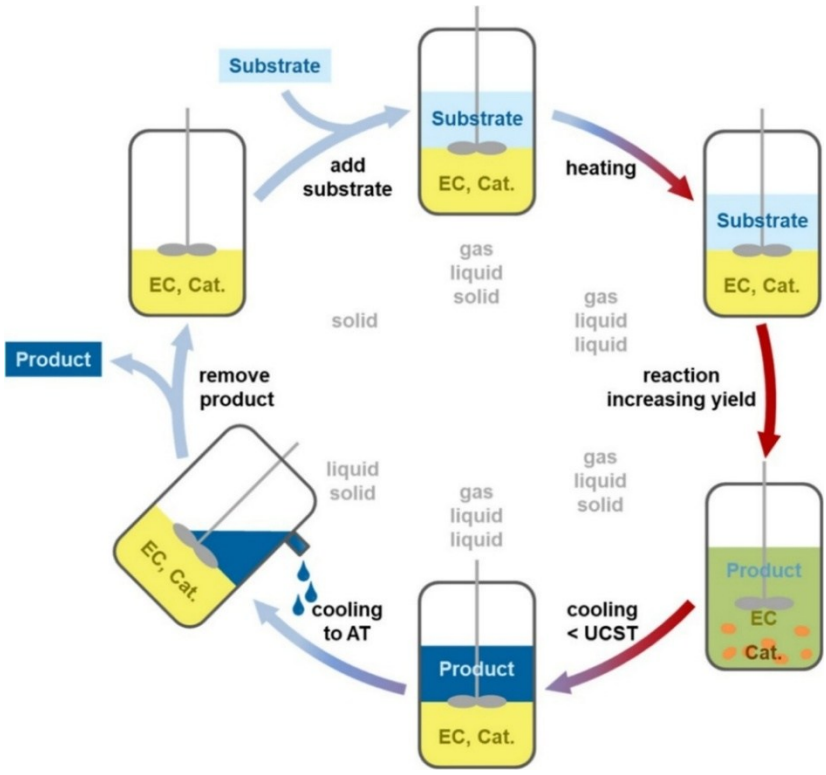

Figure 2.4. Schematic representations of the temperature-dependent phase behaviour in the MPS-assisted hydroformylation of 1-octene. Reprinted from [28] under the terms of the Creative Commons CC BY license.

The latter proved robust over 12 subsequent runs without significant activity deterioration: elevated TON up to 9770 mol_{Oct}/mol_{Cat} and a very good *n*/*iso* selectivity (ratios up to 98:2) were obtained, with a minimal leaching of 0.54% for the rhodium and 0.10% for the phosphorus into the product phase. However, experiments failed to achieve high aldehyde yields that across all the tested reaction conditions, did not exceed 70‑80% in pure ethylene carbonate. Borescope techniques were used to explore the behaviour of the MPS at different temperatures, and to offer plausible reasons why yields could not rise. This analysis indicated that during the first 6 h of the reaction, the conversion and yield increased almost linearly, while at the same the size of the droplets of the dispersed phase steadily decreased, and the phase boundary was progressively more difficult to observe. After 7 h, the reaction mixture turned to a monophasic solution, and the catalyst started to precipitate due to the decrease of the phase polarity. As a result, the reaction stagnated, with the aldehyde yield non increasing anymore. The reaction system was therefore modified by decreasing and increasing the polarity of the organic phase or the catalyst phase, respectively. In the first case, the addition of decane (30 vol.%) to the organic phase avoided the catalyst precipitation and, notwithstanding a lower Turnover Frequency (TOF), it allowed a full conversion with a selectivity of 89% towards the aldehyde. In the second case, the addition of water was even more advantageous, inducing a further improvement of the selectivity up to 93% at full conversion, without any catalyst precipitation.[28]

The hydroformylation steps in the processes described above are refinements of the Ruhrchemie/Rhône-Poulenc Oxo process, which, as previously mentioned in Section 1.3, represents a pioneering and still valuable multiphasic process, commercially applied since 1984. This process produces carbonylated compounds from alkenes in the presence of syngas, a Rh-based catalytic system bearing sulphonated, triaryl-phosphine ligands (TPPTS, known as Kuntz-Cornils catalyst), and water works as catalyst carrying phase.[29,30]

The model of self-separating liquid-liquid biphasic systems in which a phase, typically the product phase, autogenerate itself during the reaction and separates from the main phase that contains the catalyst and reagents, has been proposed also for the catalytic hydrogenation of CO_2 or CO_2-derivatives, such as dimethylcarbonate (DMC), to methanol.[31] The water/methanol polar phase, generated as the reaction outcome, self-separates from the catalyst-carrying non-polar phase of *n*-decane during the catalytic process (**Figure 2.5**).

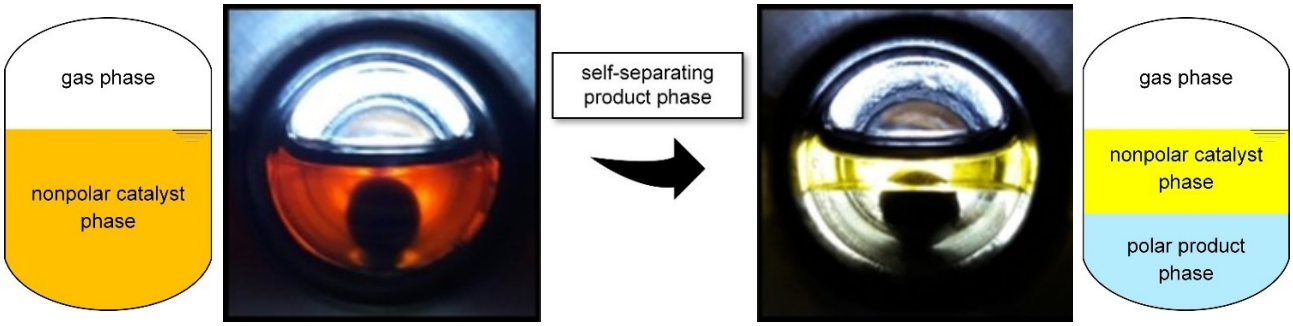

Figure 2.5. Schematic and pictorial representations of the self-separating product phase for the MPS-assisted hydrogenation reaction of DMC to MeOH over Ru-based catalysts. Reproduced from [31] under the terms of the Creative Commons CC BY license.

Particularly, the design of the Ru-based catalyst [Ru(CO)ClH(MACHO-C_{12})], with MACHO-C_{12}=bis{2-[bis(4-dodecylphenyl)phosphino]ethyl}amine, was challenging to ensure not only its confinement in the hydrocarbon solvent, but also its double performance to convert both DMC and CO_2. Selected ligands based on aryl phosphine and the assistance of *N,N'*-dimethylethane-1,2-diamine (DMEDA) for the direct CO_2 hydrogenation were necessary. The level of productivity was unexpectedly high. After 24–48 hours at 140 °C and pH_2= 200 bar, quantitative conversion of both DMC and CO_2 to methanol was reached with an average selectivity towards methanol of 96%. Only minor amounts of formamides and formates were detected as byproducts. The catalyst phase was recycled over ten subsequent batch runs with a total TON of 19235; while, at the end of each test, the final mixture showed two clearly separated liquid phases that allowed an easy and efficient isolation of the product. Notwithstanding this, ICP-MS analysis confirmed a consistent Ru-leaching corresponding to an overall metal loss of 37%. Authors claimed that from a comparison with the state-of-the-art in the literature, the presented system was among the best-performing recycling concepts for homogeneously catalysed hydrogenation of CO_2 to methanol.

A valuable example of an ionic liquid-based MPS was described using a thermomorphic ionic liquid microemulsion system.[32] Microemulsions are thermodynamically stable colloids composed of two or more intrinsically immiscible solvents and one or more surfactant species, and form spontaneously when the components are mixed under specific conditions. The resulting optically transparent system, apparently homogeneous, is composed of nanometre-sized droplets of one liquid phase dispersed into another, stabilised by surfactant amphiphilic additives.

A crucial ability of microemulsion is the simultaneous solubilisation of both hydrophilic and hydrophobic species. In the above-cited example, a thermomorphic microemulsion was used to combine the solubilisation advantages and the temperature-dependent behaviour of a liquid-liquid MPS. In particular, using hydrophilic chiral ligands, such as *N*-[(2-(amino)-(1*R*,2*R*)-diphenylethyl]-p-toluensulphonyl (*R,R*-TsDPEN), that pushed and immobilised a poorly soluble Ru-based catalyst into the microemulsion phase, the asymmetric transfer hydrogenation of a variety of aromatic and aliphatic ketones to the corresponding chiral secondary alcohols can be carried out with excellent results. For instance, after 20 hours at 60 °C, the reduction of acetophenone to 1-phenylethanol was achieved with 99% conversion and 95% enantiomeric excess for (*R*)-1-phenylethanol using a MPS composed of water, *n*-heptane, and $[C_{12}MIm][(^{i}C_8)_2PO_2]$, an imidazolium-based ionic liquid, as a surfactant additive. Sodium formate was used as a hydrogen donor (**Figure 2.6**).

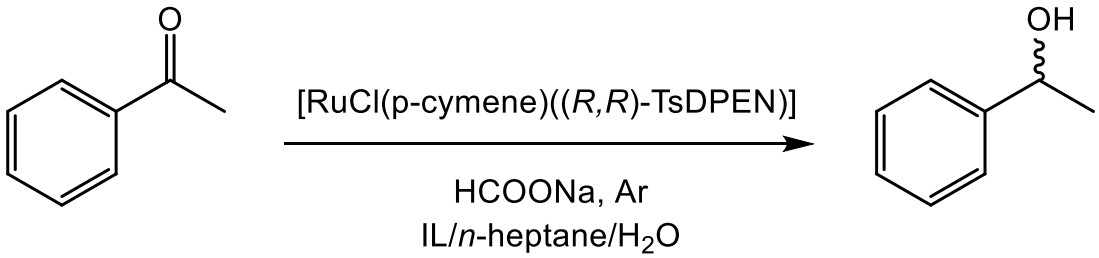

Figure 2.6. The enantioselective reduction of acetophenone using a thermomorphic ionic liquid microemulsion.

In this system, water acted both as the catalyst-carrying phase and as the solvent for sodium formate, the hydrogen donor. Authors indicated that the transfer hydrogenation protocol not only avoided H_2-pressurised vessels and their potential risks, but thanks to a surface-active ionic liquid, it favoured the contact of contact between hydrophilic and hydrophobic reagents and catalyst in the microemulsion environment. The thermomorphic system allowed an easy separation of products with a built-in recycle of the catalyst over multiple runs. An excellent level of enantioselectivity was maintained up to three subsequent runs, despite the conversion decreased from one recycle test to another.

Another interesting application of thermomorphic MPS was proposed for a continuous flow homogeneously catalysed reductive amination.[33] The investigated reaction (**Figure 2.7**) started with the condensation of 1-decanal (**1**) with diethylamine (DEA) to provide *N,N*-

diethyldecylenamine (**2**) that, in turn, was hydrogenated to *N,N*-diethyldecylamine (**3**) as the desired product.

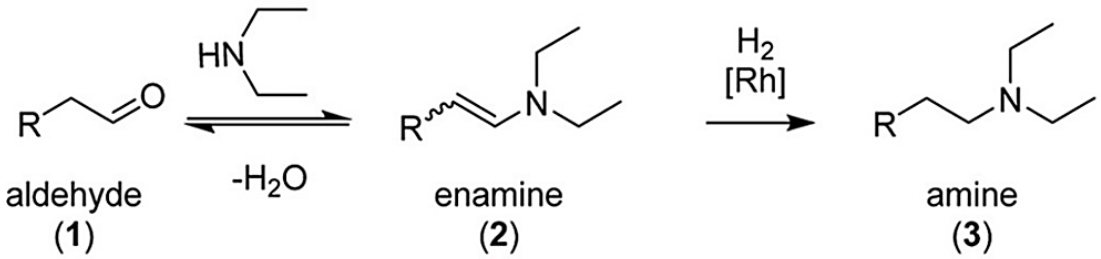

Figure 2.7. Schematic representation of the reductive amination reaction of 1-decanal. Adapted from [33].

The thermomorphic MPS was comprised of dimethylformamide (DMF), in which a Rh-based catalyst obtained by the combination of Rh(acac)(cod) and triphenylphosphine (PPh_3) proved highly soluble, and *n*-dodecane as a non-polar solvent suitable for both the reactant and the product. Initial studies under batch conditions demonstrated that after only 1 hour at 100 °C, pH_2= 30 bar and a DEA/decanal ratio of 4:1, a 76% conversion and 96% selectivity towards *N,N*-diethyldecylamine (**3**) were obtained, while a reaction time prolonged up to 2 hours was necessary to reach a product yield around 90%. An accurate analysis of the phase behaviour of the DMF/dodecane/decanal ternary system showed that between -5 and 20 °C phase separation occurred within minutes with 5 °C identified as the optimal temperature to enable efficient decantation. Thereafter, the transition from small-scale batch experiments to flow was investigated, achieving a 60-fold scale-up in a fully automated mini-plant. The continuous-flow process took place with yields of **3** exceeding 90% over 90 hours and minimal catalyst leaching (<1%/h), thereby underscoring the efficiency and stability of the developed system.

2.1.2 Multiphase Systems in Heterogeneous Catalysis

This section delves into the role of liquid-liquid MPS for the use of heterogeneous catalysts. These systems involve the coexistence of multiple immiscible liquids, with one of them specifically acting as a catalyst-philic phase able to segregate the heterogeneous catalyst. Compared to conventional heterogeneous liquid-phase protocols, where the separation of a solid catalyst (at the end of the reaction) is often a processing bottleneck requiring costly and time-consuming filtration steps,[34,35] heterogeneous multiphase configurations inherently integrate a facile isolation of the reaction products with an *in-situ* recycle of the catalyst which is never removed from the reactor, nor it needs activation before reuse (**Figure 2.8**).

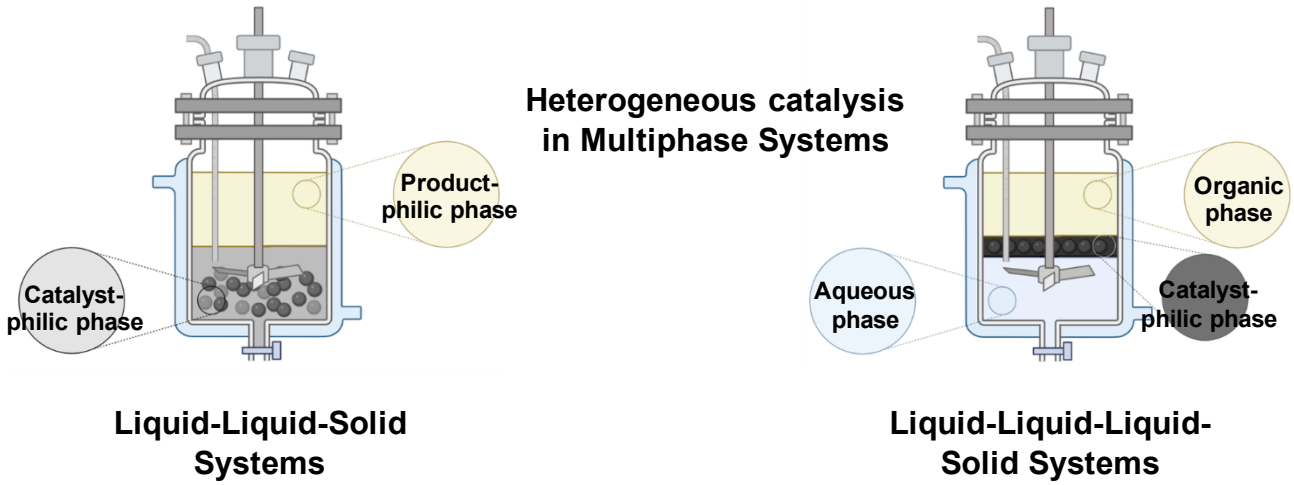

Figure 2.8. Schematic representation of L-L-S and L-L-L-S multiphasic systems in heterogeneous catalysis (left and right, respectively).

Typical biphasic and triphasic configurations are denoted as L–L–S and L–L–L–S, respectively, where catalyst-philic phases may encompass a variety of polar and apolar phases from hydrocarbons to polyethylene glycols (PEGs) and ionic liquids to name a few. These systems not only reduce costs, but for a given catalyst, they also provide a powerful tool to control the products distribution of a reaction, allowing the selective access to different derivatives by the change of the composition of the multiphase. Our group contributed to this subject by designing MPS for a variety of transformations including hydrogenations, hydrogenolyses, and oxidations.[36–41]

Figure 2.9 and **Table 2.1** summarise some of the most representative results of these studies, especially focused on the valorisation of biobased molecules, where a single heterogenous catalyst as Ru/C was used.

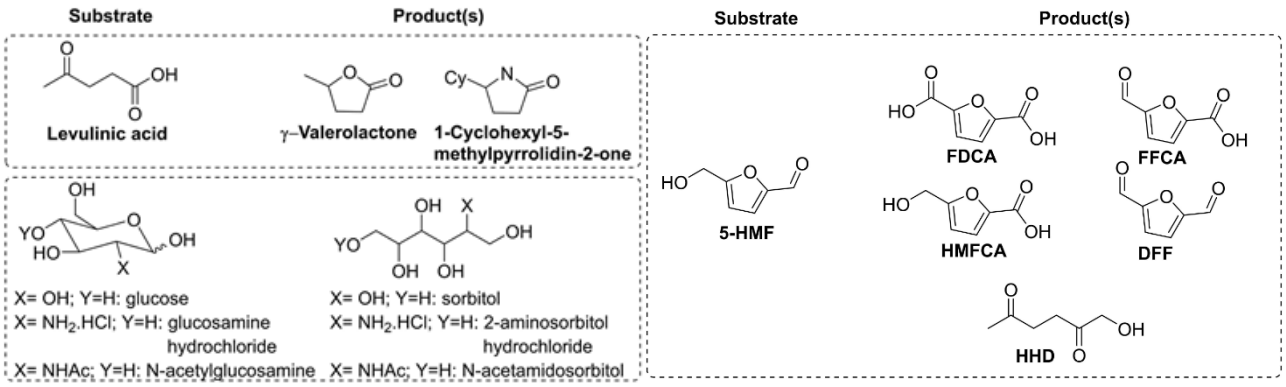

Figure 2.9. Structures of substrates and related products of the MP-assisted reactions reported in **Table 2.1.**

Table 2.1. Multiphase reactions over Ru/C for the valorisation of biobased molecules.

Entry	Substrate	MP conditions [a]	T, p, t (°C, bar, h)	Product (Conv./Sel.%)	Ref.
1	Levulinic acid	H_2O/iOct/$[P_{8881}]NTf_2$	100, 35, 4	GVL (100, >99)	36
2		H_2O/iOct	100, 35, 1	GVL (100, >99)	37
3		H_2O/iOct/FA [b]	150, 35, 16	CHP (>99, 88)	
4	5-HMF	H_2O/iOct	130, 8, 10	FDCA (>99,>99)	38
5		H_2O/iOct/$[N_{8881}]Cl$	90, 8, 16	FFCA (>99, 95)	
6		H_2O/iOct/$[N_{8881}]Cl$	90, 20(H_2), 1	HMFCA (>99,>99)	
7		ACN/cyclooctane	110, 8, 16	DFF (>99,>99)	
8		H_2O/iOct/$[P_{8881}]NTf_2$	100, 50, 18	HHD (>99,>99)	39
9		H_2O/iOct/$[N_{8881}]Cl$	100, 40, 2	HHD (>99,>99)	40
10	D-glucosamine HCl	H_2O/iOct/THF	110, 40, 12	2-NH_2-D-sorbitol (>99,>99)	41
11	N-Ac-D-glucosamine	H_2O/iOct/THF	110, 40, 12	2-AcNH-D-sorbitol (>99,>99)	
12	Glucose	H_2O/iOct/THF	120, 20, 12	Sorbitol (>99, 87)	

[a] $[P_{8881}]NTf_2$ = trioctylmethylphosphonium bistriflimide; $[N_{8881}]Cl$ = trioctylmethylammonium chloride; i-Oct = iso-octane.
[b] Formic acid (FA) was used as a selective catalyst deactivator.

Carbon-supported Ru is one the best options among heterogeneous systems for processing water-soluble bio-sourced organic reactants, not only for its activity but also for its moderate cost, which is about 4% compared to that of other precious metals such as Au and Pt.[42,43] Moreover, this catalyst proves excellent for multiphase processes, such as those reported in **Table 2.1**, since it is hydrophobic enough to reside in a separate phase, typically a hydrocarbon or ionic liquid, distinct from that where reaction occurs, usually an aqueous solution. Albeit the confinement of carbon-supported metals (Pd/C, Pt/C, and Ru/C) in both organic and ionic liquids media is a known phenomenon, its origin is far from being elucidated. More details about this confinement effect will be discussed in Section 2.2.2.

Characterisation studies of several carbons used as catalytic supports (activated carbons, carbon nanotubes, and F-doped carbons) have led to conclude that the segregation of such materials in organic media is not a general behaviour. The confinement effect of carbons is somewhat correlated to the presence of functional groups (mainly carboxylic, phenolic, and lactonic groups) on their surface the confinement effect: indeed, the hydrophobic/hydrophilic properties of these supports can be tuned by acid pretreatments and are associated to the combination of surface acidity and the presence of Na-based impurities (0.1-0.2%) in the supports.[37,44,45] Different studies have also hypothesised that the embodiment/segregation observed for a variety of carbon-supported metals in ionic liquids is mostly determined by the occurrence of strong polar interactions between the dense and viscous organic liquids and the acid functionalities available on the surface of carbons.[46] In the multiphase reaction therefore, ILs act concurrently as catalyst-philic phases and as interfacial boundary layers through which the migration (adsorption/desorption) of the liquid/gaseous reagents and products to and from the catalyst, respectively, took place. Whatever the role of the ionic liquid and the carbon support, results of **Table 2.1** highlighted how the effect of the phases separation impacted on the catalytic performance and the reaction outcomes.

The first considered example is levulinic acid (LA), one of 12 most attractive platform chemicals that can be produced from wood-based feedstocks.[47] Initial studies proved that under multiphase conditions, specifically in a liquid triphasic system comprised of water, *i*-octane and an ionic liquid, LA was quantitatively hydrogenated to γ-valerolactone (GVL, entry 1).[36] Upon a screening of several ionic liquids, the choice fell on an onium salt, $[P_{8881}][NTf_2]$ (trioctylmethylphosphonium bistriflimide), for its stability, hydrophobicity, and its ability to segregate Ru/C and made it available for reuse, up to 8 recycles, without any loss of performance. In a subsequent study of the same reaction in a water/*i*-octane biphasic system, it was unexpectedly noticed that by adjusting the relative amounts and

concentration of the two liquids, Ru/C was selective confined in the hydrocarbon phase (entry 2). Although acting out of the aqueous phase in which the reaction took place, the catalyst displayed an activity (TOF= 234 h^{-1} at 80 °C) only slightly lower than that reported for the hydrogenation of LA catalysed by 5% Ru/C in conventional water solution (TOF= 273 h^{-1}, 70 °C, pH_2= 30 bar).[43] The water/*i*-octane biphase proved successful also to carry out the reductive amination of LA with cyclohexylamine, producing 1-cyclohexyl-5-methylpyrrolidin-2-one with an 88% selectivity at complete conversion (entry 3).[37] In this case, the addition of the water-soluble formic acid (FA) to the MPS was necessary to selectively inhibit the adsorption of LA on Ru/C and hinder the competitive hydrogenation of LA to GVL.

Another substrate of **Table 2.1** is 5-HMF (5-hydroxymethylfurfural), the most representative member of bio-based furanics. The multiple functionalisation of HMF makes the molecule extremely versatile towards a variety of transformations, but at the same time, conditions for any given reaction must be carefully selected to control the products distribution. This was accomplished in the multiphase Ru/C-catalysed oxidation of HMF where three MPS, namely water/*i*-octane (MP1), water/[N_{8881}][Cl]/*i*-octane (MP2; [N_{8881}][Cl]: trioctylmethyl ammonium chloride), and acetonitrile/cyclooctane (MP3), were developed to selectively oxidise HMF using air atmosphere (not exceeding 8 bar) as a green oxidant.[38] Particularly:

i) MP1, 2,5-furandicarboxylic acid (FDCA, >99% yield) was obtained by complete oxidation of both the aldehyde and the alcohol group of HMF (entry 4);
ii) MP2, a total oxidation of the hydroxymethyl function afforded FFCA (5-formyl-2-furancarboxylic acid) in a 95% selectivity at complete conversion (entry 5);
iii) MP3, DFF (2,5-diformylfuran, >99%) was the exclusive product achieved from the partial alcohol-to-carbonyl conversion (entry 7).

Interestingly, even HMFCA, one of trickiest derivatives of HMF possessing both an easily oxidisable primary hydroxyl and a fully oxidised carboxyl group, was obtained by a two-step synthesis based on an orthogonal assisted tandem reaction: MP2 was simultaneously used for the initial oxidation of HMF to FFCA followed by the partial hydrogenation of FFCA to the desired HMFCA (entry 6). Importantly, in all these cases, the same catalyst (Ru/C) was used, and it acted in a phase (hydrocarbon or ionic liquid) different from that where the reaction occurred (water or acetonitrile). Multiphase conditions proved therefore fundamental for the control of the reaction selectivity to 4 distinct products derived from full or partial oxidation of HMF. All multiphasic configurations proved suitable for an in-situ recycle of the catalyst

through the semicontinuous design exemplified in **Figure 2.10** for the case of the synthesis of FFCA. After the first reaction (1 → 2), the water solution containing the product was removed from the bottom of the reactor (2 → 3). To the biphasic i-octane/IL mixture with the suspended catalyst (4) was added a fresh aqueous solution of the reactant to restore the initial reaction conditions (6), and implement the 1st recycle (6 → 2). Both conversion (>99%) and selectivity (98–99%) were stable during recycles, with negligible metal leaching – below 0.6 ppb, determined by inductively coupled plasma mass spectrometry (ICP-MS).

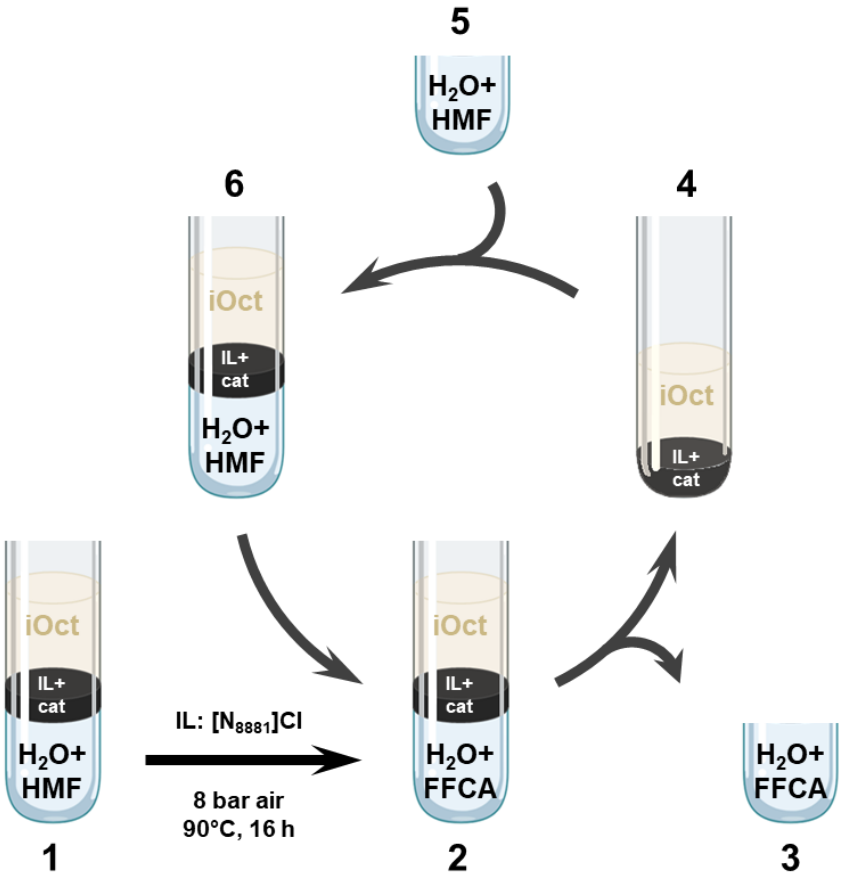

Figure 2.10. Schematic representation of the semicontinuous Ru/C recycling process during the multiphase oxidation of HMF to FFCA (entry 5, **Table 2.1**). Ru/C is confined in the IL phase. Adapted from [38].

Besides oxidative pathways, the hydrogenation/hydrogenolysis of HMF for its selective conversion to HHD (1-hydroxyhexane-2,5-dione) was also carried out under multiphase conditions. The product was obtained in a 99% selectivity at a quantitative conversion, and in an isolated yield of 85%, one of the best results so far obtained for this synthesis (entries 8 and 9). Furthermore, the implementation of a semi-continuous procedure like that of **Figure 2.10**, allowed a reaction productivity up to 9.7 mmol/(g_{cat} · h) of HHD, which made the process amenable for gram-scale syntheses.

The preparation of HHD compulsorily required an ionic liquid assisted MPS which was comprised of water/*i*-octane and an onium salt as $[P_{8881}][NTf_2]$, $[N_{8881}][Cl]$, or commercial Aliquat336 (Starks' catalyst: $[N_{xxx1}][Cl]$ with x=8,10), into which Ru/C was successfully confined. Interestingly, the switch from the phosphonium to the ammonium salts significantly impacted on the reaction rate which increased by approximately 1 order of magnitude: albeit the HHD selectivity was not altered, the conversion of HMF was quantitative after 18 h (entry 8),[39] and 2 h (entry 9),[40] respectively, with the two types of salt. Several aspects were considered to account for the role of the IL including catalyst adsorption, the cation acidity, ion pair interactions, poor water solvation, that affected the kinetic/thermodynamic profiles of the reaction at the phase boundary. Particularly, the adsorption of the ILs on the catalyst modify the reactants accessibility to catalytic sites, by reshaping the reaction energy requirements. Cationic acidity, ion-pair interactions, poor aqueous solvation, introduce an additional layer of complexity by contributing to the mobility of ions, the charge distribution at the interface, and the mass transport to and from the phase boundary.

The last example of **Table 2.1** deals with the selective hydrogenation of water-soluble sugars and sugars-like substrates as glucose, *D*-glucosamine hydrochloride and *N*-acetyl- *D*-glucosamine.[41] Attempts of using MPS like those previously described as water/*i*-octane gave poor results or proved totally ineffective if an IL was present. A different approach was designed by introducing a third organic liquid able to reduce the energy barrier at the liquid–liquid interphase. After screening various solvents as tetrahydrofuran (THF), 2-methyl-tetrahydrofuran (MeTHF), methylisobutyl carbinol (MIBC), and cyclopentyl-methyl-ether (CPME), the choice fell on THF. Interestingly, the THF–water pair exhibits unique properties: at a temperature between 60-145 °C and a 0.3-2.8 THF/water mass ratio, the two solvents spontaneously phase-separate, while below and above this range, they are fully miscible with each other.[48,49] This temperature-mediated miscibility gap which has already proven attractive for the processing of lignin,[50] was successful in the generation of a water/*i*-octane/THF liquid triphase system where the Ru/C-catalysed hydrogenation of glucose and glucosamine or *N*-acetylglucosamine was finally accomplished.

The expected products (sorbitol, 2-amino-*D*-sorbitol, and 2-acetamido-*D*-sorbitol) were obtained with a selectivity of 87-99%, at complete conversion (entries 10-12). Ru/C was completely excluded from the aqueous phase, remaining confined into *i*-octane and into a third THF layer located between the hydrocarbon and the water. According to the procedure of **Figure 2.10**, the catalyst was recycled for up to 9 subsequent runs without loss of

performance, on condition that the amount of THF partitioned in water was topped up from one run to another. The reaction was implemented on a gram scale for glucosamine and a productivity up to 0.89 mmol/(g_{cat} · h) of 2-amino-*D*-sorbitol was reached.

Another interesting approach was proposed for the conversion of sugars to FDCA via the intermediary of 5-HMF.[51,52] A MPS comprised of tetraethylammonium bromide (TEAB), methylisobutyl ketone (MIBK) and water was used. The dehydration of sugars (typically fructose and glucose) to HMF was carried out in the onium salt phase where an acidic catalyst as Amberlyst-15 was present. The oxidation of MHF was catalysed by Au/HT (HT: Mg–Al hydrotalcite) and took place in water. Finally, MIBK was required to transfer HMF from the onium salt to the water phase. The highest yield of FDCA (78%) was obtained from fructose.

A recent review has disclosed the potential of liquid biphase systems for the upgrading of biomass derived molecules via heterogeneously catalysed hydrodeoxygenation (HDO).[53] This reaction reduces the oxygen content of the starting derivatives by operating under a H_2 atmosphere, and it is integral to various biomass conversion methodologies, including the hydrotreating of bio-oils, hydropyrolysis, hydrogenolysis, aqueous- phase reforming of carbohydrates for fuel production, and the hydrotreating of organic acids. Despite significant progresses in HDO for biomass-derived oxygenates, several drawbacks persist, including severe reaction conditions, high costs associated with precious metal catalysts, and in some cases, limited selectivity towards target products. Multiphase conditions may help in this respect. For example, stable Pickering emulsions formed from a water/decalin system were effective for the HDO of vanillin (a model for bio-oil) in the presence of carbonaceous microsphere-supported Pd-based catalysts. Under these conditions, the desired product, *p*-creosol, was achieved in up to a 94% selectivity (**Figure 2.11**).[54]

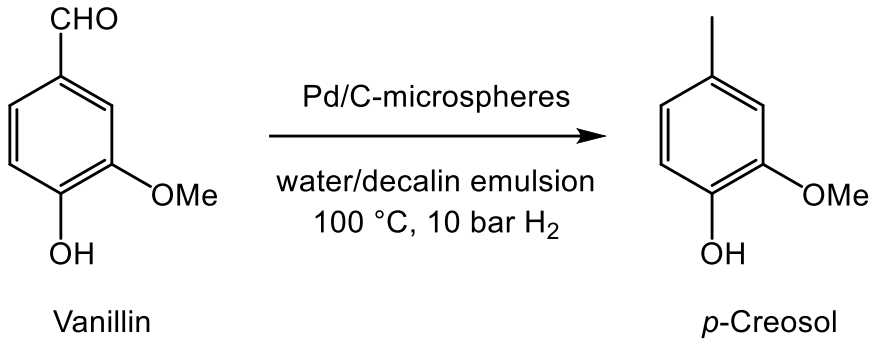

Figure 2.11. Schematic representation of the MPS-assisted HDO of vanillin to *p*-creosol. Adapted from [54].

Also, at 220 °C and pH_2=50 bar, the HDO of other lignin-derived phenolic compounds took place with an excellent selectivity (>90%, 13 examples) using a dodecane/water biphase system and a carbon nanotube-supported (CNT) Ru as a catalyst.[55] This configuration resulted in an efficient separation and protection of the products by continuously extracting them in the hydrocarbon phase.

A significant example of continuous-flow application of MPS is reported by Voß D. et al. A mini plant, based on a continuous stirred tank reactor, was engineered to implement the oxidation of sucrose to formic acid using a water/1-hexanol biphase, a HPA-5 ($H_8PV_5Mo_7O_{40} \cdot 12\ H_2O$) heteropoly acid as a catalyst, and O_2 as the oxidant.[56] At 100 °C and 20 bar O_2, a TON of 840 and an average TOF of 1.3 h^{-1} were reached with a maximum space-time yield of 1.1 $g_{FA} \cdot L^{-1} \cdot h^{-1}$ over 4 weeks (670 h). This configuration represented the first continuous-flow production of FA from a biomass derived sugar with built-in product separation and catalyst recycling.

Inventive multiphase solutions have been proposed also for the synthesis of biobased polymers. For example, a crucial step in the preparation of *L*-polylactic acid (PLA) is the condensation of *L*-lactic acid to the so-called called *L*-lactide (LD) (**Figure 2.12**). This transformation was carried out using a water/*o*-xylene biphase where the reactant *L*-lactic acid was in the aqueous solution while the catalyst, a H-beta zeolite, was confined in the organic layer.[57]

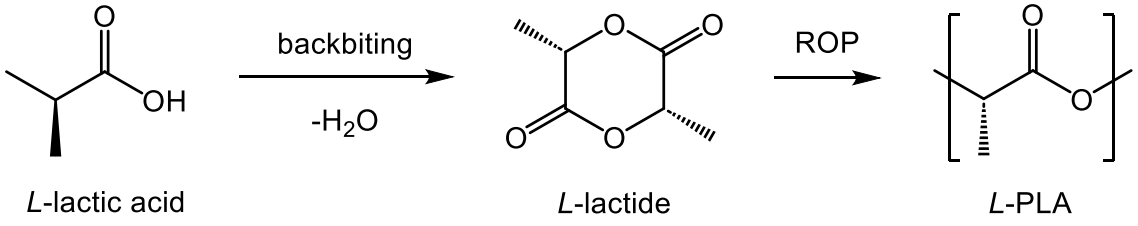

Figure 2.12. Schematic representation of the synthesis of *L*-PLA. Adapted from [57].

Compared to other soluble or solid Bronsted acids, the production of LD was favoured over large LA oligomers within the confined space of the pores of the zeolite. Yields up to 83% were obtained at 144 °C, with an LD productivity >250 $g \cdot L^{-1} \cdot h^{-1}$. Interestingly, the process was devoid of racemisation, giving a >99% *L*-lactide stereoselectivity when the feed was *L*-lactic acid. Moreover, LD separation was proven to be straightforward by extraction, and the catalytic system was stable over 6 runs.

A multiphase set-up based on an aqueous alkaline solution and toluene was recently described for the Pt/C-catalysed partial hydrogenation of cinnamaldehyde, a non-edible biobased feedstock from cinnamon bark,[58] to cinnamyl alcohol.[59] In this case, an interaction between the metal cation from the aqueous base (KOH) and the carbonyl of the aldehyde affected the adsorption of the reactant onto the catalyst, leading to preferential reduction of the C=O bond over the C=C bond. Moreover, by taking advantage of a continuous helical coil reactor, Authors demonstrated that under a given set of conditions (50 °C, 20-50 bar of H_2), the production rate of cinnamyl alcohol (0.44-1.5 kg/day) was doubled compared to that of a batch reactor, and the amount of the required catalyst was 32% less in the continuous mode.

Further studies on multiphase catalysis have been proposed by Pera-Titus et al. who focused their analysis on the advantage of particle stabilised dispersions based on Pickering emulsions, bicontinuous jammed emulsion gels, foams, and liquid marbles.[60] These systems integrate easy phase separation, efficient compartmentalisation of reactants and products, and catalysts reuse, with precise engineering of interphase contact at the nanoscale, thereby offering unique credentials for sustainable chemistry and catalysis. To cite only few reactions pertinent to heterogeneous catalysis under Pickering Assisted Catalysis (PAC) and Pickering Interfacial Catalysis (PIC) conditions, the alkene epoxidation catalysed by particles of ammonium salts of polyoxometalates in water-in-toluene emulsions,[61] the styrene hydrogenation catalysed by Pd-nanoparticles supported on silica microspheres in ethyl acetate/water emulsions,[62] and the biooil photo-reforming for the sustainable production of H_2 catalysed by $Ag_2O/TiO_2/SiO_2$ nanoparticles in bio-octanol/water emulsions,[63] exemplify applications offering not only outstanding selectivity and productivity but also the possibility to recycle the catalysts for up to dozens of times without loss of performance. In summary, the use of Pickering emulsions in PAC and PIC conditions provides a robust catalyst platform with excellent cycling performance. The controlled environment, prevention of catalyst leaching, and improved mass transfer contribute to the efficient operation of these catalytic systems over multiple cycles.

2.1.3 Conclusions and Future Perspectives

The conclusions of this section aim to highlight the contribution that liquid MPS represent as versatile tools for catalysis. The analysis of the current state of research progress in the multiphase field, mostly based on advances/reports published in the last five/six years, allows to reframe this subject not into a fully resolved discipline, but rather into a still promising area of investigation, with potential and resources yet to be explored.

The design of different configurations involving two, three, or even more, immiscible components not only simplifies downstream operations, such as product purification and solvent recovery, but also improves catalyst reuse, minimising the loss of precious metals.

Nevertheless, several challenges remain. The correlation between the nature and the proportions of the liquid phases, the presence of functional groups on the support surface of heterogeneous catalysts, the chemical nature of ligands of homogeneous systems, still represent a largely unexplored area. Moreover, the intrinsic diffusional and interfacial limitations of MPS call for advanced strategies to maximise interfacial area and enhance mass transfer. Innovative approaches, such as the design of thermomorphic systems, particle-stabilised emulsions, and intensified reactor configurations (such as stirred tank reactors, ejector reactors and microreactors), have shown brilliant results in addressing these issues.

Ongoing research is crucial to deepen the mechanistic understanding of MPS and to optimise their performance, with particular attention to scale-up and productivity, to make multiphase-assisted processes viable for commercial applications. In addition, the integration of biomass-derived feedstocks and bio-sourced molecules into such systems further enhance the potential of this research area by the role of MPS into a circular and sustainable chemical framework.

Having outlined the current knowledge and potential of multiphase catalytic systems, the groundwork is now established to move towards a more specific case study. In particular, the following section will focus on the selective oxidation of primary alcohols as a representative application.

2.2 Selective MP-Assisted Oxidation of Bio-Sourced Primary Alcohols over Ru- and Mo-Carbon Supported Catalysts

This section is part of the experimental work carried out in this Thesis. Most of the work was performed by the Author, who contributed to the optimisation, execution, and interpretation of the multiphase reaction conditions, the catalytic activity investigations, and part of the characterisation of the catalytic samples. The results described on this paragraph have been published as the Research Article: **C. Bersani**, D. Rodríguez-Padrón, D. Ballesteros, E. Rodríguez-Castellón, A. Perosa, M. Selva, *ChemSusChem* (**2025**), 18.

The reaction chosen for this study was a multiphase-assisted, heterogeneously catalysed oxidation process where representative bio-based primary and benzyl-type alcohols were selectively converted into aldehydes. The MPS consisted of three mutually immiscible liquid components as water, *i*-octane, and methyltrioctylammonium chloride [N_{8881}][Cl] (**Figure 2.13**) as a hydrophobic ionic liquid. The catalyst involved was either an *ad-hoc* synthesised carbon-supported Mo or a commercial 5% Ru/C, and air was used as the oxidising agent.

The reaction proceeded as an interfacial process with Mo/C or Ru/C perfectly segregated in the ionic liquid phase, and the reactants/products dissolved in the aqueous solution. This environment proved excellent to convert quantitatively benzyl alcohols into the corresponding aldehydes with a selectivity up to 99%, without overoxidation to carboxylic acids. The nature of the catalyst, however, affected the operating conditions with Ru/C being active at a lower T and t (130 °C, 4 h) compared to Mo/C (150 °C, 24 h). The phase confinement was advantageous also to facilitate the products isolation and the recycle of the catalyst. Notably, in the Mo/C-catalysed oxidation of benzyl alcohol, benzaldehyde was achieved with unaltered selectivity (>99%) at complete conversion, for five subsequent reactions through a semicontinuous procedure in which the catalyst was reused *in situ*, without ever being removed from the reactor or treated in any way.

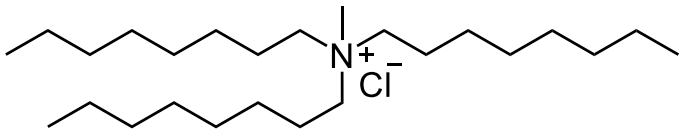

Figure 2.13. Structure of methyltrioctylammonium chloride [N_{8881}][Cl].

2.2.1 Introduction

Heterogenous catalysis is fundamental to most diverse society needs, from the chemicals and polymers synthesis to the energy and waste management, e-chemistry (fossil fuel-free) transition, and more.[64,65] In response to this global demand, the design of catalysts has become so sophisticated that the properties of such systems, including stability and reuse over time, are currently highly reliable and reproducible.[66] Just think for example, to heterogeneous single-cluster catalysts (SCCs) that promise to disclose a new frontier for complex and technically relevant reactions.[67] The selection of a catalyst for a given process, however, is neither obvious nor straightforward. Issues and criticalities concern the use of endangered metals, particularly Pt, Pd, Ir, Os, Rh and Ru which are consumed by more than 90% in the electronics and catalyst manufacturing,[68] the geopolitical instability of areas that provide such elements and the volatility of the corresponding markets,[69] and their release in the planet ecosystems. Interesting studies have been proposed to classify metals by both their risk of depletion and ecofriendly character.[70,71] Albeit at the date of the cited study (2015), the depletion rate could not foresee the future development of recycling technologies nor the discovery of new reserves, certain non-noble metals resulted far more sustainable over precious ones (**Figure 2.14, left**: compare yellow, ochre, and red boxes). On the other hand, a multicriteria evaluation with the TOPSIS methodology, demonstrated that ruthenium, iron, and molybdenum systems were the most favourable alternatives from the standpoint of toxicity, release, and life cycle assessment (LCA)-related parameters (**Figure 2.14, right**).

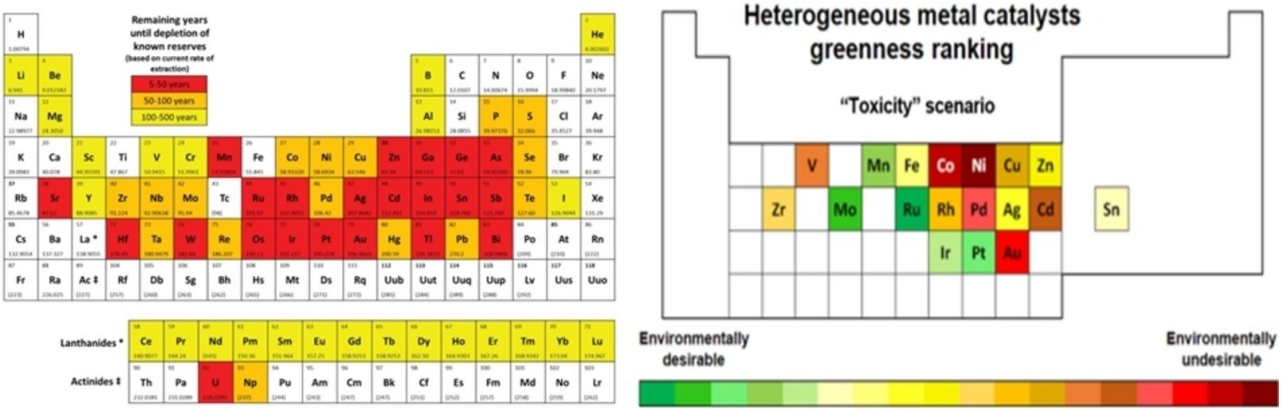

Figure 2.14. Left: remaining years until depletion of known reserves of elements; r**ight**: ranking of heterogeneous metal-based catalysts by their greenness. Reproduced from [70,71] with permission.

These concepts have been largely transposed by the recent literature on heterogeneous catalysis, where hundreds of studies have been aimed to compare the performance and the environmental impact of non-noble metal supported systems with respect to their noble counterparts.[72–76] An attractive field in this vast scenario deals with catalytic oxidations. The research group where this Thesis was developed, recently contributed this subject by designing a library of catalysts comprised of core-shell nanoparticles of metal/metal-oxides based on nickel, iron, cobalt and molybdenum supported on bio-sourced N-doped carbons, that proved effective for the oxidation of different primary alcohols.[77] In the presence of air as an oxidant, supported Mo was the most promising system to control the products distribution and achieve conversion and selectivity both above 90% towards the corresponding aldehydes as products of partial oxidation. Results were satisfactory, yet the procedure required both a harmful solvent (acetonitrile) to ensure oxygen solubility and a costly/time-consuming catalyst/product separation and catalyst recycle. These aspects prompted us to reconsider the oxidation processes by designing different reaction conditions, in a multiphase configuration.

Multiphase-assisted protocols for catalytic organic synthesis have been widely investigated by our group, especially procedures based on combinations of two or more immiscible liquids such as water, hydrophobic ionic liquids, and organic solvents, have been well explored.[37,38,40,78] The multiple advantages of the multiphase-methods include:

i) the built-in separation of reagents/products/catalyst;
ii) the tuning of the reaction kinetics and the selectivity thanks to the changes in solvation and adsorption occurring at the liquid-liquid interphases;
iii) the segregation of the catalyst in a phase different from that where the reaction takes place;
iv) the catalyst reuse which improves sustainability through process intensification and steps economy and minimises waste and energy/mass consumption.

In the current work, most, if not all, the i)-iv) characteristics were exploited to develop an innovative methodology for the oxidation of primary and benzyl-type alcohols under batch conditions. A multiphase-environment, never previously explored for such reaction, was designed using two immiscible liquids as water and *i*-octane, with and without a hydrophobic ionic liquid as methyltrioctylammonium chloride $[N_{8881}][Cl]$ as a third liquid component. The reaction occurred in the aqueous solution in the presence of air as the cheapest available oxidant, while a heterogeneous catalyst was segregated either in the *i*-octane or in the ionic

liquid phase. An *ad-hoc* synthesised carbon-supported Mo catalyst (6.1 wt.%), as well as a commercial 5 wt.% Ru/C catalyst were employed. Both were chosen with the aim to include environmentally desirable metals active in oxidation reactions, and, in the specific case of Mo, the choice was further motivated by its status as a non-noble element that is not in danger of extinction.

Multiphase-conditions offered an original unprecedented arrangement to control the reaction selectivity; particularly, the ionic liquid-assisted process allowed to achieve only partially oxidised derivatives as aldehydes, notwithstanding the marked propensity of such products towards overoxidation to carboxylic acids. **Figure 2.15** below highlights the reaction of benzyl alcohol (BnOH) as a model oxidation process.

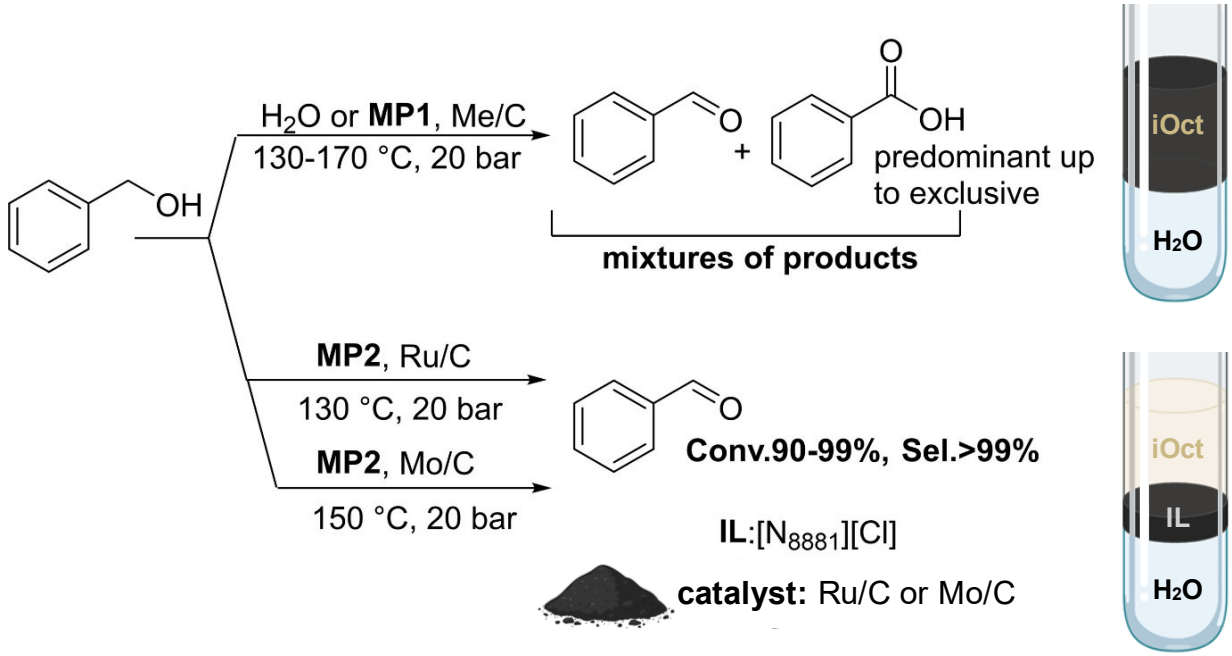

Figure 2.15. The oxidation of benzyl alcohol under multiphase conditions (with and without the ionic liquid as catalyst-philic phase) and in water, in the presence of Mo/C or Ru/C catalysts.

In water or in the water/*i*-octane biphase (**MP1**), mixtures of products were generally achieved, and if experiments were prolonged up to 12–24 h, benzoic acid was obtained as an exclusive derivative (>99%; top). By contrast, the ionic liquid-assisted system (**MP2**) proved excellent to isolate benzaldehyde in a >99% selectivity, at conversion above 90% (bottom). The products distribution was mostly determined by the choice of the reaction environment (water, **MP1** or **MP2**), but the nature of catalyst affected the operating conditions with Ru/C active at a lower T and t (130 °C, 4 h) compared to Mo/C (150 °C, 24

h). Furthermore, a perfect phase separation of products and catalyst was achieved using both **MP1** and **MP2**: products were confined in the polar media (water), while the catalyst was segregated in the hydrocarbon (*i*-octane) or in the ionic liquid phase, where it was recycled. Changes in the properties of Mo/C after its use were thoroughly documented across a variety of characterisation analyses. However, despite these transformations, the activity and selectivity of the catalyst were preserved over five subsequent reuses. This remarkable resilience due to the catalyst's confinement not only ensured practical reusability but prevented any metal contamination of the product or loss of metal into the water phase. Similar results were also obtained with other benzyl-type alcohols bearing *p*-Br, *p*-OCH_3, *p*-OH, *o*-OH or *m*-OCH_3-*p*-OH as aryl substituents.

In contrast, the oxidation of aliphatic alcohols was far less selective, regardless of conditions and catalysts. These substrates were not only overoxidised to the corresponding carboxylic acids but also underwent competitive C–C bond cleavage process, yielding shorter chain derivatives. For example, *n*-butyl alcohol was quantitatively converted to a mixture of butanoic, propanoic and acetic acids in a 70–75%, 20–23% and 3–6%, respectively.

2.2.2 Results and Discussion

Catalytic Materials

Ru/C

C-supported Ru is one the best options among heterogeneous catalysts for processing water-soluble organic reactants, not only for its activity but also for its moderate cost which is about 4% compared to that of other precious metals such as Au and Pt.[43,44,79,80] As thoroughly discussed in Section 2.1.2, a substantial body of work from our group has previously demonstrated that Ru/C-based systems are highly effective catalysts for a variety of multiphase processes (such as hydrogenation and reductive aminations of levulinic acid,[37] hydrogenation of sugars,[41] oxidation of HMF[38]). These reasons, along with the easy commercial availability, prompted us to choose a 5% Ru/C sample sourced by Aldrich, as a benchmark catalyst for this study. The characterisation of this system (lot# MKBW5890 V) for its structural, morphological, and acid properties was already available in literature.[37,38]

Mo/C

Mo-based materials have been largely explored in the literature as non-noble metal alternatives for catalytic oxidations.[81–83] One of the most famous examples is the Formox process for the conversion of methanol into formaldehyde, where either the original catalyst (iron molybdate on excess molybdenum oxide) or innovative systems as supported molybdenum oxide on hydroxyapatites offer excellent conversions and selectivity, both above 90%.[84,85] This result, and more generally the catalytic behaviour of Mo in oxidation processes, were explained also by theoretical studies that highlighted the role of the partially filled metal d-band in enhancing the metal affinity for reactants or adsorbates.[86]

In this study, a carbon-supported Mo-based material was designed to achieve a catalyst suitable for the multiphase oxidation of bio-sourced alcohols. The sample was *ad-hoc* synthesised by adapting a procedure recently reported by our group,[77] in which $(NH_4)_2MoO_4$ and microcrystalline cellulose (lot # MKBN6866 V), both supplied by Merck, were used as a metal and carbon precursors, respectively.

Further ICP analyses proved that Mo-loading was 6.1 wt.%. It is worth noting that, in this case, controlling the metal content on the catalyst was not straightforward, as it strongly depended on the nature of the cellulose. It is indeed well-known that cellulose undergoes depolymerisation upon heating; particularly, in presence of a N_2 atmosphere and above 350 °C, an extensive cleavage of glycosidic bonds takes place, with the release of levo-glucosan and the formation of a charred residue. However, the extent of this degradation process and the corresponding weight loss of the starting biopolymer may vary significantly according to its crystallinity.[87,88] In this work, the used cellulose proved an excellent choice to ensure a reproducible preparation and to confer hydrophobicity to the final carbon support: the resulting Mo/C sample was able to segregate in a non-aqueous phase as described above for Ru/C. Details on the synthesis of Mo/C are provided in the experimental section, while its comprehensive characterisation is discussed later on.

Catalysts Characterisation

A comprehensive characterisation study of both fresh and spent Mo/C catalyst – thus before and after the catalytic tests, respectively – was conducted by employing multiple techniques such as XRD, XPS, TEM, and N_2-physisorption. Particularly, if not otherwise specified, data for the spent sample were gathered after its use for the oxidation of BnOH under the optimised conditions of 150 °C, p_{air}=20 bar, 24 h, which are further described later in the Catalytic Activity section of this chapter.

XRD

The X-ray diffraction (XRD) patterns of the Mo/C catalyst are illustrated in **Figure 2.16**. Both the fresh and the used sample displayed two distinctive peaks at around 25° and 43° which were attributed to the (002) crystallographic plane of the parallel arrangement of graphene-like layers and the (100) crystallographic plane of graphitic carbon within a honeycomb network, respectively. The broad profile at ca 25° primarily stemmed from the amorphous nature of the samples. The XRD diffractogram of the Mo/C fresh system also showed well-defined peaks around 26°, 35°, and 51°, likely indicating the presence of MoO_2 species in the bulk material. However, these signals were absent in the spent catalyst, possibly due to a reduced metal concentration in this sample.

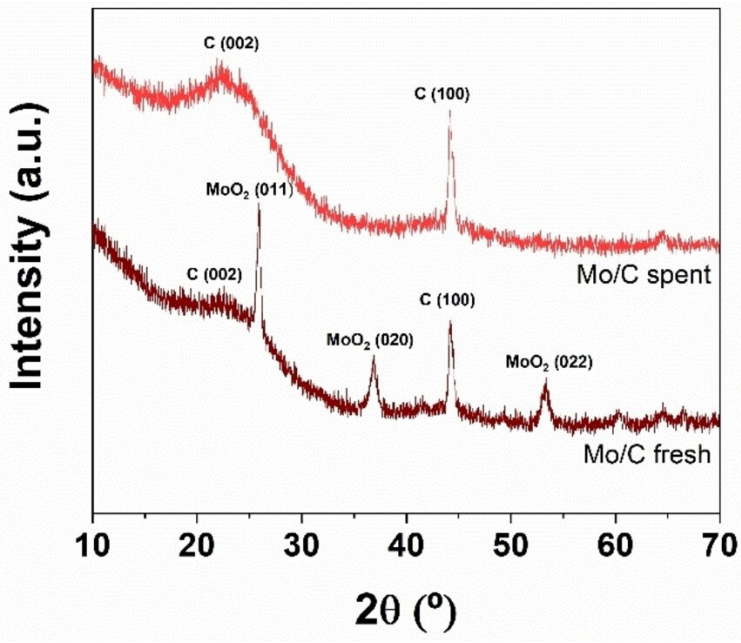

Figure 2.16. XRD patterns of Mo/C catalyst before (fresh) and after (spent) the oxidation reaction of BnOH.

XPS

The high-resolution C 1*s*, O 1*s*, and Mo 3*d* core level XP-spectra are shown in **Figure 2.17**, with binding energy values (in eV) and surface chemical compositions (in at.%) detailed in **Table 2.2** below.

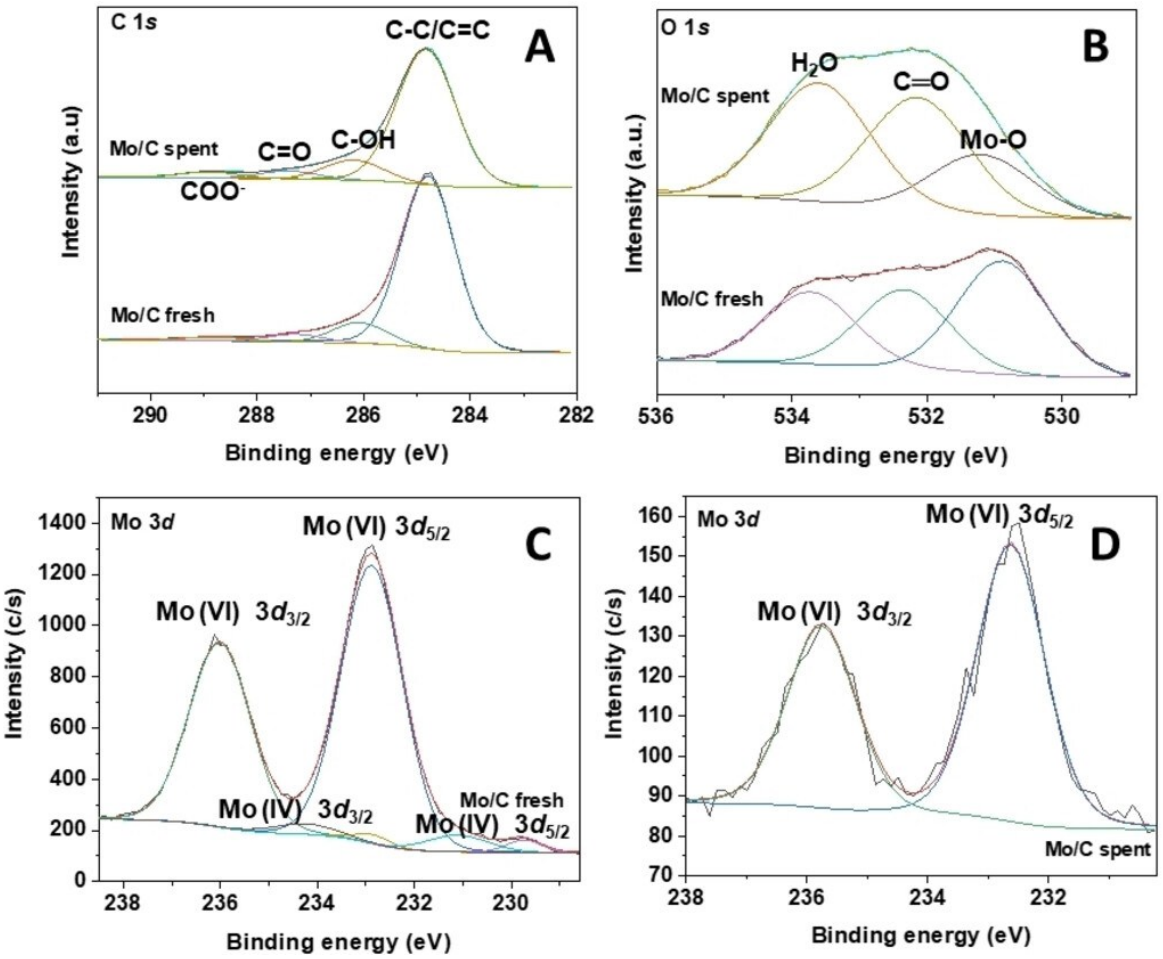

Figure 2.17. High resolution C 1*s*, O 1*s*, Mo 3*d* core level spectra of Mo/C catalyst before (fresh) and after (spent) the oxidation reaction of BnOH.

The C 1*s* core level spectrum of the fresh catalyst was deconvoluted into four contributions at 284.8, 286.1, 287.3, and 288.8 eV, attributed to graphitic and adventitious carbon, C–OH and C–O–C bonds, C=O bonds, and carboxylic groups, respectively. The C 1*s* spectrum showed minimal modification in the used sample, presenting four contributions at similar binding energies, albeit with slightly different relative intensities. Additionally, the O 1*s* core level spectra were deconvoluted into three contributions at 530.9, 532.3, and 533.7 eV for the fresh sample and at 531.2, 532.1, and 533.6 eV for the spent catalyst.

Although the values were similar, significant differences were noticed in the relative intensities. For instance, contributions at lower binding energy (530.9–531.2 eV), assigned to lattice oxygen of molybdenum oxide, exhibited lower intensity in the spent catalyst. This was consistent with the loss (leaching) of metal during the use of the Mo/C sample. The high-resolution Mo 3*d* spectrum for the fresh catalyst displayed three doublets Mo $3d_{5/2}$-Mo $3d_{3/2}$ at 229.7–232.9 eV, 231.1– 234.2 eV, and 232.9–236.0 eV. The predominant doublet was assigned to Mo(VI) as MoO_3, while those at lower binding energy corresponded to reduced Mo species, primarily Mo(IV).

Table 2.2. Binding energy values (eV) and surface chemical composition (at.%) of the constituent element of the Mo catalyst (fresh and spent). Mo wt.% and Mo at.% are calculated via EDX (see HRTEM section).

Catalyst	C 1s (%)	O 1s (%)	Mo $3d_{5/2}$ (%)	C %	O %	N %	Mo %	Mo wt.%	Mo at.%
Mo/C fresh	284.8 (84)	530.9 (42)	229.7 (3)	90.27	8.54		1.19	3.53	0.46
	286.1 (10)	532.3 (30)	231.1 (6)						
	287.3 (4)	533.7 (28)	232.9 (91)						
	288.8 (2)								
Mo/C spent	284.8 (80)	531.2 (20)	232.6 (100)	86.87	11.45	1.61	0.07	2.09	0.27
	286.2 (11)	532.1 (39)							
	287.4 (5)	533.6 (41)							
	288.9 (4)								

Apparently, XRD and XPS measurements indicated the prevalent presence of Mo (IV) species in the bulk material, and of almost fully oxidised Mo(VI) on the surface of the sample, respectively. A single doublet Mo $3d_{5/2}$-Mo $3d_{3/2}$ at 232.6– 235.8 eV, coherent with the presence of Mo(VI), was observed also in the case of the spent catalyst. However, the analysis of the surface chemical composition of **Table 2.2** revealed that the Mo content decreased significantly from 1.19% to 0.07% in the fresh and spent sample, respectively, thereby indicating a substantial Mo leaching after the use of the catalyst.

This was further confirmed by the ICP-MS analyses (**Table 2.3**) which determined a metal concentration of 1.5 wt.% in the used Mo/C, equal approximately to only 25% of the initial Mo concentration (6.1 wt.%) in the fresh specimen. XPS also revealed the presence of a not

negligible amount of nitrogen (1.61%) on the spent sample, which was more than likely related to the adsorption of the ionic liquid ($[N_{8881}][Cl]$ in the **MP2** system) on the catalyst surface. Apparently, the ionic liquid strongly interacted with the carbon support so that it was not removed in the post-reaction treatment, even after full rinsing by organic solvent during filtration. By contrast, the fresh sample was nitrogen-free thereby confirming the full thermal degradation of the precursor $(NH_4)_2MoO_4$ during the catalyst preparation.

Further details regarding ICP-MS analysis will be discussed later in this section, in conjunction with catalyst recycling experiments.

Table 2.3. ICP-MS analysis of the **MP2** system and the catalysts before and after the recycle operations.

Entry	Sample	Mo µg/mL [a]	Mo wt.% [b]	Ru µg/mL [a]
1	Water	0.04		0.05
2	*i*-octane	0.06		0.04
3	Ionic liquid	1775		15
4	Spent catalyst		1.5	

[a] Metal concentration (µg/mL) in each of the liquid components of the **MP2** system.
[b] Content of Mo in the spent catalyst recovered after recycles of **Figure 2.26B**.

High-resolution Transmission Electron Microscopy

HRTEM micrographs revealed the laminar structure of the carbonaceous support, in the fresh and used catalysts (**Figure 2.18**), from which is possible to appreciate that, in both cases, molybdenum nanoparticles were uniformly dispersed within the carbonaceous structure. In the fresh sample, Mo nanoparticles presented an average diameter of 8.1–4.3 nm, with most falling within the range of 4–8 nm. Conversely, the spent catalyst exhibited a bimodal size distribution with most metal particles ranging between 4–6 nm and 10–14 nm (average diameter: 9.5–4.9 nm). Such results suggested a partial sintering of Mo nanoparticles under the conditions employed for the oxidation reaction. Mapping analysis confirmed both a high dispersion and a uniform distribution of the metal (**Figure 2.19**).

Table 2.2 presents the atomic concentration percentage and total weight percentage calculated via Energy Dispersive X-ray Spectroscopy (EDX).

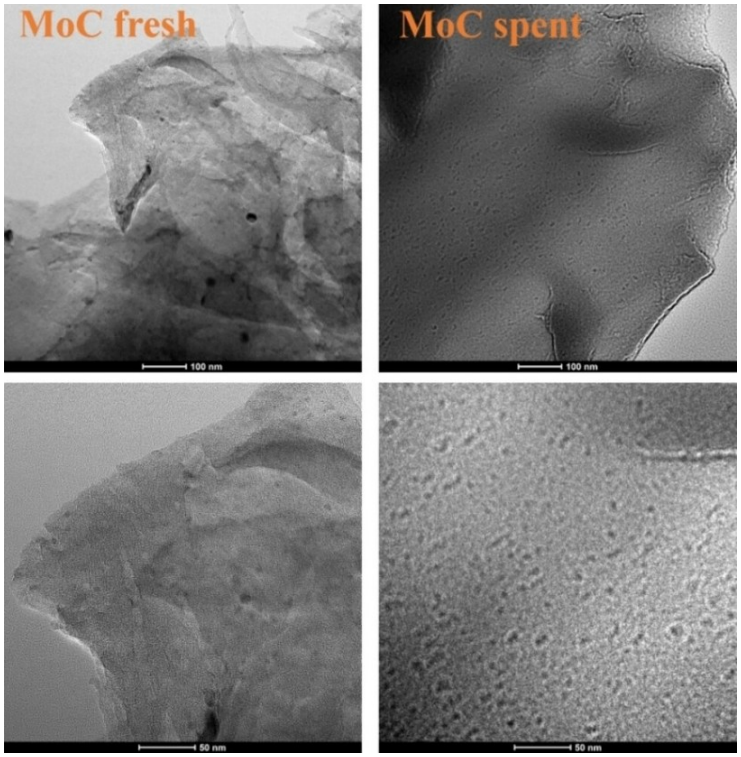

Figure 2.18. High resolution TEM images of the fresh (left) and spent (right) Mo/C catalyst.

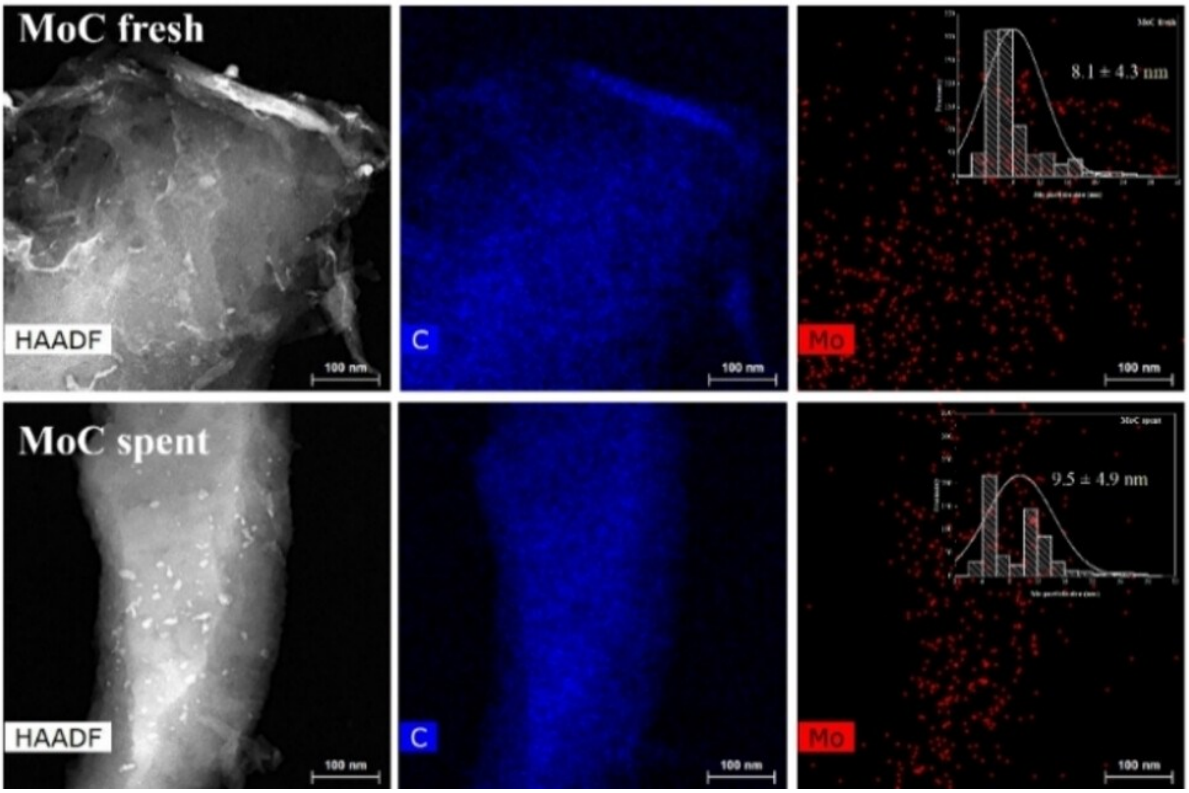

Figure 2.19. STEM and EDX images of the fresh (top) and spent (bottom) Mo/C catalyst, and Mo particle size distribution.

N_2-Physisorption

The fresh Mo/C (**Figure 2.20A**) exhibited a type IV isotherm and type II adsorption hysteresis, indicative of the development of mesoporous material and the existence of disordered networks.

The corresponding measures of the textural properties including surface area, pore diameter, and pore volume, provided values of 520 m^2/g, 4.3 nm, and 0.2 m^3/g, respectively. Compared to these features, the textural properties of the spent sample (**Figure 2.20B**) underwent a drastic change, as shown, for example, by the reduction of the surface area down to 4.3 m^2/g as well as a decrease of the pore volume (0.01 m^3/g) and a slight increase in mean pore size (6.7 nm).

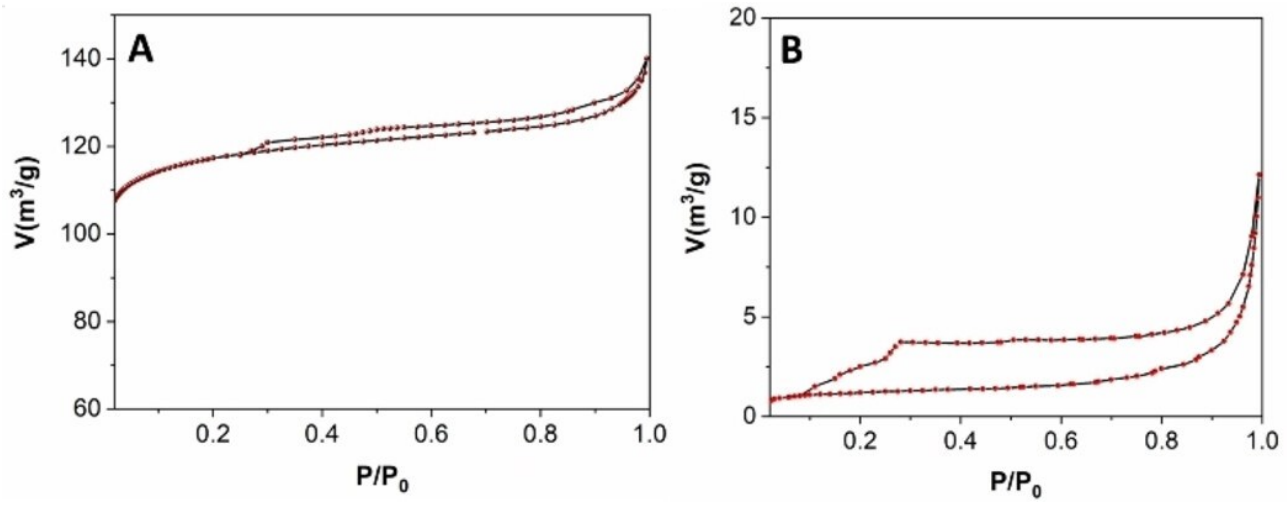

Figure 2.20. N_2-physisorption isotherms of Mo/C catalyst before (**A**, fresh) and after (**B**, spent) the oxidation reaction of BnOH.

This was attributed to the experimental conditions used for the oxidation tests which resulted in the breakdown of the carbonaceous architecture and the occurrence of pore occlusion phenomena due to the adsorption of organic entities, most likely the ionic liquid, on the catalyst support.

Despite these significant alterations, Mo/C was a recyclable catalyst when used under multiphase conditions (**MP2** system): its catalytic performance did not show any appreciable change even after five subsequent reuses (see later in the Catalysts Recycling section).

Catalytic Activity

The oxidation of benzyl alcohol

Benzyl alcohol (BnOH) was chosen as a model substrate to begin the investigation. The partial oxidation of BnOH to benzaldehyde was the target of the study. This is a highly desirable reaction in the design of biomass valorisation strategies, not only for BnOH is a representative bio-based molecule but also for the intrinsic value of benzaldehyde as a versatile intermediate and a flavouring agent.[77] Oxidation tests were conducted in a batch mode using a stainless-steel autoclave. In the presence of the catalysts above described (5 wt.% Ru/C or 6.1 wt.% Mo/C; 100 mg each), three different reaction environments (shown in **Figure 2.21**) were explored. These were comprised of:

i) water (5 mL),
ii) a liquid biphase of water (5 mL) and *i*-octane (5 mL), identified as system **MP1**,
iii) a liquid triphase of water (5 mL), *i*-octane (5 mL), and methyltrioctylammonium chloride [N_{8881}][Cl] as an ionic liquid, 500 mg), identified as system **MP2**.

In the **MP1** and **MP2** systems, the relative proportions of each phase were calibrated from our previous works to obtain a perfect separation of the liquids, with water on the bottom, *i*-octane on top, and the ionic liquid (when present) in the middle (**Figure 2.21**). Even more interesting was that both the carbon-supported catalysts appeared perfectly confined in *i*-octane or, alternatively, in the ionic liquid phase. This confinement phenomenon was known and expected for Ru/C,[38,40] but it could not be taken for granted for the Mo/C sample investigated in this work. Further considerations on this aspect are given in this section.

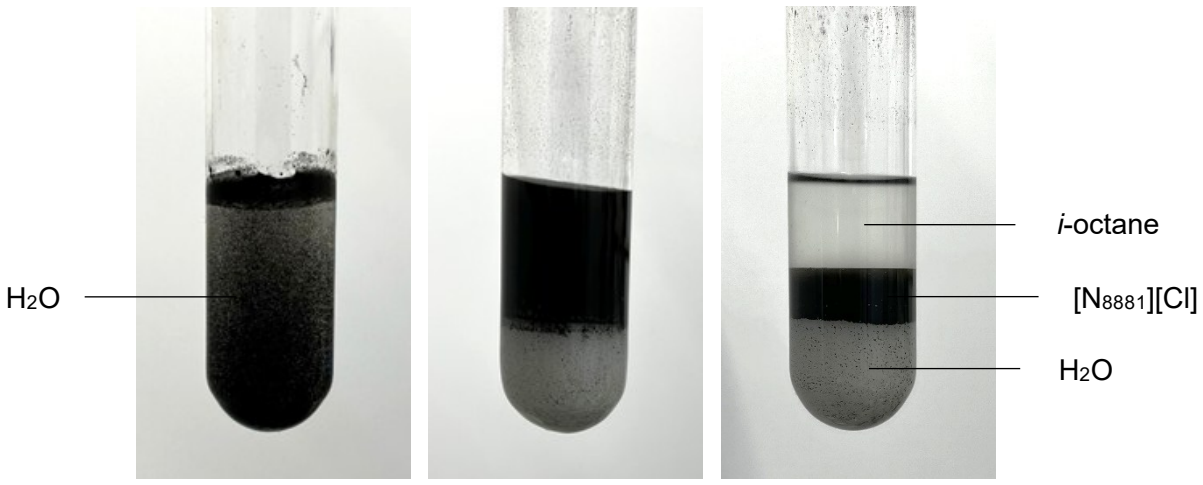

Figure 2.21. From left to right, pictorial representation of the Ru/C catalyst suspended/confined in: i) water; ii) **MP1** system comprised of water and *i*-octane; iii) **MP2** system comprised of water, *i*-octane and [N_{8881}][Cl].

The substrate, BnOH (2 mmol) was dissolved in water according to its solubility limit (3.50 g/100 mL at 20 °C,[89]). The resulting solution was 0.4 M. Air was chosen as an oxidant, either in water or in multiphase, to improve the safety and sustainability of the protocol. A variety of experiments were carried out by varying temperature and pressure in the range of 110–150 °C and 10–20 bar, according to both a literature inspection on the oxidation of BnOH and previous results from our group.[77] Results are summarised in **Table 2.4**.

Table 2.4. Catalytic oxidation of BnOH in water, **MP1** and **MP2** systems. Conversion and products distribution were determined by GC and GC/MS.

Entry	Medium	Catalyst	T (°C), *p* (bar), t (h)	Conversion %	Selectivity %	
					PhCHO	$PhCO_2H$
1	Water	Ru/C	130, 20, 2	60	88	12
2			130, 20, 4	>99	14	86
3			130, 20, 12	>99	-	>99
4		Mo/C	130, 10, 4	50	92	8
5			110, 20, 4	85	70	30
6			130, 20, 24	60	>99	-
7			140, 20, 24	75	74	26
8			150, 20, 24	>99	10	90
9	**MP1**	Ru/C	130, 20, 2	45	48	52
10			130, 20, 4	>99	28	72
11		Mo/C	130, 20, 24	40	>99	-
12			140, 20, 24	58	77	23
13			150, 20, 24	98	5	95
14	**MP2**	Ru/C	130, 20, 2	50	>99	-
15			130, 20, 4	>99	>99	-
16		Mo/C	130, 20, 24	45	>99	-
17			140, 20, 24	68	>99	-
18			150, 20, 24	96	>99	-

In *water*, no combination of temperature, pressure, and reaction time parameters enabled the selective oxidation of BnOH to PhCHO using the Ru-based catalyst. Even at a moderate conversion (60%, reached at 130 °C after 2 h) the reaction consistently produced a mixture of products, with a non-negligible amount of benzoic acid (12%, entry 1). Doubling the reaction time led to the complete conversion of the substrate, but with a further decrease in selectivity, due to the overoxidation to benzoic acid that increased progressively to 86% after 4 h (entry 2) and 99% after 12 h (entry 3). The effect of reaction time on conversion and product distribution is illustrated in **Figure 2.22A**.

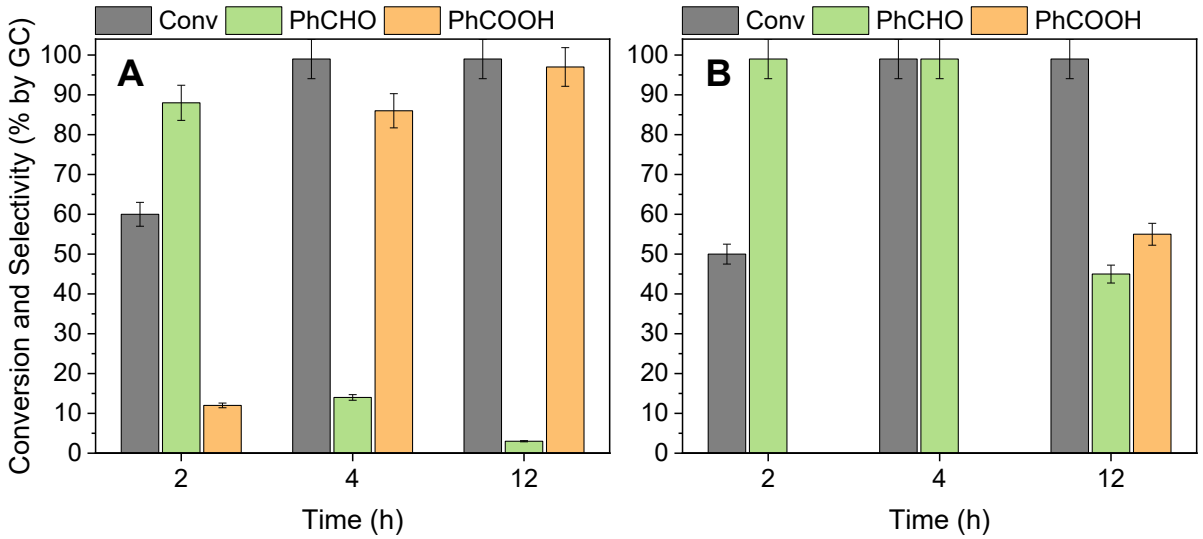

Figure 2.22A-B. Effect of increasing the reaction time (from 2 to 12 h) on the Ru-catalysed reaction conversion and products distribution in: **A)** water and **B)** the **MP2** system, where complete conversion and >99% selectivity towards the partially oxidised product (PhCHO) were achieved after 4 h.

Achieving complete conversion of benzyl alcohol over Ru/C after 4 h at 130 °C and 20 bar of air suggested that both the thermal input and the internal availability of O_2 as oxidant were already sufficient to drive the reaction forward and did not require any further increase.

However, to suppress substrate overoxidation and improve selectivity towards the partially oxidised product, further experiments were carried out by lowering either temperature or pressure. As shown in **Figure 2.23** despite a slight improvement in aldehyde selectivity, conversion dropped from 99% to 50% upon reducing air pressure from 20 to 10 bar (other conditions were 130 °C and 4 h, entry 4), and from 99% to 85% upon lowering the temperature from 130 to 110 °C (other conditions were 20 bar air and 4 h, entry 5). In both cases, the amount of benzoic acid remained significant (10% and 30%, respectively), indicating that such modifications were not beneficial. The most plausible reasons were adverse effects on both the reaction energetics and the solubility of the oxidant (O_2) in the

reaction mixture. Overall, this confirmed that both high temperature and pressure were necessary to achieve complete conversion of the alcohol.[90,91]

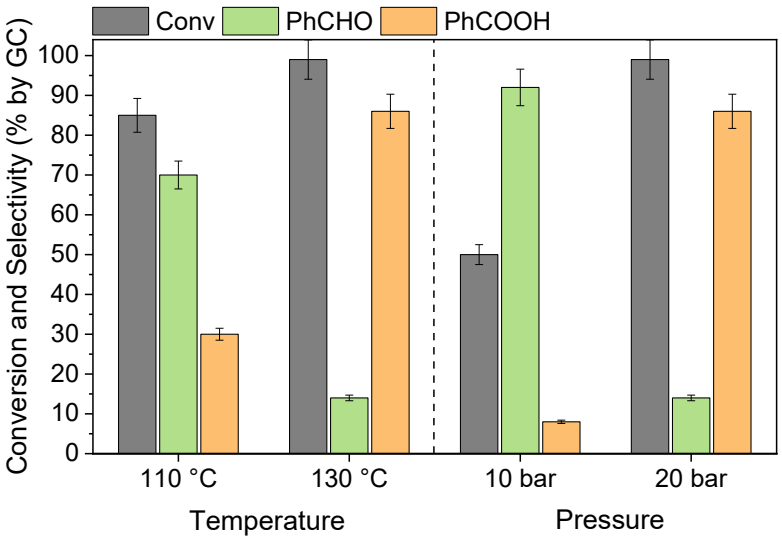

Figure 2.23. Effect of reduced pressure (from 20 to 10 bar, at 130 °C) and reduced temperature (from 130 to 110 °C, with 20 bar air) on the Ru-catalysed reaction conversion and products distribution in water.

Mo/C was far less active than Ru/C, though it was apparently more selective. The aldehyde was achieved as an exclusive product (>99%) at 130 °C, but the conversion did not exceed 60% after 24 h (entry 6). Increasing the temperature to 140 and then 150 °C improved conversion to 76% and then quantitative, respectively (entries 7 and 8); however, it brought an abrupt drop of the aldehyde selectivity and made benzoic acid becoming predominant (26 to 90%), as shown in **Figure 2.24A**.

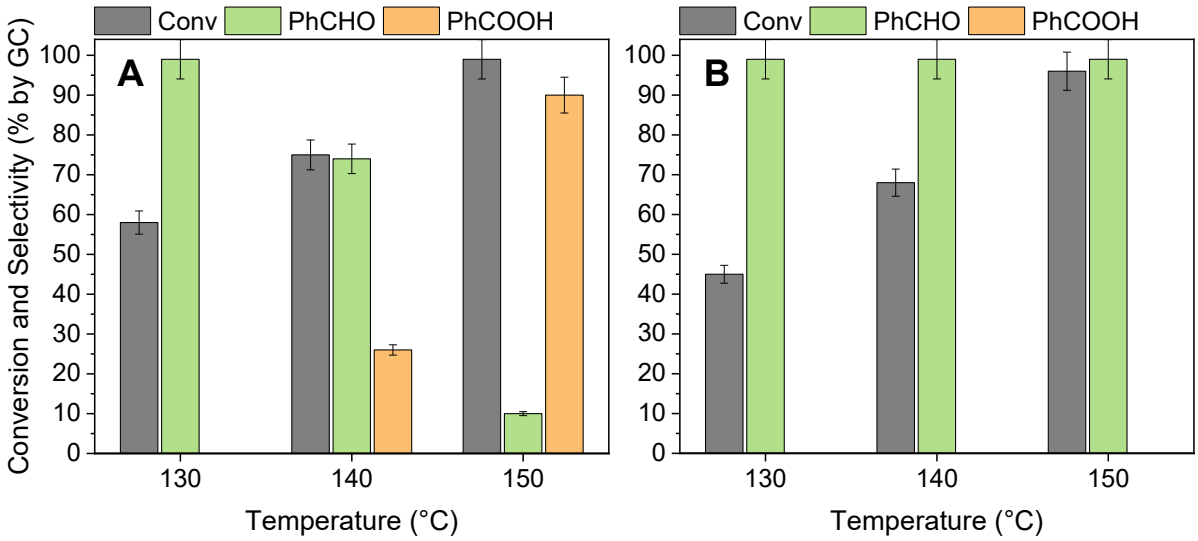

Figure 2.24A-B. Effect of increased temperature (from 130 to 150 °C, with 20 bar air) on the Mo-catalysed reaction conversion and products distribution in: **A)** water and **B)** the **MP2** system, where 96% conversion and >99% selectivity towards the partially oxidised product (PhCHO) were achieved after 24 h at 150 °C.

In the ***MP1*** *(water/i-octane) biphasic system*, a satisfactory benzaldehyde selectivity was obtained only at a moderate conversion (40%), while a not negligible to deep oxidation to benzoic acid was prevalent otherwise. The oxidation of BnOH was slightly slower in **MP1** because both Ru/C and Mo/C, confined in the *i*-octane phase, acted at the water-organic interface, in contrast to the water-only system where the catalysts were directly suspended in the reactants solution. This generally resulted in lower conversions, consistently with previous studies on the kinetics of multiphase-assisted transformations[38,39,41,78]. For instance, the Mo catalyst gave 40% conversion at 130 °C in the **MP1** system vs 60% in water (entries 6 and 11, respectively), and the reaction required 24 h to reach an almost quantitative conversion (98%) upon increasing the temperature up to 150 °C (entry 13) Similarly, with Ru catalyst, only 45% conversion was reached in the **MP1** system vs the 60% in water under the same conditions (entries 1 and 9, respectively), and the reaction took 4 h for complete conversion (entry 10). Product distribution, however, appears to follow the same general trends as in water, with the main issue always being the overoxidation of BnOH to benzoic acid at high conversion (72 and 95%, entries 10 and 13 respectively). In no way could the aldehyde be achieved as an exclusive product.

In the ***MP2*** *(water/i-octane/ionic liquid) triphasic system*, an outstanding control of products distribution was achieved using both the Ru/C and Mo/C catalysts: oxidation proceeded exclusively through partial oxidation of BnOH to benzaldehyde, obtained with >99% selectivity at 96–99% conversion. For Ru/C, benzaldehyde was the only observed product: after 2 h at 130 °C and 20 bar air, conversion was moderate (50%, entry 14), but prolonging the reaction time to 4 h, a complete conversion was reached while maintaining >99% selectivity (entry 15; see **Figure 2.22B**). For Mo/C, selectivity towards benzaldehyde (99%) was also consistently preserved in the **MP2** system. In this case, however, conversion was low-to moderate at 130-140 °C (45 to 68%, entries 16 and 17); only at 150 °C, the reaction was quantitative (entry 18; see **Figure 2.24B**). Experimental conditions were identical to those in water and in the **MP1** system.

The confinement effect

In the **MP2** system, the catalyst was confined in the ionic liquid phase, while the reaction occurred in the water solution. The role of *i*-octane, apparently inconsequential, was necessary to achieve both phase separation and catalyst segregation, as already extensively described in some works by our group.[38,40,78] Several previous investigations demonstrated that the catalyst confinement in both organic media and in ionic liquids, was observed for a variety of carbon-supported metals (Pd/C, Pt/C, and Ru/C) and in all cases, it significantly impacted their catalytic performance.[41,47,80]

As mentioned in section 2.1.2, the segregation phenomenon is far from being understood because of the complexity of interactions occurring in MPS,[92] but some aspects deserve attention. An in-depth characterisation study of a variety of carbons led to conclude that only some samples could segregate in apolar liquids, specifically those materials combining a low surface acidity (due to carboxylic, phenolic, and lactonic groups) to the presence of Na-based impurities (0.1-0.2%) on the carbon itself. The properties of the supports used in this study for Ru and Mo, and in this case, the cellulose-derived material designed and used to disperse Mo, apparently fulfilled these requisites, and made the investigated catalysts suitable to the confinement in *i*-octane. Interestingly, the tuning of the hydrophobic/hydrophilic balance was reported by acid pretreatments of a variety of carbons as carbon nanotubes (CNTs), activated carbons (AC), and F-doped carbons used for the synthesis of Pd-, Ni- and Au-based catalysts.[44,45]

On the other hand, in section 2.1.2, it was underlined the embodiment phenomena of metal catalysts dispersed on carbons in ionic liquid media was associated also to the occurrence of strong polar interactions between the dense and viscous liquids and (mostly) the surface functionalities of the catalysts support.[86] Whatever the reasons for the effects of the ionic liquid, the catalysts segregation allowed an excellent benzaldehyde selectivity and was advantageous for the separation of the liquid products without resorting to filtration and/or centrifugation. Both these operations are costly and time-consuming especially for carbon-supported systems.[34,35]

Catalysts Recycling

The findings of **Table 2.4** demonstrated that Ru/C displayed a higher oxidation activity implying a lower energy demand compared to the reactions catalysed by Mo. The latter, however, was approximately 340 times less costly than Ru,[93] and more sustainable since not at risk of depletion like Ru. These aspects are critical in any liquid-phase reaction where a metal-based catalyst may cost up to one third of the total cost of the process, and its reuse is imperative.[94] In this context, the potential of the **MP2** system was explored to design additional experiments aimed to an *in-situ* recycle of the catalyst in the ionic liquid phase. The semicontinuous procedure schematised in **Figure 2.25** (step1 1–3) was used.

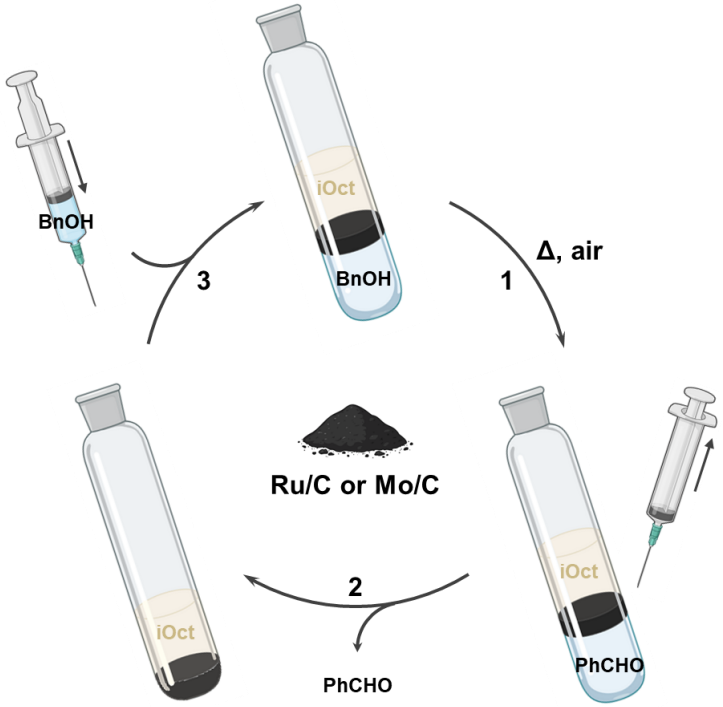

Figure 2.25. Semicontinuous design for the in-situ recycling procedure of the catalytic system.

A first reaction was carried out under the conditions of entry 15 or entry 18 of **Table 2.4**, using Ru/C or Mo/C, respectively (step 1). After the experiment was complete, the aqueous phase (containing the reaction products) was withdrawn using a syringe (step 2) and replaced with an equal volume of a fresh aqueous solution of BnOH (5 mL, 0.4 M) (step 3). Thereafter, a second oxidation was run. The overall sequence was repeated for five subsequent reactions. Results are reported in **Figure 2.26A** and **B** which refer to the recycle of Ru/C and Mo/C, respectively. The conversion dropped from 99% to about 80% in the case

of Ru/C, and from >90% to about 75% for Mo/C, after the first run. Thereafter, from the second reaction on, conversion remained substantially steady for both catalysts.

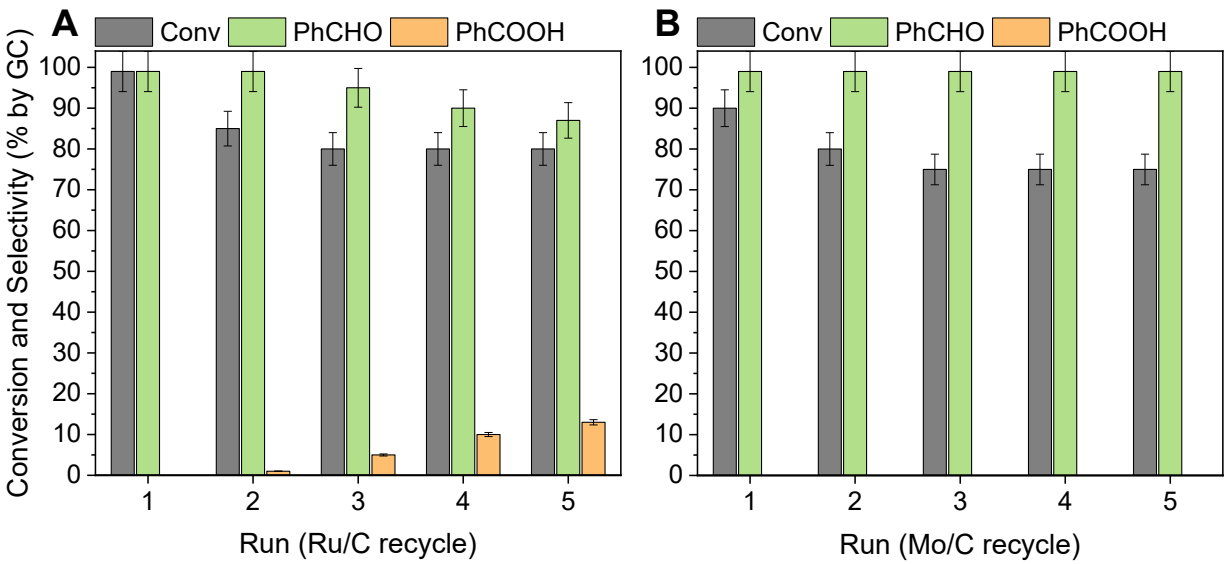

Figure 2.26A-B. Semicontinuous recycle of the catalyst during the selective oxidation of BnOH to PhCHO carried out in the **MP2** system. Conditions for each run: aqueous solution of BnOH (0.4 M, 5 mL); *i*-octane (5 mL), methyltrioctylammonium chloride ([N_{8881}][Cl]; 500 mg), 20 bar air. **A)** Ru/C (100 mg) as the catalyst, 130 °C, 4 h; **B)** Mo/C (100 mg) as the catalyst, 150 °C, 24 h.

A similar behaviour was previously noticed by us for other multiphase-assisted processes:[38,80] the conversion drop after the 1st test was explained by the help of the visual inspection of such systems during the recycle operations. At the start of the first reaction, the catalyst appeared dispersed throughout the multiphase, *i. e.* partitioned in the three liquid components (water, *i*-octane, ionic liquid). This meant that either Ru/C or Mo/C were partially available for the direct adsorption of the reactants in the aqueous phase, thereby favouring the kinetics of the oxidation. Upon stirring the multiphase, however, the catalyst progressively moved in the ionic liquid layer where it appeared fully segregated from the first recycle on. Under such conditions, the reaction was slower since it occurred only at the phase boundary. Additional experiments – not reported in **Figure 2.26** – were also carried out even after the fifth use, by further recycling the ionic liquid-confined Mo/C twice at a higher temperature of 160 °C. The conversion in these two reactions was not only steady but even returned to values as high as those observed in the first oxidation cycle (>90%).

Figure 2.26 also indicated that the selectivity towards benzaldehyde was always ≥99% in the case of Mo/C, while it progressively decreased to 88% for the Ru-catalysed reactions due to the formation of benzoic acid up to 12% in the last recycle.

This apparent drop in the catalytic performance (selectivity) was no longer investigated. However, among plausible causes, it was hypothesised that the prolonged exposure of Ru nanoparticles to both oxygen and reaction intermediates or by-products accumulated on their surface across multiple cycles, did play a role in modifying the adsorption mechanism and activation of reactants over Ru/C. This aspect will be the object of future studies.

ICP-MS Analyses and Sheldon Tests

ICP-MS analyses were performed to shed light on the reliability of the catalyst recycle. At the end of the experiments shown in **Figure 2.26A-B**, each liquid component of the **MP2** system and the spent catalysts were examined. Water and *i*-octane were quantitatively withdrawn from the reactor using a syringe. The ionic liquid phase was doubly filtrated over a microporous membrane (0.22 μm) to remove the solid catalyst. The three clear liquid phases (H_2O, *i*-octane, and the ionic liquid) were then analysed. After filtration, the solid catalyst was recovered and dissolved completely in a water solution by combining strong oxidizing conditions and MW heating (further details are in the Experimental Section).

Results are reported in **Table 2.3**. The presence of both metals, Ru and Mo, in the aqueous solution and in the *i*-octane was negligible (40-60 ppb, entries 1–2). In the ionic liquid phase, the leaching of Ru was very low (ca 0.15 wt.% of the total metal amount in the starting catalyst) and consistent with the behaviour of the same Ru/C sample in a variety of previously explored reducing/oxidising conditions,[39,80] while the loss of Mo/C was remarkable (entry 3). The amounts of Mo found in ionic liquid phase and Mo loading of the spent catalyst were, however, incongruent with the overall mass balance of the metal since they accounted for only 16% and 25% (total 41%), respectively, of the metal concentration in the fresh sample (6.1 wt.%). The reasons for this result were not yet clarified, but a hypothesis was formulated based on the (unexpected) presence of nitrogen (1.61%, **Table 2.2**) detected by XPS analyses, on the surface of the used catalyst. This was associated to the adsorption of organic moieties coming from the ionic liquid in the **MP2** system. It was reasonable to assume that this adsorption/deposition on the spent catalyst brought about an increase of its content of carbon and a decrease of its Mo loading, respectively. The adsorption of the ionic liquid as such or of species originated from it, was further substantiated by the occlusion of the catalyst pores detected by the N_2-physisorption measures (**Figure 2.21**).

Sheldon tests were designed to evaluate the activity of metals leached into the ionic liquid phase and compared to a blank multiphase reaction carried out without any added catalyst. To this purpose, an oxidation reaction was carried out with Ru/C under the conditions of entry 15 in **Table 2.4** (130 °C, 20 bar, 4 h), and with Mo/C under the conditions of entry 18 in **Table 2.4** (150 °C, 20 bar, 24 h). Thereafter, the two solid catalysts suspended in the **MP2** systems were filtered through a 0.22 µm microporous membrane. The corresponding aqueous phases containing the products were removed and replaced by fresh aqueous solutions of BnOH (0.4 M, 5 mL). A second oxidation run was then carried out with both systems, according to the procedure described in **Figure 2.25**. In parallel, a blank multiphase reaction was performed without any added catalyst. In all cases, conversion, selectivity and products nature were determined/assigned by GC and GC/MS. Results are reported in **Table 2.5** below.

Table 2.5. Sheldon tests for the oxidation of benzyl alcohol in the **MP2** system. Conversion and products distribution were determined by GC and GC/MS.

Entry	Removed catalyst	T (°C), *p* (bar), t (h)	Conversion %	Selectivity %	
				PhCHO	$PhCO_2H$
1	**Ru/C**	130/20/4	21%	>99%	-
2	**Mo/C**	150/20/24	14%	>99%	-
3	**None (blank)**	150/20/24	6%	>99%	-

The corresponding conversion was 21% and 14% for the Sheldon test after using Ru and Mo, and 6% in the blank test, respectively.

Notwithstanding its almost insignificant concentration (only 50 ppb of metal were determined in solution after 5 catalyst recycles), dissolved Ru displayed a significant activity (entry 1). However, the study of the catalyst recycles (**Figure 2.26A**) indicated that at a high conversion, a substantial amount of benzoic acid was achieved. This drop of selectivity was plausibly due to the effect of “homogeneous” Ru leached in the solution that was more active towards the overoxidation of benzyl alcohol than the supported metal. By contrast, the comparably higher amount of Mo soluble in the ionic liquid phase (whatever this species was) did not affect the formation of benzaldehyde, which was always the exclusive product (entry 2; see also **Figure 2.26B**). This indirectly demonstrated that the multiphase oxidation

predominantly took place over the Mo/C solid, the performance of which, particularly the selectivity, was steered by the adsorption of the ionic liquid on its surface. Overall, all characterisation analyses were consistent with a profound alteration of the properties of Mo/C during use and recycles, but the resilience of the catalyst was surprising: its confinement in the ionic liquid layer of the MPS not only preserved in full its activity and selectivity for five (and more) subsequent reuses, but it facilitated its practical reusability avoiding any metal contamination of the product or metal loss in water/i-octane phases. The reasons for Mo-leaching in the ionic liquid-phase will be explored in future studies, with the aim of designing a more robust catalytic system and to further investigate its potential under multiphase conditions.

Substrate Scope

The triphasic **MP2** system was further explored to assess its general applicability to the oxidation of other benzyl-type and aliphatic alcohols. Five benzyl-type alcohols including 4-hydroxy-, 4-methoxy-, 4-bromo-, 2-hydroxy-, and 4-hydroxy-3-methoxy-benzyl alcohol were initially considered (substrate 1–5, **Table 2.6**).

Vanillic alcohol (5) belongs to the so called "vanillin platforms" and is among the most important derivatives of the lignin depolymerisation,[95] while for anisyl alcohol (2) and hydroxy-substituted benzyl alcohols (1 and 4), albeit still prepared from non-renewable petrochemical resources, innovative bio-based approaches have been successfully reported using engineered microbes and inexpensive feedstocks from protein waste hydrolysate.[96,97] These alcohols and their aldehydes find relevant applications in the cosmetics, perfume and food industries. To the best of our knowledge, 4-bromobenzyl alcohol (3) is not a bio-based compound, but it represents a good benchmark substrate to compare the oxidation reactivity of the class of alcohols investigated here.

Reaction parameters were set according to entries 15 and 18 of **Table 2.4**, for Ru/C and Mo/C catalytic systems, respectively. In particular, the reaction conditions were the same as those employed for the oxidation of model benzyl alcohol in the **MP2** system: an aqueous solution of the selected benzyl-type alcohol (0.4 M, 5 mL) was set to react in the presence of *i*-octane (5 mL), ionic liquid ($[N_{8881}][Cl]$; 500 mg), and the catalyst (Ru/C or Mo/C; 100 mg), under 20 bar air. Temperature and reaction time were set to 130 °C for 4 h with Ru/C, and 150 °C for 24 h with Mo/C.

The results are reported in **Table 2.6**. Both catalysts displayed an exceptional performance with conversion and selectivity to the aldehyde products above 92% and 98%, respectively, in all cases except for 4-bromobenzyl alcohol (3) for which a slightly lower conversion was observed for the reaction catalysed by Mo/C (76%, entry 3). The same behaviour was noticed and previously reported for substrate 3 also during its oxidation over a Mo–N/C system in acetonitrile solvent.[77] Electron-withdrawing properties of the *p*-bromide substituent plausibly contributed to this difference. However, regardless of the used substrate, the **MP2** system allowed the perfect segregation of the catalyst in the ionic liquid-phase from the reactants/products in the aqueous solution.

Table 2.6. Oxidation of benzyl-type alcohols in the **MP2** system using both Ru/C and Mo/C. Conversion and products distribution were determined by GC and GC/MS.

Entry	Substrate	Product	Conversion, selectivity %	
			Ru/C	Mo/C
1	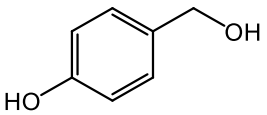	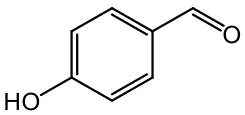	>99, >99	95, >99
2	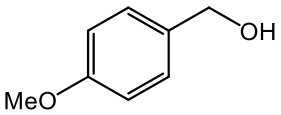	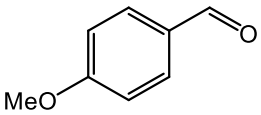	>99, >99	92, 98
3	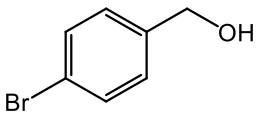	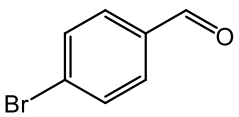	98, 98	76, >99
4	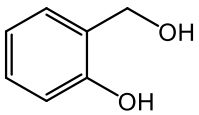	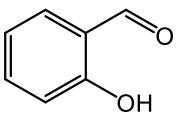	>99, >99	>99, >99
5	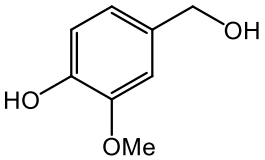	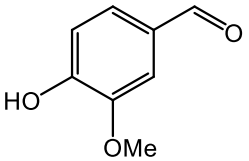	>99, >99	>99, >99

Comparison to Literature Results

A comparative assessment of the **MP2**-assisted protocol proposed in this work against a selection of representative methods available in the literature for the selective oxidation of BnOH was finally carried out. Reactions designed in water and water/organic biphase and in the presence of supported Ru or Mo catalysts were considered. Results are summarised in **Table 2.7.**

Literature procedures generally reported conditions milder than those used in this work, with temperatures not exceeding 90 °C and ambient pressure, but they required both strong hazardous oxidants as oxygen and concentrated H_2O_2, and a complex multistep design of catalysts, co-catalysts and reactors. In the case of Ru, this meant:

i) the fabrication of single atoms (SA) anchored onto a nitrogen-doped carbon (entry 1) or bimetallic nanoparticles supported on carbon nanotubes (entry 2), and

ii) the use of randomly methylated β-cyclodextrins as co-catalysts (entry 3) or super amphiphilic carbon (entry 4) which made the metal active in Pickering emulsions.

Table 2.7. Comparison of the **MP2**-assisted procedure to selected literature methods for the oxidation of BnOH in water and water/organic biphase.

Entry	Cat. (recycle)	Oxidant	Medium	T(°C), *p*(bar), t(h)	Conv./Sel. %	Ref.
1	Ru_1/NC[a] (yes)	O_2	Water	90/1/2	99/99	[98]
2	Pt_xRu_y/CNT[c] (none)	O_2	Water	80/1/3	59/90	[99]
3	Ru/C-RaMeβ-CD[b] (yes)	O_2	Water	75/n.i.[d]/24	99/99	[100]
4	Ru/C – s.a. C[e] (none)	H_2O_2	Water/toluene	90/1/2.5	94/94	[101]
5	Ru/C (yes)	Air	**MP2**	130/20/4	99/99	This work
6	$(NH_4)_6Mo_7O_{24}$ $4H_2O$[f] (none)	H_2O_2	Water/alcohol	60/n.i.[d]/4	48/98	[102]
7	$Py_3PMo_{12}O_{40}$[g] (none)	H_2O_2	Water/organic	70/1/3	n.i.[d]/85	[103]
8	Mo/C (yes)	Air	**MP2**	150/20/24	90/99	This work

[a] Ru single atom (SA) anchored onto a geometrically deformed nitrogen-doped carbon (Ru1/NC) support.
[b] Bimetallic nanoparticles supported on carbon nanotubes (CNT).
[c] 10 % Ru/C with randomly methylated β-cyclodextrins.
[d] n.i.: not indicated.
[e] 5 % Ru/C in combination with a super amphiphilic carbon (s. a. C).

[f] Ammonium molybdate in a flat membrane reactor.
[g] A pyridinium substituted hetero-polyacid used in combination with ionic liquids.

For Mo, instead, the catalyst active phase was either made to flow through a flat membrane reactor fitted with a hydrophobic polymeric film (entry 6) or made available as a pyridinium exchanged α-Kegging anion, not suitable for recycle (entry 7). Overall, though inventive and effective, all these methods implied the engineering of costly and environmentally impactful syntheses and the use of expensive starting materials to obtain active metals and suitable supports and reactors. By contrast, the **MP2**-based procedure was conceived for being easily accessible via simple and safe combinations of catalyst/conditions for oxidation reactions in water. This was achieved using air as an oxidant, cheap commercially available compounds ($[N_{8881}][Cl]$, *i*-octane), and catalysts which were sourced from conventional suppliers (Ru/C from Merck) or prepared by a straightforward synthesis (Mo/C) still from commercial inexpensive precursors (ammonium molybdate and cellulose). The multiphase protocol did not ensure the catalyst stability at least for Mo/C, but nonetheless it made possible the control of the reaction selectivity and an effective recycle across successive runs.

Two more considerations should be finally placed based on the CHEM21 toolkit for green practices in chemical synthesis:[104] a recent evaluation of ionic liquids through the metrics of this standard, ranked onium salts as tetralkyl substituted ammonium cations and chloride anion as green compounds/media for their positive technoeconomic impact; processes at T≥150 °C generally raise concerns for the energy costs. This aspect, however, appeared mitigated, if not offset, for **MP2**-based oxidations catalysed by Mo, an element which is characterised by a price steadier and far lower compared to precious metals.[105]

The oxidation of n-Butyl alcohol

n-Butyl alcohol (*n*-BuOH) was selected as a model substrate representative of water-soluble primary aliphatic alcohols. Oxidation reactions were carried out in a batch mode using a stainless-steel autoclave in the presence of the two Ru- and Mo-based catalytic systems described earlier in this section, with air as the oxidant. In light of the results obtained with the oxidation of benzyl alcohol, only two reaction environments were explored in this case:

i) an aqueous solution of *n*-BuOH (0.5 M, 5 mL) employed as such, and

ii) a triphasic mixture of aqueous *n*-BuOH (0.5 M, 5 mL), *i*-octane (5 mL) and the methyltrioctylammonium chloride ($[N_{8881}][Cl]$, 500 mg) as an ionic liquid to generate the **MP2** system.

A preliminary screening highlighted that the reaction conditions previously optimised for benzyl alcohol were not suitable for *n*-BuOH oxidation, as overoxidation was found to dominate even at conversions far from quantitative. This prompted us to halve the amount of catalyst (5 wt.% Ru/C or 6.1 wt.% Mo/C; 50 mg for each system).

However, simply lowering the catalyst loading did not alter the product distribution, and the oxidation of *n*-BuOH still proceeded with extensive overoxidation and concurrent C–C bond cleavage (**Figure 2.27**). Overall, the major product was butyric acid (1), accompanied by smaller amounts of butanal (4), short-chain carboxylic acids such as propanoic acid (2) and acetic acid (3), and minor amounts of esters (5) potentially formed through esterification between residual alcohol and the carboxylic acids produced.

Figure 2.27. Schematic representation of the overoxidation of *n*-BuOH using Ru/C and Mo/C systems.

Therefore, a parametric study of the oxidation of *n*-BuOH was then conducted by varying temperature (in the range of 110–150 °C), air pressure (from 10 to 50 bar), and reaction time (from 2 to 24 h). **Table 2.8** summarises the most representative results.

Table 2.8. The oxidation of *n*-BuOH using Ru/C or Mo/C systems in water (or acetonitrile). Conversion and products distribution were determined by GC and GC/MS.

Entry	Catalyst	Medium	T (°C), *p* (bar), t (h)	Conversion %	Products distribution %				
					1	2	3	4	5
1	Ru/C	Water	130, 30, 6	65	58	3	1	21	17
2			150, 50, 6	>99	75	20	3	1	1
3			140, 50, 6	92	66	27	4	1	2
4			130, 50, 6	88	63	20	3	3	11
5			120, 50, 6	70	60	20	2	12	4
6			110, 50, 6	58	55	14	1	25	5
7			150, 40, 6	95	66	22	3	2	7
8			150, 30, 6	76	73	17	1	7	2
9			150, 20, 6	79	65	17	1	8	9
10			150, 10, 6	61	72	6	-	19	3
11			150, 10, 12	80	80	10	-	8	2
12			150, 50, 4	90	69	24	4	2	1
13			150, 50, 3	86	67	22	2	3	6
14			150, 50, 2	77	67	17	1	10	5
15[a]			150, 50, 6	-	>99	-	-	-	-
16		Acetonitrile	150, 50, 6	79	76	4	1	9	10
17			150, 10, 6	52	62	5	1	20	12
18			150, 10, 12	62	72	5	1	8	14
19	Mo/C	Water	150, 50, 6	3	-	-	-	>99	-
20[b]			150, 50, 24	42	36	15	4	15	30
21[b]			180, 50, 24	80	51	23	14	8	4
22[b]			200, 50, 24	>99	61	23	16	-	-

[a] oxidation reaction was performed on butyric acid as the starting reagent.
[b] Mo/C loading was increased from 50 to 200 mg.

In the case of the Ru-based catalytic system in aqueous environment, complete conversion of *n*-BuOH was only achieved under relatively high temperature and pressure and prolonged time (150 °C, 50 bar air, 6 h, entry 2). Nevertheless, none of the parameter combinations tested, even under milder conditions and incomplete conversion, allowed us to drive the reaction selectivity towards a single product. Specifically, the effect of temperature variation was evaluated by gradually lowering the reaction temperature from 150 to 110 °C (entries 2–6; see also **Figure 2.28A**). At each temperature decrease, a slight but consistent reduction in the short-chain derivatives (2 and 3) was observed, accompanied by a modest increase in butanal (4) up to 25%. The selectivity towards butyric acid (1) also decreased, while on the other hand the substrate conversion dropped consistently from >99 to 58%. Similarly, lowering the air pressure from 50 to 10 bar (entries 7–10; see also **Figure 2.28B**) resulted in a significant decrease in conversion, from >99% to 61%, without producing any meaningful improvement in selectivity except for a small, but appreciable reduction of short-chain products at 10 bar. This result prompted us to further investigate the reaction at low pressure and at a prolonged time, extended to 12 h. Under these conditions, selectivity towards butyric acid (80%) was slightly improved, although conversion did not exceed 80% (entry 11). By contrast, progressive reduction of the reaction time from 6 to 2 h (entries 12–14; see also **Figure 2.28C**) had no impact at all on the products distribution but caused, once again, a decrease in overall yield from >99% to 77%.

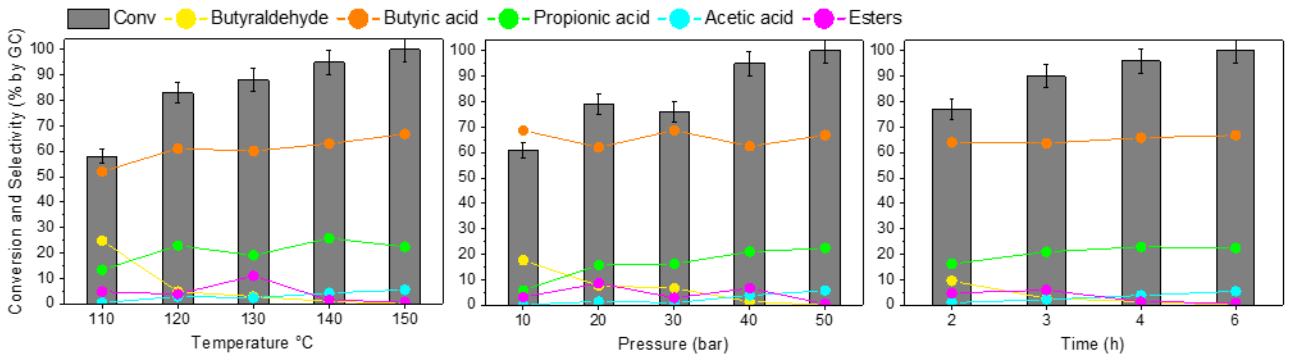

Figure 2.28A-C. Effect of **A)** temperature, reduced from 150 to 110 °C; **B)** pressure, reduced from 50 to 10 bar air; and **C)** reaction time, reduced from 6 to 2 h, on the Ru-catalysed oxidation reaction of *n*-BuOH in terms of conversion (green bars) and products distribution (lines).

The observed C-C bond (oxidative) cleavage of unstrained alcohols is not a new process. Excellent reviews have been reported on this subject.[106,107] Given the inertness of the Csp^3-Csp^3 σ bond, the cleavage requires activation by transition metals and the predominant pathway for such a process is β-carbon elimination. Coordination of the alcohol to the metal

via the oxygen atom facilitates interaction with the adjacent β-position, which in turn promotes bond cleavage. In support of this mechanistic interpretation, when *n*-BuOH was replaced with a 0.5 M aqueous solution of butyric acid under identical conditions (entry 15: 50 mg Ru/C, 150 °C, 50 bar air, 6 h), the carboxylic acid was recovered unaltered, indicating that the β-carbon elimination mechanism was exclusive for the alcohol. On this basis, a tentative mechanistic scheme for the oxidative C-C cleavage of n-BuOH is proposed in **Scheme 2.1**. Nevertheless, it should be noted that the proposed pathway is intended as a plausible interpretation rather than a definitive mechanism, and further experimental investigations are required to validate the individual steps involved.

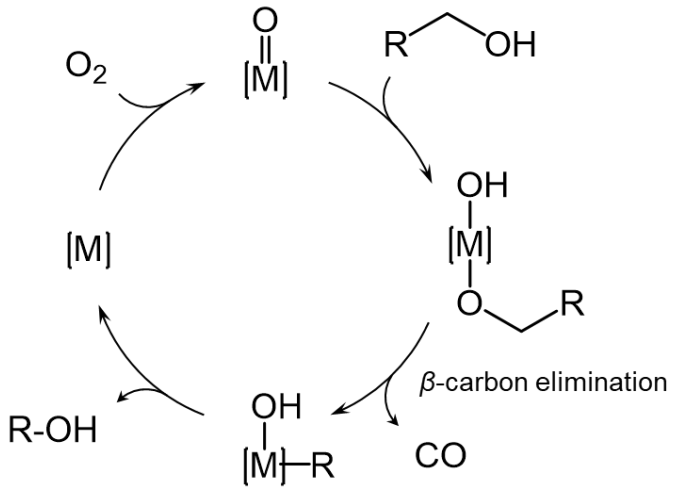

Scheme 2.1. Proposed catalytic cycle for the metal-mediated β-carbon oxidative cleavage of a primary alcohol, leading to the loss of one carbon unit.

A strategy based on β-C-C bond breaking coupled to decarboxylation has been recently demonstrated also for carboxylic acids, but it required copper-mediated photoredox catalysis.[108]

An additional test (not reported in **Table 2.8**) was performed using toluene as the starting substrate. In this case, 2.5 mmol of toluene (immiscible in water, and therefore potentially reacting “on water”) were oxidised under Ru/C catalysis at 150 °C and 50 bar of air for 24 h, affording 63% conversion and the following products distribution: 2% benzaldehyde, 66% benzoic acid, and 32% of other oxidised derivatives, mainly benzoic acid esters (such as benzyl benzoate). Similarly to the methylene moiety of toluene, the shorter-chain fragment generated from the β-C-C bond cleavage can undergo further oxidation, enable new metal coordination and promoting additional β-scission steps, and ultimately leading to a cascade of oxidative degradations promoted by the same catalytic system. Such a pathway provides

a plausible explanation for the observed mixture of C4, C3, and C2 carboxylic acids detected in the product mixture, and highlights the intrinsic difficulty of controlling selectivity in the oxidation of aliphatic alcohols under the present conditions.

The most promising experiments (entries 2, 10, and 11) were repeated by replacing water with acetonitrile as solvent, while keeping all other reaction conditions unchanged (entries 16, 17 and 18). In these cases, an improvement in selectivity towards butyric acid was observed (76%, 62%, and 72%, respectively), though conversion was always penalised, as the oxidation of *n*-BuOH proved slower using this solvent. The larger fraction of unreacted alcoholic substrate also resulted in an increased formation of ester derivatives, while extending the reaction time to 12 h was not sufficient to achieve a complete conversion (62%, entry 18). Apparently, the best result achieved with the Ru/C catalyst remained that obtained at 150 °C and 50 bar of air for 6 h in water, corresponding to >99% conversion and 75% selectivity towards butyric acid (entry 2).

The Mo-based catalytic system was then evaluated in water. Initially, the reaction conditions optimised for the oxidation of *n*-BuOH over Ru/C were reproduced, obtaining a substrate conversion surprisingly low (3%, entry 19). The catalyst loading was therefore increased to 200 mg, and the reaction time was extended to 24 h. This led to 42% conversion of the aliphatic alcohol (entry 20) with predominant overoxidation and C–C bond cleavage: observed products were butyric acid (36%), C3-C2 short-chain acidic derivatives (19%), butanal (15%), and esters (30%). A temperature screening was also carried out, increasing the temperature from 150 to 180 °C (entry 21) and ultimately to 200 °C (entry 22), where full substrate consumption was finally achieved. The best results obtained with both catalytic systems in water were then reproduced under multiphasic conditions, using the **MP2** system. Results are summarised in **Table 2.9**.

In the presence of Ru/C or Mo/C, the selectivity for the oxidation of *n*-BuOH in the **MP2** system proved far less satisfactory than that obtained for benzyl alcohol. Not only more moderate conversions were achieved here (82% and 70% after 6 h with Ru/C and 24 h with Mo/C, respectively; entries 2 and 4) moving from water to the **MP2** system, but also no improvement at all in selectivity towards a single product was observed: butyric acid, short-chain derivatives, butanal, and butyl esters were all formed following the same general trends as in the water-only system.

Nonetheless, in the **MP2** system the confinement of Ru/C or Mo/C was still effective in the ionic liquid phase, so that the catalyst/product separation was successful and the catalyst recycle – though not further explored herein – was likely possible under such conditions.

Table 2.9. The oxidation of *n*-BuOH using Ru/C and Mo/C catalysts (50 and 200 mg, respectively) in the **MP2** system in comparison to results obtained in water from **Table 2.8**. Conversion and products distribution were determined by GC and GC/MS.

Entry	Catalyst	Medium	T (°C), *p* (bar), t (h)	Conversion %	Products distribution %				
					1	**2**	**3**	**al**	**5**
1	Ru/C	Water	150, 50, 6	>99	75	20	3	1	1
2		**MP2**		82	74	15	3	4	4
3	Mo/C	Water	180, 50, 24	80	51	23	14	8	4
4		**MP2**		70	63	16	9	6	6

2.2.3 Conclusions

The proposed study unveils insights into a pivotal process of contemporary chemical reactions as the catalytic oxidation of primary benzyl-type alcohols. The design of an innovative sustainable method is described where the potential of MSP is integrated with the use of air as a green and safe oxidant, and carbon supported catalysts based on environmentally desirable metals, particularly the non-noble Mo. In the presence of an *ad-hoc* prepared Mo/C or a commercial Ru/C catalyst, the comparison of different reaction environments proves that a specially designed liquid triphasic system (**MP2**: water/*i*-octane/[N_{8881}][Cl]) is an extraordinary option to control the products distribution of the oxidation of benzyl alcohol. The selectivity towards the formation of the partially oxidised derivative, benzaldehyde, can be enhanced up to 99% at complete conversion. The general viability of the multiphase protocol has been confirmed for a small, but representative library of benzyl alcohols (five examples), including substrates bearing *para*- and *ortho*-substituents with different electronic properties, such as methoxy, hydroxy and bromo groups, which were quantitatively transformed into the corresponding aldehydes.

Crucial to these results is the role of the ionic liquid component [N_{8881}][Cl] of the MPS that acts as a catalyst-philic phase able to confine both Mo/C and Ru/C and keep them separated from water-soluble reactants and products. This confinement phenomenon, mostly due to the properties of the carbon supports of the catalysts and their adsorption/interactions with the ionic liquid, makes the oxidation proceeds as an interfacial process which is not only critical to the selectivity control, but it also allows the recovery of products from an aqueous medium, free from metal contaminations, and an *in-situ* semicontinuous recycle of both catalysts. The behaviour of the two catalytic systems, however, has been different from each other upon subsequent reuses. Ru/C is comparably more active and stable over time, while Mo/ C undergoes both a leaching of the active metal in the ionic liquid phase and a significant alteration of its morphological properties and carbonaceous architecture. Notwithstanding this, Mo/C is extremely resilient during recycles allowing a steady conversion from one run to another and a selectivity (always >99% to benzaldehyde) even better than that achieved with Ru/C. The reasons of this robustness are not yet clarified: albeit the cellulose-derived carbon support and/or the procedure used to prepare Mo/C do not preserve its structure under multiphase conditions, they might allow a dynamic leaching/adsorption of the metal in the ionic liquid and on the support which confers the peculiar behaviour of the catalyst in the recycle operations. It is agreed that leaching and sintering are detrimental phenomena for a catalyst. However, in the specific case of Mo/C, adverse effects due to alterations of its properties appear strongly mitigated, if not offset at all, by the experimental conditions studied here. The integration of Mo/C into a MPS offer a unique design fulfilling requisites of practical reusability of the catalyst with performance integrity and prevention from metal contamination of the product and/or metal loss, which in the last analysis, are compelling evidence towards improving of the process sustainability.

The **MP2**-assisted protocol (nor the same reaction in water or water/*i*-octane) does not prove equally efficient for aliphatic alcohols. As demonstrated for the case of *n*-butyl alcohol, phenomena such as overoxidation and oxidative C–C bond cleavage through a β-carbon elimination mechanism, took place during the reaction, producing mainly carboxylic acids and shorter chain acid derivatives. Both reactions are interesting, but their competitiveness and modest selectivity make the procedure less attractive at the present stage. This aspect along with the design of more stable Mo-based catalysts offer some stimulating challenges that will be the object of future studies in our Labs.

2.2.4 Experimental Section

Materials and Equipment

Benzyl alcohols ($XC_6H_4CH_2OH$; X=H, *p*-Br, *p*-OCH_3, *p*-OH, *o*-OH, *m*-OCH_3, *p*-OH), *n*-butyl alcohol, $(NH_4)_2MoO_4$, 5% Ru/C, 2-propanol, microcrystalline cellulose were commercially available compounds sourced from Sigma-Aldrich. If not otherwise specified, reagents and solvents were employed without further purification. Compressed air was supplied from SIAD, Italy. GC-MS (EI, 70 eV) analyses were performed on an HP5-MS capillary column (L=30 m, Ø=0.32 mm, film=0.25 mm). GC (flame ionisation detector; FID) analyses were performed with an Elite-624 capillary column (L=30 m, Ø=0.32 mm, film=1.8 mm). ^{1}H and ^{13}C NMR spectra were recorded using a Bruker Advance III HD 400 WB equipped with a 4 mm CP/MAS probe, at 400 and 101 MHz, respectively. Chemical shifts were reported downfield from tetramethyl silane (TMS) and MeOD, DMSO-d_6 and $CDCl_3$ were used as solvents. Further equipment is described in the catalyst's characterisation section.

Synthesis of the Mo/C Catalyst

The preparation of the Mo/C sample was accomplished by adjusting a procedure recently reported by our group and based on a two-step run-in protocol (**Figure 2.29**).[77] The molybdenum salt $(NH_4)_2MoO_4$ (1 mmol) was dissolved in 2-propanol (60 mL) under stirring. The solution was then added with microcrystalline cellulose (5 g) and kept under magnetic stirring for 9 h at the reflux temperature (80 °C).

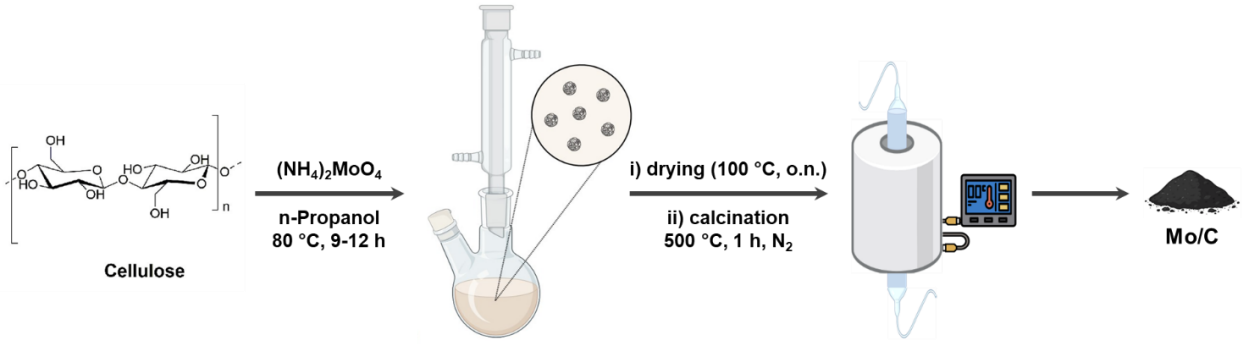

Figure 2.29. Schematic representation of the two-step synthetic protocol of the Mo/C catalytic material.

The suspension was filtered, dried at 100 °C, and the recovered solid was subjected to a thermal treatment at 500 °C under a N_2 flow for 1 h (10 mL/min, heating rate of 5 °C/min). The final sample was ground to powder, stored in a glass vial, and labelled as Mo/C.

Catalyst Characterisation Analyses

Both fresh and exhausted catalysts used in this work were characterised by a multi-technique approach.

The X-Ray Diffraction (XRD) analysis, using Cu Kα radiation as the X-Ray source, was employed to examine the crystalline structure of the samples. This involved monitoring the 2θ values within the range of 10-80° at a rate of 0.08° min^{-1}.

Textural properties such as surface area, pore volume, and pore size were determined through N_2-physisorption at -196 °C. The samples underwent a 2-h outgassing at 120 °C before recording adsorption–desorption isotherms at -196 °C. Specific surface areas, pore volumes, and pore size distributions were calculated using the BET method for adsorption isotherms and the Barrett, Joyner, and Halenda (BJH) algorithm.

The surface of the fresh and used catalysts was analysed by X-ray photoelectron spectroscopy (XPS). The experiments were carried out in an ultrahigh vacuum chamber using a Physical Electronics VersaProbe II Scanning XPS spectrometer equipped with a monochromatic X-ray Al Kα source (1486.6 eV). The C 1*s* line of adventitious carbon was used for binding energies calibration at 284.8 eV. The accuracy of the binding energy (BE) values was ±0.2 eV.

ICP-MS analyses were performed using a Perkin Elmer Nexion 350X spectrometer, to quantify the metal content of the catalysts and evaluate metal leaching after use. To the scope, both fresh and used (post-reaction) catalysts (5 mg each), and a small fraction (100-200 µL) of each one of the liquid components of the **MP2** system, were subjected to a MW-assisted (Ethos UP Milestone) digestion procedure under oxidant conditions. In particular, samples were treated with 5 mL of a 3:1 HCl:HNO_3 mixture and 2 mL of ultrapure H_2O_2, then heated at 210 °C for 20 min. The resulting solutions were diluted to 50 mL with ultrapure water and analysed. Mo(λ=202.031) and Ru(λ=240.272) were quantified by means of an external seven-point calibration curve (100, 200, 500, 1000, 2500, 5000, 10000 ppb). The linear fit was automatically calculated by the ICP software, with correlation coefficients of 0.9999 (Ru) and 1.0000 (Mo). The metal content recorded for each analysis was the average of 6 subsequent acquisitions.

Morphology of the materials and nanoparticle distribution were obtained with a High-Resolution Transmission Electron Microscopy (TALOS F200x), that also operate in STEM mode (Scanning Transmission Electron Microscopy). The instrument possesses a HAADF

detector, working at 200 kV and 200 nA. The mapping images were obtained with an EDX Super-X system provided with 4 X-ray detectors and an X-FEG beam. The molybdenum particle size distribution was performed by Image J software, counting at least 700 particles selected in several different parts of each sample.

Catalytic Activity

The oxidation of alcohols was explored using both Ru/C and Mo/C catalysts and air as an oxidant. All reactions were performed in duplicate to verify reproducibility. Unless otherwise stated, conversions, selectivity, and yields (determined by GC-FID and GC-MS) differed by less than 5 % from one test to another. The structure of the products was assigned by GC/MS. Multiple consecutive/parallel processes of oxidation (to aldehydes and carboxylic acids), C–C bond cleavage and esterification were observed in this work. Accordingly, the selectivity towards any of the observed products was not defined for a single reaction but calculated with respect to the total amount of the products derived by all the occurring processes. The following expression was used:

$$S_i = [mol_i/con_v \cdot alcohol] \cdot 100$$

where S_i is the selectivity (%) for the single compound *i* and mol_i stands for the total moles of compound *i* (by GC calibration).

Three different reaction environments were examined:

i) *Water.* A 15-mL round-bottomed glass reactor was charged with a solution of the chosen alcohol (2 mmol) in water (5 mL) and the catalyst (100 mg). The reactor was placed in a stainless-steel autoclave equipped with two needle valves and a manometer, charged with air at 8-20 bar, and heated under magnetic stirring at the desired temperature for 2-24 h. The autoclave was then cooled to rt, gently purged, and opened. The aqueous phase was syringed out, strained through a microporous filter (0.22 µm) and analysed by GC and GC/MS.

ii) *Water/i-octane.* The procedure above described for water was followed with the further addition of i-octane (5 mL) to obtain a biphase liquid system (**MP1**). Interestingly, the catalyst appeared clearly confined within the organic upper phase (*i*-octane). The reaction and the resulting final mixture were subjected to the same treatment outlined in point i).

iii) Water/*i*-octane/[N_{8881}][Cl]. The procedure above described for water was followed with the further addition of i-octane (5 mL) and methyltrioctylammonium chloride (500 mg) as an ionic liquid to obtain a triphase liquid system (**MP2**). Interestingly, the catalyst appeared clearly confined within the ionic liquid phase (middle layer). The reaction and the resulting final mixture were subjected to the same treatment outlined in point i).

Catalysts Recycle

The recycle of the catalysts was investigated when the **MP2** system was used. Once a first reaction cycle was complete, the aqueous phase containing the products was syringed out and replaced by an equivalent volume (5 mL) of fresh solution of the reactant alcohol. Then, a second oxidation test was run. The overall sequence was repeated for five subsequent experiments. Both the ionic liquid-phase containing the catalyst and the hydrocarbon were never removed from the reactor.

Bibliography

1. Patel, K. D., Subedar, D. & Patel, F. Design and development of automotive catalytic converter using non-nobel catalyst for the reduction of exhaust emission: A review. *Mater. Today Proc.* **57**, 2465–2472 (2022).
2. Kamal, M. S., Razzak, S. A. & Hossain, M. M. Catalytic oxidation of volatile organic compounds (VOCs) – A review. *Atmos. Environ.* **140**, 117–134 (2016).
3. Valera-Medina, A. *et al.* Review on Ammonia as a Potential Fuel: From Synthesis to Economics. *Energy & Fuels* **35**, 6964–7029 (2021).
4. Widianto, A. Y., Aubin, J., Xuereb, C. & Poux, M. Gas-liquid-liquid reactions: Contacting mechanisms and effective process technologies. *Catal. Today* **346**, 46–57 (2020).
5. Liu, M. *et al.* Enhancing reductive C–N coupling of nitrocompounds through interfacial engineering of MoO 2 in thin carbon layers. *Chem. Commun.* **59**, 12443–12446 (2023).
6. Dong, X. *et al.* Enabling room-temperature reductive C–N coupling of nitroarenes: combining homogeneous and heterogeneous synergetic catalyses mediated by light. *Green Chem.* **24**, 4012–4025 (2022).
7. Dong, X. *et al.* Enabling Efficient Aerobic 5-Hydroxymethylfurfural Oxidation to 2,5-Furandicarboxylic Acid in Water by Interfacial Engineering Reinforced Cu−Mn Oxides Hollow Nanofiber. *ChemSusChem* **15**, (2022).
8. Yang, F. *et al.* Reductive C−N Coupling of Nitroarenes: Heterogenization of MoO 3 Catalyst by Confinement in Silica. *ChemSusChem* **14**, 3413–3421 (2021).
9. Pan, H., Chen, X.-Z., Liang, X.-F., Zhu, L.-T. & Luo, Z.-H. CFD simulations of gas–liquid–solid flow in fluidized bed reactors — A review. *Powder Technol.* **299**, 235–258 (2016).
10. Howard, J. L., Cao, Q. & Browne, D. L. Mechanochemistry as an emerging tool for molecular synthesis: what can it offer? *Chem. Sci.* **9**, 3080–3094 (2018).
11. Espro, C. & Rodríguez-Padrón, D. Re-thinking organic synthesis: Mechanochemistry as a greener approach. *Curr. Opin. Green Sustain. Chem.* **30**, 100478 (2021).
12. Muñoz-Batista, M. J., Rodriguez-Padron, D., Puente-Santiago, A. R. & Luque, R. Mechanochemistry: Toward Sustainable Design of Advanced Nanomaterials for Electrochemical Energy Storage and Catalytic Applications. *ACS Sustain. Chem. Eng.* **6**, 9530–9544 (2018).
13. Shelke, Y. G., Yashmeen, A., Gholap, A. V. A., Gharpure, S. J. & Kapdi, A. R.

Homogeneous Catalysis: A Powerful Technology for the Modification of Important Biomolecules. *Chem. – An Asian J.* **13**, 2991–3013 (2018).

14. Kumar, A., Daw, P. & Milstein, D. Homogeneous Catalysis for Sustainable Energy: Hydrogen and Methanol Economies, Fuels from Biomass, and Related Topics. *Chem. Rev.* **122**, 385–441 (2022).
15. Bender, T. A., Dabrowski, J. A. & Gagné, M. R. Homogeneous catalysis for the production of low-volume, high-value chemicals from biomass. *Nat. Rev. Chem.* **2**, 35–46 (2018).
16. Hayler, J. D., Leahy, D. K. & Simmons, E. M. A Pharmaceutical Industry Perspective on Sustainable Metal Catalysis. *Organometallics* **38**, 36–46 (2019).
17. Fulgheri, T., Della Penna, F., Baschieri, A. & Carlone, A. Advancements in the recycling of organocatalysts: From classical to alternative approaches. *Curr. Opin. Green Sustain. Chem.* **25**, 100387 (2020).
18. Hübner, S., de Vries, J. G. & Farina, V. Why Does Industry Not Use Immobilized Transition Metal Complexes as Catalysts? *Adv. Synth. Catal.* **358**, 3–25 (2016).
19. Vural Gürsel, I., Noël, T., Wang, Q. & Hessel, V. Separation/recycling methods for homogeneous transition metal catalysts in continuous flow. *Green Chem.* **17**, 2012–2026 (2015).
20. Shende, V. S., Saptal, V. B. & Bhanage, B. M. Recent Advances Utilized in the Recycling of Homogeneous Catalysis. *Chem. Rec.* **19**, 2022–2043 (2019).
21. Abernethy, D. R., DeStefano, A. J., Cecil, T. L., Zaidi, K. & Williams, R. L. Metal Impurities in Food and Drugs. *Pharm. Res.* **27**, 750–755 (2010).
22. Keim, W. Multiphase catalysis and its potential in catalytic processes: the story of biphasic homogeneous catalysisThis work was presented at the Green Solvents for Catalysis Meeting held in Bruchsal, Germany, 13–16th October 2002. *Green Chem.* **5**, 105–111 (2003).
23. Keim, W. Oligomerization of Ethylene to α-Olefins: Discovery and Development of the Shell Higher Olefin Process (SHOP). *Angew. Chemie Int. Ed.* **52**, 12492–12496 (2013).
24. Bianga, J. *et al.* Tandem Catalytic Amine Synthesis from Alkenes in Continuous Flow Enabled by Integrated Catalyst Recycling. *ACS Catal.* **10**, 6463–6472 (2020).
25. Reppe, W. Neuere Entwicklungen auf dem Gebiete der Chemie des Acetylens und Kohlenoxyds. *Experientia* **5**, 93–110 (1949).
26. Kalck, P. & Urrutigoïty, M. Tandem Hydroaminomethylation Reaction to Synthesize

Amines from Alkenes. *Chem. Rev.* **118**, 3833–3861 (2018).

27. Strohmann, M., Vossen, J. T., Vorholt, A. J. & Leitner, W. Recycling of two molecular catalysts in the hydroformylation/aldol condensation tandem reaction using one multiphase system. *Green Chem.* **22**, 8444–8451 (2020).
28. Vossen, J. T., Leitner, W. & Vorholt, A. J. Exploring the Hurdles in Thermomorphic Multicomponent Systems in the Rhodium-Catalyzed Multiphase Hydroformylation. *ACS Sustain. Chem. Eng.* **11**, 10462–10470 (2023).
29. Kohlpaintner, C. W., Fischer, R. W. & Cornils, B. Aqueous biphasic catalysis: Ruhrchemie/Rhône-Poulenc oxo process. *Appl. Catal. A Gen.* **221**, 219–225 (2001).
30. Herrmann, W. A. & Kohlpaintner, C. W. Wasserlösliche Liganden, Metallkomplexe und Komplexkatalysatoren: Synergismen aus Homogen- und Heterogenkatalyse. *Angew. Chemie* **105**, 1588–1609 (1993).
31. Diehl, T., Lanzerath, P., Franciò, G. & Leitner, W. A Self-Separating Multiphasic System for Catalytic Hydrogenation of CO 2 and CO 2 -Derivatives to Methanol. *ChemSusChem* **15**, (2022).
32. Hejazifar, M., Pálvölgyi, Á. M., Bitai, J., Lanaridi, O. & Bica-Schröder, K. Asymmetric Transfer Hydrogenation in Thermomorphic Microemulsions Based on Ionic Liquids. *Org. Process Res. Dev.* **23**, 1841–1851 (2019).
33. Künnemann, K. U. *et al.* Process Development for the Rhodium-Catalyzed Reductive Amination in a Thermomorphic Multiphase System. *Org. Process Res. Dev.* **24**, 41–49 (2020).
34. Eisenbeis, C., Guettel, R., Kunz, U. & Turek, T. Monolith loop reactor for hydrogenation of glucose. *Catal. Today* **147**, S342–S346 (2009).
35. Zhang, X. *et al.* Platinum-Catalyzed Aqueous-Phase Hydrogenation of <scp>d</scp> -Glucose to <scp>d</scp> -Sorbitol. *ACS Catal.* **6**, 7409–7417 (2016).
36. Selva, M., Gottardo, M. & Perosa, A. Upgrade of Biomass-Derived Levulinic Acid via Ru/C-Catalyzed Hydrogenation to γ-Valerolactone in Aqueous–Organic–Ionic Liquids Multiphase Systems. *ACS Sustain. Chem. Eng.* **1**, 180–189 (2013).
37. Bellè, A. *et al.* A Multiphase Protocol for Selective Hydrogenation and Reductive Amination of Levulinic Acid with Integrated Catalyst Recovery. *ChemSusChem* **12**, 3343–3354 (2019).
38. Polidoro, D., Perosa, A. & Selva, M. Tunable Multi-Phase System for Highly Chemo-Selective Oxidation of Hydroxymethyl-Furfural. *ChemSusChem* **15**, (2022).
39. Rodríguez-Padrón, D., Perosa, A., Longo, L., Luque, R. & Selva, M. Tuning the

Selectivity of the Hydrogenation/Hydrogenolysis of 5-Hydroxymethylfurfural under Batch Multiphase and Continuous-Flow Conditions. *ChemSusChem* **15**, (2022).

40. Polidoro, D., Mihai, I. E., Perosa, A. & Selva, M. High-Yield Synthesis of 1-Hydroxyhexane-2,5-dione via Hydrogenation/Hydrolysis of 5-Hydroxymethyl-furfural in Ionic Liquid-Assisted Multi-Phase Systems. *ACS Sustain. Chem. Eng.* **11**, 2520–2530 (2023).
41. Polidoro, D. *et al.* Multiphase Hydrogenation of <scp>d</scp> -Glucosamine Hydrochloride, N-Acetyl- <scp>d</scp> -Glucosamine, <scp>d</scp> -Glucose, and <scp>d</scp> -Maltose over Ru/C with Integrated Catalyst Recovery. *ACS Sustain. Chem. Eng.* **10**, 2844–2858 (2022).
42. Michel, C. & Gallezot, P. Why Is Ruthenium an Efficient Catalyst for the Aqueous-Phase Hydrogenation of Biosourced Carbonyl Compounds? *ACS Catal.* **5**, 4130–4132 (2015).
43. Fulignati, S. *et al.* Insight into the hydrogenation of pure and crude HMF to furan diols using Ru/C as catalyst. *Appl. Catal. A Gen.* **578**, 122–133 (2019).
44. Xiang, Y. *et al.* Carbon Nanotubes and Activated Carbons Supported Catalysts for Phenol in Situ Hydrogenation: Hydrophobic/Hydrophilic Effect. *Ind. Eng. Chem. Res.* **53**, 2197–2203 (2014).
45. Cui, Y. *et al.* High-Performance Electrocatalytic CO 2 Reduction for CO Generation Using Hydrophobic Porous Carbon Supported Au. *ACS Sustain. Chem. Eng.* **11**, 11229–11238 (2023).
46. Tundo, P. & Perosa, A. Multiphasic heterogeneous catalysis mediated by catalyst-philic liquid phases. *Chem. Soc. Rev.* **36**, 532–550 (2007).
47. Werpy, T. A., Holladay, J. E. & White, J. F. *Top Value Added Chemicals From Biomass: I. Results of Screening for Potential Candidates from Sugars and Synthesis Gas*. http://www.osti.gov/servlets/purl/926125-eeUkhS/ (2004) doi:10.2172/926125.
48. Smith, M. D., Mostofian, B., Petridis, L., Cheng, X. & Smith, J. C. Molecular Driving Forces behind the Tetrahydrofuran–Water Miscibility Gap. *J. Phys. Chem. B* **120**, 740–747 (2016).
49. Smith, M. D., Cai, C. M., Cheng, X., Petridis, L. & Smith, J. C. Temperature-dependent phase behaviour of tetrahydrofuran–water alters solubilization of xylan to improve co-production of furfurals from lignocellulosic biomass. *Green Chem.* **20**, 1612–1620 (2018).
50. Patri, A. S. *et al.* A Multifunctional Cosolvent Pair Reveals Molecular Principles of

Biomass Deconstruction. *J. Am. Chem. Soc.* **141**, 12545–12557 (2019).

51. Deshan, A. D. K. *et al.* Heterogeneous Catalytic Conversion of Sugars Into 2,5-Furandicarboxylic Acid. *Front. Chem.* **8**, (2020).
52. Hommes, A., Heeres, H. J. & Yue, J. Catalytic Transformation of Biomass Derivatives to Value-Added Chemicals and Fuels in Continuous Flow Microreactors. *ChemCatChem* **11**, 4671–4708 (2019).
53. Wei, H., Wang, Z. & Li, H. Sustainable biomass hydrodeoxygenation in biphasic systems. *Green Chem.* **24**, 1930–1950 (2022).
54. Zhu, Z., Tan, H., Wang, J., Yu, S. & Zhou, K. Hydrodeoxygenation of vanillin as a bio-oil model over carbonaceous microspheres-supported Pd catalysts in the aqueous phase and Pickering emulsions. *Green Chem.* **16**, 2636–2643 (2014).
55. Chen, M.-Y., Huang, Y.-B., Pang, H., Liu, X.-X. & Fu, Y. Hydrodeoxygenation of lignin-derived phenols into alkanes over carbon nanotube supported Ru catalysts in biphasic systems. *Green Chem.* **17**, 1710–1717 (2015).
56. Voß, D., Kahl, M. & Albert, J. Continuous Production of Formic Acid from Biomass in a Three-Phase Liquid–Liquid–Gas Reaction Process. *ACS Sustain. Chem. Eng.* **8**, 10444–10453 (2020).
57. De Clercq, R., Dusselier, M. & Sels, B. F. Heterogeneous catalysis for bio-based polyester monomers from cellulosic biomass: advances, challenges and prospects. *Green Chem.* **19**, 5012–5040 (2017).
58. Hirose, D., Kusuma, S. B. W., Ina, D., Wada, N. & Takahashi, K. Direct one-step synthesis of a formally fully bio-based polymer from cellulose and cinnamon flavor. *Green Chem.* **21**, 4927–4931 (2019).
59. Khan, M. Y., Joshi, S. S. & Ranade, V. V. Continuous Hydrogenation of Cinnamaldehyde: Gas–Liquid–Liquid–Solid Helical Coil Reactor. *Ind. Eng. Chem. Res.* (2023) doi:10.1021/acs.iecr.3c00841.
60. Dedovets, D. *et al.* Multiphase Microreactors Based on Liquid–Liquid and Gas–Liquid Dispersions Stabilized by Colloidal Catalytic Particles. *Angew. Chemie Int. Ed.* **61**, (2022).
61. Leclercq, L. *et al.* Pickering Emulsion Stabilized by Catalytic Polyoxometalate Nanoparticles: A New Effective Medium for Oxidation Reactions. *Chem. – A Eur. J.* **18**, 14352–14358 (2012).
62. Yang, H., Zhou, T. & Zhang, W. A Strategy for Separating and Recycling Solid Catalysts Based on the pH-Triggered Pickering-Emulsion Inversion. *Angew. Chemie*

Int. Ed. **52**, 7455–7459 (2013).

63. Wang, C. *et al.* Enhanced photoreforming hydrogen production: Pickering interfacial catalysis from a bio-derived biphasic system. *Renew. Energy* **134**, 113–124 (2019).
64. Polidoro, D., Perosa, A., Selva, M. & Rodríguez-Padrón, D. Metal-Free Carbonaceous Catalytic Materials: Biomass Feedstocks for a Greener Future. *ChemCatChem* **15**, (2023).
65. Papanikolaou, G., Centi, G., Perathoner, S. & Lanzafame, P. Catalysis for e - Chemistry: Need and Gaps for a Future De-Fossilized Chemical Production, with Focus on the Role of Complex (Direct) Syntheses by Electrocatalysis. *ACS Catal.* **12**, 2861–2876 (2022).
66. Heitbaum, M., Glorius, F. & Escher, I. Asymmetric Heterogeneous Catalysis. *Angew. Chemie Int. Ed.* **45**, 4732–4762 (2006).
67. Li, X. *et al.* Advances in heterogeneous single-cluster catalysis. *Nat. Rev. Chem.* **7**, 754–767 (2023).
68. Smith, B. *et al. Platinum Group Metal Catalysts: Supply Chain Deep Dive Assessment*. https://www.osti.gov/servlets/purl/1871583/ (2022) doi:10.2172/1871583.
69. Report on critical raw materials for the EU. (2014).
70. Hunt, A. J., Matharu, A. S., King, A. H. & Clark, J. H. The importance of elemental sustainability and critical element recovery. *Green Chem.* **17**, 1949–1950 (2015).
71. Bystrzanowska, M., Petkov, P. & Tobiszewski, M. Ranking of Heterogeneous Catalysts Metals by Their Greenness. *ACS Sustain. Chem. Eng.* **7**, 18434–18443 (2019).
72. Mane, R., Jeon, Y. & Rode, C. A review on non-noble metal catalysts for glycerol hydrodeoxygenation to 1,2-propanediol with and without external hydrogen. *Green Chem.* **24**, 6751–6781 (2022).
73. Yi, S.-S., Zhang, X.-B., Wulan, B.-R., Yan, J.-M. & Jiang, Q. Non-noble metals applied to solar water splitting. *Energy Environ. Sci.* **11**, 3128–3156 (2018).
74. Ren, Y., Yang, Y. & Wei, M. Recent Advances on Heterogeneous Non-noble Metal Catalysts toward Selective Hydrogenation Reactions. *ACS Catal.* **13**, 8902–8924 (2023).
75. Choi, H. *et al.* Review—Non-Noble Metal-Based Single-Atom Catalysts for Efficient Electrochemical CO 2 Reduction Reaction. *J. Electrochem. Soc.* **167**, 164503 (2020).
76. North, M. *Sustainable Catalysis: With Non-Endangered Metals, Part 1*. (The Royal Society of Chemistry, Cambridge (UK), 2016).

77. Polidoro, D. *et al.* Controlled alcohol oxidation reactions by supported non-noble metal nanoparticles on chitin-derived N-doped carbons. *Catal. Sci. Technol.* **13**, 2223–2238 (2023).
78. Bersani, C., Perosa, A., Rodríguez-Padrón, D. & Selva, M. Unlocking the Potential of Liquid Multiphase Systems for Metal-Catalysed Reactions. *ChemCatChem* **16**, (2024).
79. Zhao, D., Su, T., Wang, Y., Varma, R. S. & Len, C. Recent advances in catalytic oxidation of 5-hydroxymethylfurfural. *Mol. Catal.* **495**, 111133 (2020).
80. Mori, S. *et al.* A simple and efficient oxidation of alcohols with ruthenium on carbon. *Chem. Commun.* 5159 (2009) doi:10.1039/b908451g.
81. Ji, J., Bao, Y., Liu, X., Zhang, J. & Xing, M. Molybdenum-based heterogeneous catalysts for the control of environmental pollutants. *EcoMat* **3**, (2021).
82. Védrine, J. C., Hutchings, G. J. & Kiely, C. J. Molybdenum oxide model catalysts and vanadium phosphates as actual catalysts for understanding heterogeneous catalytic partial oxidation reactions: A contribution by Jean-Claude Volta. *Catal. Today* **217**, 57–64 (2013).
83. Ravi, M., Ranocchiari, M. & van Bokhoven, J. A. The Direct Catalytic Oxidation of Methane to Methanol—A Critical Assessment. *Angew. Chemie Int. Ed.* **56**, 16464–16483 (2017).
84. Rellán-Piñeiro, M. & López, N. The Active Molybdenum Oxide Phase in the Methanol Oxidation to Formaldehyde (Formox Process): A DFT Study. *ChemSusChem* **8**, 2231–2239 (2015).
85. Thrane, J. *et al.* Highly Stable Apatite Supported Molybdenum Oxide Catalysts for Selective Oxidation of Methanol to Formaldehyde: Structure, Activity and Stability. *ChemCatChem* **13**, 4954–4975 (2021).
86. Liao, X. *et al.* Tunability of MoO 3 Thin-Film Properties Due to Annealing in Situ Monitored by Hard X-ray Photoemission. *ACS Omega* **4**, 10985–10990 (2019).
87. Kong, L., Miao, P. & Qin, J. Characteristics and pyrolysis dynamic behaviors of hydrothermally treated micro crystalline cellulose. *J. Anal. Appl. Pyrolysis* **100**, 67–74 (2013).
88. Trache, D., Donnot, A., Khimeche, K., Benelmir, R. & Brosse, N. Physico-chemical properties and thermal stability of microcrystalline cellulose isolated from Alfa fibres. *Carbohydr. Polym.* **104**, 223–230 (2014).
89. https://www.merckmillipore.com/.

90. Pray, H. A., Schweickert, C. E. & Minnich, B. H. Solubility of Hydrogen, Oxygen, Nitrogen, and Helium in Water at Elevated Temperatures. *Ind. Eng. Chem.* **44**, 1146–1151 (1952).
91. Tromans, D. Modeling Oxygen Solubility in Water and Electrolyte Solutions. *Ind. Eng. Chem. Res.* **39**, 805–812 (2000).
92. Holmberg, N., Sammalkorpi, M. & Laasonen, K. Ion Transport through a Water–Organic Solvent Liquid–Liquid Interface: A Simulation Study. *J. Phys. Chem. B* **118**, 5957–5970 (2014).
93. https://tradingeconomics.com/commodity/molybden. https://tradingeconomics.com/commodity/molybden.
94. Sádaba, I., López Granados, M., Riisager, A. & Taarning, E. Deactivation of solid catalysts in liquid media: the case of leaching of active sites in biomass conversion reactions. *Green Chem.* **17**, 4133–4145 (2015).
95. Liguori, F., Moreno-Marrodan, C. & Barbaro, P. Biomass-derived chemical substitutes for bisphenol A: recent advancements in catalytic synthesis. *Chem. Soc. Rev.* **49**, 6329–6363 (2020).
96. Pan, H., Li, H., Wu, S., Lai, C. & Guo, D. De Novo Biosynthesis of Anisyl Alcohol and Anisyl Acetate in Engineered Escherichia coli. *J. Agric. Food Chem.* **71**, 3398–3402 (2023).
97. Chen, Y., Chen, Y., Liu, L., Zhang, Y. & Yuan, J. Microbial synthesis of 4-hydroxybenzoic acid from renewable feedstocks. *Food Chem. Mol. Sci.* **3**, 100059 (2021).
98. Dong, X. *et al.* Molten salt-induction of geometrically deformed ruthenium single atom catalysts with high performance for aerobic oxidation of alcohols. *Chem. Eng. J.* **451**, 138660 (2023).
99. Chen, H. *et al.* Microwave-assisted synthesis of PtRu/CNT and PtSn/CNT catalysts and their applications in the aerobic oxidation of benzyl alcohol in base-free aqueous solutions. *Catal. Sci. Technol.* **3**, 328–338 (2013).
100. Akkilagunta, V., Reddy, V. & Kakulapati, R. Aqueous-Phase Aerobic Oxidation of Alcohols by Ru/C in the Presence of Cyclodextrin: One-Pot Biomimetic Approach to Quinoxaline Synthesis. *Synlett* **2010**, 2571–2574 (2010).
101. Fan, H. *et al.* Superamphiphilic carbon from sawdust activated by oxygen/argon mixtures promoting the oxidation of benzyl alcohol in Pickering emulsion. *Green Chem.* **23**, 6341–6348 (2021).

102. Buonomenna, M. G. & Drioli, E. Benzyl Alcohol Oxidation to Benzaldehyde in Multiphase Membrane Reactor. *Org. Process Res. Dev.* **12**, 982–988 (2008).
103. Tundo, P., Romanelli, G. P., Vázquez, P. G. & Aricò, F. Multiphase oxidation of alcohols and sulfides with hydrogen peroxide catalyzed by heteropolyacids. *Catal. Commun.* **11**, 1181–1184 (2010).
104. Jacobs, B. *et al.* Sustainable lignin modifications and processing methods: green chemistry as the way forward. *Green Chem.* **25**, 2042–2086 (2023).
105. Henckens, M. L. C. M., Driessen, P. P. J. & Worrell, E. Molybdenum resources: Their depletion and safeguarding for future generations. *Resour. Conserv. Recycl.* **134**, 61–69 (2018).
106. Liu, H., Feng M., Jiang X. Unstrained Carbon-Carbon Bond Cleavage. *Chem. Asian J.* **9**, 3360 – 3389 (2014).
107. Lutz, M.D.R., Morandi, B. Metal-Catalyzed Carbon−Carbon Bond Cleavage of Unstrained Alcohols. *Chem. Rev.* **121**, 300−326 (2021).
108. Li, R., Dong, Y., Khan, S.N. *et al.* Decarboxylative oxidation-enabled consecutive C-C bond cleavage. *Nat. Commun*. **13**, 7061 (2022).

Chapter 3. Biowaste Valorisation

The steady growth of world's population and the rising global demand for energy are tightly interwoven with the expansion of agriculture and food production sectors. A direct consequence is the generation of a large amount of biowaste, including agricultural and forestry residues, food processing by-products, fishery waste, gardening waste, livestock manure, sludge, natural fibres, as well as any biodegradable material of biological origin.[1] Among these, food waste is the largest share, defined as edible or non-edible food discarded at any stage of the food chain, from manufacturing, logistics, and storing, to postconsumer phase.[2] According to the 2019 State of Agriculture report by the Food and Agriculture Organisation (FAO) of the UN, approximately 14% of the annual food produced globally is lost or wasted between harvest and retail.[3]

The disposal of this massive waste volume brings major challenges in terms of pollution and land required for its storage. When organic waste ends up in landfills or dumpsites, it decomposes anaerobically and produces methane, that has a GWP 28 times higher than CO_2, and accounts alone for nearly 90% of the waste sector's direct contribution to GHG emissions.[4] Beyond climate impacts, poorly managed biowaste can lead to contamination of soils and water, harming biodiversity, and even entering human food chain. An additional issue is the loss of an incredible variety of valuable materials, bioactive compounds and energy[5], whose recovery could promote more resilient food and energy systems worldwide.

"Valorisation" refers to the process of transforming something that is traditionally considered waste into a product with new added value, by applying innovative technologies and green methods. In a sustainability framework, rethinking waste through a circular approach can offer opportunities to save resources, reduce pollution and help addressing the actual climate and energy crisis[6]. Whitin this Chapter, the concept of valorisation has been framed as a strategy to recovery and re-use waste streams from the fishery supply chain, a topic that is further discussed in Section 3.1 as a prelude to another central theme of this Thesis: the extraction of a precious bioactive compound, i.e. chitin, from biowaste, which will be explored more specifically in Section 3.2.

3.1 Fishery waste upgrading: an overview

The valorisation of by-products from the fish and seafood industry is gaining increasing attention due to two main reasons: the large volumes generated worldwide, together with the associated environmental drawbacks, and their remarkable richness in valuable nutrients, which are certainly worth recovering and upgrading.

Humble strategies to address these matters include composting or converting the organic residues into animal feed or fertilizers. Fishery waste is particularly rich in amino acids, peptides, collagen, chitin, and other nitrogen-based compounds[7], a valuable element for soil nutrition. However, these low-tech and non-selective processes rely on uncontrolled thermal degradation or enzymatic digestion, which break down raw materials and lead to products of limited nutritional quality and low added value. Although these options are preferable to landfilling, current research is focused on developing more refined and sustainable valorisation pathways for fishery by-products (**Figure 3.1**).[8]

Among the compounds worth recovering are ω-3 fatty acids, originally synthesised by algae and phytoplankton and accumulated in fish as lipid reserves. These molecules play an essential role in cardiovascular and neural functionality, and their dietary deficiency – since they cannot be synthesised endogenously by mammals – may lead to health disorders[9,10]. Other bioactive compounds, such as essential amino acids and enzymes represent a high-value protein fraction due to their excellent nutritional properties. Collagen and gelatine are also interesting: they are widely employed in cosmetic formulations (like anti-aging creams) and food additives, respectively[11,12]. Many products and supplements derived from a wide range of bioactive compounds obtained from fish waste are commercially in high demand because of their antioxidant, antihypertensive, antibacterial, and immunomodulatory properties. Overall, these bioactive compounds are extensively used in the nutraceutical, pharmaceutical, cosmetic, agrochemical, and biomaterials sectors.

Among many valuable components of fish by-products, chitin, a structural polysaccharide mainly found in the exoskeletons of marine arthropods, is gaining increasing attention from the scientific community, both for its unique properties and for the enormous quantities produced: within the global fishery waste stream, chitin-containing residues are estimated at 10^{12}-10^{14} tons per year.[13] Given chitin's relevance to the present work, the following section is dedicated to frame this research within the context of the current scientific literature.

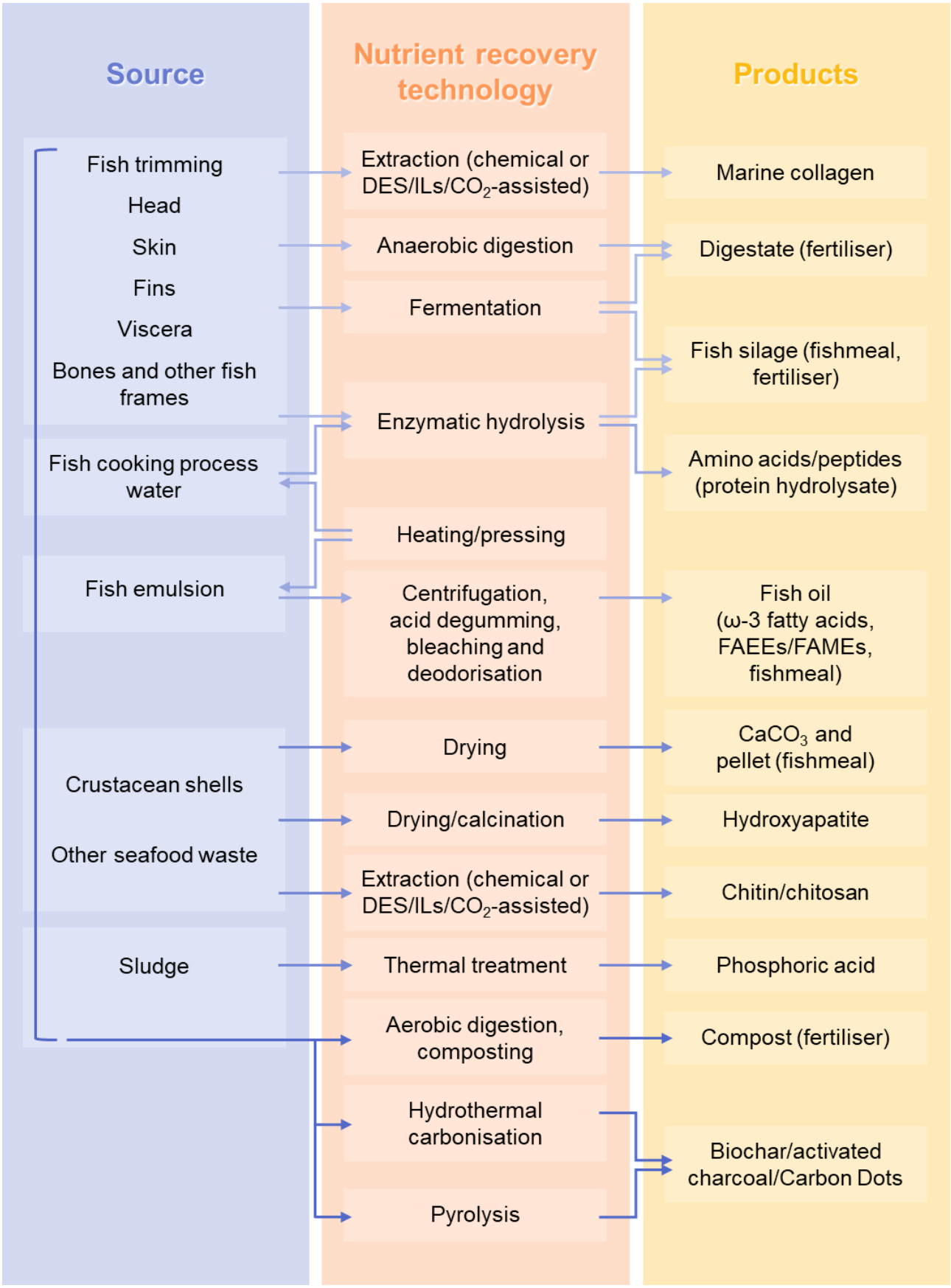

Figure 3.1. Schematic representation of fish waste recovery and valorisation pathways. Adapted from [14].

Chitin

Chitin was firstly discovered in 1799 by Charles Hatchett, who reported it as “a material particularly resistant to usual chemicals”.[15] Today we know that chitin is a structural polysaccharide composed by N-acetyl-D-glucosamine units connected by glycoside linkage β-(1→4)[16], mainly found in the exoskeleton of crustaceans and insects, in the cell walls of fungi, in the cartilage of molluscs, and in marine sponge. About 7 wt.% of chitin is made up of nitrogen (**Figure 3.2**), which gives the biopolymer unique properties that make it superior to cellulose, its structural analogue to which chitin is second only in abundance in nature[17].

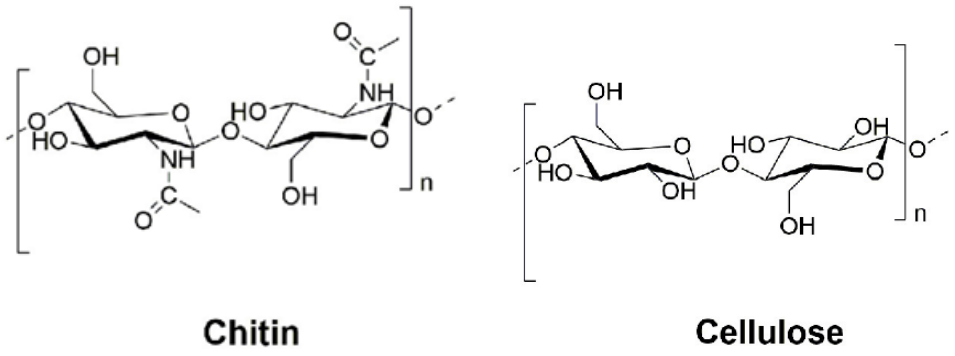

Figure 3.2. Schematic representation of Chitin and Cellulose chemical structures.

Thanks to its biocompatibility, biodegradability and non-toxicity, chitin, together with its deacetylated product chitosan, has been intensively studied in recent decades for a wide range of pharmaceutical, nutraceutical (food additives and supplements), cosmetical, physiological, and biomedical applications.[17]

Indeed, chitin and chitosan have shown haemostatic and antimicrobial activities against a variety of pathogens, including fungi and bacteria, as well as the promotion of wound healing,[18] with chitosan-based dressings enabling the acceleration of blood clotting via platelet aggregation while suppressing bacterial growth when in combination with TiO_2 nanoparticles. Chitosan also exhibit mucoadhesive properties, meaning it can cling to mucosal membranes found in nose, mouth, and gastrointestinal system, which is useful for the development of medication delivery systems for oral and nasal administration.[19] Moreover, chitin and chitosan also proved to elicit biological responses and enhance immune activity, which make them perfectly suitable as adjuvants (chemical compounds that boost immunity and promote a vaccine’s potency) in formulation and development of

vaccines.[20,21] Nanocomposites of chitin have been widely studied as tissue engineering scaffolds,[22,23] and for a range of drug delivery applications,[24] diagnosis and treatment of various types of cancer cells, such as human monocyte and myeloid leukemia cells, human melanoma cells, and HeLa cells.[25–27] An example within this context is the use of chitin nanocomposites embedded with other antimicrobial agents, such as silver or copper nanoparticles, that exhibited an enhanced cytotoxicity in human breast cancer (MCF-7) cells compared to the metal nanoparticles alone.[28]

Beyond medical uses, chitin and chitosan have also been used in packaging materials to maintain the quality of a wide range of food items and partially replace conventional plastics,[29] but also in textiles applications,[30] as well as electronics and nanotechnologies, where they are employed in biobased electric devices[31,32] or as precursors for nitrogen-doped carbon materials useful for catalytic applications.[33] As discussed in Chapters 1 and 2, combining biomass-derived activated carbons with nitrogen doping represents a promising strategy to enhance the selectivity of sustainable catalytic systems, thanks to the presence of defects generated on the surface of the carbon matrix by differences in electronegativity, atomic radius, and bond structure between carbon and nitrogen. These defects cause an uneven distribution of charge density, leading to formation of active sites and strong coordination centres for metal ions.[17]

The countless properties of chitin and its derivatives, and consequently all the potential applications to them associated, are due to the unique structural characteristics of this biopolymer. Chitin is known for having striking mechanical properties due to its high level of crystallinity, provided by the presence of intra- and intermolecular hydrogen bonding between the chains of the biopolymer, which confers to the material a low chemical reactivity and high resistance to solubilisation and degradation, in water and most organic solvents.[34] Chitin occurs in three crystalline allomorphs (**Figure 3.3**) – α-, β-, and γ-chitin – which differ mainly in the direction arrangement of their polymer chains.[17,35,36]

α-Chitin is the most abundant and stable form, commonly found in crustacean shells, insect cuticles, and fungal cell walls. Its chains are arranged in an anti-parallel orientation, allowing for a dense network of both intra- and inter-molecular hydrogen bonds. The result is a material that is highly crystalline, rigid, and resistant to swelling in water.

β-Chitin, by contrast, is characterised by a parallel chain arrangement, which allows fewer hydrogen bonds to form between adjacent sheets, lacking this way the strong intramolecular interactions typical in α-chitin. Therefore, β-chitin is less crystalline, more flexible, and more

susceptible to hydration and chemical modification. Indeed, in the presence of water molecules, which can act themselves as hydrogen bond donors and acceptors, under acidic conditions β-chitin tends to swell and convert spontaneously into more stable α-chitin.[37]

γ-Chitin is relatively rare and structurally more complex. It contains a mixture of parallel and anti-parallel arrangement sections, which gives it intermediate properties between α- and β-allomorphs.[38]

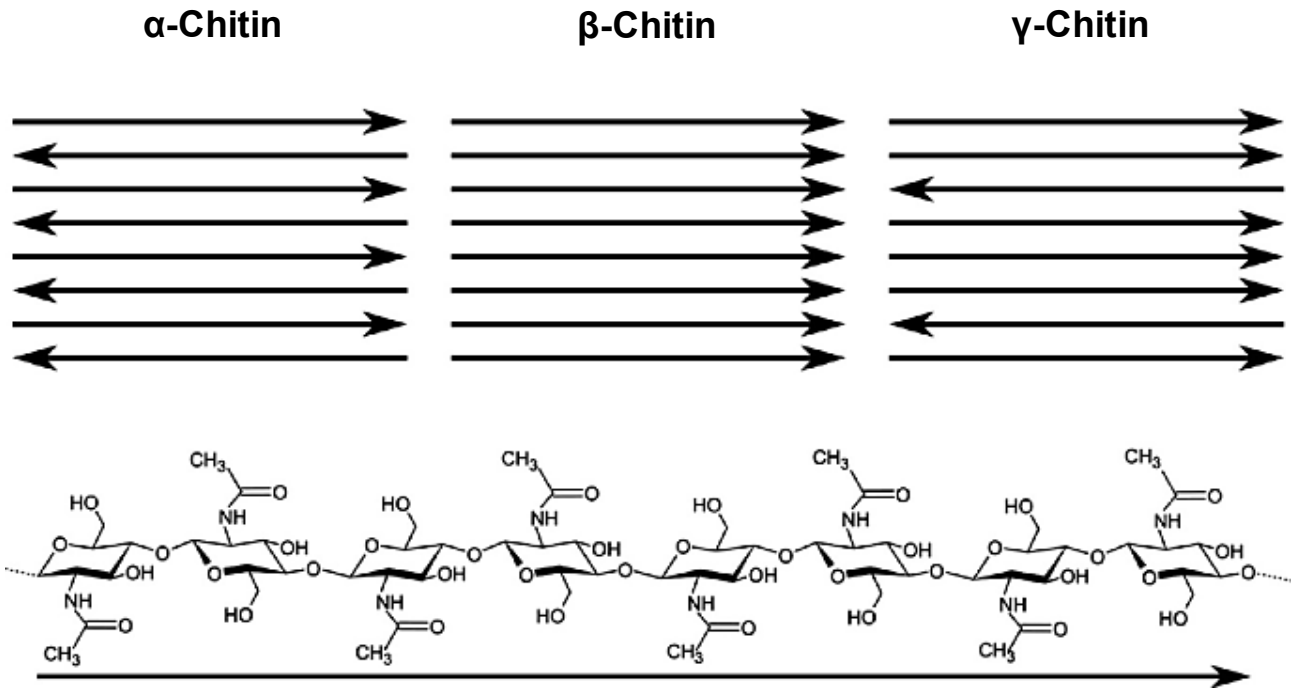

Figure 3.3. From left to right, the schematic representation of the three crystalline allomorphs α-, β-, and γ-chitin. Reprinted from [39] with permission.

In crustacean shells, where α-chitin predominates, the crystalline polymer is embedded in a highly organised hierarchical composite material, which includes an inorganic mineral phase (mainly calcium carbonate) and an organic matrix of proteins and chitin fibres, arranged across multiple length scales, from the nanoscale to the macroscale (**Figure 3.4**), following Bouligand's structure].[40] Each level of structural rearrangement provides an added contribute to the mechanical strength and toughness of the final material, whose resilience towards diverse physical and chemical treatments is therefore unsurprising, and fulfills the exoskeleton's primary function of protection.

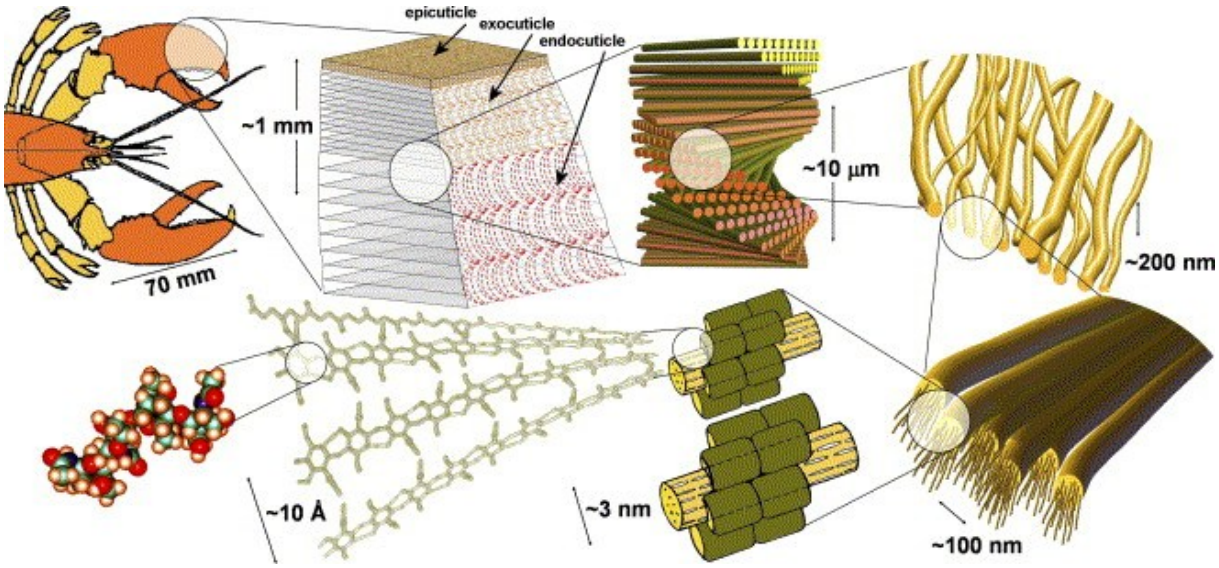

Figure 3.4. Schematic representation of the structural levels of crustacean shells, from nano to macroscale. Chitin nanofibers composed of α-chitin chains are braid with proteins and mineral nanocrystals into Bouligand structures. Reprinted from [40] with permission.

Up to date, crustacean (prawns, crabs, lobsters, shrimps) shells are the primary industrial source of chitin, which content can vary widely from species to species, but also according to age, sex, season, nutrition, and health status. This variability in the chemical composition of chitinous biomass, although completely natural, can impact the extraction process, and therefore the outcome.[41,42] Regarding crab shells, specifically, their composition is generally made up of about 57-58% of minerals, 21% proteins, 20% chitin, and a small fraction of lipids, pigments, and metal traces, as will be better discussed in Section 3.2, which illustrates how this biowaste was studied as starting material for the extraction of chitin through a green method optimised in our lab.[43]

The hardness of these materials requires the employment of extraction techniques that need to be both efficient and robust, capable of coping with the compositional variability of the organic feedstock. Conversely, the valorisation of fishery waste for the production of bioactive compounds and advanced materials should not rely on processes that use or generate large amounts of hazardous chemicals. Conventional industrial extraction methods still rely on strong acids and bases in multistep processes, which generate significant waste streams. Therefore, the development of truly sustainable methodologies for biowaste valorisation is both highly desirable and increasingly urgent.

Conventional extraction methods

Most industrially produced chitin is obtained from the extraction of chitinous biomass (mainly shrimp shells) through multistep procedures. Conventional chemical treatments typically involve inorganic minerals removal (demineralisation) by strong mineral acids, proteins removal (deproteinisation) by alkaline solution and finally, – since the product has usually a yellowish colour – a final decolouration step oxidising agents like $KMnO_4$, H_2O_2, or NaClO, to remove residual pigments. Other details will be given in section 3.2.1.

Efforts to replace aggressive reagents have included the use of milder organic acids (like formic and acetic acid) in the demineralisation step,[44] as well as chelating agents such as ethylenediaminetetraacetic acid (EDTA, which binds to metal ions such as calcium and magnesium) and CO_2,[45] though these have shown lower efficiency compared to mineral acids.

However, chitin extracted by conventional chemical methods is generally not suitable for food, pharmaceutical, or cosmetic applications, due to the potential presence of chemical residues.[46] To overcome these drawbacks, several eco-friendly extraction methods are getting common, offering the dual advantages of expanding the potential applications of the – generally less contaminated – extracted chitin, and enabling the simultaneous recovery of proteins and minerals for reuse in other processes.[47] Among these, enzymatic hydrolysis and microbial fermentation have shown promising: enzymes, bacteria, and fungi can produce organic acids and proteolytic enzymes able to remove $CaCO_3$ and proteins.[48,49] Main drawbacks of these approaches lie in their extreme sensitivity to small oscillations in parameters such as pH and temperature, as well as long processing times and high costs, which limit their broadening to highly specialised industrial plants.[50,51]

Alternative extraction pathways

While biological methods represent a valid, yet limited, alternative to conventional extraction methods, efforts have been made to develop new green approaches for chitin extraction, employing deep eutectic solvents (DESs), natural deep eutectic solvents (NADESs), and ionic liquids (ILs), which are capable of the disruption of chitin's hydrogen bonding network, and thus demonstrated great potential for increased yields and improved quality of the extraction outcome, especially when used in combination with other non-conventional treatments such as ultrasound, steam explosion and microwaves.[52–54]

DESs are binary or ternary mixtures in which acceptors (HBA, **Figure 3.5A**) and hydrogen bond donors (HBD, **Figure 3.5B**) are combined in an extensive hydrogen-bonding network which confers unique properties to the system, such as melting points significantly lower than the single components.

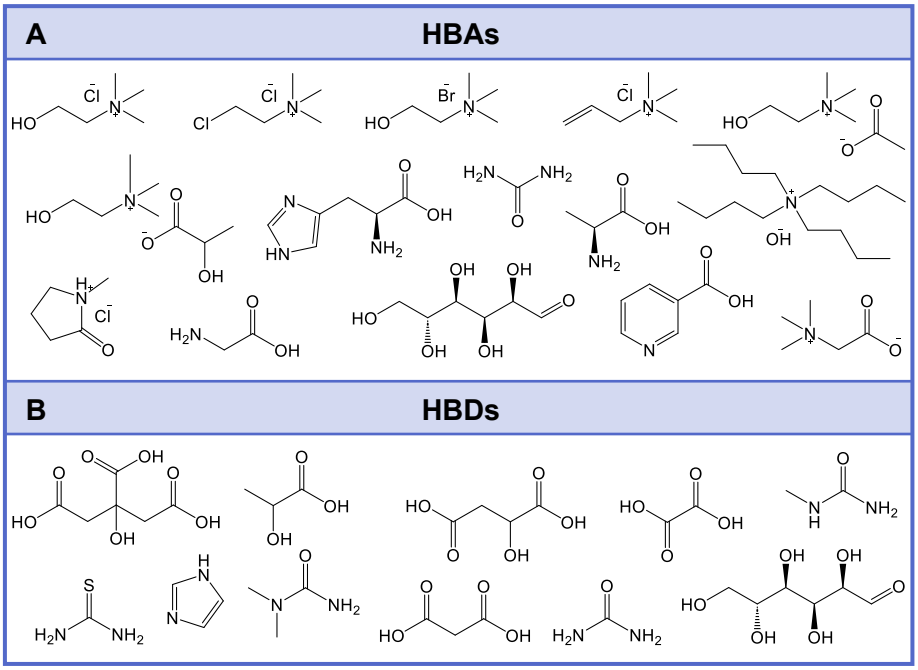

Figure 3.5. Schematic representation of commonly used **A:** HBA and **B:** HBD in DESs. Adapted from [53].

Choline chloride/urea (ChCl/urea) DES, for example, was found to have a melting point of 12 °C, compared to 302 °C for choline chloride and 133 °C for urea alone.[55] This richness in hydrogen-bonding species makes DESs perfectly suitable for biomass valorisation purposes, including chitin pulping (which is the process of dissolving everything but chitin). For instance, a ChCl/malonic acid (CCMA) DES proved efficient in isolating chitin from lobster shells with a crystallinity index of 67-80 % and a yield (20 wt.%) higher than that obtained for conventionally extracted chitin, after treating a 7 wt.% biomass loading at 50 °C for 2 h, followed by a decolouration step carried out using 10% w/v H_2O_2 at 80 °C.[56] Among DESs, NADESs represent a subclass composed entirely of natural compounds. A ChCl/lactic acid (1:1) NADES effectively extracted chitin from Brown crab (*Cancer Pagurus*) shells with 98 % purity after a treatment at 130 °C, followed by a H_2O_2 decolouration step, yielding chitin with properties comparable to those of the conventionally extracted material.[57]

As already mentioned in Chapter 2, ILs, also called liquid organic salts, consist exclusively of equivalent amounts of oppositely charged and mostly organic ions[58] (**Figure 3.6**).

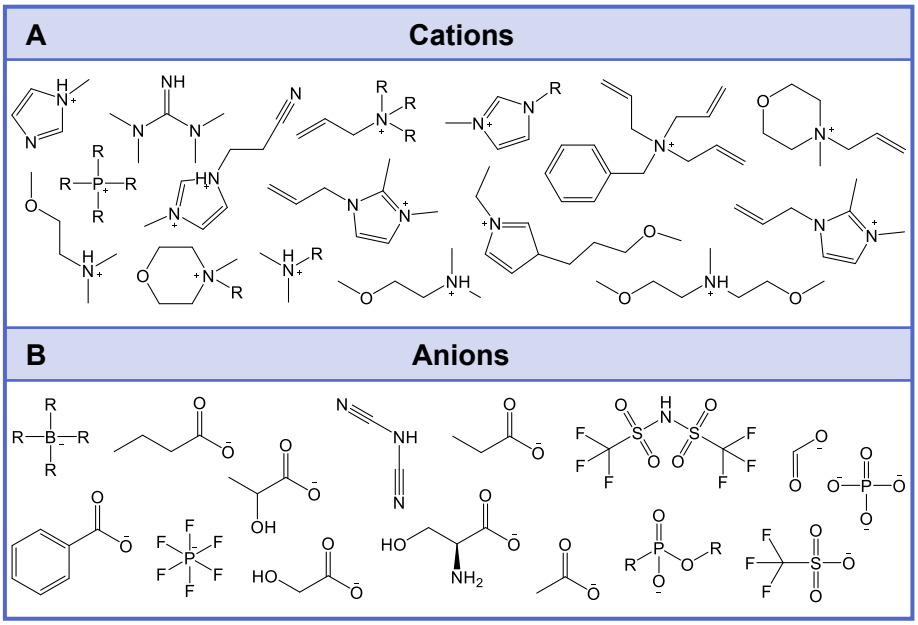

Figure 3.6. Schematic representation of commonly used **A:** cations and **B:** anions in ILs. Adapted from [53].

The pioneering work of R.D. Rogers over the past three decades has been key to unlocking the industrial potential of biopolymers like chitin and cellulose using ILs.[59] Among these, imidazolium-based ILs with basic anions, such as 1-ethyl-3-methylimidazolim and 1-butyl-3-methylimidazolim acetate and chloride ([C_2mim][OAc], [C_4mim][OAc], [C_2mim]Cl, and [C_4mim]Cl) – widely common for biopolymers and biomass valorisation – proven effective in isolating chitin from shrimp shells, crab shell, and squid pens.[60,61] Another interesting example involves 1-allyl-3-methylimidazolium bromide ([AMIM][Br]) used for chitin extraction from crab shells treating 10 wt.% of biomass at 120 °C for 24 h, followed by citric acid demineralisation to yield a 12.6 % chitin recovery, a degree of acetylation of 93 %, and a molecular weight up to 1.5×10^5.[62] DFT studies showed that the effectiveness of this IL lies in the bromide anion, which is able to penetrate between the biopolymer chains and promotes a "peeling" mechanism by destabilising interchain hydrogen bonding.[63] Moreover, a binary mixture of two imidazolium-based ILs – 1-ethyl-3-methylimidazolium acetate ([EMIM][OAc]) and 1-butyl-3-methylimidazolium bromide ([BMIM][Br]) – was found to efficiently extract chitin after treatment at 110 °C for 24 h, followed by citric acid–assisted demineralisation. The resulting extracted chitin exhibited yields 1.14–2.04 times higher than those obtained through conventional chemical extraction, properties comparable to commercial chitin, and a noticeable bleaching effect, confirming the potential of such ILs mixtures for chitin-rich biomass valorisation.[64]

3.2 Green Extraction of Chitin from Hard Spider Crab Shells

This section is part of the experimental work carried out in this Thesis. The author contributed to the design and the execution of the extraction tests, and to part of the characterisation tests of the extracts. The results described on this paragraph have been published as a Research Article in: C. Campalani, I. Bertuol, **C. Bersani**, R. Calmanti, S. Filonenko, D. Rodríguez-Padrón, M. Selva, A. Perosa, *Carbohydrate Polymers* (**2024**), 345.

Abstract. A green protocol to extract chitin from crab shells using water compatible ionic liquids is here reported. Compared to conventional multistep acid-base extraction methods, this one-pot procedure achieves pulping of recalcitrant crustacean waste shells by employing ammonium acetate, ammonium formate and hydroxylammonium acetate as water-compatible, low-cost and easy to prepare ionic liquids. An extensive parametric analysis of the pulping process has been carried out with different ionic liquids, different ratios, temperature and time. The optimised protocol provides a high-quality chitin comparable, if not better, to commercial chitin. The best results were obtained at 150 °C with ammonium formate prepared *in-situ* from aqueous ammonia and formic acid (**Figure 3.7**): chitin was isolated in a 17 wt.% yield (based on dried crab shells as starting biowaste), a degree of acetylation (DA) above 94%, a crystallinity index of 39–46%, a molecular weight up to 6.6 × 10^5 g/mol and a polydispersity of ca 2.0.

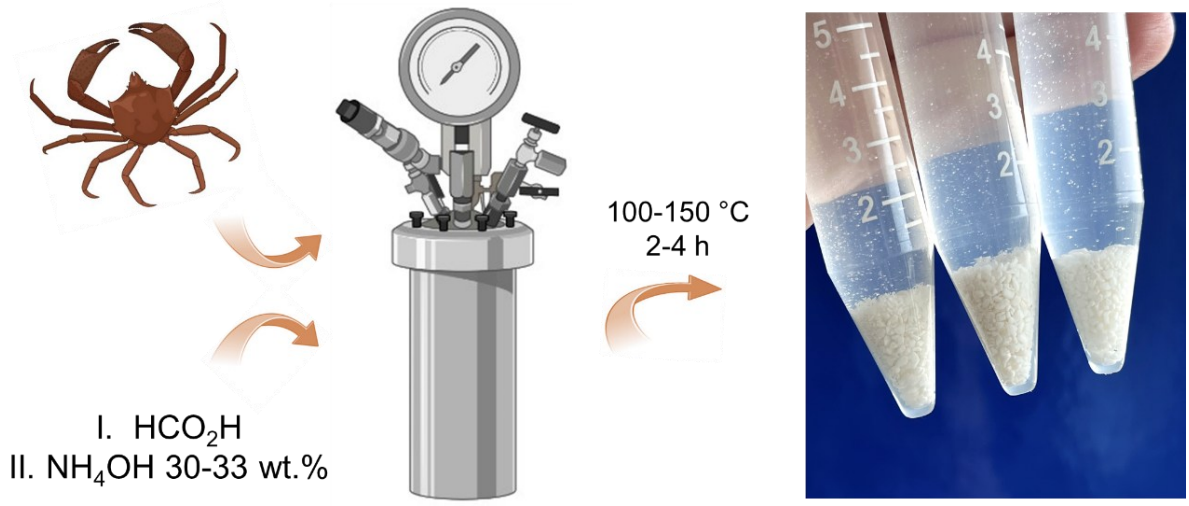

Figure 3.7. Schematic representation of our one-pot pulping method to isolate chitin from hard Spider crab shells using *in-situ* prepared ionic liquids.

3.2.1 Introduction

The Food and Agriculture Organisation (FAO) has reported that fishery and aquaculture production will reach 202 million tonnes/year by 2030.[7] This sector is recognised in the context of food security and nutrition by the UN 2030 Agenda for Sustainable Development. A consequence of the increasing consumption of fishery derived food is the production of waste, which is currently estimated in the order of dozens of million tons per year. Fishery waste represents a valuable source of chemical richness as it includes oil (such as ω-3 fatty acids), as well as amino acids, bioactive peptides, collagen, chitin, gelatine, and pigments.[7,65] The recovery and upgrading of such waste. Not only it provides marketable products but also contributes to reducing the effect of the anthropic exploitation of marine resources and to preserve coastal environments.

Crustacean shell biorefining places a special emphasis on chitin, (poly *β*-(1→4)-*N*-acetyl-D-glucosamine), which is the second most abundant natural polysaccharide after cellulose.[13,66,67] Its total annual production is estimated around 2.8×10^{10} kg from species of freshwater and 1.3×10^{12} kg from species of marine ecosystems, respectively, the latter including prawns, crabs, shrimps, and lobsters.[68] Crustacean exoskeletons are composed of ca. 20–30% chitin, 30–50% minerals (mainly calcium carbonate), 30–40% proteins and other substances including lipids (up to 14%) and pigments (such as astaxanthin).[69] Since chitin is insoluble in water and in most organic solvents, its isolation is a laborious multistep process based either on chemical or on biological (microbial) methods[47] (**Figure 3.8**).

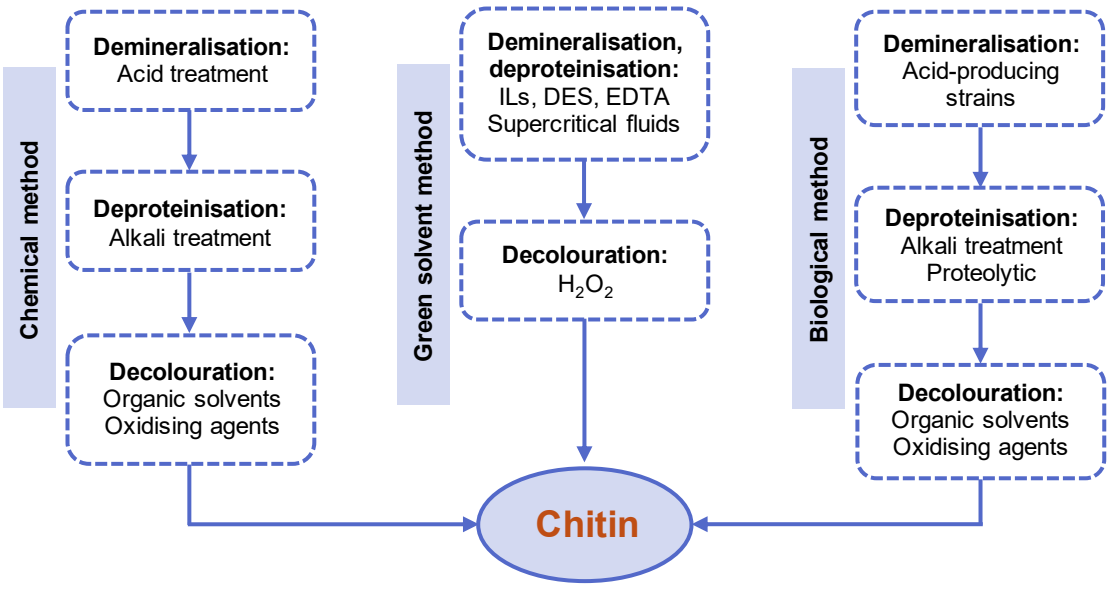

Figure 3.8. Schematic representation of the common routes for chitin extraction.

Chemical pulping involves initial crushing and/or milling of the biomass, followed by deproteinisation, demineralisation, and decolouration to remove protein, inorganic components and pigments (astaxanthin, canthaxanthin, astacene, lutein and β-carotene), respectively[70,71] (**Figure 3.9**). Such treatments typically take advantage of highly concentrated solutions of strong mineral acids, alone or in mixtures, to remove the mineral phase. The most common are HCl, HNO_3, and H_2SO_4, usually employed for 1-3 h at room temperature.[72] Deproteinisation is then carried out under strongly alkaline conditions, often using concentrated solutions of NaOH, KOH, $Ca(OH)_2$, Na_2CO_3, Na_3PO_4, Na_2S at temperatures ranging from 65 to 160 °C for several hours or days.[73] Discolouration is generally achieved using organic solvents, such as acetone, ethyl acetate, or ethanol, which dissolve and extract pigments, or bleaching treatments with oxidising agents like $KMnO_4$, H_2O_2, or NaClO, sometimes assisted by physical treatment such as ultrasound as alternative to conventional heating

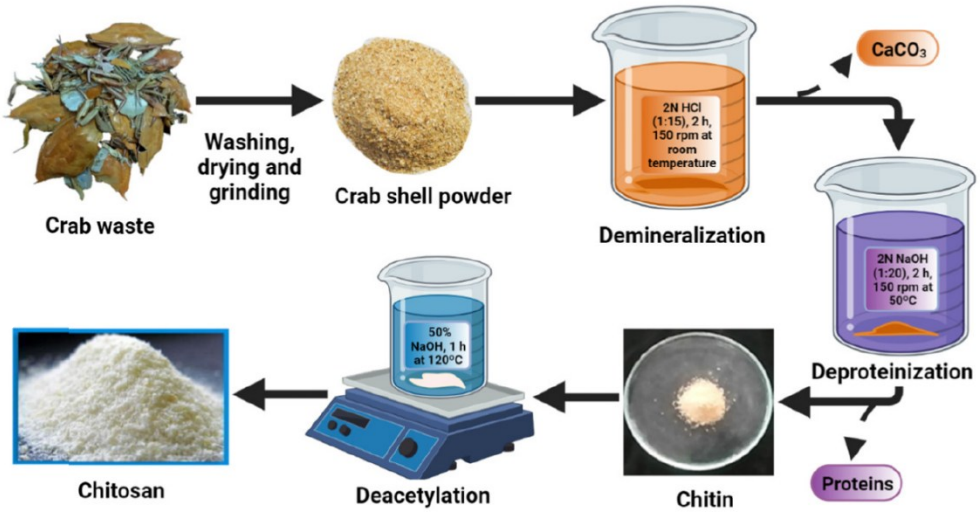

Figure 3.9. Illustration of the conventional chemical extraction route. Reprinted from [50] with permission.

These different treatments imply several drawbacks. On one hand, they may induce potential adverse effects on the properties of extracted chitin: e.g., if acid/basic conditions for demineralisation and deproteinisation are not strictly controlled, hydrolysis of the glycosidic bond may cause the formation of oligomers,[74] while the degree of acetylation and the crystallinity index can both decrease.[75] Moreover, compared to biological methods, chemical procedures are generally aggressive for ecosystems, energy-intensive,[47] time consuming and generate large amounts of wastewater.

For instance, in a typical chemical extraction, about 1 L (972 mL) of concentrated HCl (35 wt.%) is required to demineralise 100 g of chitin from crab shell waste, releasing 220 g (112 L at standard temperature and pressure) of CO_2 in the atmosphere.[76] Nonetheless, chemical treatment of arthropod shells is still the preferred route for the extraction and production of commercial chitin.

In search of alternative solvents for chitin isolation, other approaches were conceived by the combined application of microwave energy and highly solvating ionic liquids such the imidazolium-based salts mentioned in the previous paragraph. For example, 1-ethyl-3-methylimidazolium acetate ([EMIM][OAc]) proved effective not only to dissolve pure chitin, but also directly shrimp shells.[77] It was demonstrated that cheaper and readily accessible ionic liquids, including 2-hydroxyethyl ammonium acetate ($[NH_3(CH_2)_2OH][OAc]$) and hydroxylammonium acetate ($[NH_3OH][OAc]$) were effective in the pulping of shrimp shells.[78] Chitin was obtained in good yields (ca. 75–95%) with around 70–80% purity using 10% loading of biomass in the ionic liquid. However, some Authors noticed that a partial hydrolysis of chitin occurred due to the highly acidic nature of hydroxylammonium acetate that afforded lower MW chitin. Additional issues were the toxicity and explosive nature of hydroxylamine, the large amounts of ionic liquids that in view of an economically viable process must be recovered and reused, and the nature/consistency of the biomass source (shrimp shells, for example, are softer and more easily pulped compared to harder crab shells).[60] Based on this seminal work by Rogers et al., part of this Thesis work has been developed with the aim of designing a more accessible, efficient and robust pulping protocol applicable to a wider variety of crustaceans and particularly including hard crab shells.

Our pulping technique was based on cost-effective, safe and easily available ionic liquids,[79] and targets spider crab shells (*Maja Squinado,*[80]), one of the biggest and most abundant crabs, that in our view represents a benchmark waste biomass source for chitin extraction. Spider crab shells possess a higher chitin content and are more tenacious and resistant to processing than commonly described shrimp shells.[81] A reported procedure for the treatment of crab shells as a biowaste described the use of 1-allyl-3-methylimidazolium bromide ([AMIM][Br]) but due to the tenacity of the matrix, the extracted chitin required further purification with aqueous citric acid to remove the excess calcium carbonate yielding chitin in only 13% yield.[62,82]

In this Thesis work, the pulping of *Maja Squinado* shells was carried out with ammonium acetate (AA) and ammonium formate (AF), two easy to synthesise and low-cost ionic liquids

illustrated in **Figure 3.10**. These compounds were prepared either *ex-ante* or by sequential addition of aqueous ammonia and acetic or formic acid to the biowaste.

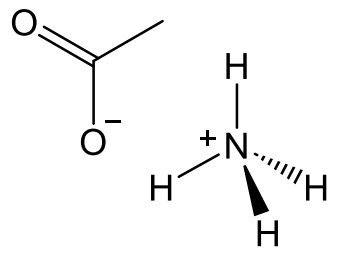

Ammonium Acetate (AA)

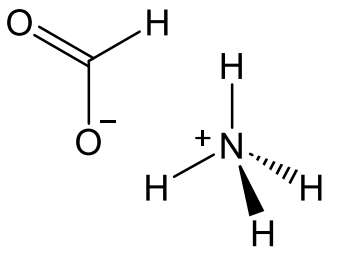

Ammonium Formate (AF)

Figure 3.10. Schematic representation of the ionic liquids used in this study.

Both ionic liquids contained an alkaline anion and an acidic cation that contributed to the deproteinisation and the demineralisation of the target biowaste in a single step. Chitin was obtained in ca. 17-20 wt.% yield (this value was close to a quantitative extraction yield calculated based on the chitin content in the dry biomass), with a MW of 6.6×10^5 g/mol, 39–46% crystallinity, and a DA of 94%. The pulping performance of AA and AF were compared to that of hydroxylammonium acetate (HA) which, to date, has been reported as the most effective ionic liquid for the pulping of shrimp shells.[79]

3.2.2 Result and Discussion

Characterisation of the starting feedstock

Spider crab shells were sourced as a waste of a local restaurant in Venice. The shells were initially ground, and the powder was analysed by TGA and FT-IR, as reported in **Figure 3.11A-B**. The thermogram displayed three main weight losses of ca. 6, 20 and 33%, at around 100, 330 and 720 °C, associated with loss of water, decomposition of the organic fraction and decarboxylation of calcite, respectively.[83] The FT-IR spectrum exhibited bands consistent with O–H and N–H stretching vibrations and the presence of amide and carbonate groups. Overall, both TGA and FT-IR confirmed the presence of proteins, chitin, and a high mineral content, mainly calcite.

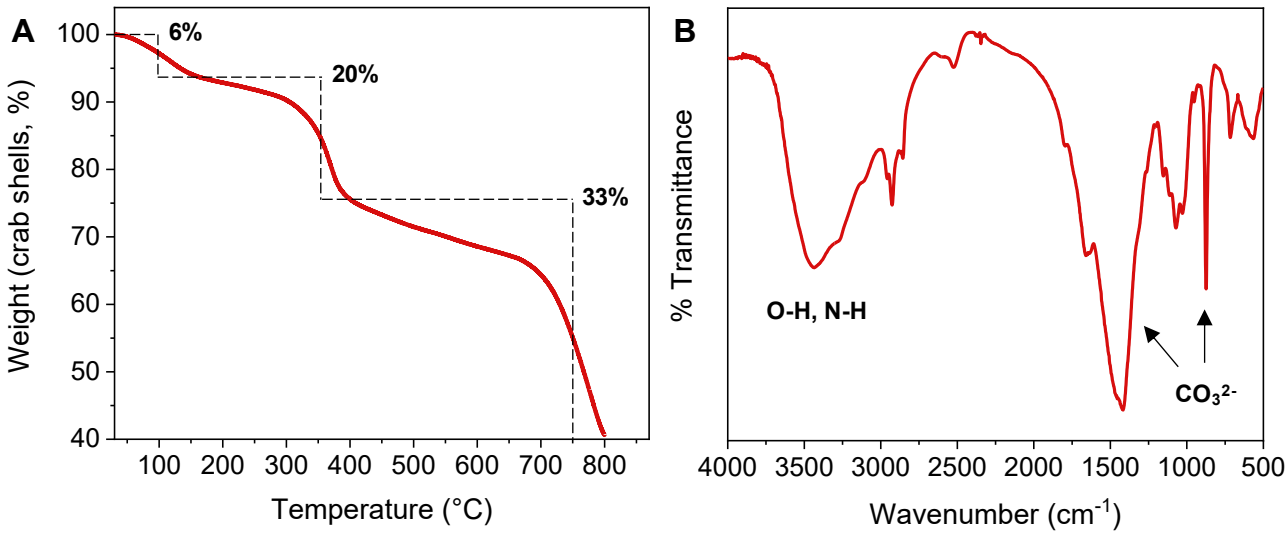

Figure 3.11. Spider crab shells characterisation by **A:** TGA, in the range of 30-800 °C under N_2 atmosphere, and **B:** FT-IR spectroscopy, 1 mg in KBr pellet (100 mg).

Next, the chemical composition of the shells was determined, as illustrated in **Figure 3.12**. Inorganic components were measured by the standard test method (ASTM E1755-01, details of the procedure are discussed in the Experimental Section at the end of this Chapter) for determining ash in biomass by dry oxidation, while protein content was measured by difference between dry biomass and deproteinised biomass. The measured contents of ash and protein were 57 wt.% and 21 wt.% respectively, relatively to the weight of the starting dry crab shells, thereby confirming that inorganic matter was the major component of crab shells. The percentage of chitin was estimated by difference, around 20 wt.%.

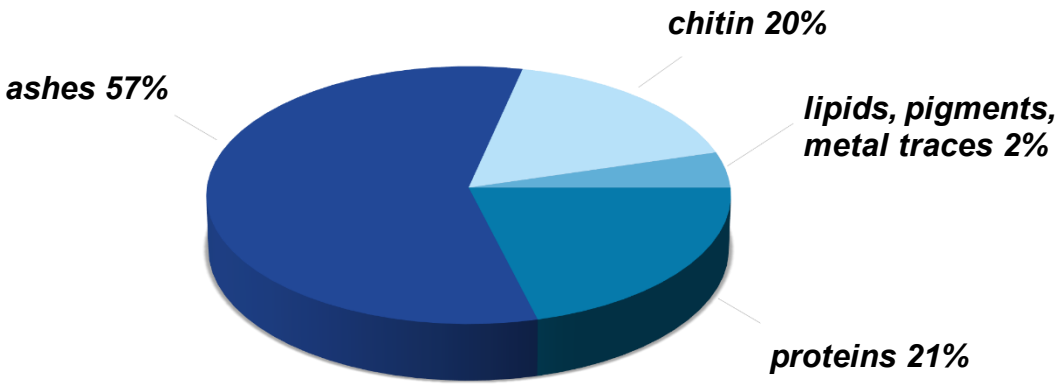

Figure 3.12. Graphical representation of the chemical composition of the Spider crab shells used in this study.

Finally, the content of calcium salts, mainly carbonate, was quantified by ICP-OES, resulting to be 52 wt.% on a dry basis. This result was consistent with the ash content analysis and proved that almost 90% of ash residue in the treated biowaste was due to the presence of calcium salts. Lipids, carotenoids, and metal traces constituted only a minor fraction of the matrix. All these results (chemical composition and ICP analyses) were in good agreement with previous works on the characterisation of Spider crab shells (*Maja Squinado,*[80]).

Conventional stepwise extraction of chitin from Spider crab shells

A sample of powdered crab shells was subjected to a conventional stepwise procedure for the extraction of chitin with HCl and NaOH. More details about this procedure, that was adapted from a reported method,[84] are discussed in the Experimental Section. Chitin was obtained as a white solid in 17 wt.% yield, and characterised by TGA, FT-IR and ^{1}H-NMR.

TGA (in **Figure 3.13A-B**) showed two weight losses of 3-5 and 70-74% at 100 and 334 °C, correlated to the release of water and to the decomposition/depolymerisation of the material through deacetylation and cleavage of glycosidic linkages, respectively. A further progressive weight-loss at higher temperatures (415–670 °C) was related to the thermal destruction of the pyranose ring and the decomposition of the residual carbon containing fraction.

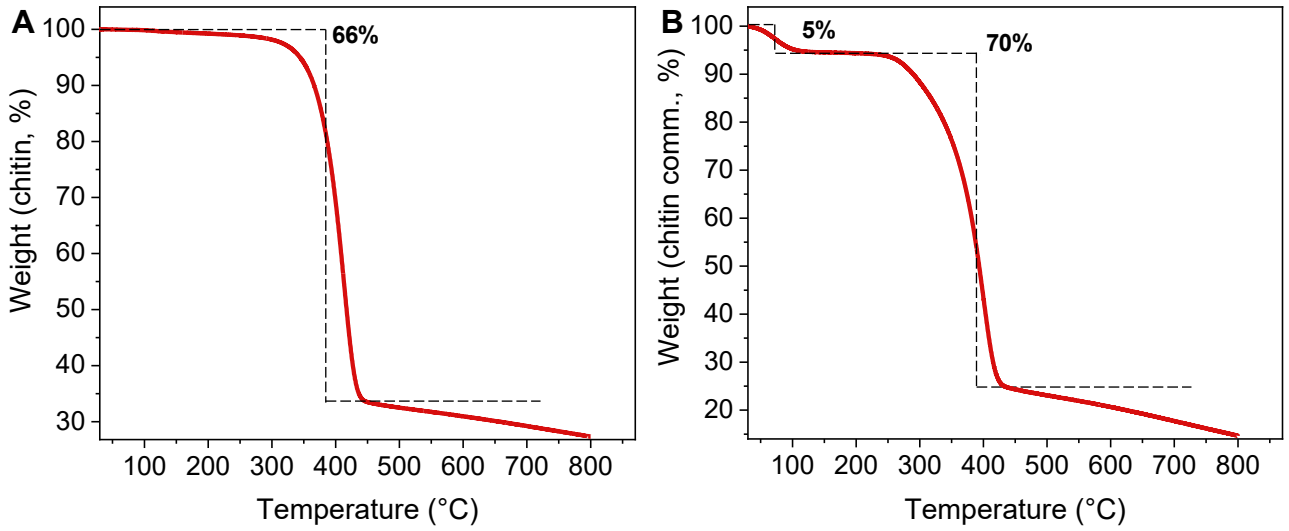

Figure 3.13. TGA of **A:** conventionally extracted and **B:** commercial chitin, 30-800 °C under N_2 atmosphere.

The FT-IR spectra of both conventionally extracted and commercial chitin (**Figure 3.14A-B**) exhibited signals between 1700 and 1000 cm^{-1}, related to stretching of C–O in amide I group in the neighbouring intrasheet chain, to hydrogen bonding between carbonyl and hydroxyl-methyl groups of two-chitin moieties in the same biopolymer chain, to N–H bending (amide II) and to C–N stretching (amide III), respectively.

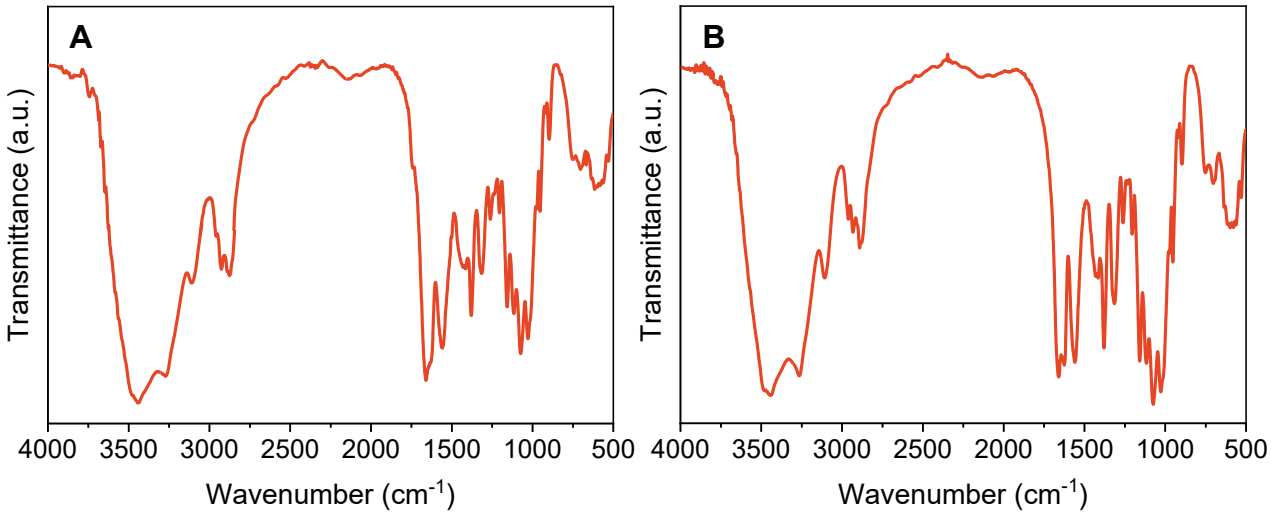

Figure 3.14. FT-IR spectroscopy analyses of **A:** conventionally extracted and **B:** commercial chitin, 1 mg in KBr pellet (100 mg).

Compared to the IR spectrum of the Spider crab shells, the disappearance of the carbonate band (around 1400 cm^{-1}) and the sharp peak at 870 cm^{-1} typical of calcite confirmed the removal of the mineral portion.[85]

Further characterisation tests were carried out by ^{1}H NMR analyses. An issue with NMR experiments was the poor solubility of chitin in any solvent including water. This required the design of a specific analytical procedure adapted from the literature,[86] whereby a mixture of DCl 35 wt.% in D_2O was employed as NMR solvent upon thermal treatment of the sample at 50 °C. No resonances other than the ones attributed to the chitin structure were observed, indicative of a good purity achieved. However, the time needed for dissolution of chitin in acidic D_2O remarkably affected the ^{1}H-NMR spectrum. As shown in **Figure 3.15**, ^{1}H-NMR spectra recorded after 10, 20 and 30 min of dissolution treatment revealed the progressive appearance and increase of signals characteristic of depolymerisation.

Specifically, a comparison of the spectra indicated variations in the relative intensities of the different signals assigned to anomeric H-1 in the region between 4.5 and 5.5 ppm after 10, 20 and 30 min (box highlighted in light blue in the Figure). These changes indicated a

decrease of the H-1 resonance associated with the native polymeric chitin chain, accompanied by the appearance of α-H-1 and β-H-1 typical of the terminal proton generated upon hydrolysis (depolymerisation) of the glycosidic bonds due to the acidic conditions.

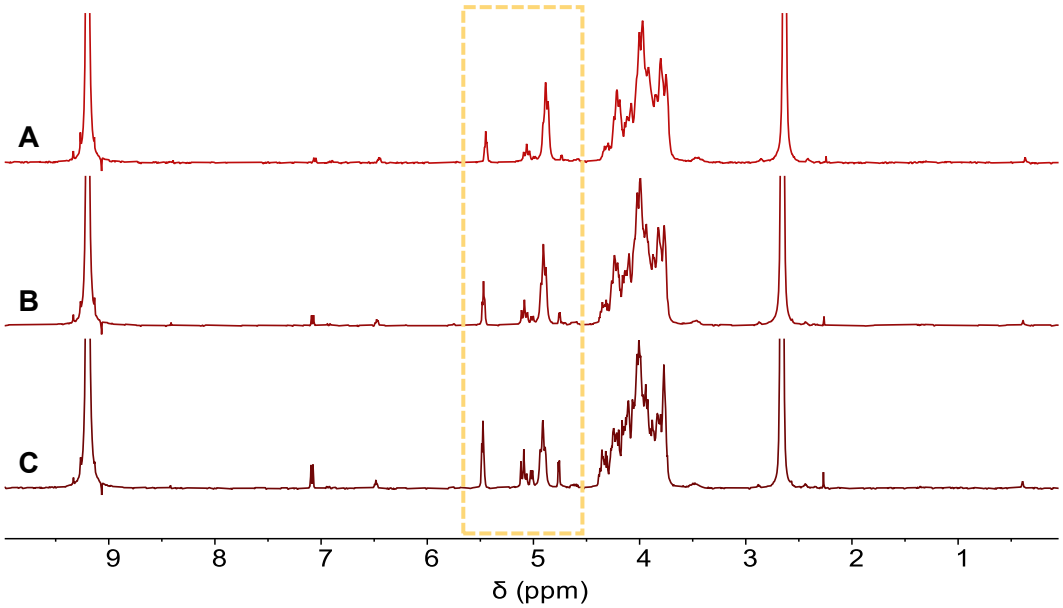

Figure 3.15. ^{1}H-NMR spectra of commercial chitin treated at 50 °C in DCl 35 wt.% for **A:** 10, **B:** 20 **C:** 30 min.

To ensure maximum reproducibility of the results, all NMR experiments were conducted under identical standardised conditions: spectra were acquired using 35 wt.% DCl in D_2O as deuterated solvent, in which chitin was treated at 50 °C for 30 minutes. Under these conditions, depolymerisation unavoidably occurs, yielding to a mixture of oligomers and glucosamine monomer, and thus reducing the proportion of intact native chitin in the final solution. Nonetheless, the rate constant for hydrolytic depolymerisation is much faster than deacetylation[86] yet allowing us to use ^{1}H-NMR analyses for the determination of the degree of acetylation (DA) of chitin.

NMR analyses of chitin from both the commercial supplier and the conventional (chemical) extraction above described, are compared in **Figure 3.16A-B.** The protein content and degree of acetylation (DA) of the two samples were determined according to the procedures and the equations described in the Experimental Section. A DA of 92% for both the conventionally extracted and commercial chitin was calculated based on the resonances of the characteristic protons. This preliminary investigation led us to conclude that the conventional treatment of the waste Spider crab shells allowed to extract chitin which, based

on characterisation by TGA, FT-IR, and NMR, showed properties comparable to those of a commercial chitin specimen.

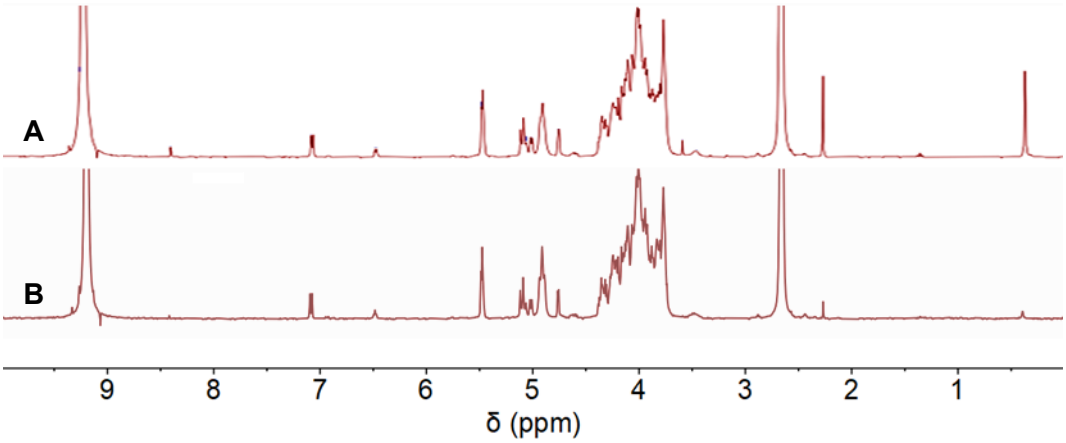

Figure 3.16. ^{1}H-NMR spectra of **A:** conventionally extracted and **B:** commercial chitin in DCl 35 wt.%.

Pulping strategies based on the use of ionic liquids for chitin extraction

The complexity of biomass and especially biowaste processing is such that any change on the feedstock usually requires rethinking the treatment conditions and the implementation of novel protocols. Indeed, the lack of broad-based conversion technology is still a major challenge of modern biorefineries,[87] and the ionic liquid-assisted extraction of chitin from crustacean shells is not an exception. Most, if not all, of the available studies on the pulping of arthropods shells with ionic liquids for the extraction of chitin have been referred to shrimp shells as the starting feedstock. The seminal work by Shamshina et al. (2016) pioneered this protocol, demonstrating the efficacy of hydroxylammonium acetate as an extraction medium and exploring the transition of ionic liquid-based extraction from academia to industrial application.[79] As previously mentioned in the introduction, Spider crab shells are particularly rich in chitin, but their structure is tougher and more resistant to processing than that of shrimp shells.

The ionic liquids selected for this study were two commercially available protic ammonium salts, ammonium acetate (AA) and ammonium formate (AF), which can be directly and easily derived from a weak acid and a weak base, and have already found applications in energy storage and in the treatment of lignocellulosic biomass.[88,89] The behaviour of both AA and AF was investigated in comparison to that of the above-mentioned hydroxylammonium acetate (HA), was synthesised according to a method reported

elsewhere.[78] Further details on the synthesis and characterisation of ammonium salts are available in the Experimental Section, and in the Appendix Section.

Once ground to powder, the Spider crab shells were initially processed by testing three alternative approaches, illustrated in **Figure 3.17** and summarised as follows:

i) the selected neat ionic liquid – AA, AF, or HA, prepared ex-ante or purchased – was directly mixed with 10 wt.% of crab shells powder and heated at 130 °C, a temperature high enough to melt the onium salt (**Strategy 1**, left);

ii) the selected acid, acetic or formic, was mixed with 10 wt.% of crab shells powder. Then an aqueous ammonia or hydroxylamine solution was added dropwise to generate in-situ the corresponding onium salt, and the resulting suspension was heated at 100 °C under stirring (**Strategy 2**, middle);

iii) the *in-situ* formed onium salts were obtained by reversing the addition order of point ii), thus mixing the base with 10 wt.% of crab shells powder, then adding the corresponding acid and heating at 100 °C under stirring (**Strategy 3**, right).

In each case, the heating treatment was carried out for 2 h. Thereafter, the suspension was cooled to room temperature, added with water, and filtered. The residual white solid was further rinsed with water, dried under vacuum, and characterised by TGA, NMR, ICP-OES, and FT-IR. The solid was isolated in different yields ranging from 16 to 30 wt.% (based on the weight of starting crab shell powder) that depended upon the use of different onium salts and alternative strategies (1, 2, or 3). The main results are summarised in **Table 3.1**.

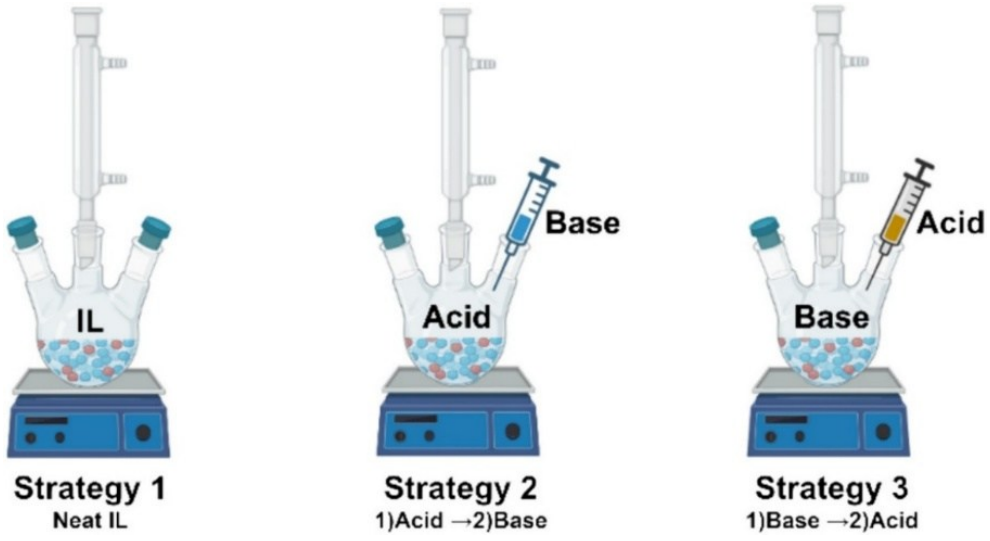

Figure 3.17. Schematic representation of the three different pulping strategies investigated in this study for chitin isolation from Spider crab shells.

Table 3.1. Experimental conditions and outcome of the pulping strategies (1, 2 or 3) for chitin extraction using ionic liquids.

Entry	IL	Strategy	T (°C)	Yield (wt.%)	$CaCO_3$ (wt.%)	Ca^{2+} (wt.%)	DA (%) by NMR[b]	
					by TGA[a]	by ICP-OES[a]	Method 1	Method 2
1		1	130	16	-	4	99	99
2	AA	2	100	30	14	33	88	93
3		3	100	27	9	19	97	97
4		1	130	20	6	11	94	95
5	AF	2	100	17	-	1	97	97
6		3	100	18	-	1	94	95
7		1	130	29	10	37	-	-
8	HA	2	100	20	7	18	96	97
9		3	100	21	6	24	93	94

[a] Amount of carbonates (wt.%) and calcium (wt.%) species were determined after the pulping treatment.
[b] The degree of acetylation (DA, %) was determined by NMR according to two methods based on Equation (3) and Equation (4), respectively, reported in the Experimental Section.

In most cases the extract still contained a significant residual amount of $CaCO_3$ (up to 37 wt.% entry 7), highlighting that an incomplete demineralisation of the starting material occurred, especially when using AA (entries 2 and 3) and HA (entries 7–9). The presence of mineral residues was confirmed from TGA profiles (available in the Appendix Section), which showed a weight loss between 700 and 800 °C due to the release of CO_2 from calcium carbonate decomposition. A more accurate quantitative determination of Ca^{2+} content was obtained by ICP-OES analysis following complete acid digestion of the samples (further details about the procedure are discussed in the Experimental Section). It should be noted, however, that the two techniques provide different analytical information and rely on different sensitivities. TGA selectively determines carbonate species through thermal decomposition, whereas ICP-OES measures the total calcium content with high sensitivity, independently of its chemical speciation. As a result, discrepancies between content values derived from the two techniques are expected and primarily reflect the intrinsic limitations and detection principles of the two methods.

An incomplete demineralisation, and, therefore, the presence of inorganic residues within the extracted products explained why several AA- and HA-assisted pulping experiments, regardless of the temperature or strategy applied, gave an extraction yield apparently higher (27-30%, entries 2, 3, and 7) than the theoretical chitin content in Spider crab shells (17-20%). By contrast, AF-assisted pulping of crab shells powder performed at 100 °C showed the best performance, giving yields (17–18%, entries 5 and 6) consistent with the expected amount of chitin in the starting biowaste. Both TGA and ICP-OES of the extracts from AF-treatment confirmed a negligible content of mineral residue (≤1 wt.%).

These preliminary results led us to conclude that for the extraction of chitin:

i) despite the higher temperature applied, the direct suspension of crab shell powder into neat ionic liquids (strategy 1) often resulted in a less efficient demineralisation step. The only exception was that of entry 1 in **Table 3.1**. The higher viscosity of neat ionic liquids, compared to that of the *in-situ* synthesised ones, where water is present, plausibly hindered the diffusion and efficient interaction between the pulping agents and the chitin chains, thereby resulting in an incomplete demineralisation;

ii) notwithstanding the good result with AA (entry 1), an aspect emerging from **Table 3.1** was that less energy-intensive conditions for the *in-situ* formation of AF and HA at 100 °C, generally afforded better results. A complete demineralisation was observed using AF ($CaCO_3$ < wt.1%, entries 5 and 6), while AA was far less effective under comparable conditions ($CaCO_3$ 9–33%, entries 2 and 3). This difference was attributed to the higher acidity of formic acid compared to acetic acid, which made the in-situ generated ammonium formate more effective in dissolving minerals;

iii) as for the in-situ preparation of the ionic liquids, apparently, the order of addition (acid first or base first) seemed to play secondary role, as yields and mineral contents were generally comparable within each ionic liquid tested (see entries 2 vs 3, 5 vs 6, and 8 vs 9).

^{1}H-NMR analyses of the samples in **Table 3.1** were carried out under the previously described standardised conditions (35 wt.% DCl in D_2O at 50 °C for 30 min). The calculated degree of acetylation (DA) was generally very high, above 94% in almost all cases. This confirmed that the pulping conditions did not significantly compromise the acetylation degree of the polysaccharide, regardless of the strategy employed. A partial exception was

observed with the AA-assisted extraction of entry 2, which gave a slightly lower DA. Moreover, when neat solid HA was used, the determination of the DA was hindered by the overlapping of H-2 signals of internal deacetylated units with impurities possibly still present in the sample (entry 7).

A representative ^{1}H-NMR spectrum of chitin obtained via AF-assisted pulping treatment of entry 5, found to give the best performance, is reported in **Figure 3.18B** in comparison to commercial chitin (**Figure 3.18A**). Both spectra showed all the characteristic signals of the glucosamine structural units; though, the spectrum of the pulped chitin displayed additional broad resonances between 1.0 and 1.5 ppm (highlighted area) attributed to methyl groups from residual proteins of the crab shells (bottom, [90,91]). To confirm this assignment, the pulped sample was subjected to chemical deproteinisation using an alkali solution of 1.0 M NaOH[84], as described in the Experimental Section. ^{1}H-NMR spectrum of the alkali-treated sample showed the disappearance of the 1.0-1.5 ppm signals as illustrated in **Figure 3.18C,** thereby corroborating their protein origin and the proposed assumption.

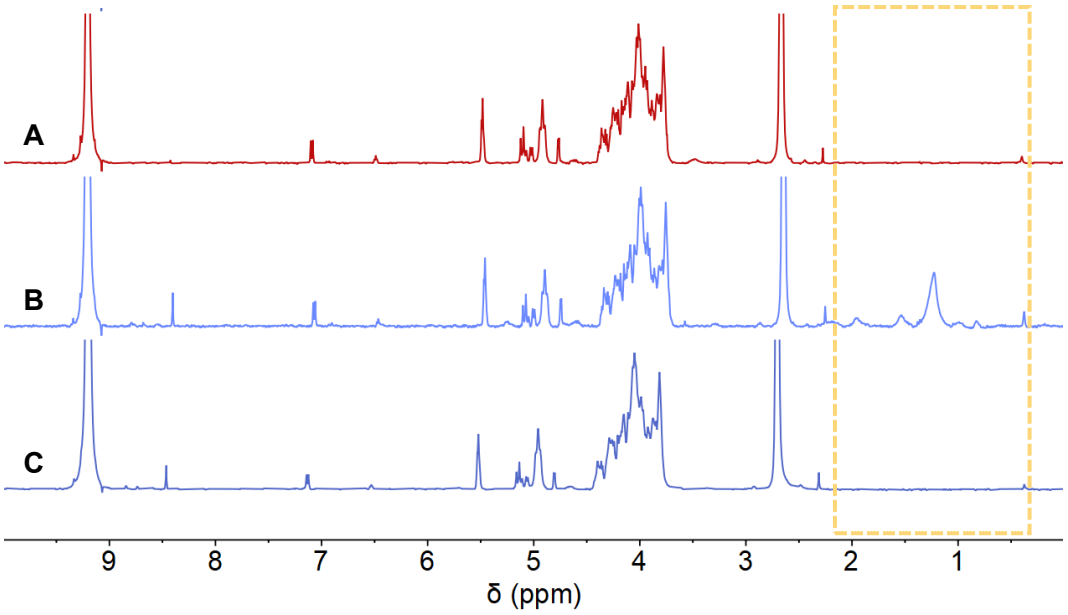

Figure 3.18. ^{1}H-NMR spectra of **A:** commercial chitin compared to chitin pulped with AF **B:** before and **C:** after the deproteinisation treatment. Spectra recorded using 35 wt.% DCl in D_2O as solvent.

Further characterisation by XRD was carried out on the chitin samples obtained by using the AF-assisted pulping protocol. **Figure 3.19** reports the results (right) and the comparison of XRD profiles with commercial chitin (left), which gave insight on the crystallinity of the pulped samples.[92] The extracts prepared by using AF as a solid salt or by sequential addition

of formic acid followed by ammonia displayed comparable crystallinity index (CI = ca. 39% in both cases), while by using the strategy 3 (base first, then acid), a higher CI value of 46% was determined. These values were slightly lower than the CI of the commercial sample (56.5%).

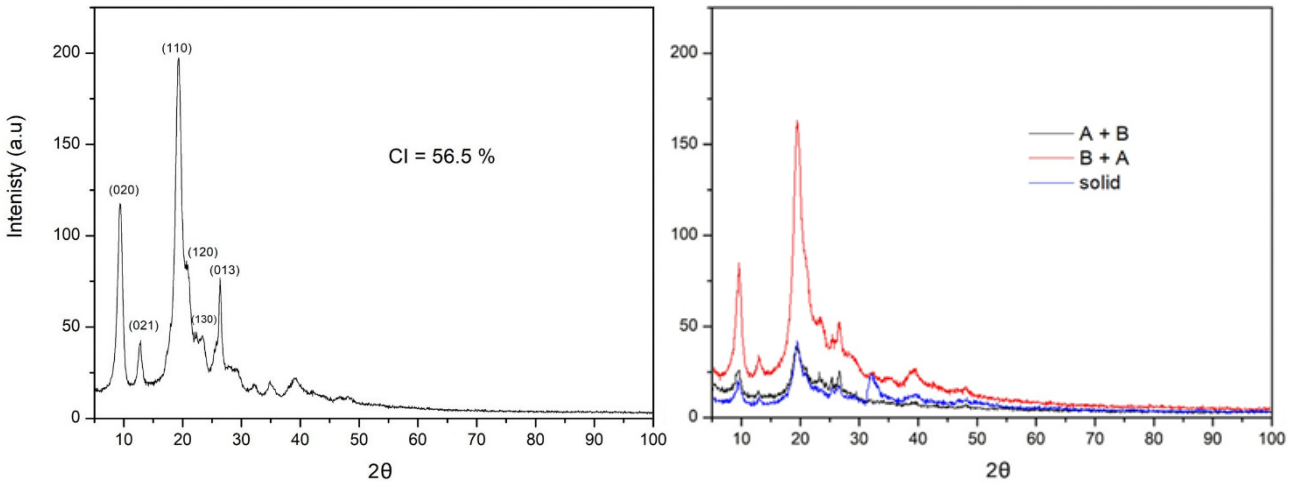

Figure 3.19. XRD diffractograms of commercial chitin (left) and chitin pulped with ammonium formate in the form of solid salt (blue, entry 4) or prepared in-situ by sequential addition of acid and base (black, entry 5) or base and acid (red, entry 6) at 100 °C.

Parametric analysis of the pulping procedure

Experiments of **Table 3.1** allowed us to identify AF as the most convenient ionic liquid for chitin isolation: the best result so far was achieved by pulping crab shells powder at 100 °C for 2 h. Although residual proteins were still detectable after the pulping procedure, a parametric analysis of the extraction conditions was performed in order to evaluate the effect of biomass loading wt.%, pulping time and temperature. Among the different strategies investigated, the less energy-intensive and easier to operate *in-situ* preparation of ionic liquids was selected as the preferred option.

Three different experiments were simultaneously carried out. Starting from the extraction conditions of entry 5, **Table 3.1**, biomass loading was varied from 10 to 20 wt.%, pulping time was extended from 2 up to 24 h, and temperature was increased from 100 to 150 °C. Extracts were characterised by ^{1}H-NMR. Results are reported in **Figure 3.20**.

For all the experiments: i) the extraction yield was within the expected range (17–18%); ii) the mineral content was negligible (carbonate decomposition was never detected by TGA; **Figure 3.21** shows the profile of chitin pulped at 100 °C for 24 h, as an example); and iii) the DA (≥94%) was comparable to that reported in **Table 3.1**. The results indicate that none

of the three parameters varied in these preliminary screening tests led to highly significant changes in the characteristics of the final extracts. Though, the protein residue around 1.0–1.5 ppm was persistent in all cases, indicative of incomplete deproteinisation (Yellow dashed box, right side, **Figure 3.20**).

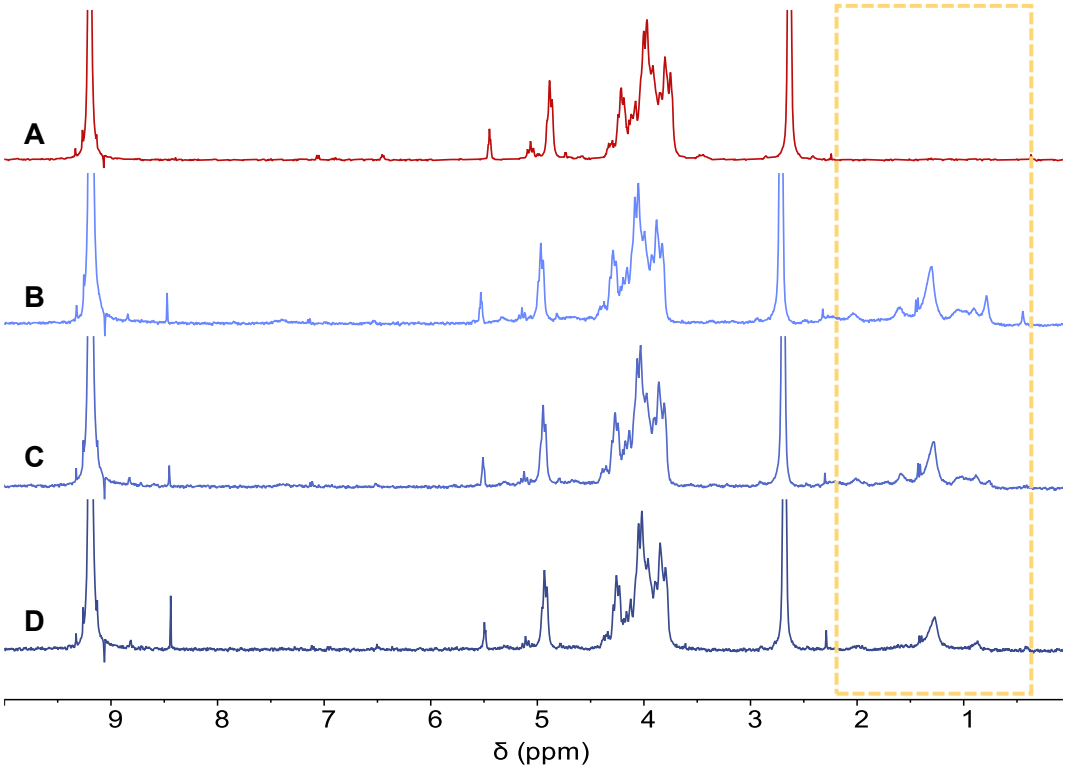

Figure 3.20. ^{1}H-NMR spectra of **A:** commercial chitin and chitin pulped using *in-situ* prepared AF, varying **B:** loading (from 10 to 20 wt.%), **C:** pulping time (from 2 to 24 h), **D:** temperature (from 100 to 150 °C).

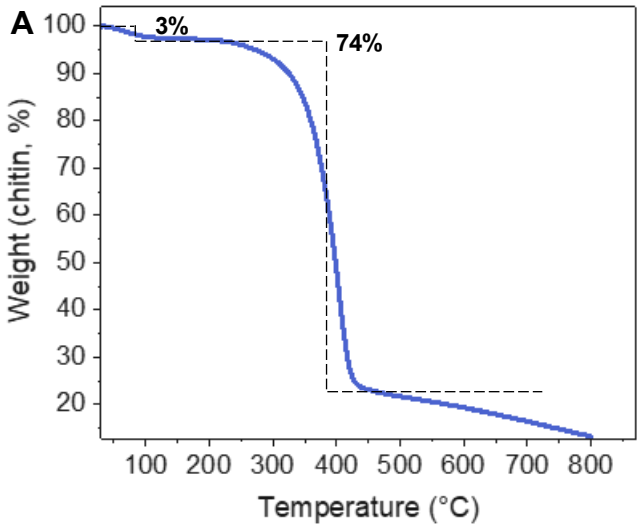

Figure 3.21. TGA of chitin pulped using *in-situ* prepared AF (10 wt.%, 100 °C, 24 h), 30-800 °C under N_2.

Since organic residues from proteins were subjected to mould proliferation that could alter the characteristics of the extracted biopolymer, efforts were directed to a further investigation of the extraction conditions to ensure a complete deproteinisation. In the crustacean shells, proteins are covalently anchored to chitin and are get together within the matrix due to an extensive of Hydrogen-bonding network. Therefore, the hydrolysis and denaturation processes that are typically required for the removal of proteins (deproteinisation) are rather slow reactions. Bearing this in mind, further experiments of the AF-assisted extraction of chitin were designed by using a biomass loading within a range of 5–20 wt.%, and by prolonging all pulping tests up to 24 h.

Tested conditions are summarised in **Table 3.2**.

Table 3.2. Study of the biomass loading (wt.% of crab shells powder) variation on the AF-assisted pulping procedure performed at 100 °C for 24 h.

Entry	Biomass loading (wt.%) at 100 °C, 24 h	Yield (wt.%)	DA (%) by NMR[a]	
			Method 1	Method 2
1	5	22	97	94
2	10	17	94	92
3	15	19	97	96
4	20	20	94	97

[a] The degree of acetylation (DA, %) was determined by NMR according to two methods based on Equation (3) and Equation (4), respectively, reported in the Experimental Section.

^{1}H-NMR spectra of the obtained samples are reported in **Figure 3.22**. The intensity of all spectra was normalised with respect to the intensity of the acetyl group signal at 2.76 ppm. Thus, any other variations in the intensity or chemical shift of other signals related to the pyranosidic ring in the region between 3.5–5.5 ppm, were attributable to minor differences in acquisition timing, which did not actually affect the protein content of the chitin samples. NMR analyses show a slightly decreasing trend of the residue protein content in correspondence of increasing biomass loadings. This apparently counterintuitive result was correlated to an increase in the viscosity of the system with the increase of the biomass loading. The higher viscosity – though not excessive enough to prevent diffusion – was considered sufficient to exert a stronger abrasive force on the surface of crab shells during

agitation of the mixture, thereby leading to a more effective deproteinisation. Such results prompted us to select a biomass loading of 20 wt.% for further tests.

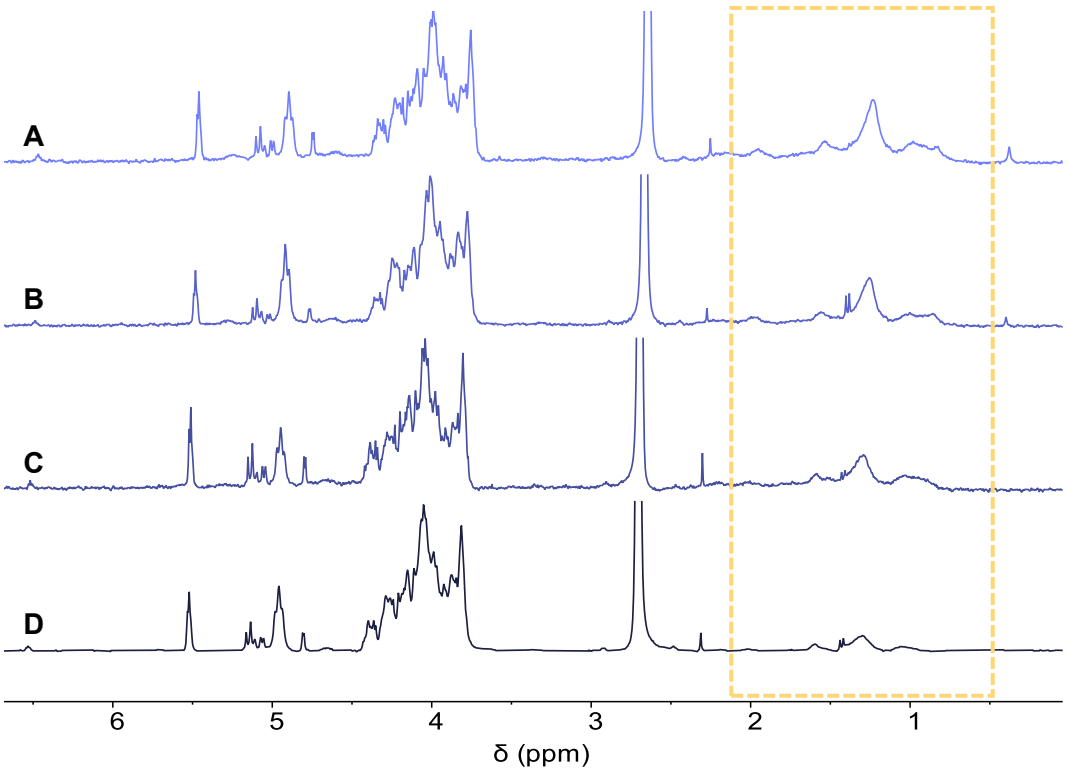

Figure 3.22. Comparative ^{1}H-NMR spectra of AF-assisted pulping of crab shells powder at 100 °C for 24 hours with **A:** 5 wt.%, **B:** 10 wt.%, **C:** 15 wt.%, **D:** 20 wt.% biomass loading.

New experiments were carried out to investigate the effect of both the pulping time in the range of 2 to 4 h, and a higher temperature of 150 °C. The residue protein content was evaluated at progressive hourly intervals, as summarised in **Table 3.3.**

Table 3.3. Study of the AF-assisted pulping procedure performed at 150 °C for 2, 3, and 4 h, with a biomass loading of 20 wt.% crab shells powder.

Entry	Pulping time (h) at 150 °C, 20 wt.% load.	Yield (wt.%)	DA (%) by NMR[a]	
			Method 1	Method 2
1	2	18	95	96
2	3	18	92	94
3	4	17	93	94

[a] The degree of acetylation (DA, %) was determined by NMR according to two methods based on Equation (3) and Equation (4), respectively, reported in the Experimental Section.

Figure 3.23 shows the corresponding ^{1}H-NMR spectra. Nearly complete deproteinisation was finally achieved after 4 h at 150 °C, as indicated by the disappearance of the signal between 1.0 and 1.5 ppm.

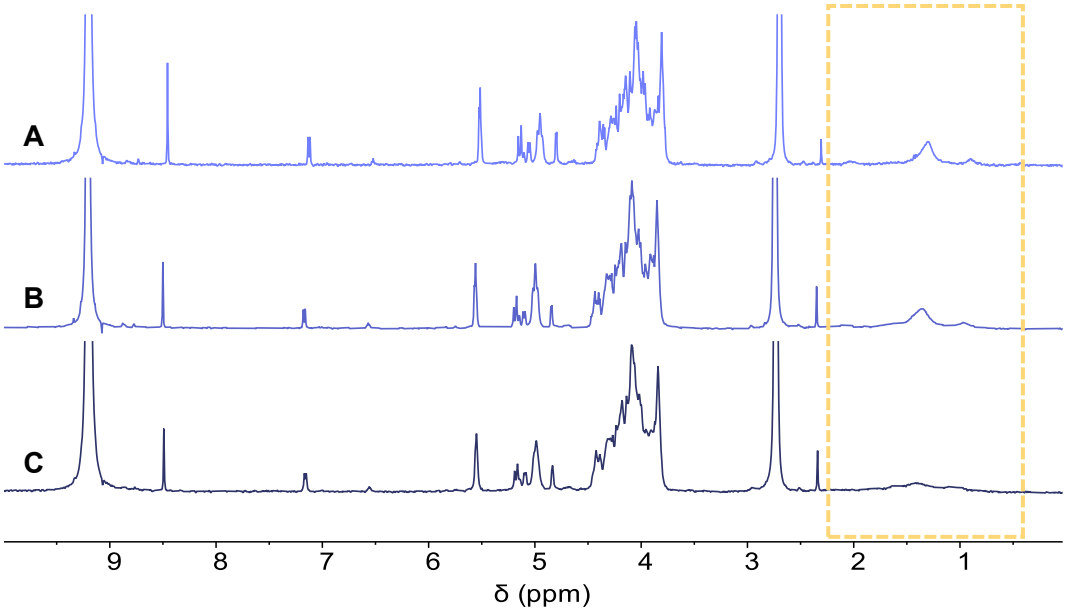

Figure 3.23. Comparative ^{1}H-NMR spectra of AF-assisted pulping of crab shells powder (20 wt.% loading) at 150 °C for **A:** 2 h, **B:** 3 h, and **C:** 4 h.

A scalability test was then carried out under the optimised conditions of **Figure 3.23C** (i.e. 20 wt.% of biomass loading, 150 °C, 4 h) by increasing the extraction volume by a factor of 5. Remarkably, no mineral content was detected in the extract, but residual proteins were still observed by ^{1}H-NMR (**Figure 3.24B**) highlighting the challenges associated with extraction efficiency upon scale-up. This led us to conclude that further process optimisations were required. This study, however, was beyond the scope of this work and will be the object of future investigations.

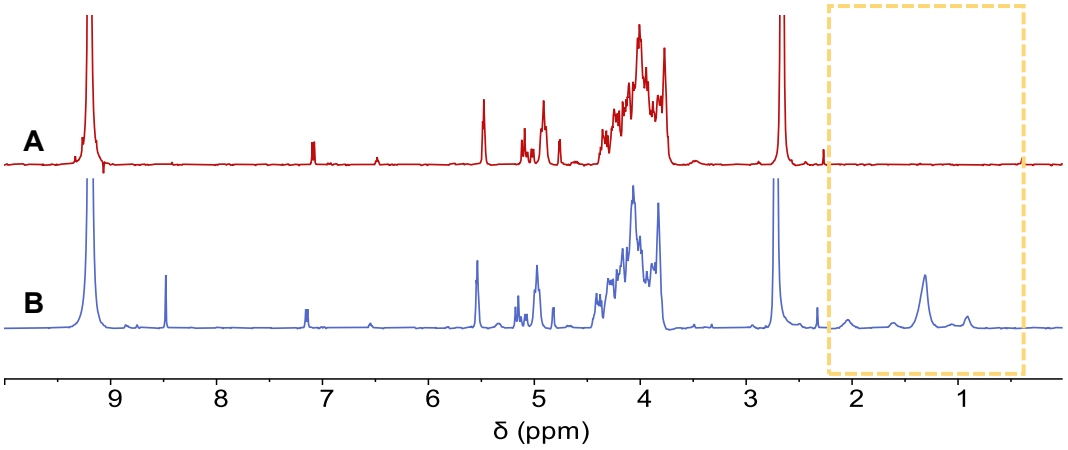

Figure 3.24. Comparative ^{1}H-NMR spectra of **A:** commercial chitin and **B:** scaled-up pulped chitin.

Residual protein content could be estimated also by UV-spectroscopy. Indeed, proteins typically contained in the crab shells absorb in the near-UV region (280 nm) primarily due to their Tyr and Trp content, with minor contributions from Phe and disulfide bonds. UV analyses were carried out on two representative samples from extractions performed: i) at 100 °C for 24 h, and ii) at 150 °C for 4 h, with *in-situ* prepared AF. The results are reported in **Figure 3.25** and confirmed the trend observed by NMR analyses: compared to 100 °C/24h, a clear reduction (by four times) of the protein content was achieved at 150 °C/4h.

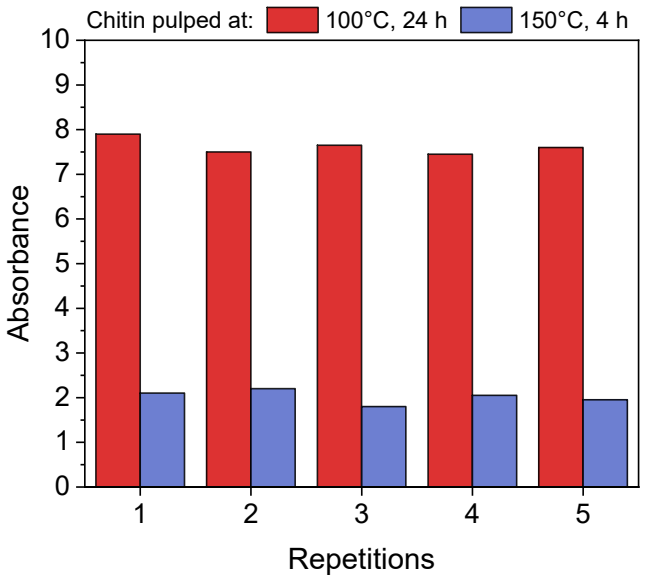

Figure 3.25. Protein estimation by Near UV Absorbance (280 nm) on two representative sample of pulped chitin at different conditions. More details are discussed in the Experimental Section.

Further characterisation of the pulped chitin

Molecular weight

The MW distribution of the pulped chitin was evaluated for 6 different samples obtained by the procedure 2 carried out at different temperatures (100 and 150 °C), pulping times (2–24 h), and a biomass loading of 20wt%. Each sample was dissolved in a 5% LiCl/NMP (*N*-methyl-2-pyrrolidone) solution,[93] and analysed by GPC, using polystyrene as internal standard (more details are discussed in the Experimental Section). MW and polydispersity are reported in **Table 3.4** while GPC curves are reported in the Appendix Section.

Table 3.4. Study of the AF-assisted pulping procedure performed at 150 °C for 2, 3, and 4 h, with a biomass loading of 20 wt.% crab shells powder.

Entry	t (h)	T (°C)	Wt.% loading	MW (g/mol)*10^5	PD
1	24	100	5	11.9	2.2
2	24	100	10	11.4	2.5
3	24	100	20	11.4	2.3
4	2	150	20	6.7	2.0
5	3	150	20	4.3	1.7
6	4	150	20	5.1	1.9
7	Commercial chitin			5.9	2.3

Compared to commercial chitin (entry 7), samples extracted at 100 °C for 24 h exhibited a nearly double MW regardless of the ionic liquid/substrate ratio (entries 1–3), potentially indicating reduced hydrolysis under these conditions. Polydispersity was similarly high for both commercial and pulped chitin, though in the first case it was due to a broad yet symmetrical molecular weight distribution, while for the latter an additional high molecular weight component was observed. This feature was attributed to the presence of protein residues still anchored to the chitin fibres extracted through the pulping process at 100 °C (as shown in **Figure 3.22**), and it reflected the milder (extraction/deproteinisation) action of these ionic liquids compared to the conventionally used acids and bases.[77,92] Pulping at 150 °C for 2–4 h reduced the MW of the extracts closer to the value of commercial chitin, and

resulted in complete deproteinisation, as indicated by a symmetrical distribution with polydispersity (PD) narrower than that of commercial chitin (entries 4–6).

This outcome may suggest that the ionic liquid-assisted pulping enabled an extraction of chitin with completely unaltered mechanical properties and good processability, thus establishing itself as a competitive alternative to the conventional routes for chitin isolation. Overall, the higher temperature revealed necessary to sustain the energy requirement to reach a complete deproteinisation, yet preserving a degree of polymerisation comparable to the one achieved through strong acid/base treatment. The resulting chitin displayed good MW and a narrower PD, further supporting the reliability, the reproducibility, and the efficacy of this pulping process.

Scanning Electron Microscopy

The morphology of chitin extracted under the optimised conditions (crab shells powder loading 20 wt.%, 150 °C, 4 h) was investigated by SEM. **Figure 3.26** below compares SEM images of Spider crab shell powder (**A-B**), commercial chitin (**C-D**), chemically extracted chitin (**E-F**), and chitin extracted through the AF-assisted pulping (**G-H**).

The differences between the samples are evident: the Spider crab shells showed a compact texture sealed with proteins and carbonate, while in the commercial chitin from shrimp shells and in the conventionally extracted chitin from ground crab shell deproteinisation and demineralisation revealed a porous network of chitin fibres, with few or no surface granules. Finally, the ionic liquid-pulped chitin displayed a highly fibrous morphology with loose and separated fibres, confirming the effectiveness of the pulping procedure, but also highlighting the unique effect of the ionic liquid-assisted extraction, which avoided fibre hornification. The ionic liquid-treatment was likely less aggressive than other methods and helped to preserve the native morphology of the biopolymer, improving its processability towards new materials. Such results are promising also in view of further functionalisation of the extracts (for example, via deacetylation to obtain chitosan), that could be favoured by a better diffusion of the reactants inside the fibrous network.[94,95]

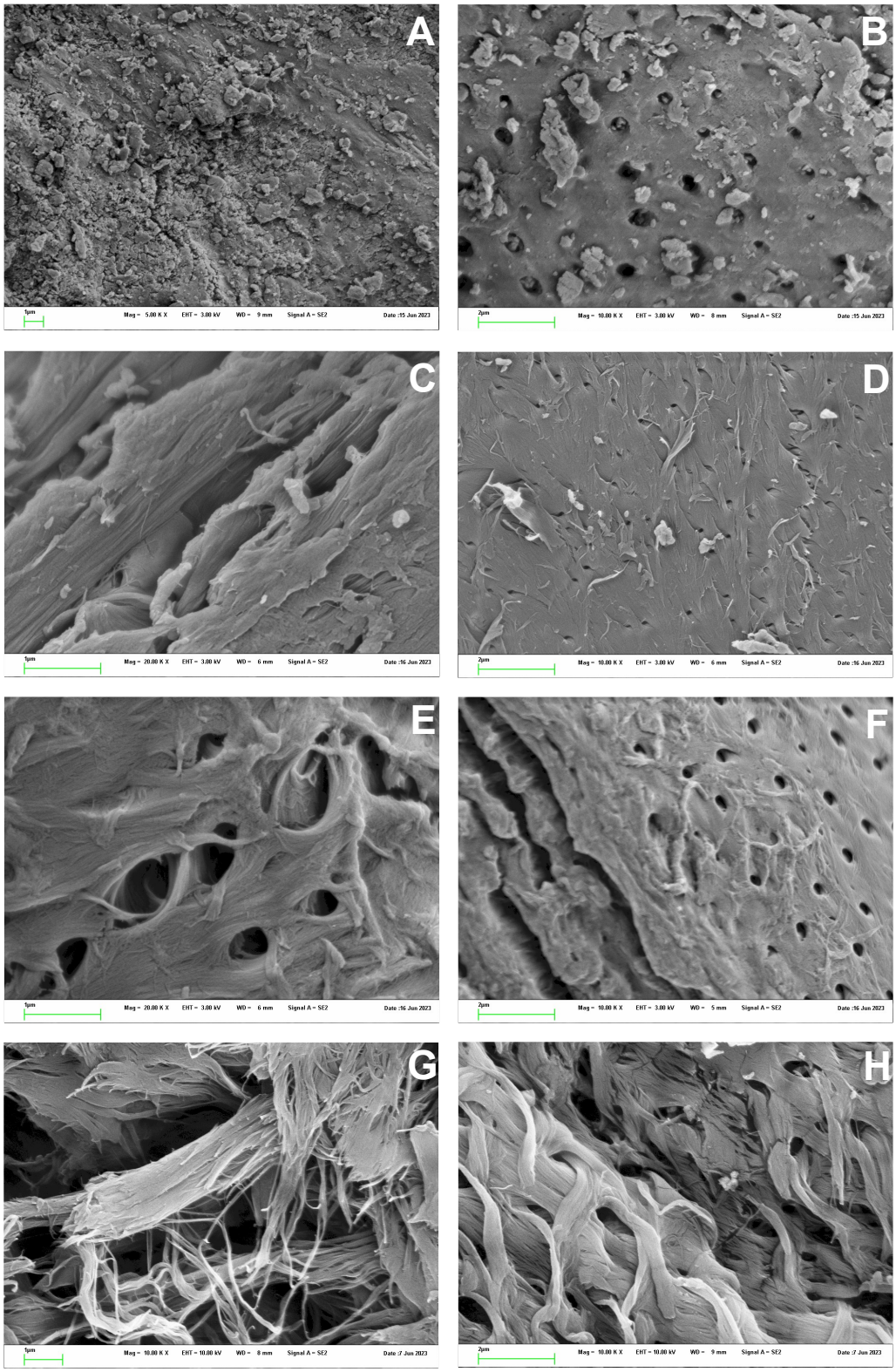

Figure 3.26. SEM images of **A-B**: Spider crab shells powder; **C-D**: commercial chitin; **E-F**: conventionally extracted chitin; **G-H**: chitin extracted through the AF-assisted pulping at 150 °C for 4 h. Magnification, **A**: 5.00 K; **B**, **D**, **G**, **F**, **H**: 10.00 K; **C**,**E**: 20.00 K.

Insights into the effect of formic acid on the chitin arrangement

Pulping tests demonstrated that AF was the most efficient agent for the extraction of chitin from crab shells. However, ^{1}H-NMR spectra of the samples obtained by the AF-assisted treatment, particularly when formic acid was used via Strategies 2 and 3, always displayed an additional signal at 8.4 ppm (as shown in **Figure 3.27A**) which was consistent with the resonance typically associated to the singlet peak of an aldehydic moiety (–CHO).[96] Interestingly, this signal persisted even after neutralisation with NaOH 1 M (**Figure 3.27B**), suggesting either the entrapment of ammonium formate within the polysaccharide network or the interaction between chitin's free $–NH_2$ or secondary –OH groups with formic acid generated by partial degradation of AF at T > 120 °C.[97]

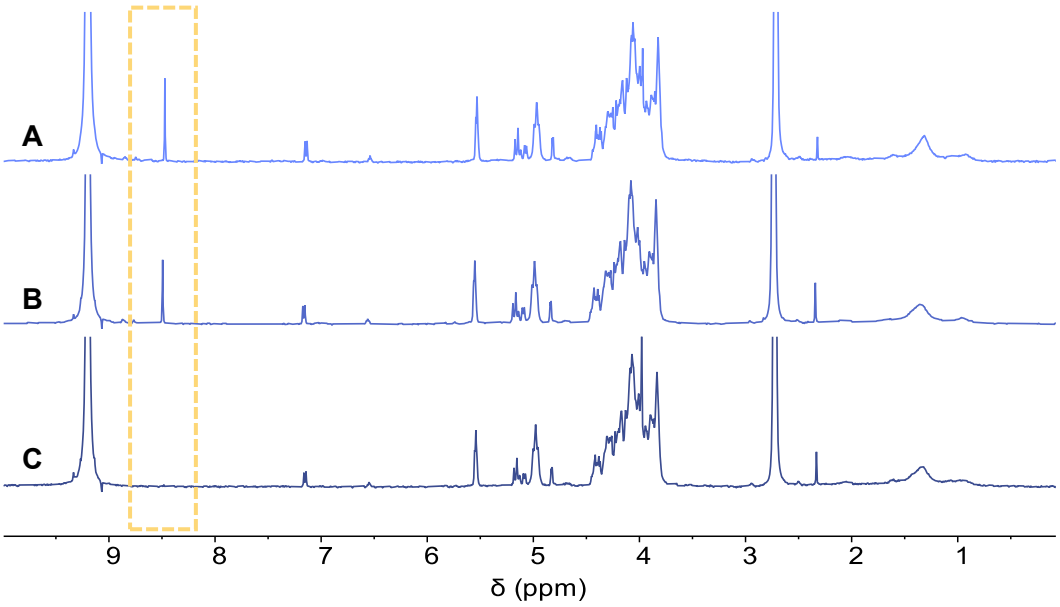

Figure 3.27. Comparative ^{1}H-NMR spectra of **A:** chitin pulped through the AF-assisted treatment, **B:** chitin after neutralisation with NaOH 1 M; **C**: chitin pulped replacing HCO_2H with DCO_2H in the AF-assisted method.

To probe this hypothesis, the AF-assisted pulping of crab shells powder (10 wt.% loading) was performed using deuterated formic acid (DCO_2H) at 150 °C for 4 h. Under these conditions, the 8.4 ppm signal was absent in the ^{1}H-NMR spectrum of the chitin sample (**Figure 3.27C**), supporting the presence of a strong interaction between pulped chitin and formic acid. While the formation of covalently bound formyl species, such as formate esters or formamides, cannot be excluded, the available spectroscopic data do not allow precise discrimination of the nature of this interaction.

Sustainability assessment of the ionic liquid-assisted pulping

The sustainability of the here proposed pulping method was evaluated using the unified metrics toolkit proposed by Clark and coworkers within the CHEM21 project.[98] Although originally designed to compare the greenness of chemical reactions, the metrics used by CHEM21 provided a benchmark to monitor the green credentials of the extraction protocol at least within the limits of the zero/first pass analysis that characterises the structure of the metrics toolkit. Particularly, the parameters that were taken into consideration, included the extraction yield (Y), the process mass intensity (PMI), the impact of the workup techniques, the energy use (E), and H-statements to identify chemicals (reagents and solvents) of concern (health and safety). This analysis compared the extraction of chitin carried out by the AF-assisted protocol to the conventional extraction process (CEP), with results reported in **Table 3.5**. The output of the CHEM21 metric toolkit (CMT) are green, amber or red indicators that mark acceptability of a given variable, with green as "preferred", amber as "acceptable/some issues" and red as "undesirable".

Table 3.5. Evaluation of chitin extraction processes from Spider crab shells using CHEM21 metrics toolkit.

Entry	Procedure	Y (%)[b]	PMI (g/g)[c]	Steps	Work-up[f]		E (T/°C)	Health and Safety
1	Conventional (CEP)	85	241	Step 1: DM[d]	Neutralis.	Centrif.	25	HCl: H290, H314, H318, H335
				Step 2: DP[e]	Neutralis.	Centrif.	70	NaOH: H290, H314, H318, H402
2	AF-assisted protocol[a]	90	29	Single step	Aqueous washing	Centrif.	100	AF
							150	

[a] Chitin extraction AF-assisted carried out under optimised conditions described in this work.
[b] Yield of extracted chitin based on the maximum amount of chitin (20 wt.%) on the dry biomass used as a feedstock.
[c] Process Mass Intensity.
[d] DM: demineralisation.
[e] DP: deproteinisation.
[f] Before centrifugation, neutralisation or washing with fresh water of the extracted chitin were necessary. These operations were considered as equivalent to a quenching into water.[98]

The CEP and the AF-assisted protocol provided a comparable 85-90% yield of chitin, based on the theoretical amount of chitin (20 wt.%) present within the dry biomass used as a feedstock. Such a yield (≤ 90%) ranked both procedures with an amber flag. The evaluation of the workup techniques and of the H-statements of the reagents did not discriminate

between the two methods of chitin extraction: both ranked one amber and two green flags, respectively. However, the AF-assisted protocol is a single step, which was remarkably more advantageous in terms of step economy and process intensification compared to the two-step CEP.[98]

While this ranking effectively mitigated the environmental burden of the pulping, nonetheless it was partly offset by the higher energy demand of the method that, especially when carried out at 150 °C (E: red flag), was out of the acceptable standard temperatures defined by the CHEM21 toolkit. The most striking difference between the two extraction procedures emerged from the comparison of one of the most important metrics that measures all mass-based inputs: the process mass intensity (PMI), defined as the ratio between the total mass used in a process and the mass of the desired product.

$$\boldsymbol{PMI}\ (Process\ Mass\ Intensity) = \frac{total\ mass\ in\ a\ process\ step}{mass\ of\ product}$$

Thanks to a more efficient and reduced use of reagents, the AF-assisted protocol achieved a >8 times lower PMI than CEP (details on the calculation are shown in **Table 3.6** below). This result contributed the competitiveness of the AF-assisted pulping compared to CEP and pointed the way for its future optimisation.

Table 3.6. Evaluation of the Process Mass Intensity for the AF-assisted protocol.

Entry	Batch of waste (g)	Y (%)	Extraction pulping step		Work-up	PMI (g/g)[a]	
			Acid (g)	Base (g)	Water (g)	Including H_2O	Excluding H_2O
1	2.5	17	7.5	2.5	250	600	29
2	500	17	1500	500	50,000	617	29

[a] PMI was evaluated with both the inclusion and the exclusion of water in analogy to the concept of simplified and complete E-factor.

Finally, a rough techno-economic analysis based on the standard costs of energy (in Italy) and research-grade reagents supplied by Merck and used in this work, was carried out to estimate the cost of chitin pulped from crab shells (**Table 3.7**). Scaling up the AF-assisted

pulping protocol from 2.5 g to 500 g of crab shell waste under otherwise identical conditions would lead to a substantial decrease in the estimated production cost, from 1208 €/kg to approximately 205 €/kg. This value represents a worst-case-scenario estimate and therefore reflects a laboratory-scale operation (and the cost of research-grade reagents supplied by Merck) rather than an optimised industrial process. Accordingly, the real overall cost of the pulping would be much lower by optimising both the utilisation of reagents and solvents through their sourcing via more cost-effective suppliers for bulk orders and the scaleup of the protocol. Additionally, enhancing the market acceptance of ionic liquid-assisted pulping technology would further contribute to cost reduction.

Notably, the chitin obtained under these conditions exhibited a molecular weight of 5.1•105 g/mol and a DA >94% that placed it on par with Merck commercial samples (MW = 5.9•105 g/mol and DA = 94%), with a catalogue price of more than 700 €/Kg (research grade, verified on www.sigmaaldrich.com in December 2025). By contrast, the actual procurement costs of bulk chitin at industrial levels are typically much lower often ranging between 50-100 €/Kg for large-volume orders, depending on purity and supplier, and therefore more competitive.

Table 3.7. Techno-economic analysis of chitin extraction from crab shells by the AF-assisted protocol [a].

Entry	Waste (g)	Y (%)	Energy [b]			t (h)	Reagents [b]				Estim. cost (€/Kg)[d]
			Peak adsorp. (W)	Consum. (kWh)	Cost (€/kWh)		NH_3		HCO_2H		
							g	€	g	€	
1	2.5	17	650	2.8	0.025[c]	4	2.5	0.074	7.5	0.44	1208
2	500	17					500	14.70	1500	87.98	205

[a] Chitin extraction AF-assisted carried out under optimised conditions described in this work.
[b] Standard costs of energy (in Italy) and research-grade reagents supplied by Merck.
[c] https://luce-gas.it/business/offerte/costo-kwh-aziende.
[d] Estimated cost per kilo of product (extracted chitin).

It should be noted here that the treatment of 0.5 kg of biowaste (crab shells, entry 2) was not carried out in this work. Moreover, our preliminary investigation of the scale-up of the method, from 0.5 to 2.5 g, indicated that further studies were necessary to improve the deproteinisation step. Within these limits, the cost of the product (chitin) should be intended as an expected value, subject to experimental validation.

3.2.3 Conclusions

In conclusion, a sustainable and cost-effective one-pot method for the extraction of chitin from Spider crab shells was developed using easily available, affordable and non-hazardous ionic liquids. Among the strategies tested (using the ionic liquid as a solid salt or by *in-situ* preparation), *in-situ* prepared ammonium formate (AF) exhibited the best performance, enabling quantitative isolation (17–20% yield) of highly pure chitin with degree of acetylation (DA) > 94%. AF resulted to be highly efficient in mineral removal, leading to a complete dissolution of all inorganic salts (confirmed via TGA, ICP-OES and FT-IR analyses) present in the starting material within 2 h of treatment at 100 °C. A complete parametric analysis was carried out to optimise the deproteinisation step, achieving the best results at 150 °C for 4 h of treatment with complete protein removal. Noticeably, the process produced chitin with high MW and narrow PD, paving the way towards an innovative, economically effective and greener alternative to conventional acid/base extraction, with improved reproducibility, scalability, and reduced environmental impact.

The growing interest in valorising fishery by-products and especially crab shells as a source of chitin, goes well beyond simple waste management. SEM analyses of extracts produced in this work revealed that, once proteins and minerals are removed, the resulting chitin structure displays a highly organised fibrous network with great potential for materials synthesis. Some members of our group have shown that natural chitin framework can be used as an excellent precursor to synthesise supports for anchoring metal nanoparticles, in particular, nitrogen-doped carbon-based materials for the preparation of Ni-, Fe-, Co- and Mo-based catalysts capable of highly controlling the selectivity of alcohol oxidation reactions, with the Mo-N/C material showing best performance in promoting the partial oxidation of benzyl alcohol to benzaldehyde.[99]

As mentioned earlier, both fishery waste and purified chitin have found valuable uses in the development of advanced materials. A further example of this approach will be presented in Chapter 4 as well, where chitin and Australian Spanner crab shells are explored as starting materials for the synthesis of additives for zinc batteries.

3.2.4 Experimental Section

All reagents and solvents were used without further purification. Commercial chitin from shrimp shells, NaOH, HCl, 50 wt.% NH_2OH solution, acetic acid, 30–33 wt.% NH_3 solution, formic acid, ammonium formate (solid salt), ammonium acetate (solid salt) and KBr were ACS grade, and all purchased from Sigma-Aldrich. Spider crab shells were obtained from a local restaurant in Venice, gently washed with a detergent solution, ground to powder, sieved into three different meshes (20, 60 and ≥ 150), and finally stored in glass sample vials at room temperature until use.

Crab shells composition

Ash content was determined using the standard test method (ASTM E1755-01) for determining ash in biomass by dry oxidation. 1.00 g of dried crab shells powder (oven-dried overnight at 105 °C and cooled in a desiccator prior to weighing) was weighed in a ceramic crucible and placed into a preheated muffle furnace at 600 °C for 3 h. The crucible was removed, cooled to room temperature in a desiccator and weighed. The sample was then returned to the furnace and heated at 600 °C for 1.0 h, cooled in the desiccator and re-weighed, repeating these three last steps until the change in crucible mass between consecutive weighing was ≤ 0.3 mg, at which point the weight was considered constant and recorded as the ash mass. The ash content (wt.%) was calculated relative to the oven-dried sample weight using **Equation (1)**, where m_{Ash} is the final weight of ash and crucible (g), $m_{crucible}$ is, unsurprisingly, the weight of crucible (g), and $m_{dry\ sample}$ is the weight of the dry crab shell powder (g) before the treatment:

$$\text{Ashes (wt.\%)} = \left(\frac{m_{Ash} - m_{crucible}}{m_{dry\ sample}}\right) * 100 \qquad \textbf{(1)}$$

Protein content was determined by chemical deproteinisation of the crab shells through an alkali treatment. 0.50 g of crab shells powder was suspended in 20 mL of 1 M NaOH solution and heated at 70 °C for 3 h under stirring. The solid residue was centrifuged at 6000 rpm for 10 min, then washed with 50 mL of water for 5 times until neutral pH was reached, and finally oven-dried at 60 °C under vacuum (15 mbar) overnight. Protein percentage was calculated relative to the crab shells dry weight using **Equation (2)**, where $m_{residue}$ is the dry weight of the deproteinised residue, and $m_{biomass}$ refers to the weight of the dry crab shell powder.

$$\text{Proteins (wt.\%)} = 100 - \left(\frac{m_{residue}}{m_{biomass}} * 100\right) \qquad \textbf{(2)}$$

Chitin percentage was estimated by employing the conventional stepwise chitin extraction protocol described below.

Conventional stepwise chitin extraction protocol

In a typical procedure, a powdered sample (1.00 g) of Spider crab shells powder was suspended in 40 mL of HCl 0.5 M and stirred at room temperature for 15 min. The residual solid was centrifuged at 6000 rpm for 10 min, then washed with 50 mL of water for 5 times until neutral pH was reached, and the resulting solid was oven-dried at 60 °C under vacuum (15 mbar) overnight. The so demineralised residue was then suspended in NaOH 1 M (20 mL of solution per g of solid residue) and heated at 70 °C for 3 h under continuous stirring. The resulting mixture was centrifuged at 6000 rpm for 10 min, washed with 50 mL of water for 5 times until neutral pH was reached, and oven-dried at 60 °C under vacuum (15 mbar) overnight, to obtain a white solid as the final product (0.169 g, yield 17%).

Synthesis of hydroxylammonium acetate (HA)

Hydroxylammonium acetate (HA) was synthesised according to a procedure reported in literature (Shamshina et al., 2016).

A 50 wt.% NH_2OH solution (26.42 g, 0.4 mol) was stirred at 0 °C under N_2 atmosphere in a 250 mL round-bottom flask, while acetic acid (26.4 g, 0.44 mol) was added dropwise over 3 h, then it was allowed to reach room temperature overnight under continuous stirring. The solution was gently purged with air and concentrated by heating at 40 °C. The resulting precipitate was washed with methanol (100 mL) and diethyl ether (100 mL) to remove residual acetic acid and then dried under reduced pressure (15 mbar) for 2 h. The final product was obtained as a white solid (11.9 g, yield 32%) and was characterised by ^{1}H- and ^{13}C-NMR spectroscopy (using DMSO-*d*6 or D_2O as solvent, see Appendix Section), with a Bruker NMR spectrometer Ascend 400 (AV400), operating at 400 MHz for ^{1}H nuclei and 100 MHz for ^{13}C at ambient temperature (298 K).

Pulping of crab shells using ionic liquid as solid salt (Strategy 1)

0.5 g of crab shells powder were mixed with the selected neat solid ionic liquid (AA, AF or HA; 4.5 g each) in a round-bottom flask equipped with a condenser. The suspension was stirred at 130 °C for 2 h. After complete melting of the ionic liquid, vigorous bubbling/foaming could be observed. A yellowish solid precipitated after 2 h, while impurities were confined in the aqueous phase. The mixture was diluted with 50 mL of deionised water and centrifuged, then the solid residue was washed with 50 mL of water for 5 times until neutral pH was reached, and finally oven-dried under reduced pressure (15 mbar) overnight. The final product was obtained as a pale yellow-white solid.

Pulping of Spider crab shells using in-situ generated ionic liquids (Strategies 2 and 3)

0.5 g of crab shells powder were placed in a two-neck round-bottom flask equipped with a condenser. Acetic acid or formic acid (60 mmol each) was added, followed by dropwise addition of an aqueous base (ammonia or hydroxylamine, 60 mmol each) in the case of strategy 2; otherwise, the aqueous base was added first to the shells powder, followed by the dropwise addition of acid in the case of Strategy 3. The mixture was then heated at 100 °C for 2 h under stirring. Purification and isolation were performed as described in the pulping procedure carried out with ionic liquids as solid salts.

Pulping of Spider crab shells using in-situ generated ionic liquids at increased temperature

The selected amount of crab shells powder was placed in a two-neck round-bottom flask equipped with a condenser. Acetic acid or formic acid (60 mmol each) was added, followed by dropwise addition of aqueous ammonia (60 mmol), following Strategy 2. The mixture was stirred for 0.5 h at room temperature until foaming ceased, then placed into a stainless-steel autoclave equipped with a Teflon reactor and heated at 150 °C for the selected pulping time under stirring. The autoclave was then cooled to room temperature. Purification and isolation were performed as described in the pulping procedure carried out with ionic liquids as solid salts. A biomass loading of 10 wt.% relative to the total mass of mixture (ionic liquid + biomass) was employed in all experiments.

Characterisation of extracted chitin

For FT-IR (Fourier-transform infrared spectroscopy) analyses, dry powdered chitin samples (1 mg) were blended with KBr salt (100 mg) and pressed into 5 mm pellets using a hydraulic press (10 tons) for 1 min. All spectra were recorded on a Perkin-Elmer Spectrum One FT-IR spectrometer in the middle infrared region (4000–450 cm^{-1}) with a resolution of 4 cm^{-1} in the absorbance mode, for 16 scans at room temperature.

For ^{1}H-NMR analyses, chitin samples were treated under standardised conditions: 15 mg of powder were dissolved in 1 mL of deuterium chloride solution (35 wt.% DCl in D_2O) under vigorous stirring at 50 °C for 30 min, then analysed within a maximum of 10-15 minutes. ^{1}H-NMR spectra were recorded using a Bruker UltraShield 300 operating at 300 MHz at ambient temperature (298 K) for 64 scans and a 20-ppm spectral window. The degree of acetylation (DA) was calculated from the NMR spectra using two different methods:

i) basing on the integrals of H-1 and H-2 signals, with **Equation (3)**;[86]
ii) based on the area of the H-2 of the glucosamine (GlcN) units and of the acetyl protons of *N*-acetyl glucosamine (GlcNAc) units, with **Equation (4)**.[100]

Minimal deacetylation occurred during dissolution of all samples in the deuterated solvent, as indicated by slight increases in acetic acid and H-2 proton signals, however, not resulting in a change in the results of the calculated DA.

$$DA\% = \frac{(I_{\alpha H1A}+I_{\beta H1D+H1D}+I_{H1A})-I_{H2D}}{I_{\alpha H1A}+I_{\beta H1D+H1D}+I_{H1A}} * 100 \qquad \textbf{(3)}$$

$$DA\% = \frac{\left(\frac{1}{3}A_{CH3}\right)}{\frac{1}{3}A_{CH3}+A_{GlcN}} * 100 \qquad \textbf{(4)}$$

Chitin signals (see also **Figure 3.29**): ^{1}H-NMR (300 MHz, 35 wt.% DCl in D_2O, 298 K) δ (ppm): 6.94 (d, H-1*), 5.33 (br, α-H1A), 4.95–4.98 (br, β-H1A + H1D), 4.87–4.88 (d, H-2*), 4.77 (br, H1A), 4.61 (d, H-3*), 3.5–4.3 (m, H2/H6), 2.53 (s, H-Acetyl), 2.13 (s, H-acetic acid). Signals marked with an asterisk correspond to the glucofuranosyl oxazolinium ion, which exists in equilibrium with GlcNAc in concentrated DCl.

Thermogravimetric analyses (TGA) were carried out in a TA instruments SDT 2960. Approximately 5 mg of each sample were heated in an alumina crucible from room temperature to 800 °C at 10 °C/min under N_2 flow (20 mL/min).

Inductive Coupled Plasma-Optical Emission Spectroscopy (ICP-OES) measurements were performed on a Perkin Elmer ICP-OES 5300 DV. All chitin samples were digested in nitric acid (3 mL) and hydrochloric acid (2 mL), dilute to a final volume of 10 mL, and heated at 150 °C for 20 min to ensure complete dissolution.

X-Ray Diffractometry (XRD) measurements were carried out on a Philips diffractometer with a PW 1319 goniometer (Bragg-Brentano geometry), equipped with a focusing graphite monochromator and a proportional counter with a pulse-height discriminator. Nickel-filtered CuKα radiation was used with a step size of 0.05° in 2θ and a collection time of 30 s per step. Background subtraction and peak deconvolution allowed separation of crystalline and amorphous domains for accurate determination of the crystallinity index (CI) of the chitin samples, which was calculated using **Equation (5)**, where I_0 is total intensity of the corrected diffractogram after subtraction of the parasitic background, I_{cr} is the crystalline scattering intensity, F_{cr} is the crystalline scattering area, and F_{am} is the amorphous scattering area:[101]

$$CI = \int I_{cr}\, d\theta \;\; / \int I_0\, d\theta = F_{cr} \,/\, (F_{cr} + F_{am}) \qquad \textbf{(5)}$$

Molecular weights of commercial and pulped chitin were determined by Gel Permeation Chromatography (GPC). For each analysis, 5 mg of chitin were dissolved in 5% LiCl/NMP (1 mg/mL) under stirring at room temperature, then filtered through a 0.45 µm syringe filter. GPC analyses were carried out on a GPC-Agilent/PSS 1260 Iso Pump instrument by using a PSS-gram-100 and a PSS-gram-1000 column in series, after a PSS-gram-precolumn. Elution was performed with 5% LiCl-NMP (flow rate of 0.5 mL/min, injection volume of 100 µL, temperature of 70 °C, measuring time of 60 min) and PSS SECcurity-UV-300 nm-1260 VWD and PSS SECcurity-RI-1260 RID were used as detectors. Calibration curves of log (Da) from retention time were built by consequently measuring a sequence of PS (Polystyrene) internal standards with molecular weight ranging from 1306 to 2,520,000 Da.

Protein estimation by Near UV Absorbance (280 nm)

Two representative dried chitin samples (50 mg each) were suspended in 20 mL of NaOH 1.25 M and heated at 100 °C for 2 h. After cooling down to room temperature, the mixtures were centrifuged, and several aliquots of the supernatant were collected and stored in the refrigerator (~4 °C) for protein determination. The absorbance of the samples at 280 nm was measured using the Eppendorf Bio-Spectrometer® basic, repeated for 4 times.

Exemplificative determination of the degree of acetylation (DA) on commercial chitin

Three representative samples (15 mg each) of commercial chitin were treated in 35 wt.% DCl in D_2O under vigorous stirring at 50 °C for 10, 20 and 30 minutes, respectively. The so obtained solutions were then analysed through ^{1}H-NMR spectroscopy to determine the degree of acetylation (DA) basing on the resonance of the characteristic protons according to **Equation (3)**, here used as an exemplificative model of calculation. All spectra (reported in **Figure 3.28** below with integrated signals) were recorder after a maximum of 10-15 minutes from the end of the dissolution treatment.

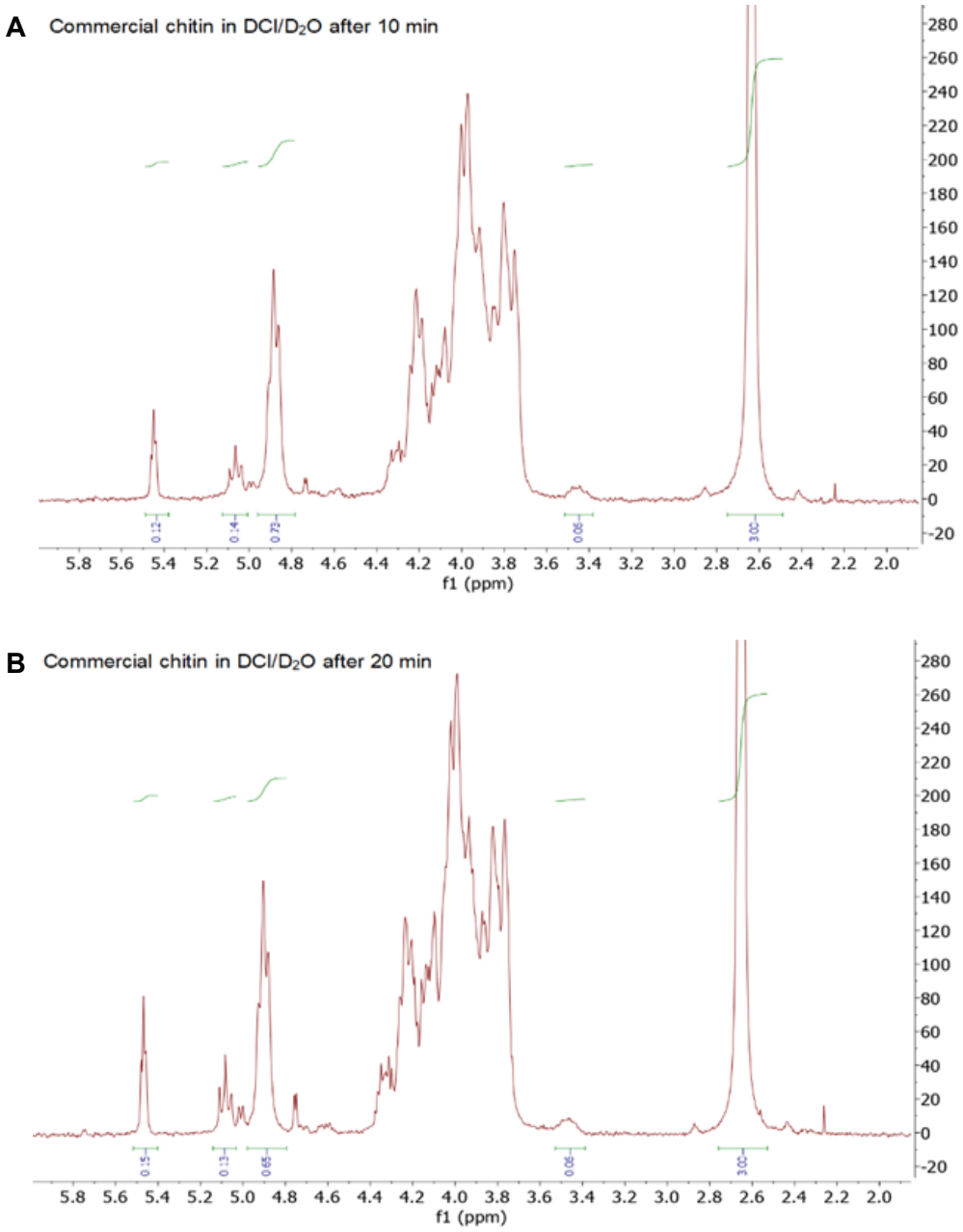

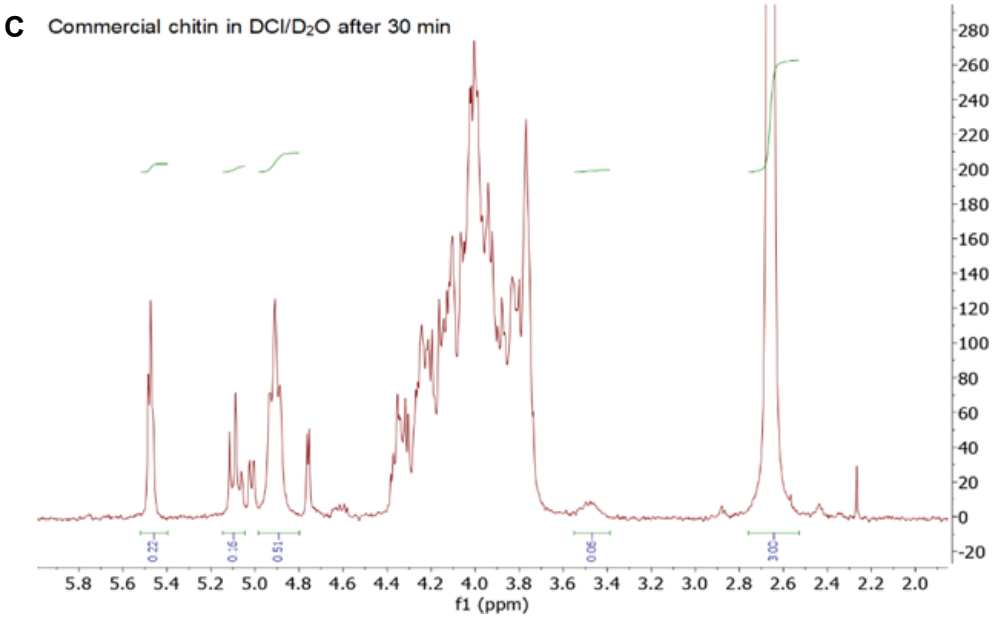

Figure 3.28A-C. Comparative ^{1}H-NMR spectra of commercial chitin treated in deuterium chloride solution (35 wt.% DCl in D_2O) under vigorous stirring at 50 °C for **A:** 10 min, **B:** 20 min, **C:** 30 min.

DA values of 94, 94 and 93% were calculated for the three samples of commercial chitin treated under the above-described conditions for 10, 20 and 30 minutes, respectively. Despite the hydrolysis of the glycosidic bonds clearly occurring during the dissolution treatment, the DA does not remarkably change, demonstrating that the deacetylation process requires different conditions to take place consistently. It is also worth noting that a slight underestimation of the DA could instead happen under these conditions.

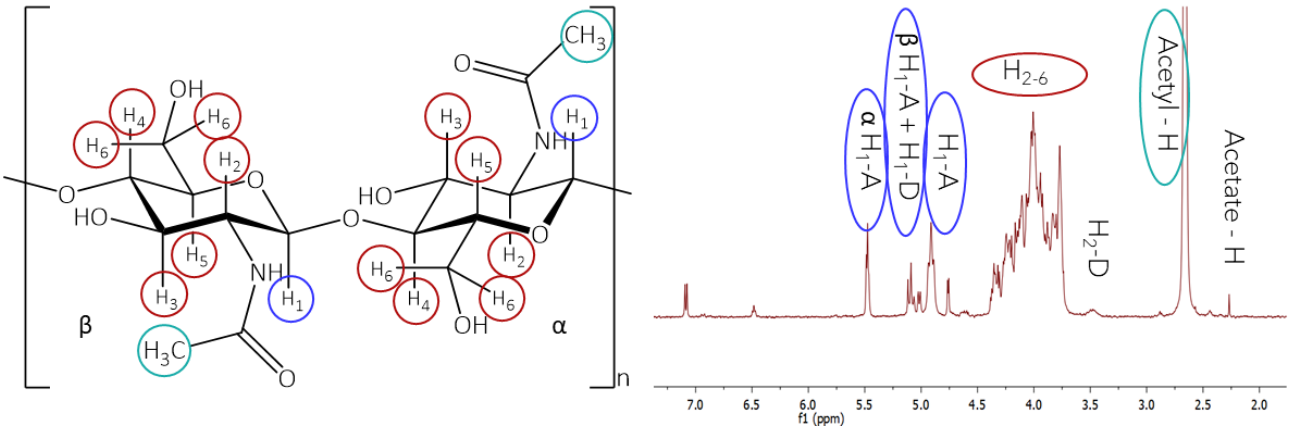

Figure 3.29. ^{1}H-NMR peaks assignment of a commercial chitin sample.

Bibliography

1. *Biomass Valorization*. (Springer Nature Singapore, Singapore, 2024). doi:10.1007/978-981-97-8557-5.

2. Carmona-Cabello, M., Garcia, I. L., Leiva-Candia, D. & Dorado, M. P. Valorization of food waste based on its composition through the concept of biorefinery. *Curr. Opin. Green Sustain. Chem.* **14**, 67–79 (2018).

3. United Nations Environment Programme. *Food Waste Index Report 2021*. https://www.unep.org/resources/report/unep-food-waste-index-report-2021 (2021).

4. Wilson, D. C., Paul, J., Ramola, A. & Filho, C. S. Unlocking the significant worldwide potential of better waste and resource management for climate mitigation: with particular focus on the Global South. *Waste Manag. Res. J. a Sustain. Circ. Econ.* **42**, 860–872 (2024).

5. United Nations Environment Programme. *Global Waste Management Outlook 2024 - Beyond an Age of Waste: Turning Rubbish into a Resource*. (United Nations Environment Programme, 2024). doi:10.59117/20.500.11822/44939.

6. Espro, C. *et al.* Sustainable production of pharmaceutical, nutraceutical and bioactive compounds from biomass and waste. *Chem. Soc. Rev.* **50**, 11191–11207 (2021).

7. Maschmeyer, T., Luque, R. & Selva, M. Upgrading of marine (fish and crustaceans) biowaste for high added-value molecules and bio(nano)-materials. *Chem. Soc. Rev.* **49**, 4527–4563 (2020).

8. Coppola, D. *et al.* Fish Waste: From Problem to Valuable Resource. *Mar. Drugs* **19**, 116 (2021).

9. Calder, P. C. Omega-3 Fatty Acids and Inflammatory Processes. *Nutrients* **2**, 355–374 (2010).

10. Calder, P. C. & Yaqoob, P. Understanding Omega-3 Polyunsaturated Fatty Acids. *Postgrad. Med.* **121**, 148–157 (2009).

11. Aksun Tümerkan, E. T. Sustainable utilization of gelatin from animal-based agri–food waste for the food industry and pharmacology. in *Valorization of Agri-Food Wastes and By-Products* 425–442 (Elsevier, 2021). doi:10.1016/B978-0-12-824044-1.00041-6.

12. Rajabimashhadi, Z., Gallo, N., Salvatore, L. & Lionetto, F. Collagen Derived from Fish Industry Waste: Progresses and Challenges. *Polymers (Basel).* **15**, 544 (2023).

13. Yadav, M. *et al.* Seafood waste: a source for preparation of commercially employable chitin/chitosan materials. *Bioresour. Bioprocess.* **6**, 8 (2019).

14. Zhang, J., Akyol, Ç. & Meers, E. Nutrient recovery and recycling from fishery waste and by-products. *J. Environ. Manage.* **348**, 119266 (2023).

15. Charles Hatchett. XVIII. Experiments and observations on shell and bone. *Philos. Trans. R. Soc. London* **89**, 315–334 (1799).

16. Meng, L., Xie, F., Zhang, B., Wang, D. K. & Yu, L. Natural Biopolymer Alloys with Superior Mechanical Properties. *ACS Sustain. Chem. Eng.* **7**, 2792–2802 (2019).

17. Lucas, N. & Rode, C. V. Marine waste derived chitin biopolymer for N-containing supports, catalysts and chemicals. *Tetrahedron Green Chem* **2**, 100013 (2023).

18. Mehrabani, M. G. *et al.* Chitin/silk fibroin/TiO2 bio-nanocomposite as a biocompatible wound dressing bandage with strong antimicrobial activity. *Int. J. Biol. Macromol.* **116**, 966–976 (2018).

19. Sogias, I. A., Williams, A. C. & Khutoryanskiy, V. V. Why is Chitosan Mucoadhesive? *Biomacromolecules* **9**, 1837–1842 (2008).

20. Da Silva, C. A., Pochard, P., Lee, C. G. & Elias, J. A. Chitin Particles Are Multifaceted Immune Adjuvants. *Am. J. Respir. Crit. Care Med.* **182**, 1482–1491 (2010).

21. Sanina, N. Vaccine Adjuvants Derived from Marine Organisms. *Biomolecules* **9**, 340 (2019).

22. Jayakumar, R. *et al.* Fabrication of chitin–chitosan/nano TiO2-composite scaffolds for tissue engineering applications. *Int. J. Biol. Macromol.* **48**, 336–344 (2011).

23. Narayanan, K. B., Zo, S. M. & Han, S. S. Novel biomimetic chitin-glucan polysaccharide nano/microfibrous fungal-scaffolds for tissue engineering applications. *Int. J. Biol. Macromol.* **149**, 724–731 (2020).

24. Parhi, R. Drug delivery applications of chitin and chitosan: a review. *Environ. Chem. Lett.* **18**, 577–594 (2020).

25. Salah, R. *et al.* Anticancer activity of chemically prepared shrimp low molecular weight chitin evaluation with the human monocyte leukaemia cell line, THP-1. *Int. J. Biol. Macromol.* **52**, 333–339 (2013).

26. Kim, E.-K. *et al.* Chitooligosaccharides induce apoptosis in human myeloid leukemia HL-60 cells. *Bioorg. Med. Chem. Lett.* **22**, 6136–6138 (2012).

27. Gibot, L. *et al.* Anticancer properties of chitosan on human melanoma are cell line dependent. *Int. J. Biol. Macromol.* **72**, 370–379 (2015).

28. Solairaj, D., Rameshthangam, P. & Arunachalam, G. Anticancer activity of silver and copper embedded chitin nanocomposites against human breast cancer (MCF-7) cells. *Int. J. Biol. Macromol.* **105**, 608–619 (2017).

29. Bose, I., Singh, R., Negi, P. & Singh, Y. Chitin as bio-based nanomaterial in packaging: A review. *Mater. Today Proc.* **46**, 11254–11257 (2021).

30. Rouhani Shirvan, A., Shakeri, M. & Bashari, A. Recent advances in application of chitosan and its derivatives in functional finishing of textiles. in *The Impact and Prospects of Green Chemistry for Textile Technology* 107–133 (Elsevier, 2019). doi:10.1016/B978-0-08-102491-1.00005-8.

31. Nicoletti, J. *et al.* Enhanced Piezoelectricity in Sustainable-By-Design Chitosan Nanocomposite Soft Thin Films for Green Sensors. *ACS Nano* **19**, 35322–35332

(2025).

32. You, J., Li, M., Ding, B., Wu, X. & Li, C. Crab Chitin-Based 2D Soft Nanomaterials for Fully Biobased Electric Devices. *Adv. Mater.* **29**, (2017).

33. Polidoro, D. *et al.* Pd-N-doped carbons for chemoselective hydrogenation of cinnamaldehyde: Unravelling the influence of particle size and support in multiphase batch and continuous-flow systems. *Appl. Catal. A Gen.* **685**, 119864 (2024).

34. Roy, J. C. *et al.* Solubility of Chitin: Solvents, Solution Behaviors and Their Related Mechanisms. in *Solubility of Polysaccharides* (InTech, 2017). doi:10.5772/intechopen.71385.

35. Hou, J., Aydemir, B. E. & Dumanli, A. G. Understanding the structural diversity of chitins as a versatile biomaterial. *Philos. Trans. R. Soc. A Math. Phys. Eng. Sci.* **379**, (2021).

36. Sawada, D. *et al.* Water in Crystalline Fibers of Dihydrate β-Chitin Results in Unexpected Absence of Intramolecular Hydrogen Bonding. *PLoS One* **7**, e39376 (2012).

37. Saito, Y., Okano, T., Gaill, F., Chanzy, H. & Putaux, J.-L. Structural data on the intra-crystalline swelling of β-chitin. *Int. J. Biol. Macromol.* **28**, 81–88 (2000).

38. Kaya, M. *et al.* On chemistry of γ-chitin. *Carbohydr. Polym.* **176**, 177–186 (2017).

39. de Oliveira Silva, M. B. & dos Santos Rosa, D. Chitin and Chitosan Based PVC Composites and Nanocomposites. in 117–128 (2024). doi:10.1007/978-3-031-45375-5_5.

40. Raabe, D., Sachs, C. & Romano, P. The crustacean exoskeleton as an example of a structurally and mechanically graded biological nanocomposite material. *Acta Mater.* **53**, 4281–4292 (2005).

41. Díaz-Rojas, E. I. *et al.* Determination of Chitin and Protein Contents During the Isolation of Chitin from Shrimp Waste. *Macromol. Biosci.* **6**, 340–347 (2006).

42. Terkula Iber, B., Azman Kasan, N., Torsabo, D. & Wese Omuwa, J. A Review of Various Sources of Chitin and Chitosan in Nature. *J. Renew. Mater.* **10**, 1097–1123 (2022).

43. Campalani, C. *et al.* Green extraction of chitin from hard spider crab shells. *Carbohydr. Polym.* **345**, 122565 (2024).

44. Rahayu, A. P. *et al.* The impact of the different types of acid solution on the extraction and adsorption performance of chitin from shrimp shell waste. *Int. J. Biol. Macromol.* **194**, 843–850 (2022).

45. Ramírez, M. Á. *et al.* Chitin Preparation by Demineralizing Deproteinized Lobster Shells with CO 2 and a Cationite. *J. Renew. Mater.* **5**, 30–37 (2017).

46. Lv, J. *et al.* Chitin and chitin-based biomaterials: A review of advances in processing and food applications. *Carbohydr. Polym.* **299**, 120142 (2023).

47. Kaur, S. & Dhillon, G. S. Recent trends in biological extraction of chitin from marine shell wastes: a review. *Crit. Rev. Biotechnol.* **35**, 44–61 (2015).

48. Hamdi, M. *et al.* Chitin extraction from blue crab (Portunus segnis) and shrimp (Penaeus kerathurus) shells using digestive alkaline proteases from P. segnis viscera. *Int. J. Biol. Macromol.* **101**, 455–463 (2017).

49. Dayakar, B. *et al.* Application of extreme halophilic archaea as biocatalyst for chitin isolation from shrimp shell waste. *Carbohydr. Polym. Technol. Appl.* **2**, 100093 (2021).

50. Mohan, K. *et al.* Green and eco-friendly approaches for the extraction of chitin and chitosan: A review. *Carbohydr. Polym.* **287**, 119349 (2022).

51. Hamed, I., Özogul, F. & Regenstein, J. M. Industrial applications of crustacean by-products (chitin, chitosan, and chitooligosaccharides): A review. *Trends Food Sci. Technol.* **48**, 40–50 (2016).

52. Li, Z. *et al.* Recent advances in extraction and processing of chitin using deep eutectic solvents. *Chem. Eng. J.* **446**, 136953 (2022).

53. Morais, E. S. *et al.* Use of Ionic Liquids and Deep Eutectic Solvents in Polysaccharides Dissolution and Extraction Processes towards Sustainable Biomass Valorization. *Molecules* **25**, 3652 (2020).

54. Shamshina, J. L. & Berton, P. Use of Ionic Liquids in Chitin Biorefinery: A Systematic Review. *Front. Bioeng. Biotechnol.* **8**, (2020).

55. Abbott, A. P., Capper, G., Davies, D. L., Rasheed, R. K. & Tambyrajah, V. Novel solvent properties of choline chloride/urea mixturesElectronic supplementary information (ESI) available: spectroscopic data. See http://www.rsc.org/suppdata/cc/b2/b210714g/. *Chem. Commun.* 70–71 (2003) doi:10.1039/b210714g.

56. Zhu, P., Gu, Z., Hong, S. & Lian, H. One-pot production of chitin with high purity from lobster shells using choline chloride–malonic acid deep eutectic solvent. *Carbohydr. Polym.* **177**, 217–223 (2017).

57. Rodrigues, L. A., Radojčić Redovniković, I., Duarte, A. R. C., Matias, A. A. & Paiva, A. Low-Phytotoxic Deep Eutectic Systems as Alternative Extraction Media for the Recovery of Chitin from Brown Crab Shells. *ACS Omega* **6**, 28729–28741 (2021).

58. Ionic Liquid. in *The IUPAC Compendium of Chemical Terminology* (International Union of Pure and Applied Chemistry (IUPAC), Research Triangle Park, NC, 2024). doi:10.1351/goldbook.08180.

59. Shamshina, J. L. & Rogers, R. D. Commercialization of Ionic Liquids in Pursuit of Green Chemistry: Must we Each Become an Entrepreneur? *Chem. Rec.* **23**, (2023).

60. Shamshina, J. L. Chitin in ionic liquids: historical insights into the polymer's dissolution and isolation. A review. *Green Chem.* **21**, 3974–3993 (2019).

61. Wu, Y., Sasaki, T., Irie, S. & Sakurai, K. A novel biomass-ionic liquid platform for the utilization of native chitin. *Polymer (Guildf).* **49**, 2321–2327 (2008).

62. Setoguchi, T., Kato, T., Yamamoto, K. & Kadokawa, J. Facile production of chitin from crab shells using ionic liquid and citric acid. *Int. J. Biol. Macromol.* **50**, 861–864 (2012).

63. Uto, T., Idenoue, S., Yamamoto, K. & Kadokawa, J. Understanding dissolution process of chitin crystal in ionic liquids: theoretical study. *Phys. Chem. Chem. Phys.* **20**, 20669–20677 (2018).

64. Dong, Q. *et al.* Extraction of chitin from white shrimp (Penaeus vannamei) shells using binary ionic liquid mixtures. *J. Ind. Eng. Chem.* **120**, 529–541 (2023).

65. Kerton, F. M., Liu, Y., Omari, K. W. & Hawboldt, K. Green chemistry and the ocean-based biorefinery. *Green Chem.* **15**, 860 (2013).

66. Cho, Y.-W., Jang, J., Park, C. R. & Ko, S.-W. Preparation and Solubility in Acid and Water of Partially Deacetylated Chitins. *Biomacromolecules* **1**, 609–614 (2000).

67. Zhu, K. Y., Merzendorfer, H., Zhang, W., Zhang, J. & Muthukrishnan, S. Biosynthesis, Turnover, and Functions of Chitin in Insects. *Annu. Rev. Entomol.* **61**, 177–196 (2016).

68. Cauchie, H.-M. Chitin production by arthropods in the hydrosphere. *Hydrobiologia* **470**, 63–95 (2002).

69. Peniche, C., Argüelles-Monal, W. & Goycoolea, F. M. Chitin and Chitosan: Major Sources, Properties and Applications. in *Monomers, Polymers and Composites from Renewable Resources* 517–542 (Elsevier, 2008). doi:10.1016/B978-0-08-045316-3.00025-9.

70. Tolaimate, A., Desbrieres, J., Rhazi, M. & Alagui, A. Contribution to the preparation of chitins and chitosans with controlled physico-chemical properties. *Polymer (Guildf).* **44**, 7939–7952 (2003).

71. Waśko, A. *et al.* The first report of the physicochemical structure of chitin isolated from Hermetia illucens. *Int. J. Biol. Macromol.* **92**, 316–320 (2016).

72. Sharma, S., Kaur, N., Kaur, R. & Kaur, R. A review on valorization of chitinous waste. *J. Polym. Res.* **28**, 406 (2021).

73. Younes, I. & Rinaudo, M. Chitin and Chitosan Preparation from Marine Sources. Structure, Properties and Applications. *Mar. Drugs* **13**, 1133–1174 (2015).

74. Percot, A., Viton, C. & Domard, A. Optimization of Chitin Extraction from Shrimp Shells. *Biomacromolecules* **4**, 12–18 (2003).

75. Li, J., Revol, J.-F. & Marchessault, R. H. Effect of degree of deacetylation of chitin on the properties of chitin crystallites. *J. Appl. Polym. Sci.* **65**, 373–380 (1997).

76. No, H. K. & Hur, E. Y. Control of Foam Formation by Antifoam during Demineralization of Crustacean Shell in Preparation of Chitin. *J. Agric. Food Chem.* **46**, 3844–3846 (1998).

77. Qin, Y., Lu, X., Sun, N. & Rogers, R. D. Dissolution or extraction of crustacean shells using ionic liquids to obtain high molecular weight purified chitin and direct production of chitin films and fibers. *Green Chem.* **12**, 968 (2010).

78. Shamshina, J. L., Barber, P. S., Gurau, G., Griggs, C. S. & Rogers, R. D. Pulping of Crustacean Waste Using Ionic Liquids: To Extract or Not To Extract. *ACS Sustain. Chem. Eng.* **4**, 6072–6081 (2016).

79. Kalb, R. S. Toward Industrialization of Ionic Liquids. in 261–282 (2020). doi:10.1007/978-3-030-35245-5_11.

80. C, P., A, M., ML, C. & I, B. Chemical Characterization of Cancer Pagurus, Maja Squinado, Necora Puber and Carcinus Maenas Shells. *Poultry, Fish. Wildl. Sci.* **05**, (2017).

81. Bastiaens, L., Soetemans, L., D'Hondt, E. & Elst, K. Sources of Chitin and Chitosan and their Isolation. in *Chitin and Chitosan* 1–34 (Wiley, 2019). doi:10.1002/9781119450467.ch1.

82. Feng, M. & Sun, J. Pretreatment and Conversion of Shrimp/Crab Shells into High-Value Products with Ionic Liquids. in *Encyclopedia of Ionic Liquids* 1–14 (Springer Singapore, Singapore, 2020). doi:10.1007/978-981-10-6739-6_112-1.

83. Kaya, M., Seyyar, O., Baran, T., Erdoğan, S. & Kar, M. A physicochemical characterization of fully acetylated chitin structure isolated from two spider species: With new surface morphology. *Int. J. Biol. Macromol.* **65**, 553–558 (2014).

84. Sagheer, F. A. Al, Al-Sughayer, M. A., Muslim, S. & Elsabee, M. Z. Extraction and characterization of chitin and chitosan from marine sources in Arabian Gulf. *Carbohydr. Polym.* **77**, 410–419 (2009).

85. Pap, S. *et al.* Synthesis optimisation and characterisation of chitosan-calcite adsorbent from fishery-food waste for phosphorus removal. *Environ. Sci. Pollut. Res.* **27**, 9790–9802 (2020).

86. Einbu, A. & Vårum, K. M. Characterization of Chitin and Its Hydrolysis to GlcNAc and GlcN. *Biomacromolecules* **9**, 1870–1875 (2008).

87. Bozell, J. J. & Petersen, G. R. Technology development for the production of biobased products from biorefinery carbohydrates—the US Department of Energy's "Top 10" revisited. *Green Chem.* **12**, 539 (2010).

88. Greaves, T. L. & Drummond, C. J. Protic Ionic Liquids: Properties and Applications. *Chem. Rev.* **108**, 206–237 (2008).

89. Schiffer, Z. J., Biswas, S. & Manthiram, K. Ammonium Formate as a Safe, Energy-Dense Electrochemical Fuel Ionic Liquid. *ACS Energy Lett.* **7**, 3260–3267 (2022).

90. Einbu, A. Characterisation of chitin and a study of its acid-catalysed hydrolysis. (2007).

91. Einbu, A., Grasdalen, H. & Vårum, K. M. Kinetics of hydrolysis of chitin/chitosan oligomers in concentrated hydrochloric acid. *Carbohydr. Res.* **342**, 1055–1062 (2007).

92. Hong, S., Yuan, Y., Yang, Q., Zhu, P. & Lian, H. Versatile acid base sustainable solvent for fast extraction of various molecular weight chitin from lobster shell. *Carbohydr. Polym.* **201**, 211–217 (2018).

93. Chen, X., Chew, S. L., Kerton, F. M. & Yan, N. Direct conversion of chitin into a N-containing furan derivative. *Green Chem.* **16**, 2204–2212 (2014).

94. Cárdenas, G., Cabrera, G., Taboada, E. & Miranda, S. P. Chitin characterization by SEM, FTIR, XRD, and 13 C cross polarization/mass angle spinning NMR. *J. Appl. Polym. Sci.* **93**, 1876–1885 (2004).

95. Chandran, R., Williams, L., Hung, A., Nowlin, K. & LaJeunesse, D. SEM characterization of anatomical variation in chitin organization in insect and arthropod cuticles. *Micron* **82**, 74–85 (2016).

96. Hudson, R. *et al.* CO 2 reduction driven by a pH gradient. *Proc. Natl. Acad. Sci.* **117**, 22873–22879 (2020).

97. Jaekel, E. E., Sirviö, J. A., Antonietti, M. & Filonenko, S. One-step method for the preparation of cationic nanocellulose in reactive eutectic media. *Green Chem.* **23**, 2317–2323 (2021).

98. McElroy, C. R., Constantinou, A., Jones, L. C., Summerton, L. & Clark, J. H. Towards a holistic approach to metrics for the 21st century pharmaceutical industry. *Green Chem.* **17**, 3111–3121 (2015).

99. Polidoro, D. *et al.* Controlled alcohol oxidation reactions by supported non-noble metal nanoparticles on chitin-derived N-doped carbons. *Catal. Sci. Technol.* **13**, 2223–2238 (2023).

100. Daraghmeh, N. H., Chowdhry, B. Z., Leharne, S. A., Al Omari, M. M., & Badwan, A. Chitin. in *Profiles of Drug Substances, Excipients and Related Methodology,* **36**, 35–102 (2011). doi:10.1016/B978-0-12-387667-6.00002-6.

101. Ioelovich, M. Crystallinity and hydrophility of chitin and chitosan. *Res. Rev. J. Chem.* **3**, 7–14 (2014).

Chapter 4. Waste valorisation for the synthesis of nanomaterials

The topic of biomass and bio-sourced substances valorisation has been introduced in both Chapter 2 and Chapter 3 in relation to the synthesis of advanced catalytic materials and the recovery of valuable compounds from biowaste from the fishery industry.

Building on Chapter 3, the current chapter is dedicated to a deeper investigation of this field, with a focus on the use of these valuable compounds for the preparation of advanced functional nanomaterials. This research was carried out within the framework of the Cotutelle PhD program between Università Ca' Foscari Venezia (Unive), Università degli Studi di Trieste (Units) and The University of Sydney (USYD), Australia. During this collaboration, the author of this Thesis had the opportunity to spend one year at USYD, conducting studies on the synthesis of advanced nanomaterials – specifically chitin- and crab shells-derived Carbon Dots (CDs) – and investigating their application in batteries as reversible energy storage systems, particularly their influence on the plating behaviour of zinc-anodes. The general concept is described by the formation of a layer of self-assembled CD modulating the zinc anode plating behaviour through electrostatic interactions such that damaging dendrites are suppressed.

4.1 Carbon Dots: synthesis, modulation and applications

Carbon Dots (CDs) were discovered in 2004 by Xu et al. during an attempt to isolate and purify single-walled carbon nanotubes.[1] This case of serendipity marked a significant turning point in nanomaterials research. Since then, CDs have become the focus of thousands of studies over the past two decades and have found applications across a wide range of fields.

CDs are effectively zero-dimensional (typically <100 nm in all three directions) carbon nanoparticles which gained fame thanks to their optical properties, especially their fluorescence, which primarily originates from two main phenomena: the quantum confinement effect, resulting from their nanoscale dimensions comparable to the Bohr radius of an exciton, and the degree of carbonisation within their carbonaceous matrix. During the carbonisation process, graphitic clusters form in the carbonaceous core, leading to a dense network of conjugated sp^2 domains, which can absorb photons, stabilise the excited states through delocalisation of π electrons, and subsequently re-emit energy through a radiative de-excitation mechanism (photoluminescence).[2–4]

An interesting feature of CDs is the possibility of tuning their optical properties by adjusting both the nature and ratios of the reagents used as well as the synthetic procedures employed. Both these aspects influence particle size, morphology, the degree of graphitisation, the presence of dopant heteroatoms and surface functionalities. In particular, heteroatom doping, promoted by the incorporation of elements such as nitrogen, oxygen, sulphur, and many others – either within the carbonaceous core or as functional groups decorating their shell – has been widely reported in literature. Such doping strategies modify the electronic structure of the material, introducing defects and enabling fine control over emission wavelength, quantum yield, their interaction with the external chemical environment, and photostability.[5,6]

Among the synthesis routes available, bottom-up approaches (**Figure 4.1, right**) offer significant advantages for the control of the characteristics of the final materials by tuning the type and ratio of the molecular precursors (usually fine chemicals), employing hydrothermal, solvothermal, or pyrolytic reaction types. These processes promote the formation of the nanoparticles through consecutive steps such as condensation, nucleation, aggregation, carbonisation and, if the temperature is high enough, graphitisation.

By contrast, top-down methods (**Figure 4.1, left**) rely on physical or chemical breakdown of bulk carbon-based materials (such as graphite rods) into nanoscale entities using techniques such as pulsed laser ablation, electrochemical oxidation, arc discharge, or ultrasonication. In this case the tuneability of the resulting material is more limited as it is largely governed by the intrinsic characteristics of the parent bulk material.[7]

It has been demonstrated that high temperature (≥160 °C) plays a crucial role in the formation of CDs by enabling subsequent stages of aggregation, which produce the crystalline graphitic domain,[8] and limiting the production of low molecular weight by-products, namely fluorophores. The latter are small, conjugated molecules, with a structure similar to 5-oxo-1,2,3,5-tetrahydroimidazo[1,2-a]pyridine-7-carboxylic acid, often identified as *IPCA-like* species, which frequently dominate the fluorescence emission of the final (unpurified) product, but lack an extended nanostructured character.[9–15]

In the synthesis of CDs several challenges still need to be addressed. Among them, reaction times are often long, the overall yield is limited by the difficulty in promoting the energy-demanding aggregation, and the purification process (typically performed by dialysis to remove fluorophores and by-products) is time-consuming.[16] The bottom-up valorisation of biomass as a carbon source, seems a more suitable approach to address and overcome

these issues. Indeed, a wide range of carbon-rich precursors, including biowaste, can be used to synthesise CDs. This drastically reduces the cost of the starting materials and enhances both the environmental and the economic sustainability of the synthesis protocol.[17,18]

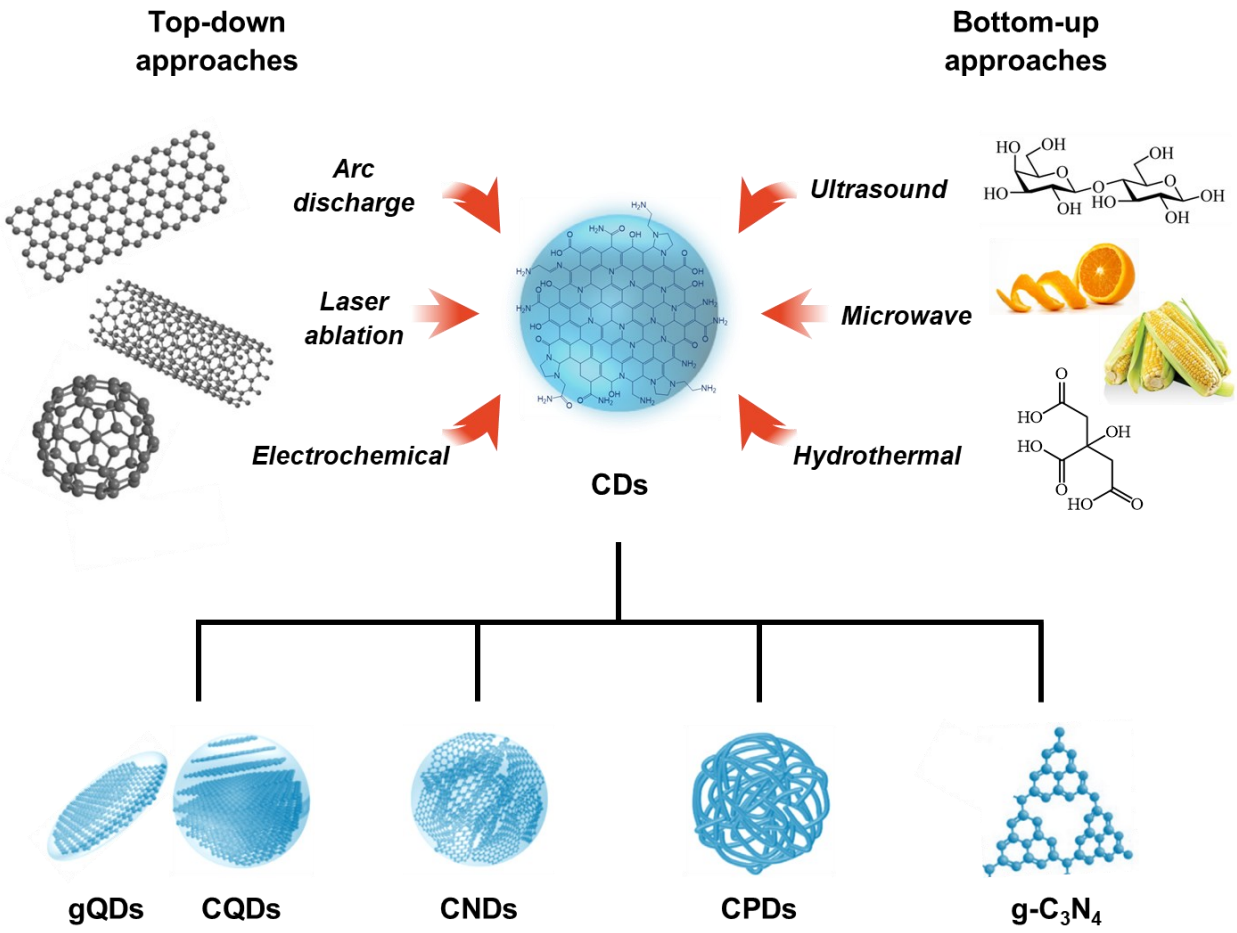

Figure 4.1. CDs synthesis routes (top-down and bottom-up approaches) and classification. Adapted from [19].

Fluorescent CDs can be classified into:

i) graphene Quantum Dots (gQDs, conjugated single or multiple graphene layers), and Carbon Quantum Dots (CQDs, quasi-spherical mixture of sp^2 and sp^3 carbon) when exhibiting the quantum confinement effect and crystalline clusters;

ii) Carbon Nanodots (CNDs, amorphous quasi-spherical dots), when lacking the quantum confinement effect;

iii) Carbon Polymer Dots (CPDs, nano-scaled π-conjugated polymers),[20]

iv) graphitic Carbon Nitride (g-C_3N_4, highly structured 2D tri-*s*-triazine polymeric material composed of carbon and nitrogen).

Thanks to their low cost, non-toxic, biocompatible, water-compatible, versatile, robust, and environmental friendly nature, CDs have found extensive applications in many fields,[21] such as photocatalysis,[22,23] sensing,[24] drug delivery and diagnostics,[25,26] bioimaging,[27] photo dynamic therapy (PDT),[28] wastewater treatment,[29] optoelectronics and solar cells,[30,31] and pollutant photodegradation.[32,33]

Our research group at Ca' Foscari has long-standing experience in the development of preparation methods for CDs and their applications.[34–42] For instance, a set of nanocomposites made of CDs-decorated graphitic Carbon Nitride (g-C_3N_4) were recently synthesised comparing two different approaches, consisting of a hydrothermal treatment and a mechanochemical extrusion. The catalytic activity of the materials was evaluated in the model reaction of oxidation of benzyl alcohol in acetonitrile, achieving 80% selectivity towards benzaldehyde and demonstrating excellent stability and reusability.[43]

More recently, CDs have gained attention also as materials for electrocatalysis, transducer technologies, and energy storage systems, such as supercapacitors and batteries.[44] Indeed, the combination of the quantum confinement effect with the presence of dopant heteroatoms induces a separation between the valence and conduction band, conferring excellent redox activity to the CDs. Additionally, their high specific surface area, the presence of surface defects, and their colloidal nature make them suitable as functional additives next-generation batteries.

4.1.1 CDs towards sustainable energy storage systems

Lithium is dominating the field of rechargeable batteries thanks to its high theoretical specific capacity (3861 mA/g) and good cycling stability. However, the flammability and chemical reactivity of lithium along with its limited reserves and the use of toxic solvent-based electrolytes pose not only safety risks and environmentally hazards[45] but also issues for large-scale recycling technologies. Only about 6% of lithium-ion batteries (LIBs) consumed are currently recycled, while most end up in landfills.[46]

Aqueous zinc-ion batteries (AZIBs) are emerging as alternative to conventional lithium-based energy storage systems. Zinc has a considerable theoretical specific capacity of 820 mA/g (compared to other materials, such as graphite – 372 mA/g[45]), a low redox potential of -0.76 V vs SHE, low toxicity, low cost, excellent water-compatibility, and high safety which make it a promising candidate for the optimisation of eco-friendly aqueous batteries.

However, some drawbacks still limit a broader use of AZIBs, with zinc dendrite formation on the anode surface representing one of the most critical. These needle-like protuberances can pierce the battery separator and cause short circuits, shortening life cycle. They can also form electrically disconnected 'islands' of zinc, reducing capacity on cycling. Moreover, parasitic side reactions due to water activity, such as corrosion and the hydrogen evolution reaction (HER), also remain major challenges.[47]

Research is currently addressing these issues through different strategies.[48] The most promising ones include anodic material design or direct application of protective coatings (e.g. TiO_2, ZrO_2, Al_2O_3) on the electrode surface.[49–53] However, such approaches are often sensitive to physical defects generated during manufacturing, leading to degradation over time, ultimately weakening zinc deposition during repeated plating and stripping processes. An alternative is represented by electrolyte engineering, which involves the direct inclusion of functional additives into the electrolyte. This strategy is operationally simple, reproducible, cost-effective, and scalable,[54–58] but the progressive consumption of the additive in solution via irreversible side reactions may limit the control of these configurations over time. In recent years, among other approaches to improve the performance of AZIBs, the use of nanomaterials, including CDs, have been explored as potential additives or surface coating agents for regulating zinc deposition.

The action of CDs in modulating zinc deposition on the electrode surface can be attributed to one or more regulation mechanisms that operate in parallel to stabilise consecutive anodic plating and stripping cycles **(Figure 4.2A-B)**. Among the most supported in literature are:

i) the interaction with Zn^{2+} in solution and the consequent modification of its solvation shell,
ii) the formation of a dynamic self-assembled layer acting as a protective coating on the anodic surface, and
iii) the modulation of the electric field lines across the electrode surface.

Among these, solvation shell modification and electric field homogenisation are generally regarded as the most influential factors governing zinc deposition morphology, while the self-assembled interfacial layer primarily contributes to long-term cycling stability.[59]

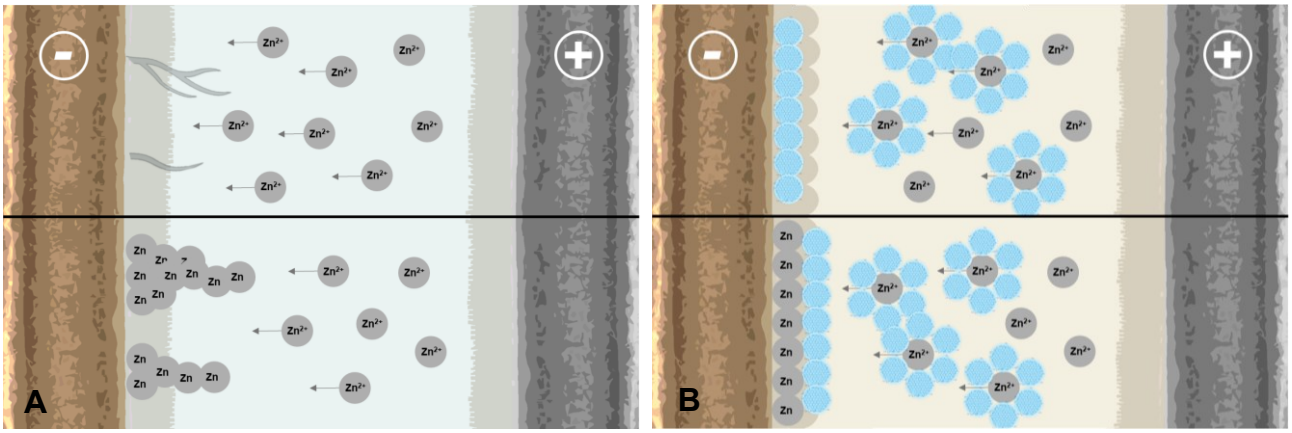

Figure 4.2. Pictorial representation of **A:** zinc-dendrites formation during the plating process due to electric field inhomogeneities, and **B:** zinc plating regulation mechanisms of CDs-based additives.

Typical $[Zn(H_2O)_6]^{2+}$ solvated complex tends to form as most stable structure in low-concentration zinc-based aqueous solutions.[60] Although water is an environmentally benign and non-toxic solvent, in zinc-based energy storage systems it could represent the origin of several critical issues that may require careful consideration.[61] The strong interaction between Zn^{2+} and water molecules within the solvation shell activates water, leading to lengthening and weakening of the O-H bond. This effect lowers the LUMO energy level of water, making it more easily reducible and promoting undesired side reactions such as hydrogen evolution (HER). The consequent H^+ depletion near the electrode surface can induce local pH fluctuations, formation of zinc hydroxide species like $Zn(OH)_4SO_4$, surface passivation, corrosion, and roughening, all of which favour the tip effect.[62] This refers to the aggregation of electrons and corresponding intensification of the electric field in regions with large curvature, resulting in locally increased surface electric potential, inhomogeneities of the electric field distribution and promotion of dendrite growth.[63,64]

As previously discussed, CDs are zero-dimensional nanoparticles characterised by a high density of surface defects and functional groups. The presence of conjugated domains and heteroatoms embedded in their carbonaceous matrix alter the local electron density, thereby generating active sites. Theoretical (DFT) calculations and computational simulations have shown that heteroatom-doped CDs and the resulting functional groups that decorate their outer shell, can establish strong interactions with zinc species. The estimated interaction energy between CDs and Zn^{2+} is lower than that between Zn^{2+} and water.[65] These interactions occur through their coordination to Zn^{2+} partially replacing water molecules in its hexa-coordinated solvation shell, thereby modulating ions migration within the electrolyte

and reducing their nucleation overpotential.[59,65] As a result, zinc ions become pre-concentrated near the electrode surface acting as a permanent zinc reservoir all over the entire area, preventing localised aggressive plating and promoting a more homogeneous galvanisation. This process yields a greater amount of nucleation sites and the uniform deposition of fine zinc crystals that form a smooth and compact plating layer.

More specifically, the presence of defects associated with electronegative elements in the carbonaceous core was demonstrated to alter the electronic properties of these nanomaterials, making them moderately conductive and able to respond to the application of electrical potential within the cell by arranging themselves at the interface between the electrode and the electrolyte, where the CDs self-assemble into a protective coating on the electrode surface, thus regulating Zn^{2+} diffusion and preventing uncontrolled and uneven zinc deposition.[59] Their moderate conductivity also results in their ability of interacting, thus modulating and homogenising the distribution of the electric field lines across the electrode surface (**Figure 4.3**), preventing their unhindered extension deep into the electrolyte, where Zn^{2+} would otherwise align along them and easily form dendrites. Consequently, uncontrolled zinc deposition along preferential growth paths is suppressed, and dendritic protrusions are effectively inhibited.[66]

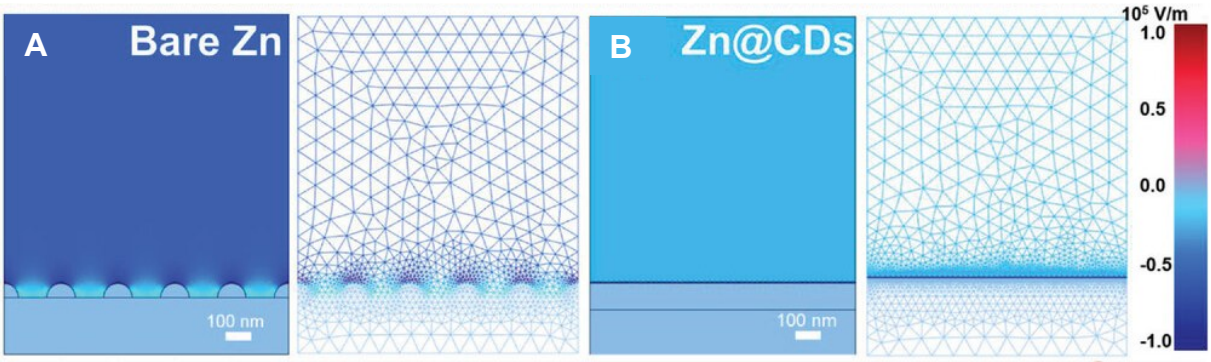

Figure 4.3. The electric field distribution of **A:** bare Zn electrode and **B:** CDs coated Zn electrode showing the suppression of high-field hotspots at protrusions and the resulting uniform current density across the electrode surface. Reprinted from [66] with permission.

In general, it has been demonstrated that the interaction between CD additive nanomaterials, Zn^{2+} and the electrode surface, strongly depend on their chemical surface features.[67,68] However, there is broad consensus that further efforts are still required to obtain a clearer understanding of this relationship and to establish a more robust description

of the action mechanisms of these nanomaterials.[69] A well-established factor is the strong dependence of the CDs activity on the inclusion of element of various nature within the carbonaceous matrix, which enhances their zincophilicity and mitigates water reactivity, thereby improving overall battery performance.

Among the most representative examples of CDs-based additives reported in literature, gQDs obtained by treating graphite powder with a 1:3 concentrated mixture of HNO_3 and H_2SO_4 at 90 °C for 11 h, followed by purification through dialysis for 4 days, demonstrated significant improvement in Zn anode stabilisation up to 2200 h at 0.8 mA/cm^2. Theoretical (DFT) and experimental investigations confirmed the correlation of this effect to the interaction of oxygen-containing functional groups (–COOH, –OH, –O–) decorating the CD's surface with the surface of the Zn anode, which regulates ions mobility within the electrolyte, reduces their nucleation overpotential and in turn promotes uniform zinc deposition.[70] Doping with electronegative elements such as nitrogen also represents one of the most interesting strategies[67] for zinc coordination and stabilisation, efficiently suppressing dendrite growth.

Many studies have reported nitrogen and sulphur co-doping strategies.[71] For instance, negatively charged N,S-doped CDs synthesised from cysteine, acetaldehyde, and a NaOH 7.5 M solution, proved effective in coordinating Zn^{2+}, reducing its nucleation overpotential thereby accelerating homogeneous galvanisation on the anodic surface. Symmetric Zn||Zn cell showed stable cycling for up to 2000 h at 1 mA/cm^2, while a full Zn||NVO cell maintained a specific capacity of 147.4 mAh/g at 1 A/g after 600 cycles and a coulombic efficiency of 99.5% after 250 cycles.[72] Similarly, S-doped CDs obtained from citric acid and poly(lithium-4-styrene sulfonate) via pyrolysis at 200 °C for 2 h and subsequent dialysis purification for 3 days, were used as an additive into a hybrid DFM/H_2O/$ZnSO_4$ electrolyte, enhancing Zn anode stability. Their negatively charged, defect-rich structure, combined with the ability of DMF to regulate the solvation shell of Zn^{2+}, provided a synergistic improvement in zinc nucleation and deposition during the plating/stripping processes, extending the symmetric Zn||Zn cell life to 4000 h at 1 mA/cm^2. Moreover, in a Zn||NVO full cell this material enabled the retention of a specific capacity of 119.2 mAh/g after 5000 cycles at 5 mA/g.[73]

Graphitic carbon nitride quantum dots (gC_3N_4QDs) synthesised from thiourea and citric acid via calcination at 200 °C for 30 min and purified by dialysis for 2 days, proved effective in suppressing anodic surface side reactions and enabling dendrite-free, homogeneous zinc deposition by forming a protective nano-layer that dynamically assembled/disassembled

during repeated charge/discharge cycles (**Figure 4.4**), maintaining 99.6% of coulombic efficiency over 200 cycles and stable operation up to 1200 h in a full Zn||MnO_2 cell.[59]

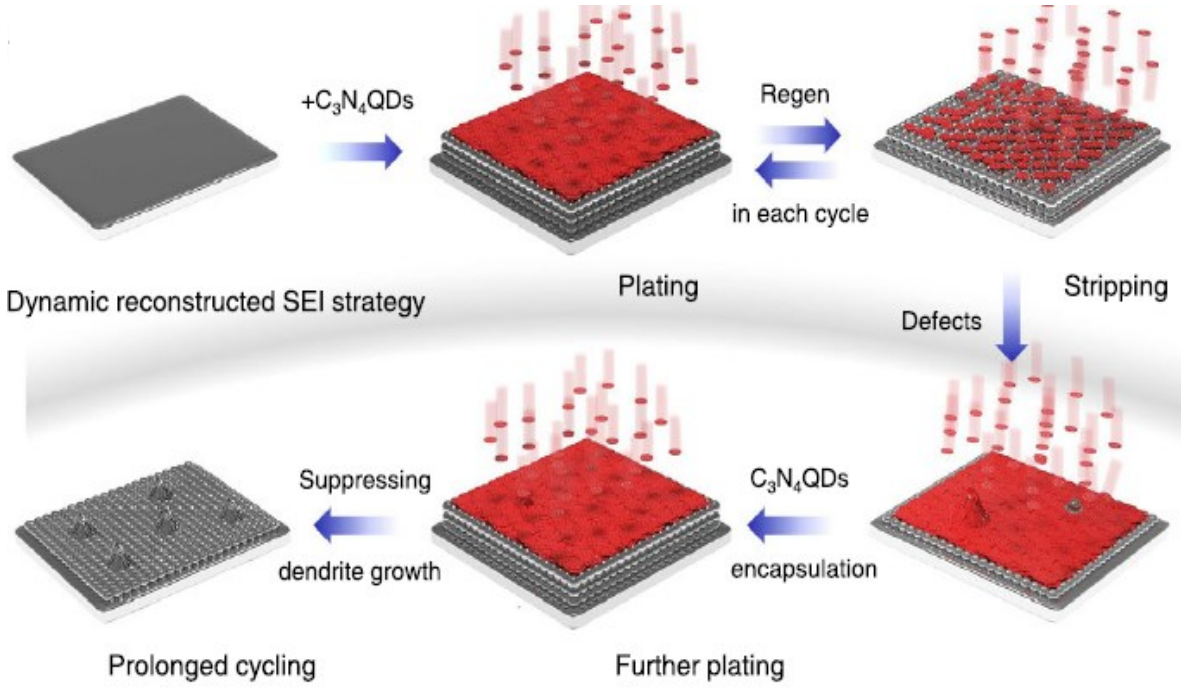

Figure 4.4. Dynamic protective layer mechanism. Reprinted from [59] under the terms of the Creative Commons CC BY license.

However, the high electronegativity and hydrophilicity of these doping elements may sometimes act as an intrinsic limiting factor when it comes to regulating parasitic reactions occurring at the electrode interface which mainly depend on water activity, such as HER and corrosion.[67,74] In this sense, different types of doping with diametrically opposed characteristics have demonstrated interesting properties. For instance, commercially available Cl-doped gQDs were reported to be effective in forming a dynamic hydrophobic adaptive interphase on the electrode surface responsible of generating electrostatically repulsion towards water, reducing its activity, and thus delaying corrosion and suppressing $Zn(OH)_4^{2-}$ passivation caused by HER.[74] [ref] This electrostatic shield efficiently promoted also uniform zinc plating, achieving stable operation in a symmetric Zn||Zn cell for up to 2000 h at 1 mA/cm^2 and 1 mAh/cm^2, seven times longer than the control test.

The introduction of zincophilic dopants has also occasionally demonstrated to promoted preferential Zn deposition along the (002) plane, resulting in a smooth electrode surface and extending the overall lifetime of the cell.[75,76] Co-doped CDs with N inclusions within the carbonaceous core and S atoms decorating the outer shell were prepared from citric acid

and metanilic acid via a solvothermal treatment at 160 °C for 5 h using DMF as solvent, followed by ethanol precipitation and purification through dialysis for three days.[65] When used as an electrolyte additive, this material being extremely rich in functional groups such as -COOH, -NH_2, -OH, and -SO_3H, showed effective in suppression of dendrite formation and parasitic reactions, promoting a uniform Zn plating along the specific (002) crystal plane and stabilising a symmetric Zn||Zn cell for up to 3000 h at 1 mA/cm^2 and 0.5 mAh/cm^2, compared to a control cell that short-circuited after only 380 h under identical conditions. DFT calculations also demonstrated multiple beneficial roles of these nanoparticles in promoting Zn^{2+} solvation, as well as stabilisation of the electrode/electrolyte interphase by reducing water activity and forming a protective surface layer.

When supported by DFT calculations or in-depth analyses of the plated electrode surface, all these strategies are univocal in establishing an electrostatic nanoparticles-based shielding layer, which modulate the uneven electric field distributed on the anodic electrode. This mitigates the “tip effect”, preventing parasitic electric discharges to permeate through the electrolyte and promote dendrite growth.[77] At the same time, these additives again strongly interact with the Zn^{2+} solvation shell, influencing both ion transport and surface approach dynamics, improving the overall zinc deposition process.

General CDs action parameters contributing to the zinc plating regulation mechanisms are summarised in **Table 4.1.**

Table 4.1. CDs contribution mechanisms on zinc plating regulation in AZIBs.

Parameter	Contribution on Zn-plating regulation	Ref.
Heteroatom doping (N, O, S, Cl, etc.)	Creates active sites and increases zincophilicity; increases local electron density; reduces H_2O activity and parasitic reactions	74–76
Surface functional groups (-COOH, -OH, -NH_2, -C=O, etc.)	Regulate Zn^{2+} coordination; reduces nucleation overpotential; suppress dendrites formation	59,65,70
Conjugated sp^2 domains/graphitisation	Increase conductivity; promotes self-assembled nanolayer; increases nucleation sites; suppress dendrites by flattening surface electric field	59,70
Colloidal stability	Ensure nanoparticles dispersion; cycling reversibility; good resilience at high current density	59

Overall, all this evidence suggest that CDs act as multifunctional regulators of plating/stripping processes in AZIBs systems, simultaneously influencing Zn^{2+} solvation, nucleation kinetics, surface electric field distribution. However, several challenges remain unresolved, including the possible consumption of CDs during prolonged cycling and their stability under high current densities. In addition, most CDs-based additive syntheses reported still rely on fine chemicals and sometimes require harsh reagents, such as DMF or concentrated NaOH, enhancing the cost of the final material and reducing the overall sustainability of the process. The high cost of these materials still represents a critical problem in a scaling up perspective, thereby cheaper carbon sources still need to be investigated.[69] This is why combining biowaste valorisation with the production of non-toxic, water-stable, and tuneable functional materials, such as CDs, can represent a promising route towards the type of additive (in itself sustainable) that is crucial in realising the environmentally benign and sustainability promise zinc-based energy storage systems (AZIBs). Building on the chitin extraction protocol from Spider crab shells described in Chapter 3, the next section will compare hydrothermally synthesised chitin- and crab shells-derived CDs with a model material obtained from fine chemicals (citric acid and diethylenetriamine), exploring their performance as additives in AZIBs through in situ optical microscopy visualisation.

4.2 Bio-sourced Nitrogen-doped Carbon Quantum Dots (CQDs) as Additives for Near Dendrite-free Zn Batteries

This section has been adapted from an advanced Research Article draft. The Author of this Thesis contributed to the optimisation of the synthetic procedures, to part of the characterisation of the CDs materials and CDs-based additives, and execution of the plating experiments. The results described below.

Abstract. A mixture comprised of a bio-sourced carboxylic acid (citric acid) and diethylenetriamine as a N-source, has been used to produce N-doped Carbon Quantum Dots (N-CQDs). These proved effective in suppressing Zinc dendrite formation during Zinc-plating experiments mimicking the anodic recharging process in AZIBs. The properties of N-CQDs were tested through electrochemical measurements and *in-situ* optical microscopy investigations. Thereafter, further N-doped nanomaterials were obtained from bio-based polymers such as commercially sourced chitin (Aldrich) or biowaste-extracted (Australian Spanner crab shells). During plating experiments these nanomaterials effectively promoted uniform Zinc deposition and prevented dendrite formation, with the best additives enabling current densities of up to 20 mA/cm² for 4 hours of plating (i.e. yielding 80 mAh/cm^2). Differences in the microstructure of the zinc plating surfaces could be rationalised and linked to additive structure-functionality relationships based on their physicochemical properties.

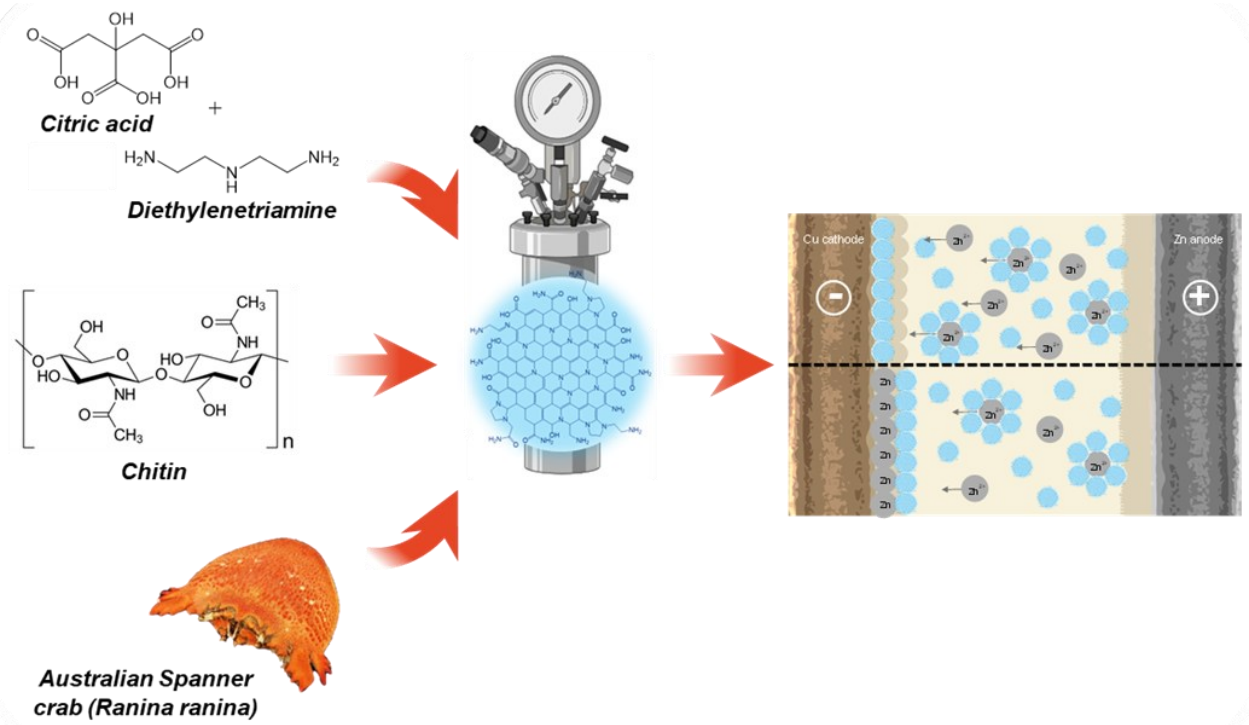

Figure 4.5. Schematic representation of the synthetic strategies for AZIBs additives preparation in this work.

4.2.1 Results and Discussion

Nitrogen-doped carbon nanomaterials

N-doping has been widely recognised to affect the properties of carbon nanomaterials through different effects: it changes the electronic distribution of the carbon matrix, boosting the local electron density and raising the HOMO energy level, thereby improving the conductivity of the material. Regions of the carbon lattice with enhanced electron density work as active sites for the adsorption and stabilisation of reactive species. This reduces the overpotential for some critical electrochemical reactions, including oxygen reduction reaction (ORR), oxygen evolution reaction (OER) and hydrogen evolution reaction (HER).[78] Through this mechanism, surfaces that are functionalised with polar organic groups comprised of nitrogen and (depending on the method of preparation) oxygen heteroatoms, can modify the chemical reactivity of these nanomaterials.[48,65,79] In the case of zinc plating as conducted in aqueous zinc batteries, the heteroatom doping enhances the zincophilic properties of the nanoparticles, resulting crucial in promoting the absorption of Zn^{2+}.[80] Moreover, the study of N-doped carbon materials as plating additives combines the study of renewable biowaste-based materials with an investigation into renewable energy storage technology.

Synthesis from citric acid and diethylenetriamine (N-CQDs)

The N-CQDs used within this work were synthesised adjusting a hydrothermal (HT) procedure previously reported by some of us.[35] Further details in the Experimental Section. The relative proportions of citric acid and diethylenetriamine (DETA) were tuned to obtain a N/C_{molar} ratio as similar as possible to that of commercial chitin (N/C_{molar} = 0.125, considering a degree of acetylation of 100%). DETA acted simultaneously as a nitrogen source and as a promoter of crosslinking between the citric acid moieties, thereby facilitating the incorporation of nitrogen into the carbonaceous core. Specific precautions were taken to ensure reproducibility and consistency of the physicochemical properties of the nanomaterial: at 180 °C, the above-quoted HT treatment used for the N-CQDs synthesis was prolonged up to 24 h, to guarantee the conversion of low-molecular-weight precursors into a well-defined nanostructured solid.

ESI mass spectrometry (**Figure 4.6**) performed on the crude material confirmed the presence of species with MW in the range of 1000-1850 Da, while the formation of light

residual species was minimised, especially those of structure similar to 5-oxo-1,2,3,5-tetrahydroimidazo[1,2-a]pyridine-7-carboxylic acid (IPCA-like compounds) which are typical fluorophores found in carbon dots prepared from citric acid and DETA.[81]

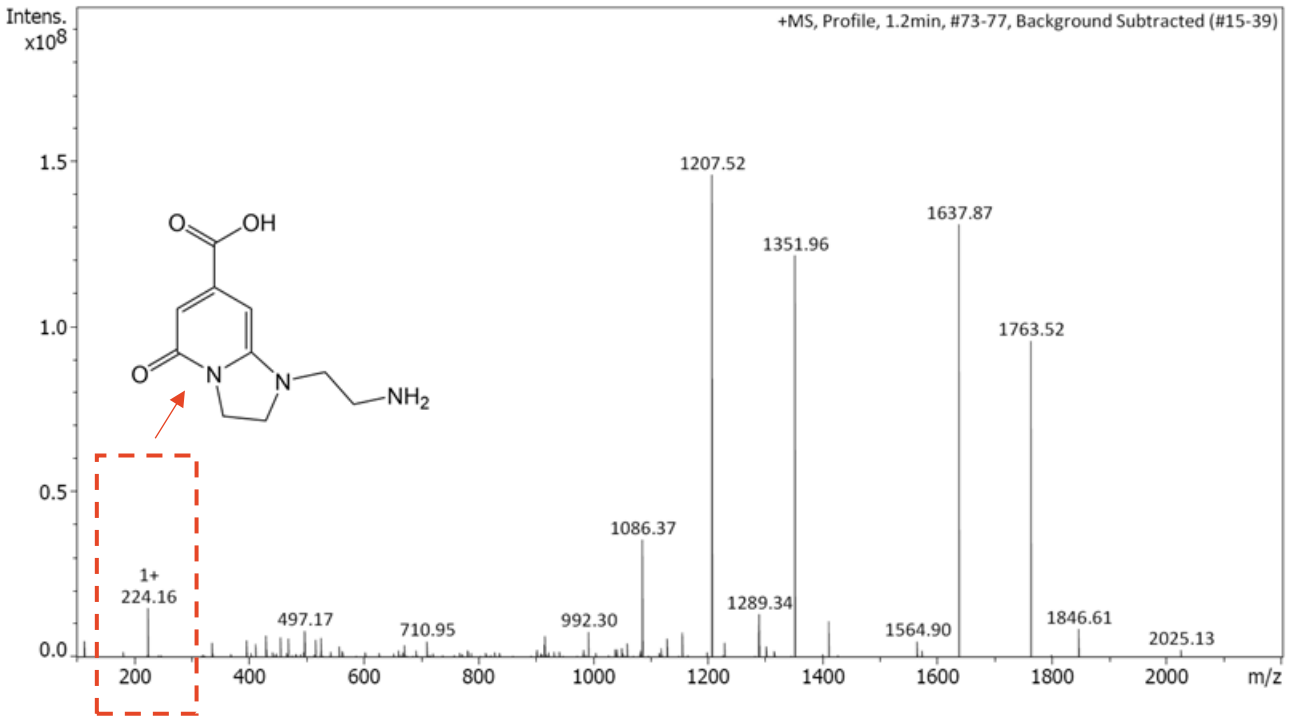

Figure 4.6. Electrospray ionisation mass spectrometry (ESI-MS) analysis of crude N-CQDs.

The crude material was purified by dialysis using 1 kDa MWCO (molecular weight cutoff) membrane bags under a meticulous pH control. It has been reported that N-CQDs are highly pH sensitive due to the presence of surface functional groups including amine, hydroxyl, and carboxylic ones (and their potential derivatives formed during synthesis).[82] Aggregation and precipitation were observed at pH<4, while fluorescence quenching was noted in the pH range of 8-9 likely due to reversible surface protonation/deprotonation and ionic interactions. Therefore, the dialysis was carried out by alternating and repeating neutral, acidic, and basic cycles. Neutral cycles primarily removed freely soluble impurities. Acidic cycles protonated surface amines, weakening electrostatic and H-bond interactions and facilitating desorption of weakly bound species. Basic cycles deprotonated carboxylic groups, increasing negative surface charge, which enhanced dispersion of aggregates and promoted release of impurities that are otherwise stabilised under acidic conditions. At each stage, water was replaced to maintain concentration gradients, and the sequence was repeated until no fluorescent impurities were detected outside the membrane, typically after

48-56 hours and 6-7 cycles. Finally, the resulting neutral aqueous solution of purified N-CQDs retained its characteristic blue fluorescence and could be characterised for its optical properties.

Overall, the procedure enabled a high degree of reproducibility in the production N-CQDs and the isolation of nanoparticles with significant size and purity, as confirmed by NMR analyses. ^{1}H- (**Figure 4.7A**) and ^{13}C- (**Figure 4.7B**) NMR spectra showed a near-complete silent profile after the dialysis, thereby highlighting the colloidal nature of the final material.

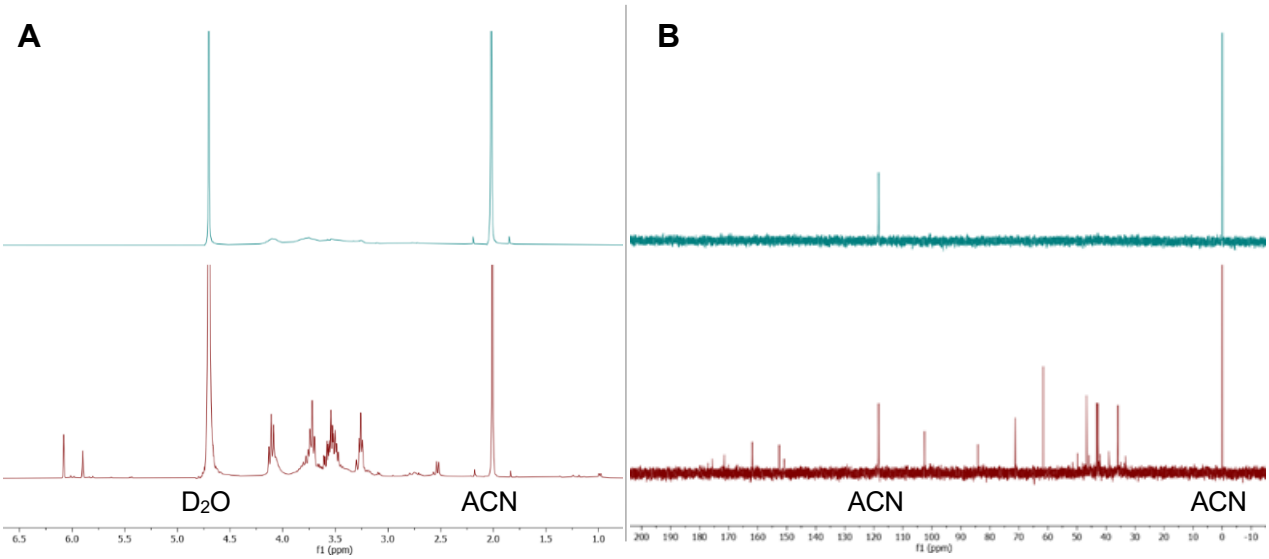

Figure 4.7A: ^{1}H- and **B:** ^{13}C-NMR spectra of N-CQDs crude (red lines, bottom) and after dialysis purification (green lines, top). D_2O was used as solvent and acetonitrile as internal standard.

Synthesis from Chitin (CTN-CDs) and Spanner crab shells (CRB-CDs)

Both commercial chitin (purchased by Sigma-Aldrich) and a biowaste, as Australian Spanner crab shells (sourced from the local Sydney Fish Market), were used as starting materials to obtain N-doped carbon dots.

Mechanochemical pretreatment. The use of chitin as a starting biopolymer to obtain bio-sourced N-doped carbon nanomaterials was not without issues. The extremely robust polysaccharidic structure of chitin confers to it a very low chemical reactivity and high resistance to solubilisation and degradation, in water and most organic solvents.[83] For example, compared to other similar polysaccharides as cellulose and hemi-cellulose that depolymerize and dissolve into high temperature/supercritical water, the presence of the N-acetyl groups in crystalline chitin makes its hydrolysis a not uniform process that alternates

phases of surface erosion and hydrogen bonding disruption,[84–86] and results in a fragmentary degradation despite the harsh and energy demanding conditions.

Interestingly, however, mechanochemistry offers a promising strategy to promote the amorphisation of chitin and enhance its solubility without resorting to strong acids or high temperatures.[87,88] This approach was also employed in this work, where chitin was subjected to a mechanochemical pretreatment via ball milling. Raw commercial chitin (0.5 g) was placed in a zirconia jar (50 mL) equipped with a zirconia grinding ball (1.5 cm diameter), and ball-milled at 25 Hz (15 min; ≈1500 rpm). The milling was then paused for 15 min to avoid overheating, after which another ball-milling cycle was started. The overall sequence was repeated 7 times. PXRD analyses of the resulting solid confirmed a drastic reduction of its crystalline domain, with details reported below in **Figure 4.8**.

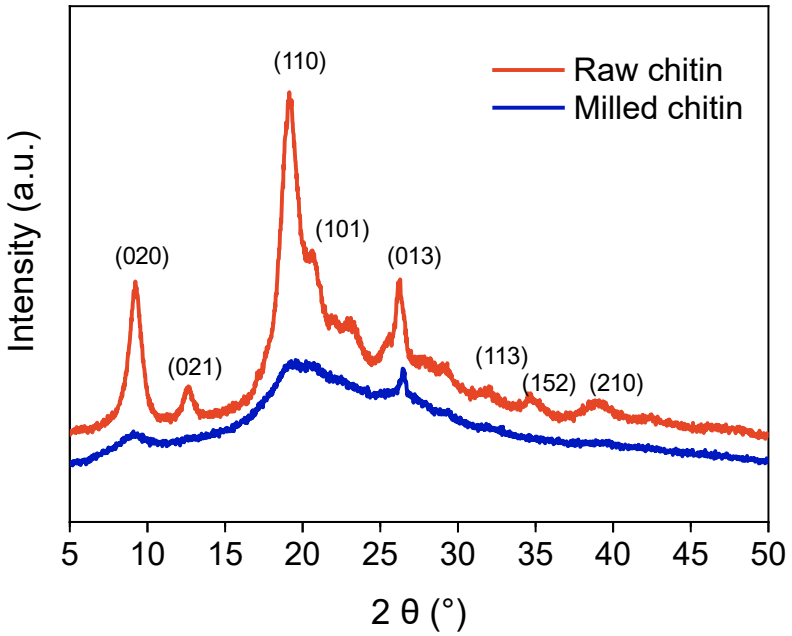

Figure 4.8. Powder X-ray diffraction analyses spectra of a commercial chitin sample prior (red line) and after (blue line) milling, respectively. Peaks were assigned based on available literature[88,89]. Raw chitin exhibited the characteristics diffraction peaks of chitin crystalline domain, with two main intense reflection at 2θ = 9.2° and 19.2°, corresponding to the (020) and (110) crystallographic planes, respectively.

Compared to the spectrum of the starting commercial sample that displayed reflections at 2θ = 9.2°, 19.2° 12.6°, 20.6°, 26.2°, 34.7°, and 38.8° typical of crystallographic planes and the crystalline unit cell, the PXRD profile of ball-milled solid displayed a hill-like profile typical of a quasi-amorphous structure, thereby indicating a loss of long-range order within the material and a strong reduction of the crystallinity of the solid.

Similar conclusions were drawn by FT-IR analyses. The spectrum (reported in **Figure 4.9**) recorded after the mechanochemical treatment showed that the main chemical backbone of chitin was preserved, except for signals related to both strong and weak intra- and inter-chains hydrogen bonding in the chitin fibres. In particular, the following signals were almost lost or less intense compared to the starting sample:

i) the O-H stretching at 3439 cm^{-1} related to weak hydrogen-bond vibrations parallel to the fibre axis (intra-chain interactions between -$O^3H\cdots O^{5'}$- and between -$O^3H\cdots O^7$=C-);[90,91]

ii) the N-H stretching around 3263 and 3103 cm^{-1} related to the strong inter-chain hydrogen-bonding perpendicular to the fibre axis (between -$N^2H\cdots O^{7'}$=C-) due to the amide-amide interaction breakage;[91]

iii) the vibrations around 1653 and 1620 cm^{-1} (related to the C=O stretching frequencies of the amide I region, typically found in the crystalline allomorph α-Chitin) merge into a single signal, as it is frequently seen with the more amorphous allomorph β-chitin;[92]

iv) the signal around 1257 cm^{-1} of the CH_2 wagging associated with the change in dipole moment during the transition from crystalline to amorphous domain.

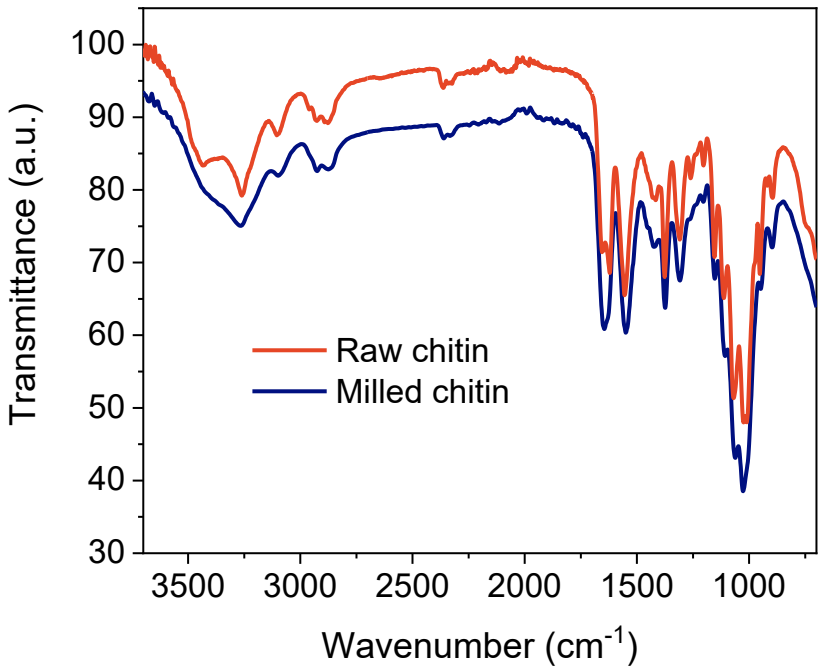

Figure 4.9. Fourier Transform Infrared (FT-IR) analyses spectra of a commercial chitin sample prior (red line) and after (blue line) milling, respectively. Peaks were assigned based on available literature.[88,89]

Finally, the unchanged intensity of the vibrational band around 899 cm^{-1}, characteristic of the beta-linkage between the N-acetyl-glucosamine monomers, demonstrates that the mechanochemical treatment does not impact the glycosidic bond.[91] Overall, both PXRD and FT-IR proved that ball milling did not affect the polymer chain length but was effective to induce an almost complete disruption of the hydrogen-bonding network in chitin.

Hydrothermal (HT) synthesis. The impact of the mechanochemically-assisted amorphisation of chitin on its solubility in water was investigated through a HT processing aimed to the synthesis of chitin-derived carbon nanoparticles. Raw (commercial chitin as such) and treated samples were compared. A suspension of raw or milled chitin (1.5 g each) and milli-Q water (40 mL) was placed into a sealed autoclave and heated at 220 °C for a time interval variable from 20 min up to 24 h. The mixture was then filtered under suction to obtain:

i) a solid residue which was dried overnight in vacuum at 60 °C and weighed. The weight difference between the starting chitin sample and the solid recovered after the HT treatment corresponded to the amount of either chitin or its low molecular weight derivatives formed during the HT treatment, which was soluble in water. This was referred to as “soluble fraction”;

ii) a solution which was added with 10 mL of NaOH 0.1 M to prevent nanoparticles aggregation, filtered on a syringe filter (0.22 µm) to remove eventual macro residues, and finally dialysed against water (1 L) using 1 kDa MWCO membrane bags for 48-56 hours. During dialysis, water was replaced many times until no fluorescent impurities were detected outside of the bag. The final solution was then freeze dried to powder and labelled CTN-CDs (chitin-derived carbon dots).

In analogy to N-CQDs, **Figure 4.10** displays NMR analysis of the CTN-CDs after purification, showing a silent profile and thereby confirming the effectiveness of the dialysis.

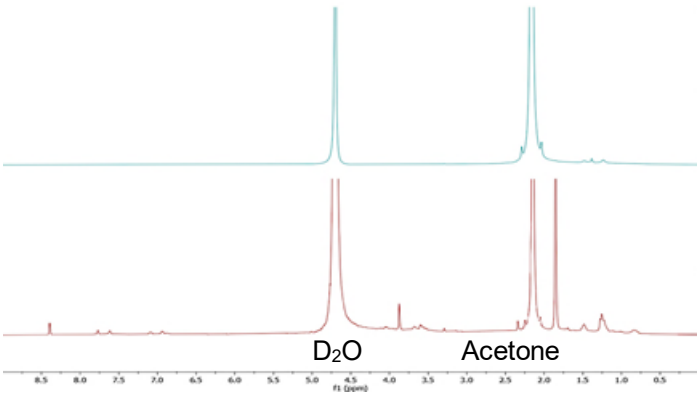

Figure 4.10. ^{1}H-NMR spectra of CTN-CDs crude (red lines, bottom) and after dialysis purification (green lines, top). D_2O was used as solvent and acetone as internal standard in the purified sample.

The same ball-milling pretreatment and the subsequent HT processing were then applied using Australian Spanner crab shells (1.5 g) as biowaste-derived instead of raw chitin. In this case, crab shells were collected at the local Sydney Fish Market, gently cleaned with water, dried under vacuum at 60 °C overnight and coarsely ground before ball milling.

At the end of the overall work-up, a brownish fine powder was obtained and labelled CRB-CDs (crabs-derived carbon dots). Results of combined mechanochemical treatment and HT synthesis are summarised in **Table 4.2**.

Table 4.2. Combined mechanochemical and HT experiments on chitin and crab shells. Raw chitin (1.5 g/sample) was subjected to HT treatment at 220 °C (entries 1-4). Milled chitin and milled crab shells (1.5 g/sample each) were subjected to 7 cycles of ball milling (15 min each at 25 Hz) followed by HT treatment at 220 °C (entries 5-8 and 9).

Entry	Starting material	HT treatment, Time (h)	Soluble fraction[a] SF, (wt.%)	Carbon dots yield (wt.%, mg)
1	*Raw chitin*	0.3	9	Nd [b]
2		2.0	18	0.9, 14
3		6.0	23	1.7, 26
4		24.0	48	2.5, 38
5	*Milled chitin*	0.3	20	Nd [b]
6		2.0	40	2.0, 30
7		6.0	46	2.5, 38
8		24.0	*62*	3.9, 59
9	*Milled crab shells*	24.0	27	3.4, 51

[a] Soluble “chitin” in water: this fraction was determined gravimetrically by the weight difference between the starting chitin sample and the solid recovered after the HT treatment.
[b] Not determined.

Both the soluble fraction and the yield of carbon-dots were affected by the duration of the HT treatments and the nature of starting material. The solubilised fraction of raw chitin increased from 9 to 48 wt.% as the HT treatment was prolonged from 20 min to 24 h (entries 1-4). However, at comparable HT processing times (20 min-6 h), the amount of milled chitin (or its light derivatives) soluble in water was almost doubled than for the raw polymer (cf. entries 1-3 to 5-7). This trend was consistent with the above-described XRD and FT-IR data

from which milled chitin resulted as an amorphous solid with a substantially poor H-bonding network, features that made the polymer more water-soluble. At a prolonged HT time up to 24 h, the increase of solubilised fraction, albeit evident and still higher for milled than for raw chitin, was less pronounced, thereby suggesting that the solubilised fraction itself was probably reaching a threshold/saturation solubility limit (cf. entries 4 and 8).

A negligible, apparently not determinable yield of carbon dots was achieved after a HT treatment as short as 20 minutes (entries 1 and 5). Though, the liquid fraction recovered at the end of the experiments with both raw and milled chitin exhibited a blue fluorescence under UV irradiation (365 nm), indicating the onset of processes of rearrangement and aromatisation of some surface chitin functions towards the formation of carbon dots. Increasing the HT processing time from 2 to 24 h brought about an increase of the CDs yield from 0.9 to 2.5 wt.% and 2.0 to 3.9% for raw and milled chitin, respectively (entries 2-4 and 6-8). This trend closely resembled that observed for the soluble fraction: this led us to conclude that compared to raw chitin, the larger formation of CDs yield obtained for mechanochemically pretreated chitin was plausibly due to a larger amount of amorphous chitin (or its lighter derivatives) acting as a CDs precursor in solution during the HT process.

A separate consideration should be made for the results achieved for milled crab shells. Crustaceans' shells are comprised of ca. 20–30% chitin, 30–50% minerals (mainly calcium carbonate), 30–40% proteins and other substances including lipids (up to 14%) and pigments (e.g., astaxanthin).[93] This composition could explain the moderate SF observed after the HT processing of milled crab shells (27 wt.%, entry 9). However, the corresponding CDs yield was surprisingly high and comparable to that obtained for milled chitin (3.4 *vs* 3.9 wt.%; cf. entries 8 and 9), thereby contrasting the above-mentioned assumption that the solubilised fraction and the formation of CDs were related to each other. This discrepancy has been associated to the fact that the final nanocarbon material incorporated some mineral components of the crab shells, which could not be removed during the purification (dialysis) step. This aspect will be further elucidated in the next paragraphs where the characterisation of CDs is described.

Zinc plating experiments

Edge plating experiments in asymmetric Zn||Cu *and* Zn||Cu-In *cells*

In-situ optical microscopy investigations were carried out to evaluate the dendrite suppression effect of the synthesised nanomaterials. Zinc plating experiments were carried out using customised asymmetric Zn||Cu cells (as shown in **Figure 4.11**), each filled with 0.6-0.7 mL of an aqueous 2M $ZnSO_4$ electrolyte containing one among our additives: N-CQDs, CTN-CDs, or CRB-CDs. A current density of 10 mA/cm^2 was applied for four hours while a microscopy camera was set on top, focused on a 1.0 mm length of the Cu-electrode to observe the metal deposition process from a side perspective.

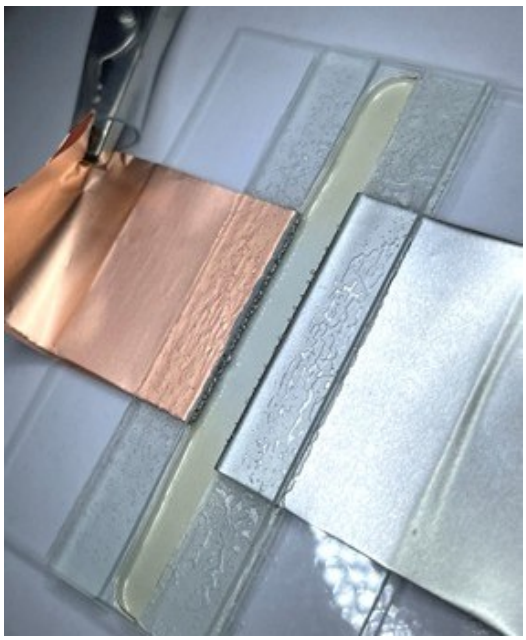

Figure 4.11. The customed asymmetric Zn||Cu cell assembled using Zn and Cu thin metal foils folded onto the side edges of two 0.1 cm thick microscope glass slides, used as structural support. The two electrode-slides were positioned parallel to each other at 7 mm distance, and two additional glass slides were then glue on the top and bottom, effectively immobilising the configuration.

Firstly, our model material N-CQDs was tested. A control experiment was also set up at the described conditions to represent the worst-case scenario, using as an electrolyte the same 2 M $ZnSO_4$ solution without any additive (pH = 4.24). In the absence of the CDs-based additive, aggressive zinc deposition occurs from the very beginning of the experiment, leading to a non-uniform plating characterised by bulky metallic formations, containing evolving hydrogen gas bubbles, resulting overall in dendritic growth across the entire area observed (**Figure 4.12A**). When the citric acid-derived nanoparticle modified N-CQDs-$ZnSO_4$ electrolyte (pH = 4.38) was used exceptional improvement could be observed. The

nanoparticles efficiently promoted the uniformity of the zinc deposition, resulting into a tightly packed layer of regular small crystals, completely suppressing dendrite formation even after four hours of plating (**Figure 4.12B**).

The voltage polarisation recorded during the plating experiment performed with the modified electrolyte doubled that of the control test, moving from 0.08 V to 0.16 V, consistent with a reduced conductivity, due to the N-CQDs material interacting with Zn^{2+}, regulating zinc deposition.

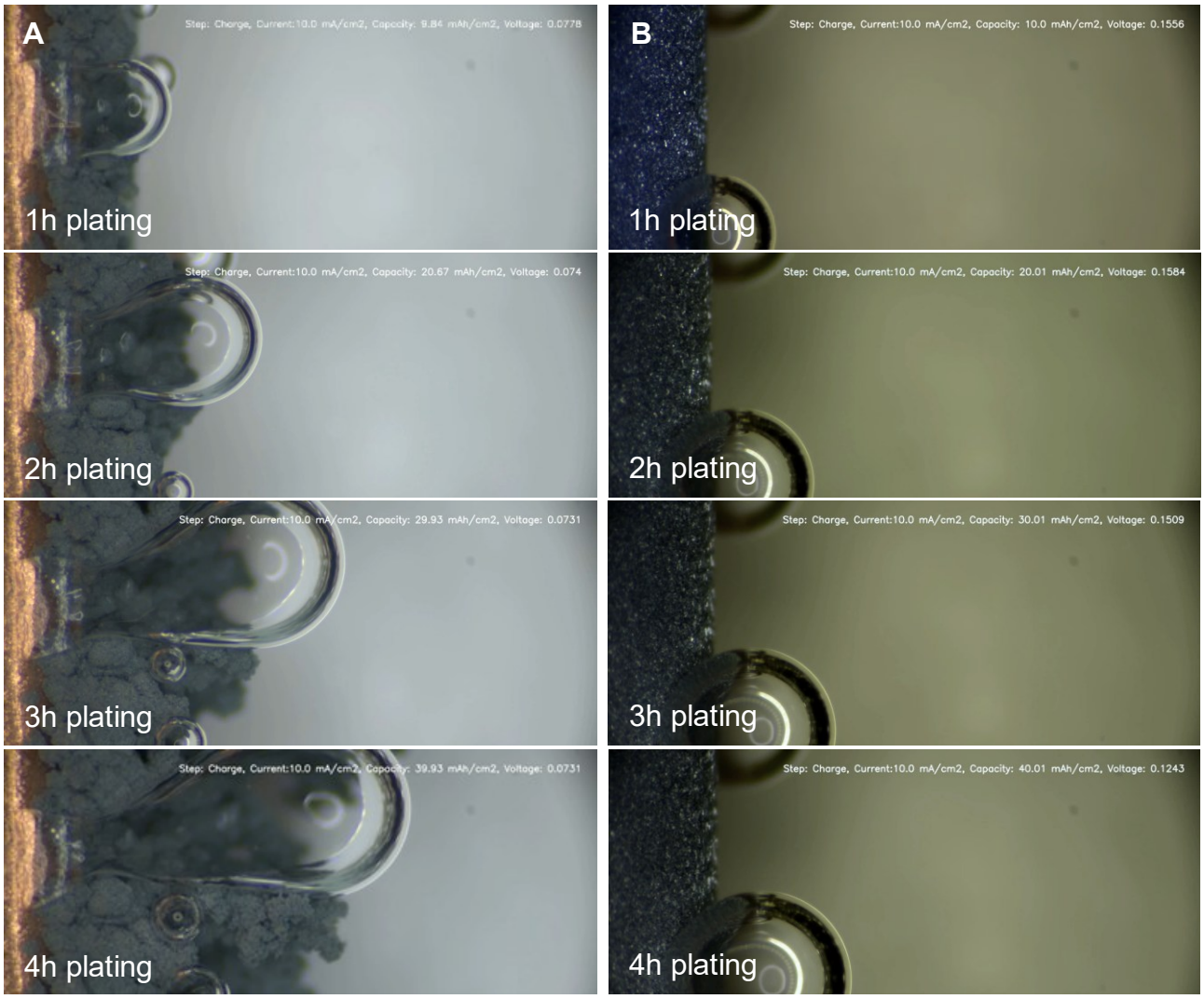

Figure 4.12. Zinc plating experiments performed at 10 mA/cm^2 for 4 h, in asymmetric Zn||Cu cells using **A:** bare 2M $ZnSO_4$ as control test and **B:** our modified N-CQDs-$ZnSO_4$ electrolyte.

At the end of the 4 hours of plating, the cell was stripped under symmetric electrochemical conditions to evaluate the reversibility of the zinc deposition. The current was inverted to induce a controlled anodic process at the Cu-electrode surface, while maintaining the same current density magnitude (10 mA/cm^2) and current flow duration (4 h) to promote the

dissolution of the previously deposited zinc back into the electrolyte. The stripping behaviour was carefully monitored with the same in-situ optical setup for both the control test and the modified N-CQDs-$ZnSO_4$ electrolyte operating cell.

As for the plating experiment, the control cell operating with just an 2M $ZnSO_4$ solution as an electrolyte exhibited irregular dissolution features during the stripping, with disruptive detachment of whole metallic zinc chips and clusters from the electrode surface, indicative of a heterogeneous and inefficient stripping process (**Figure 4.13A**). By contrast, the electrolyte containing the N-CQDs-based additive promoted a more homogeneous and gradual stripping, allowing a fine redissolution of metallic zinc into the electrolyte and its conversion into Zn^{2+}, ultimately confirming the enhanced stability of the electrode-electrolyte interphase and reversibility of the zinc plating/stripping process (**Figure 4.13B**).

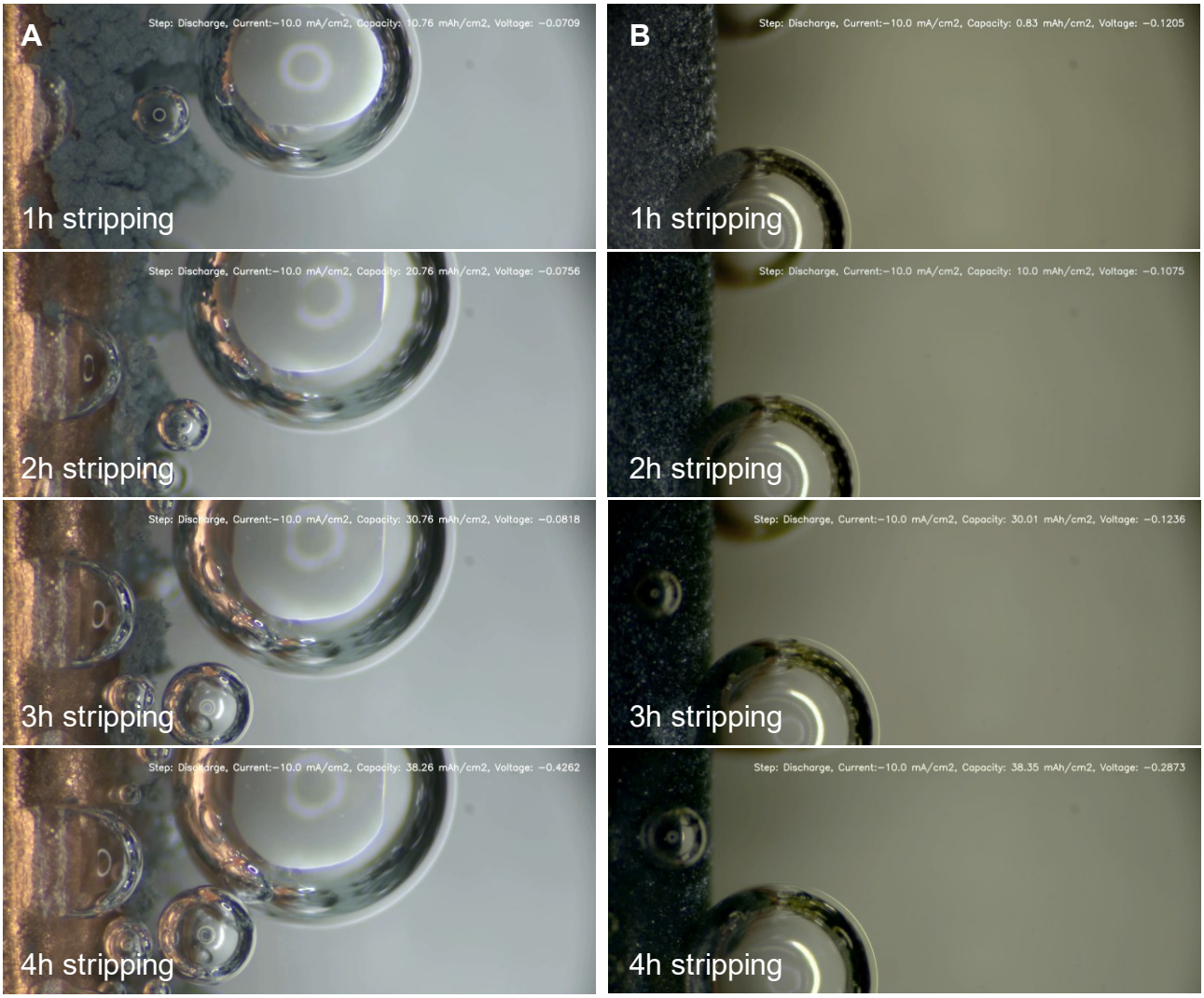

Figure 4.13. Zinc stripping experiments performed at -10 mA/cm^2 for 4 h, in asymmetric Zn||Cu cells using **A:** bare 2M $ZnSO_4$ as control test and **B:** our modified N-CQDs-$ZnSO_4$ electrolyte.

These experiments clearly demonstrate that the introduction of the N-CQDs nanomaterial as an electrolyte additive significantly improves the cell stability and the overall zinc plating on the electrode surface, resulting in a more controlled and uniform metal deposition.

Although the use of our N-CQDs-based electrolyte led to excellent results in terms of dendrite suppression, it was not sufficient to fully inhibit HER on the electrode surface. Attempts to eliminate the gas evolution by progressively increase the dots concentration up to 3.5 mg/mL (also identified as the solubilisation limit of the material in 2M $ZnSO_4$ aqueous solution) were unsuccessful. Not only were HER never completely mitigated, at concentrations higher than 3 mg/mL, bubbles (gas) generation increased. This is consistent with a reduction of the HER overpotential, induced by the presence of the dots. Indeed, some of the functional groups can be viewed as catalytic for the HER, in contrast to, e.g., glassy carbon surface that exhibits a very high HER overpotential.

The N-CQDs were derived from commodity chemicals and in that sense serve as a model material. The main focus in the context of the Thesis was the generation and use of CDs from renewable and waste sources, i.e. chitin and crab shells. Accordingly, CTN-CDs-$ZnSO_4$ (pH = 4.36) and CRB-CDs-$ZnSO_4$ (pH = 4.26) electrolytes, were also tested for the suppression of dendrite formation under identical plating conditions (10 mA/cm^2, 4 h). In contrast to the N-CQDs-$ZnSO_4$ electrolyte, the zinc deposition process within these systems appeared less uniform and progressively disturbed by the developing of hydrogen bubbles. Indeed, a pronounced HER occurred in both cases at the Cu electrode, starting from the very beginning of the experiments (**Figure 4.14A-B**).

When comparing to the control without additives (**Figure 4.12A**), the zinc plating observed for both chitin- and crab shells-derived nanomaterial additives was still more regular, i.e. disruptive nucleation and dendrite formation did not occur along the entire electrode surface, but was limited to the area where the bubbles were emerging from (and anchored to) the surface, suggesting that there was an interplay between the lower overpotential associated with sites where HER takes place preferentially and zinc nucleation. This can be rationalised by those sites having a higher surface energy and the zinc plating reducing that energy. Over time, these preferential zinc nucleation sites will lead to an increasing disruption of the local electric field homogeneity and consequently induce non-uniform current densities across the electrode, which, in turn, will lead to a further acceleration of dendrite formation.

Consistent with this model, in both cases the zinc deposition became increasingly irregular, and from the third hour of plating additional dendritic structures were observed to form

at/near the bubble adhesion sites, suggesting that, although the CDs-based additives themselves exhibited potential for promoting homogeneous metal deposition, their stabilising effect was hindered by HER, which prevented their aggregation locally and largely inhibited their protective effects.

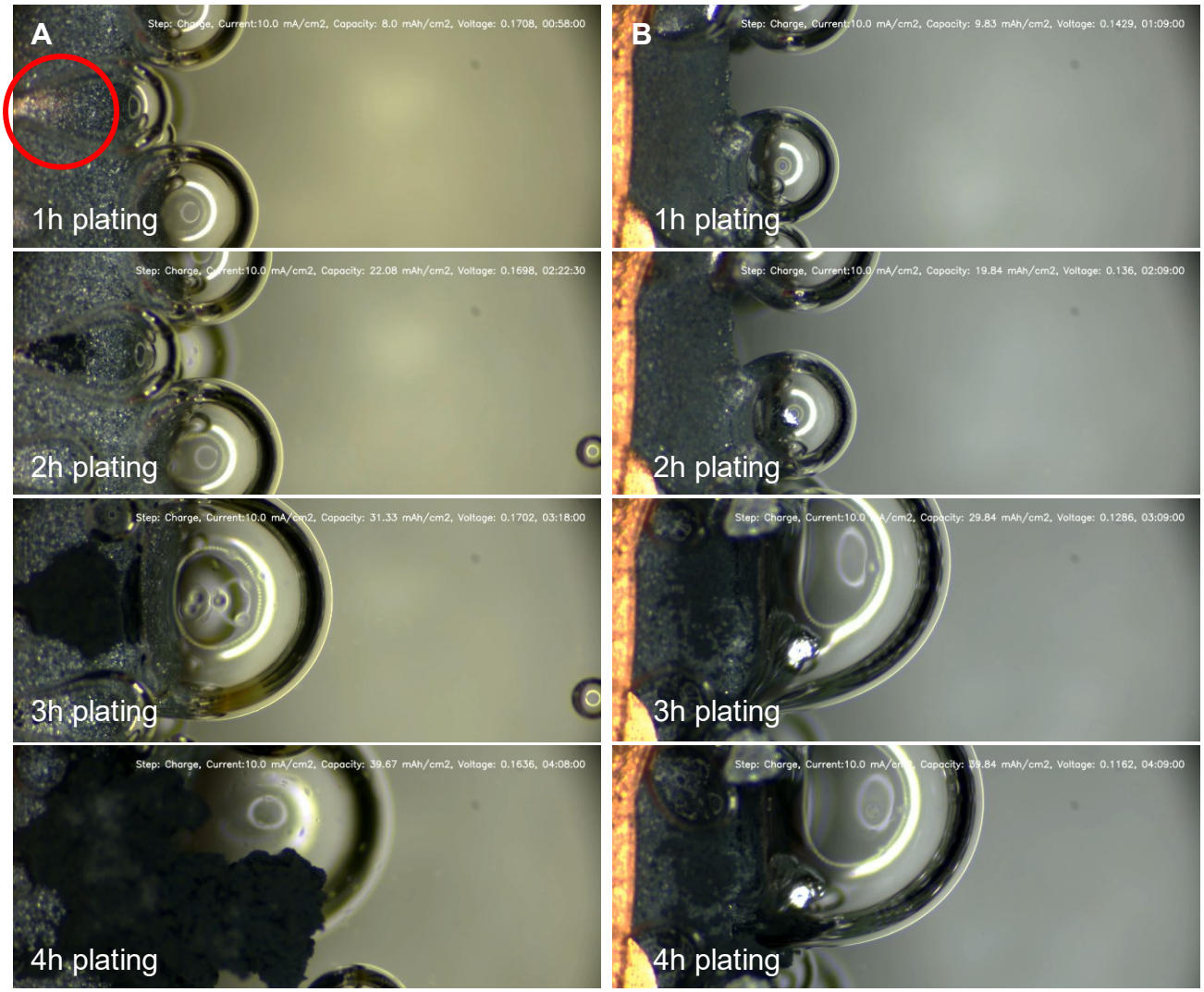

Figure 4.14. Zinc plating experiments performed at 10 mA/cm^2 for 4 h, in asymmetric Zn||Cu cells using our modified **A:** chitin-derived CTN-CDs-$ZnSO_4$ and **B:** crab shells-derived CRB-CDs-$ZnSO_4$ electrolytes.

To overcome the limitations of our systems, a multi-component approach was developed combining our CDs-based additives for dendrite suppression with Indium as an HER-mitigating agent. Indium is already known to efficiently reduce HER by increasing the overpotential in the zinc alloy it forms and promoting horizontal growth of zinc along the (002) crystal facet. In addition, it is well established that indium suppresses localised pH fluctuations on the electrode surface, inhibiting the formation of alkaline by-products and

promoting electrochemical stability and cycling longevity, making it an effective additive in aqueous energy storage systems.[94]

Indium was introduced into our Zinc plating experiments in the form of electrochemically deposited coating on the anode surface, by applying a potential of -0.8 V for 60-90 seconds to a Cu thin foil electrode immersed into a 0.1 M $InCl_3$ + 0.1 M KCl aqueous solution. The resulting Indium-coated Cu electrodes (**Figure 4.15A**) were then gently polished with ethanol on a lint-free tissue and used to assemble a customised Zn||Cu-In cell (**Figure 4.15B**), similarly as previously described.

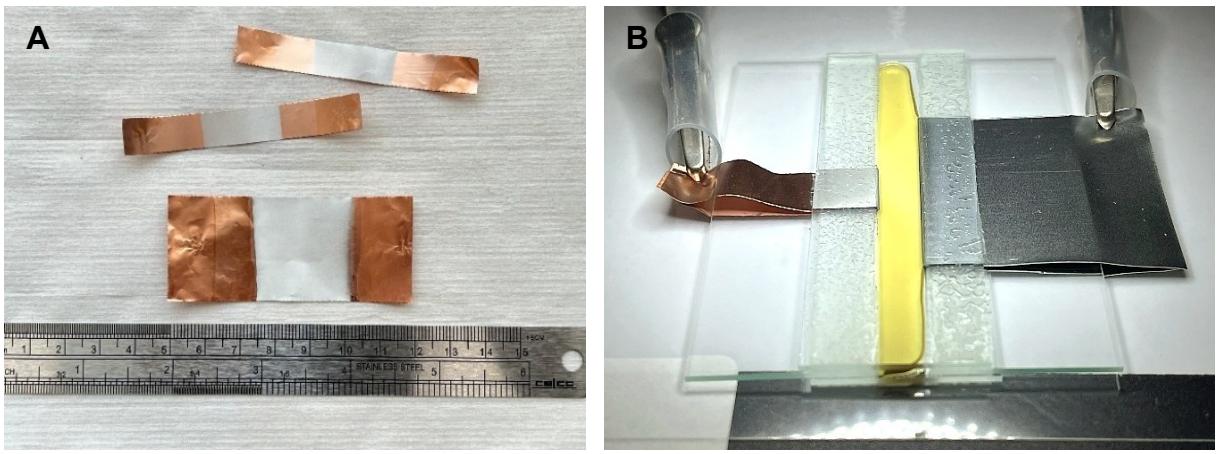

Figure 4.15. A: The indium-coated Cu electrodes obtained through electrochemical deposition, and **B**: the final customed asymmetric Zn||Cu-In cell.

Again, a 2 M $ZnSO_4$ solution without any additive (pH = 4.24) was used as an electrolyte for the control experiment. However, since the indium coating itself could also reduce the zinc nucleation overpotential while forming the alloy, as well as regulate the electric field local inhomogeneities delaying the formation of dendrites, a higher current density of 20 mA/cm^2 was required with this new configuration to replicate the morphologies observed previously. As before, the control (**Figure 4.16A**) produced large, faceted zinc crystalline protrusions with visible irregular morphology. Due to the higher current density, these were already visible within the first hour of plating. After three hours, pronounced dendritic structures started to grow from this increasingly rough surface, extending towards the electrolyte, and ultimately exacerbating into a surface fully covered by dendrites after four hours of plating.

Subsequently, a fresh solution of the modified N-CQDs-$ZnSO_4$ electrolyte (pH = 4.17) was tested in the new Zn||Cu-In cell configuration (**Figure 4.16B**). At the end of the experiment

the zinc layer turns out to be still intact, not showing any dendrite formation or protrusion. The synergistic effect of indium on suppressing HER enabled a clear observation of the intrinsic role of the dots in suppressing dendrites formation and promoting, once again, a highly uniform zinc deposition composed of numerous small, regularly arranged crystals forming a smooth surface. This highlights the remarkable efficiency of this additive in regulating the zinc ions distribution, with no visible degradation of both electrode surface and electrolyte even after four hours at a high current density.

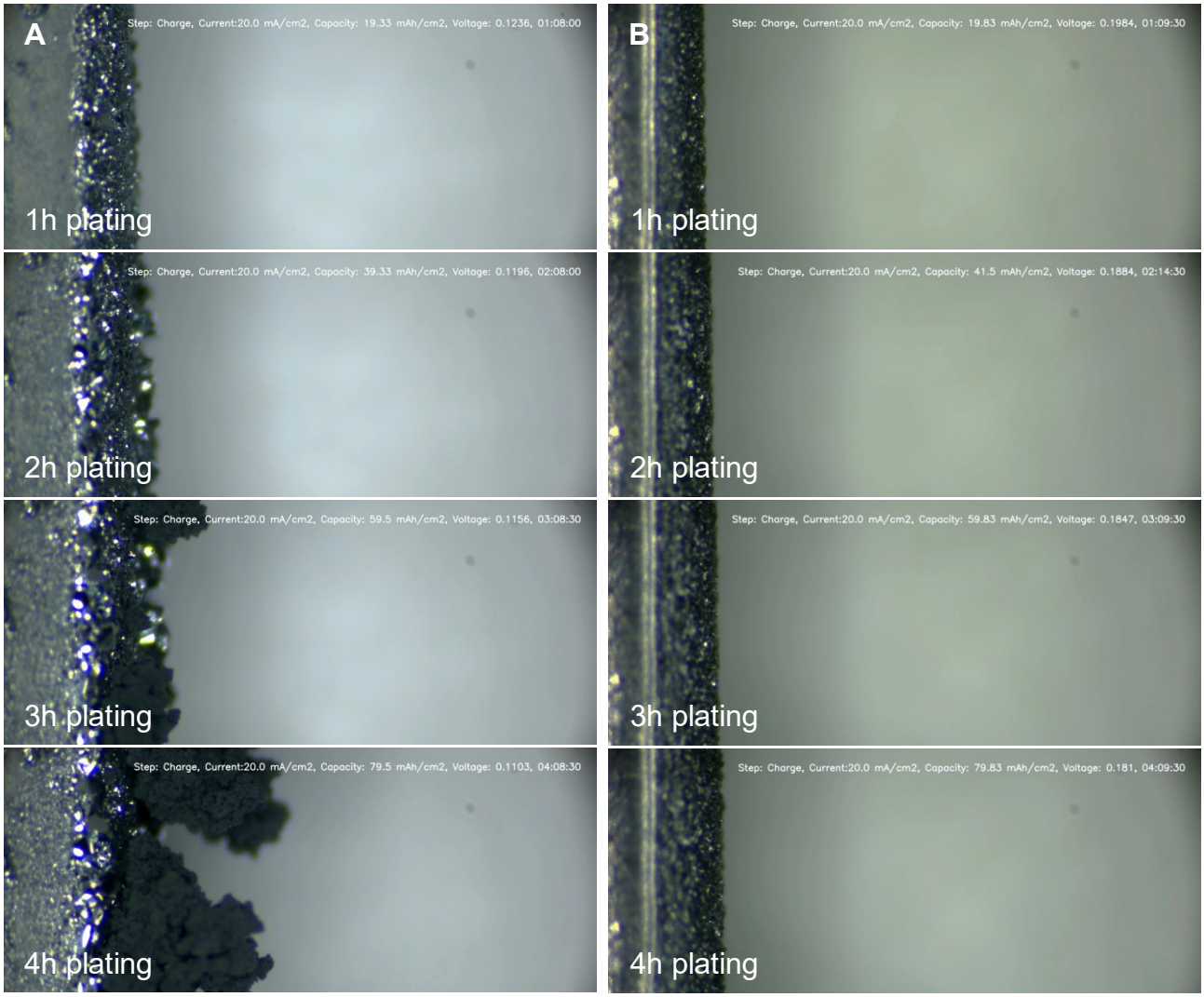

Figure 4.16. Zinc plating experiments performed at 20 mA/cm^2 for 4 h, in asymmetric Zn||Cu-In cells using **A:** bare 2M $ZnSO_4$ as control test and **B:** our modified N-CQDs-$ZnSO_4$ electrolyte.

In a further step, the modified CTN-CDs-$ZnSO_4$ (pH = 4.31) and CRB-CDs-$ZnSO_4$ (pH = 4.26) electrolytes were tested under the same electrochemical conditions (20 mA/cm^2, 4 h). Unfortunately, some issues emerged during the zinc plating experiments performed with the CTN-CDs-$ZnSO_4$ electrolyte (**Figure 4.17A**), as this chitin-derived material appeared to only

partially regulate the plating, yielding to small and mostly homogeneously distributed crystals during the first hour with subsequent overgrowth of few disseminated large zinc crystals which, much like the hydrogen bubbles observed in previous experiments, creating preferential reduction pathways for zinc deposition and, as a consequence, dendrite nucleation. By contrast, the crab shells-derived CRB-CDs-$ZnSO_4$ electrolyte yielded excellent plating performance (**Figure 4.17B**), consistent with an effective modulation of zinc ion distribution, leading to the formation of small, homogeneously distributed zinc crystals.

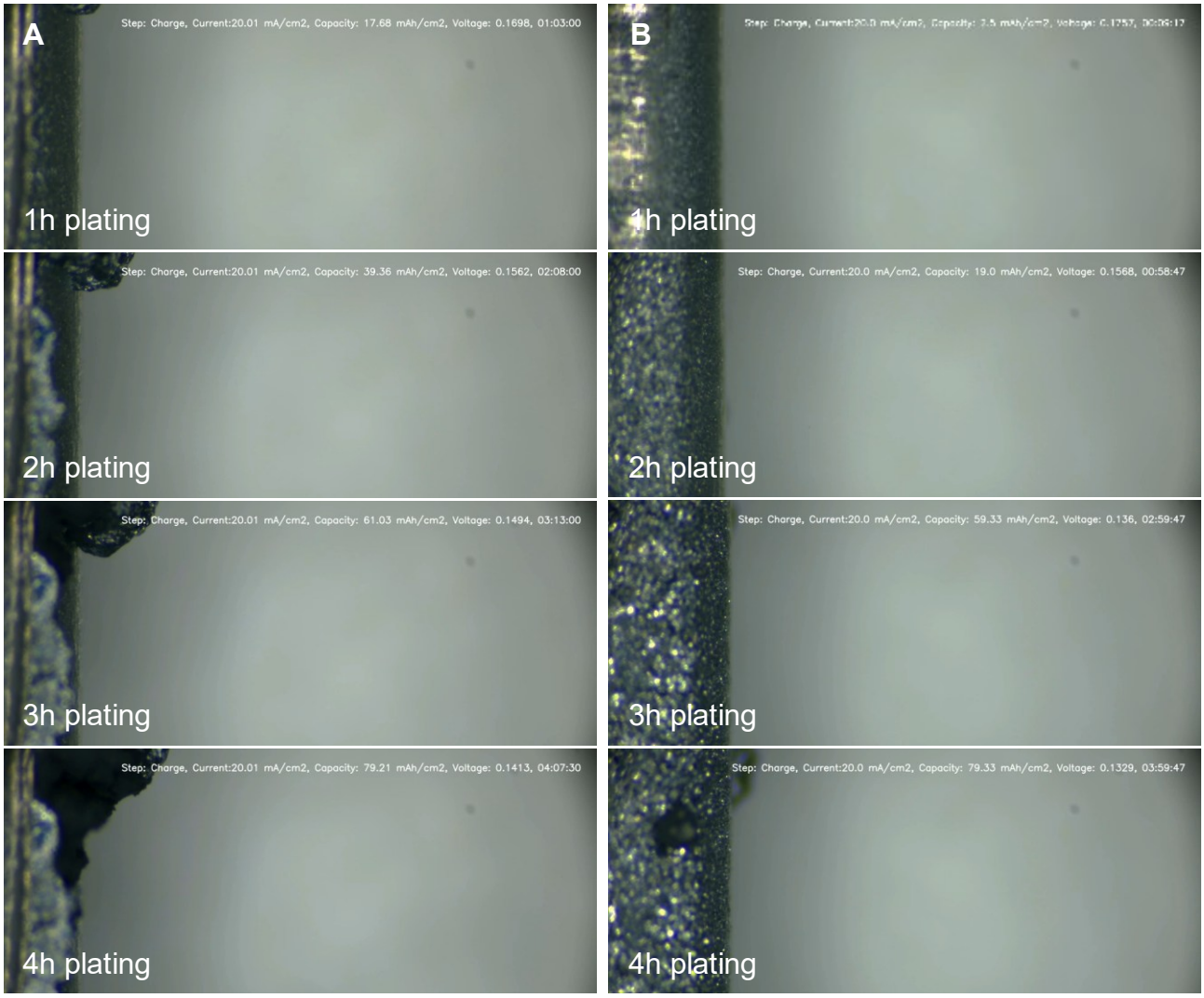

Figure 4.17. Zinc plating experiments performed at 20 mA/cm^2 for 4 h, in asymmetric Zn||Cu-In cells using our modified **A:** chitin-derived CTN-CDs-$ZnSO_4$ and **B:** crab shells-derived CRB-CDs-$ZnSO_4$ electrolytes.

Notably, although the experiment was performed at a current density of 20 mA/cm^2, only a couple of appreciable larger than the median-sized zinc clusters could be observed at the very end of the four-hour plating process, consistent with the excellent performance of the

CRB-CDs in the indium-free experiment, but now more clearly detectable in the absence of any appreciable HER activity.

Again, the voltage polarisation recorded during the zinc plating experiments in the new Zn||Cu-In cells increased when the modified electrolytes were used, moving from 0.12 V of the control test to 0.20 V, 0.17 V and 0.18 V when the N-gCQDs-$ZnSO_4$, CTN-CDs-$ZnSO_4$ and CRB-CDs-$ZnSO_4$ electrolytes were used, respectively, and similarly to the increase observed in the previous Zn||Cu configuration (0.08 V to 0.16 V). This higher voltage reflects the kinetic limitation introduced by the presence of the additive, which interacts with Zn^{2+} slowing down their transport and nucleation by a comparable increase in potential despite the different starting conditions.

This behaviour would be also consistent with the formation of a CDs-based self-assembled dynamic layer, which protects the electrode surface and regulates zinc deposition through the mechanism previously described in Section 4.1.

Similarly to the experiments previously conducted with the asymmetric Zn||Cu cells, the stripping processes in the new Zn||Cu-In cell configuration were conducted at the end of the 4 hours of plating, under symmetric electrochemical conditions (20 mA/cm^2, 4 h) to evaluate the reversibility of zinc deposition. **Figure 4.18** shows the stripping experiments performed with the N-gCQDs-$ZnSO_4$ and CRB-CDs-$ZnSO_4$ electrolytes, respectively. Due to the development of dendritic structures and parasitic reaction during the plating experiment with the CTN-CDs-$ZnSO_4$ electrolyte, the stripping process was uncontrolled and therefore not reported. During both the high-current stripping experiments, a significant gas evolution was observed on the electrode surface in parallel to the zinc redissolution. This phenomenon was primarily attributed to oxygen evolution reaction (OER), promoted by local field inhomogeneities at such high current densities. Overall, gas evolution in this case was not severe enough to hinder the progress of the zinc stripping process.

The N-CQDs-$ZnSO_4$ electrolyte promoted a gradual and homogeneous stripping behaviour up to the third hour, enabling a fine redissolution of the metallic zinc into the electrolyte. However, at such harsh conditions, which push the conversion kinetics of the deposited zinc into Zn^{2+}, larger zinc clusters began detaching from the electrode surface towards the fourth hour of stripping, suggesting partial additive degradation at high current density (**Figure 4.18A**). By contrast, the CRB-CDs-$ZnSO_4$ electrolyte promoted a fully controlled and uniform stripping process, even outperforming the model material, and resulted in a smooth, cluster-free electrode surface at the end of the experiment (**Figure 4.18B**).

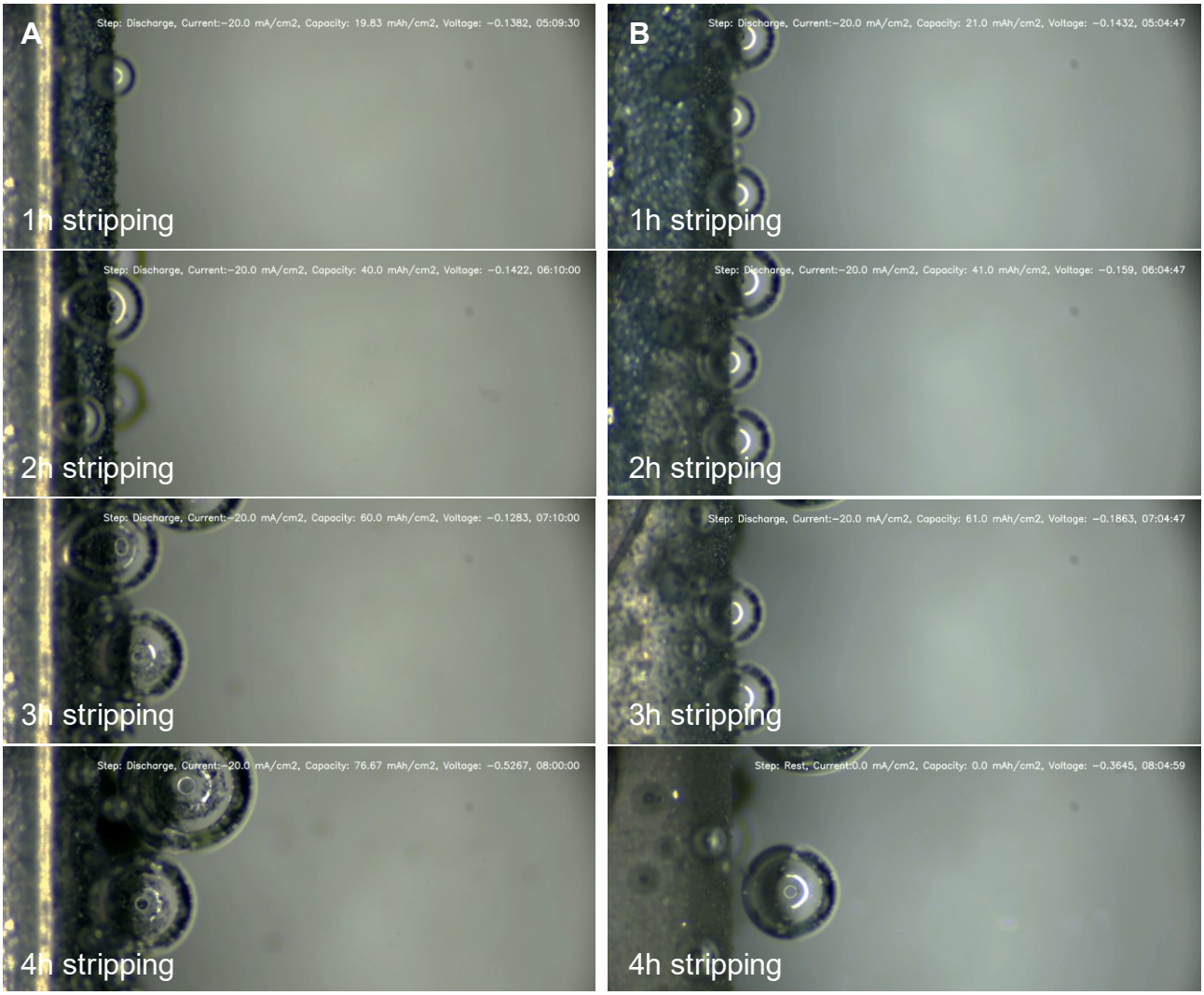

Figure 4.18. Zinc stripping experiments performed at -20 mA/cm^2 for 4 h, in asymmetric Zn||Cu-In cells using **A:** our modified N-CQDs-$ZnSO_4$ and **B:** crab shells-derived CRB-CDs-$ZnSO_4$ electrolytes.

Overall, the results of the plating experiments performed in both Zn||Cu and Zn||Cu-In configurations clearly indicate that the tested CDs-based additives contribute to regulating zinc deposition and promoting the formation of a near dendrite-free plating. Among them, the crab shells-derived material exhibited the best overall performance, particularly in terms of plating reversibility and stability at high current densities (up to 20 mA/cm^2). This behaviour can be attributed to one or more of the CDs action mechanisms described in Section 4.1. It is reasonable to assume that the dots strongly interact with Zn^{2+} within the electrolyte, altering its solvation shell and mobility in solution. Such interactions likely slow down the zinc deposition kinetics while promoting a local preconcentration of zinc ions near the electrode surface, thereby maintaining a consistent ionic reservoir. As a result, zinc nucleation becomes more uniform, and the crystal size decreases forming a more evenly

distributed layer, while effectively suppressing dendrites formation. These findings highlight the potential of such sustainable nanomaterials as promising and cost-effective additives for enhancing the performance and safety of AZIBs. To further clarify the relationship between the characteristics of nanomaterials and their ability to regulate zinc deposition, a detailed characterisation of their physicochemical properties is presented in the following section.

The three modified N-gCQDs-$ZnSO_4$, CTN-CDs-$ZnSO_4$ and CRB-CDs-$ZnSO_4$ electrolytes were also tested, along with the control 2M $ZnSO_4$ solution, in zinc plating experiments performed on transparent 3D-printed asymmetric Zn||Cu cells, using 12 mm round-shaped metal foil electrodes (**Figure 4.19A-B**). The aim of these additional experiments was to obtain representative zinc-deposited electrodes for SEM analysis.

Figure 4.19A: The round shaped Cu electrodes after the zinc plating experiments, and **B**: transparent 3D-printed asymmetric Zn||Cu cells configuration.

Once assembled, each cell was filled with 1 mL of the selected electrolyte and operated at a constant current density of 4 mA/cm^2 for 2 h – representing a worst-case scenario for this configuration. The cell was disassembled; the plated electrodes were gently rinsed with Milli-Q water and dried under N_2 flux. Optical microscopy images (**Figure 4.20A-D**), revealed clear morphological differences with CDs additives giving more homogeneous crystals.

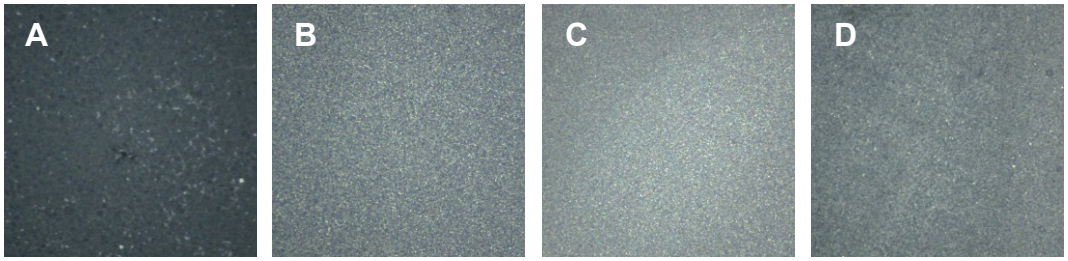

Figure 4.20. Optical microscopy images (magnification 40x) of electrode surfaces plated with **A:** bare 2M ZnSO4, **B:** N-gCQDs-$ZnSO_4$, **C:** CTN-CDs-$ZnSO_4$ and **D:** CRB-CDs-$ZnSO_4$ electrolytes.

Nanomaterials Characterisation

Optical properties

N-CQDs synthesised from citric acid and DETA displayed an UV-Vis spectrum (reported in **Figure 4.21**, solid blue profile) with absorption bands at 243 and 353 nm, typical of the strong π-π* transition of the conjugated carbonaceous core and the weaker n-π* transition related to the heteroatom (N and O) doping, respectively.[34] Bio-sourced nanomaterials, i.e. CTN-CDs and CRB-CDs samples, showed UV-Vis absorption in the same region of N-CQDs, but the corresponding profiles (solid light blue and orange curves in **Figure 4.21**, respectively) were characterised by broad absorption bands that started around 400 nm and whose intensity increased progressively towards lower wavelengths. This behaviour reflected the complexity of the matrices (chitin and crab shells) from which CTN-CDs and CRB-CDs were obtained, compared to the pure chemicals used for N-CQDs.[35]

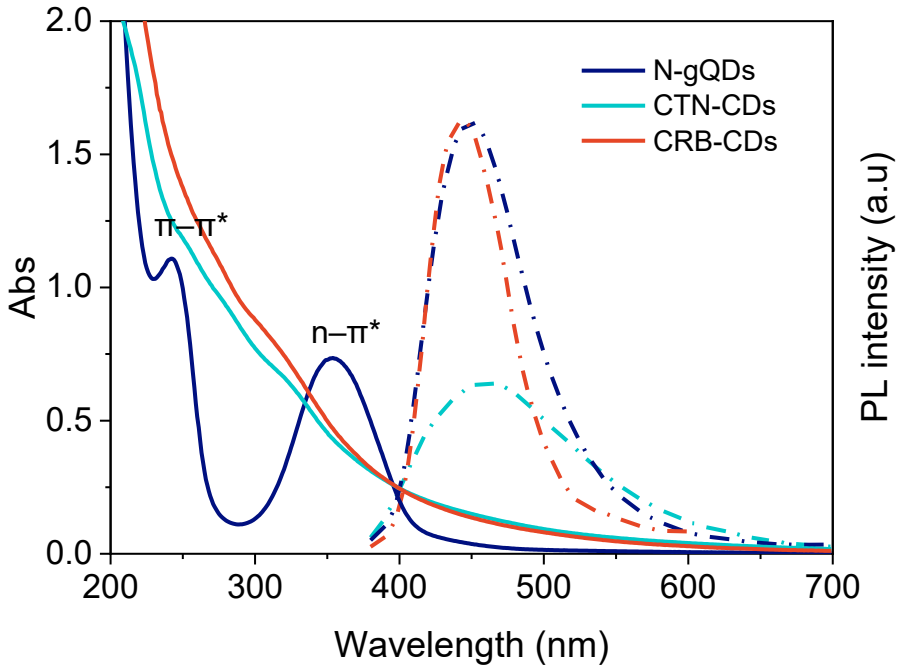

Figure 4.21. Optical properties of N-doped CDs. UV-Visible absorption (solid profiles) and photoluminescence (PL, dotted profiles) spectra of N-CQDs (blue), CTN-CDs (light blue) and CRB-CDs (orange) materials.

Photoluminescence (PL) spectra of the three materials (**Figure 4.21**, dotted lines) were recorded using an excitation wavelength of 355 nm, within a comparable absorbance range of 65-83% and using water as solvent. All three samples, when excited in the region of the n-π* transition, exhibited a significant emission centred around 450 ± 15 nm, consistent with

the predominant blue fluorescence observed for all of them. Interestingly, the emission peak of the CRB-CDs sample (orange) was the sharpest one, followed by that of the N-CQDs sample (blue). By contrast, the CTN-CDs spectrum (light blue) displayed a broader emission profile, potentially suggesting the presence of multiple emitting species (e.g. fluorophores heterogeneously decorating the outer shell of the dots).[15]

Infrared spectroscopy

FT-IR analyses were carried out to investigate the chemical composition of the synthesised nanomaterials and provide insights on the functional groups that decorated the outer shell of the nanodots. Results are shown in **Figure 4.22A-C.**

The occurrence of nitrogen doping in N-CQDs was indicated by the presence of both low intensity signals around 1180-1300 cm^{-1} related to C-N stretching vibrations and a more intense adsorption at 1647 cm^{-1} attributed to C=N groups. Stretching vibration at 1356 cm^{-1} was associated to carboxylate group, confirming the presence of surface carboxylic functionalities, while the sharp peaks at 1537 cm^{-1} and 1693 cm^{-1} were typical of C=C and C=O stretching vibrations, respectively (**Figure 4.22A**).

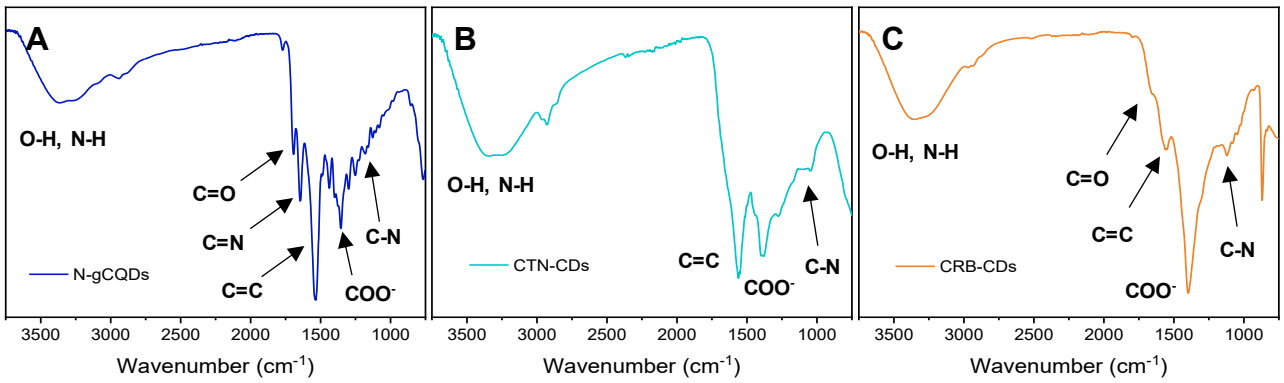

Figure 4.22. Fourier Transform Infrared (FT-IR) spectra of **A:** N-CQDs (blue), **B:** CTN-CDs (light blue) and **C:** CRB-CDs (orange) materials.

As for N-CQDs, FT-IR spectra of both CTN-CDs and CRB-CDs showed signals consistent with C-N vibrational frequencies at 1175 and 1116 cm^{-1}, respectively. The two spectra also show stretching signals of carboxylate groups at 1388 and 1397 cm^{-1}, as well as the typical stretching vibrations of C=C moieties at 1557 and 1558 cm^{-1}, respectively (**Figure 4.22B-C**). In addition, CRB-CDs spectrum also shows a low signal at 1660 cm^{-1} related to C=O frequencies. Within this sample, the prominence of the COO^- signal, along with the presence

of a sharp peak at 870 cm^{-1} (absent in the CTN-CDs spectrum), can be associated to calcium carbonate residues, suggesting that some of the mineral component of the starting crab shells was retained by the carbon nanoparticles, thereby supporting the fact that the unexpectedly high yield of CRB-CDs (**Table 4.2**, entry 9) was due a partial contamination of the material. Moreover, all spectra show other bands in the regions at 2855-2975 cm^{-1}, 3245-3250 cm^{-1}, and 3380 cm^{-1}, attributed to C-H, N-H, and O-H stretching, respectively.

X-ray photoelectron spectroscopy

XPS analyses were performed with the aim to further characterise the surface elemental composition of the nanomaterials. **Figure 4.23** displays the deconvoluted high resolution spectra of C1s, N1s and O1s for N-CQDs (**A-C**), CTN-CDs (**D-F**) and CRB-CDs (**G-I**), respectively, while survey XPS spectra of the same materials are reported in **Figure 4.24**.

N-CQDs. The C1s spectrum of this material showed three main peaks attributed to graphitic/sp^2 carbon (284.4 eV), C=N functionalities (285.6 eV), and carbonyl group (287.5 eV), respectively (**Figure 4.23A**). The presence of classic pyridinic and pyrrolic/amine-type nitrogen atoms was confirmed by two main peaks at 399.4 eV and 400.3 eV in the N1s spectrum (**Figure 4.23B**). This confirmed the incorporation of nitrogen into the carbonaceous matrix either in planar (sp^2) or a more oxidized form. Finally, the O1s spectrum (**Figure 4.23C**) displayed three main contributions from carbonyl species (530.5 eV), carboxyl groups (531.3 eV), and C-OH species (531.9 eV). The overall elemental composition of this material was C = 68%, O = 20% and N = 12%, and proved a significant nitrogen content.

CTN-CDs. The C1s spectrum of this material showed four main peaks which were associated to graphitic/sp^2 carbon (284.4 eV), aliphatic or N-adjacent carbon functionalities (285.0 eV), carboxyl (286.2 eV) and carboxylate functionalities (288.4 eV), potentially consistent with chitin rearrangements (**Figure 4.23D**). A broad signal of low intensity centred at 399.7 eV in the N1s spectrum was assigned to C-N amine/amide groups and suggested a modest retention of nitrogen from N-acetyl groups of the starting chitin (**Figure 4.23E**). Finally, the O1s spectrum displayed three major contributions associated to carboxyl groups, C-OO/C-OH mostly from esters/alcohols groups and C-OH species related to residual alcohol moieties at 531.4 eV, 531.9 eV, 532.9 eV, respectively (**Figure 4.23F**). The elemental composition of this material confirmed a carbon-rich surface (72%) with a significant oxygen content (26%) and a minor nitrogen doping (2%).

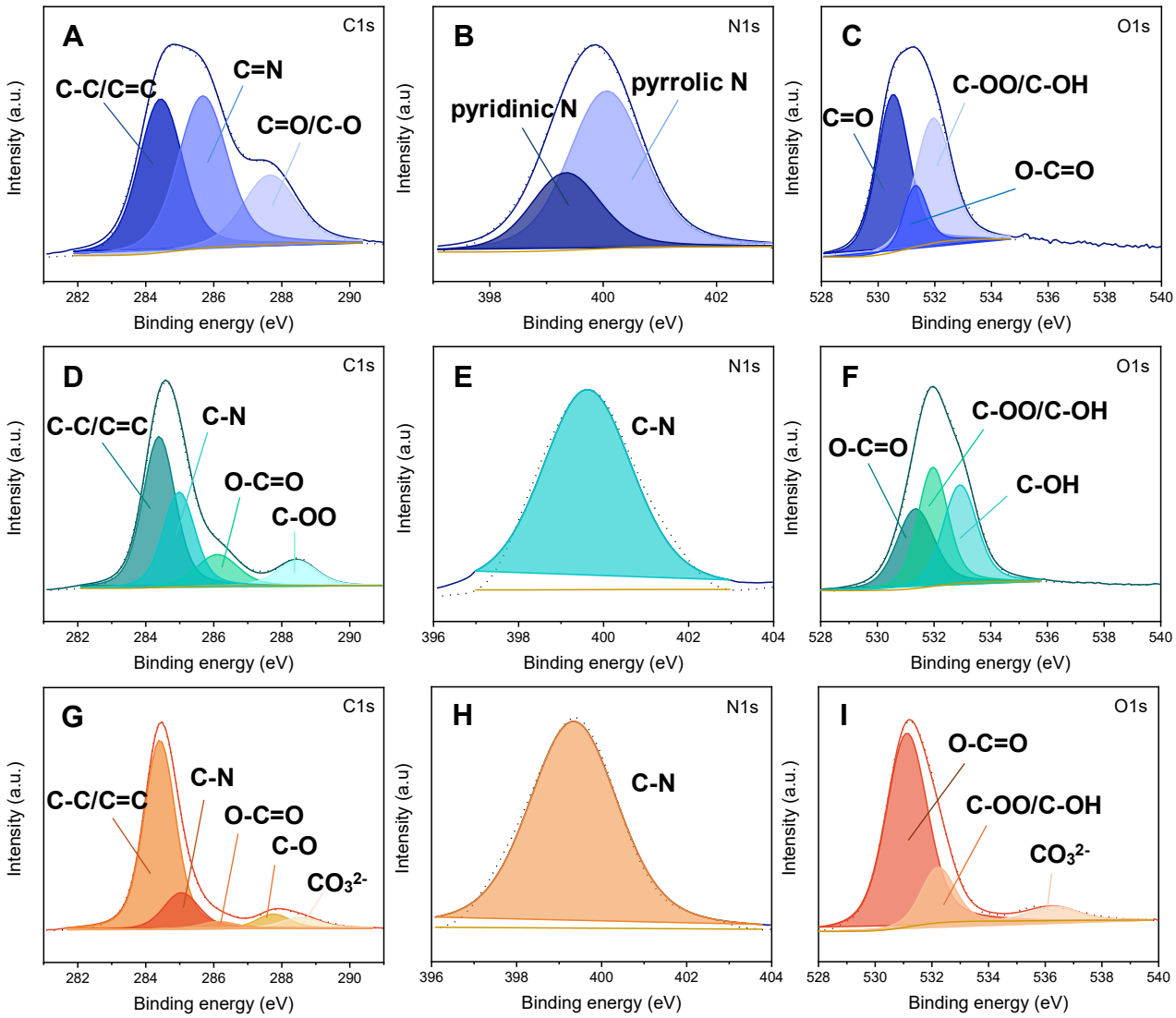

Figure 4.23. XPS spectra of C1s, N1s and O1s for N-CQDs (**A-C**), CTN-CDs (**D-F**) and CRB-CDs (**G-I**).

CRB-CDs. The C1s spectrum of this material was comprised of five main components related to graphitic/sp^2 carbon (284.4 eV), C-N functionalities (285.1 eV), carboxyl functionalities (286.2 eV), C-O oxygenated groups (287.8 eV) and a broad peak at 288.6 eV attributed to carbonate-like species derived from inorganic salts as mineral contaminants of the nanoparticles, mostly $CaCO_3$ (**Figure 4.23G**). This was further confirmed by a check of the CRB-CDs survey spectrum that showed a Ca2p doublet signal at 347.1 eV. The results agreed with the FT-IR analysis of the same material (**Figure 4.22C**) consistent with the presence of calcium minerals from the crab shells. As for the chitin-derived sample, a broad signal of low intensity centred at 399.3 eV in the N1s spectrum was assigned to mixed C-N contributions from amides and pyrrolic/amine group (**Figure 4.23H**). Finally, the O1s spectrum displayed three main contributions from carboxyl groups (531.1 eV), C-OO/C-OH

mostly from esters/alcohols groups (532.2 eV), and a broad peak at 536.3 eV that was attributed to the carbonate-related species from the mineral content of the crab shells (**Figure 4.23l**). The elemental composition of this material proved that its surface was slightly richer in carbon (73%) than CTN-CDs, with an oxygen content of 26%, a poor nitrogen doping (1.8%), and a calcium content of 2.2%.

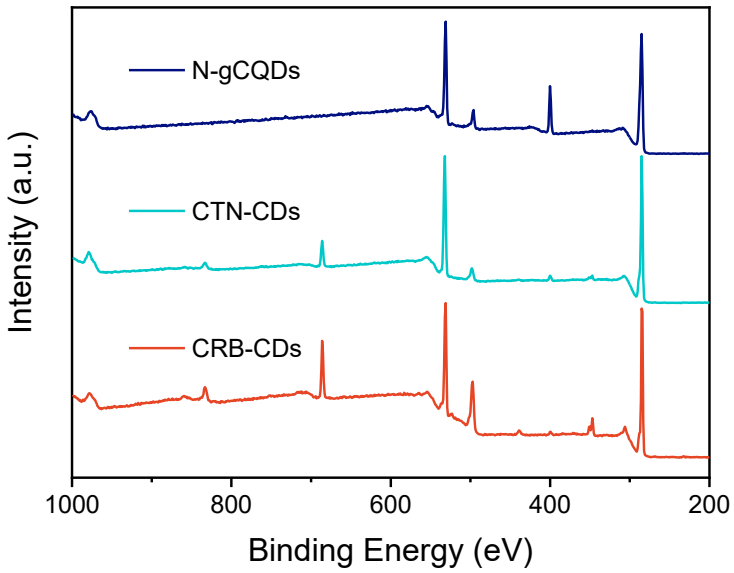

Figure 4.24. Survey XPS spectra of N-CQDs, CTN-CDs and CRB-CDs: blue, light blue and orange profile, respectively.

Overall, the nitrogen content of the bio-sourced CTN-CDs was significantly lower (2%) than expected, and far lower than that of N-CQDs (12%). Among the factors responsible for this result, the availability of nitrogen in the starting materials could play a critical role: in chitin, nitrogen is supplied in the form of acetyl amide groups, which are less reactive than the free amine groups in DETA. This difference plausibly affected the incorporation of nitrogen into the carbonaceous core of the nanomaterial, with hydrolysis and deamination processes overbearing recondensation and aromatisation, in contrast to what is typically observed in the synthesis of the N-CQDs material [ref].[35] Even more complex was the case of CRB-CDs: the starting biomass, crab shells, contains both chitin (20–30 wt.%) and proteins (30–40 wt.%) as potential N-donors,[95] but the N-doping of the resulting nanomaterial was slightly lower than that from pure chitin (CTN-CDs). This result suggested the hydrothermal treatment used for the CDs synthesis was poorly effective to remove proteins from the shells or alternatively, proteins (if detached and released in the aqueous medium) were not suitable precursors to incorporate N in the CDs. Beyond this, the CRB-CDs nanomaterial was contaminated by $CaCO_3$.

In addition, XPS and FT-IR characterisation results of CTN-CDs and CRB-CDs materials slightly differ. Especially the oxygen-containing functional groups abundantly detected by XPS are less detectable in the IR spectra. Since FT-IR provides bulk information whereas XPS is surface-sensitive, this discrepancy may indicate that C=O groups are mainly confined to the surface. What is clear, however, is that the presence of these oxygenated moieties is particularly prominent in the CRB-CDs, where they evidently play a crucial role in coordinating Zn^{2+} in solution, modulating the plating process.

Transmission Electron Microscopy

TEM analyses were then performed to further investigate the morphology of bio-sourced nanomaterials. The chitin-derived sample, CTN-CDs (**Figure 4.25, left**), showed mainly amorphous and irregular aggregates, probably related to residual chitin fragments or partially undegraded residues, sporadically characterised by the presence of small and scattered graphene-like domains. By contrast, the crab-derived material, CRB-CDs (**Figure 4.25, right**) revealed a well-dispersed cluster of nanodots, with diameters below 10 nm and a clearly appreciable graphitic lattice fringes, confirming the partial graphitisation of the carbon framework and the presence of crystalline graphene-like domains, typical of well-structured carbon Quantum Dots (CQDs).

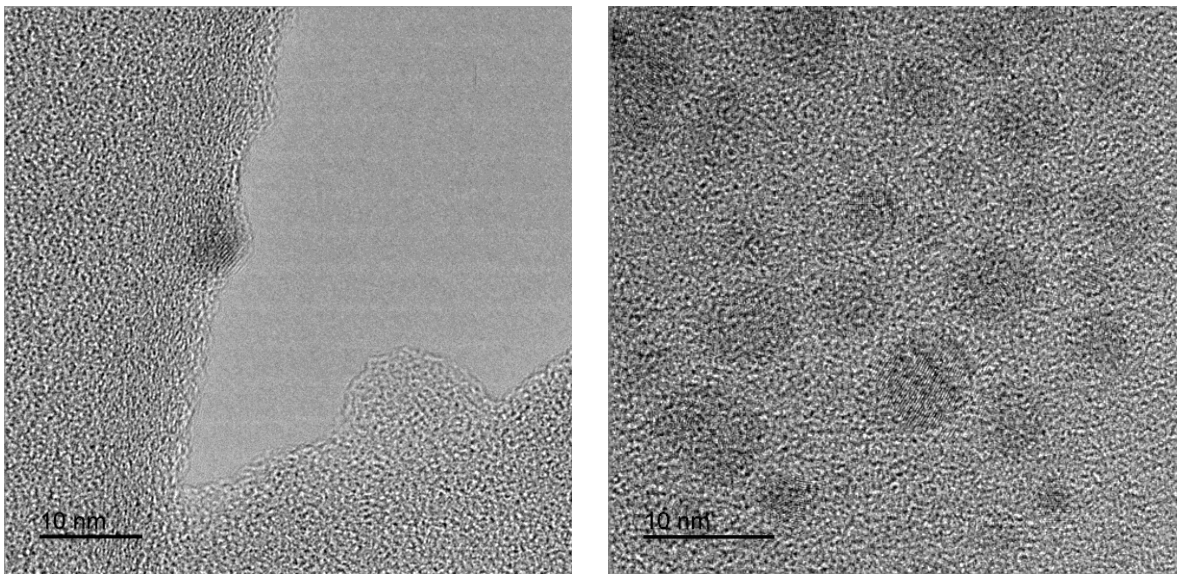

Figure 4.25. TEM images of CTN-CDs (left) and CRB-CDs (right) materials.

Overall, also the TEM analysis appears to be consistent with the observations made during the plating experiments. The crab-derived CRB-CDs material exhibits a more extended conjugated domain and a well-defined crystalline structure, which are likely to positively influence their electrical conductivity. Combined with the abundance of oxygen-containing functional groups, these features contribute to the excellent zinc plating performance. By contrast, the chitin-derived sample appears less structured, with electronic characteristics only partially comparable to those of typical carbon nanodots, which is reflected in its poorer plating stability and overall performance.

Electrolytes Characterisation

The three modified electrolytes used in the plating experiments were prepared through an operationally simple procedure, by dissolving 0.5 mg/mL of the selected sample into a 2M $ZnSO_4$ aqueous solution. The mixture was then ultrasonicated for 10 minutes and filtered through a 0.22 µm syringe filter to remove any undissolved residues. The resulting electrolytes were labelled N-CQDs-$ZnSO_4$, CTN-CDs-$ZnSO_4$ and CRB-CDs-$ZnSO_4$ respectively and were tested in comparison to a plain 2M $ZnSO_4$ aqueous electrolyte as control test in the Zinc plating experiments. The excellent aqueous dispersibility of our additives was a key factor during the preparation of the electrolytes, which resulted in perfectly stable colloidal systems, despite the $ZnSO_4$ concentration of 2M.

Cyclic voltammetry (CV)

Within this work, the interaction between our synthesised nanomaterials and the zinc ions in the modified electrolyte systems was investigated by cyclic voltammetry (CV) analyses, which was very instructive regarding the impact of these additives onto the electrochemical properties of Zn^{2+}. All the measurements were carried out at a scan rate of 100 mV/s within a potential window from -1.2 to 0.0 V vs. Ag/AgCl. The CV profiles of the modified electrolytes (conc= 0.5 mg/mL) are reported in **Figures 4.26A-C** and compared to that of a bare 2M $ZnSO_4$ solution. The addition of the nanomaterials markedly decreased the intensity of both cathodic and anodic peaks (peak currents and peak potentials are reported in **Table 4.3**), suggesting a significant modification in the charge transfer process that occurs at the interface between electrode and electrolyte.

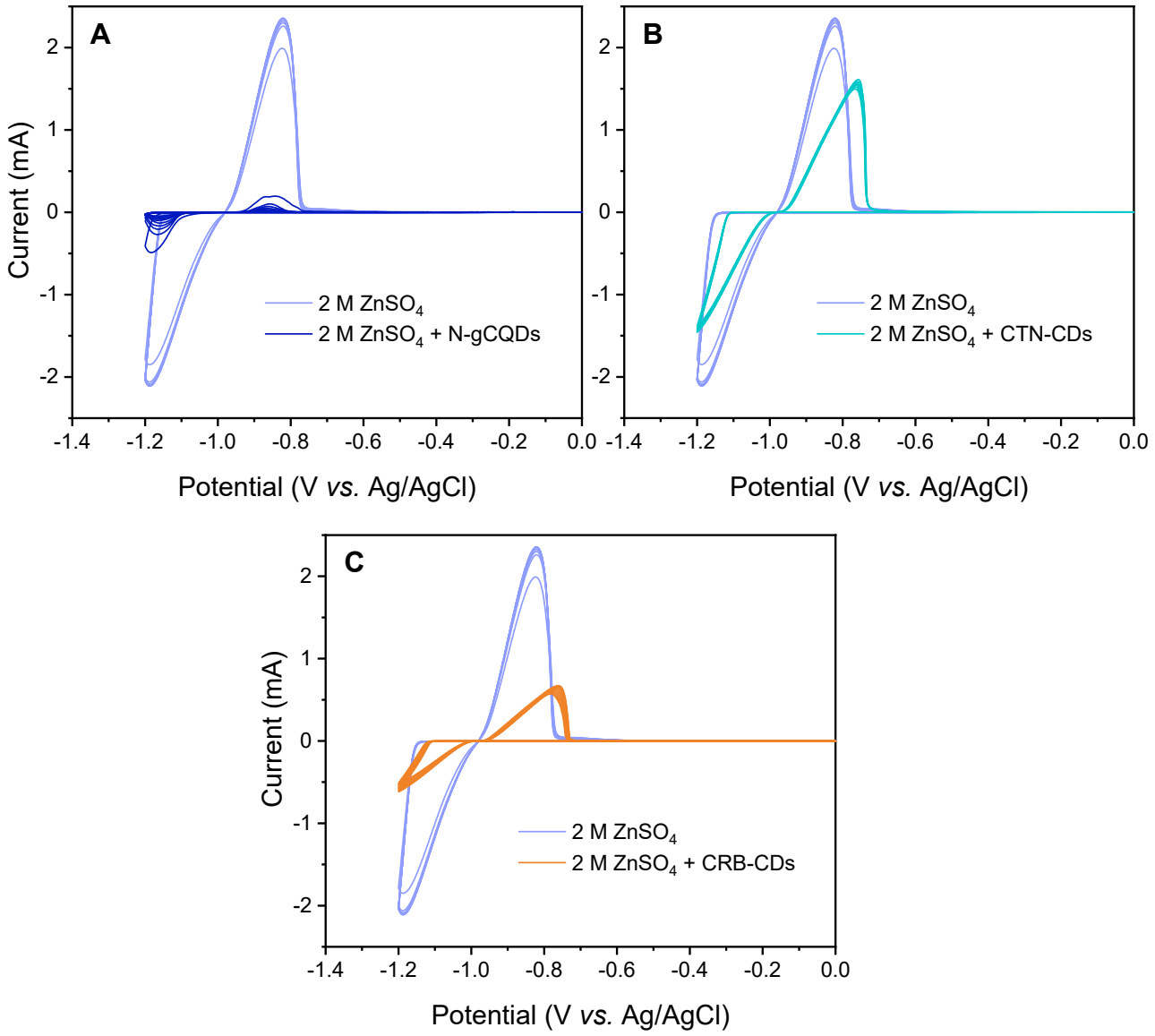

Figure 4.26. Cyclic voltammetry measurements of the three electrolytes **A:** N-CQDs-$ZnSO_4$, **B:** CTN-CDs-$ZnSO_4$ and **C:** CRB-CDs-$ZnSO_4$, compared to aqueous 2M $ZnSO_4$ (100 mV/s; E = -1.2 to 0.0 V vs. Ag/AgCl).

Table 4.3. Electrochemical parameters (onset and peak potentials, peak currents) derived from CV analyses.

Sample	E_{onset} Red.; E_{onset} Ox. (V vs Ag/AgCl)	Peak currents (mA) at peak potential (V)
$ZnSO_4$ 2M (blank)	-1.15 ; -0.76	i_c = -2.11 (-1.19); i_a = 2.35 (-0.82)
N-CQDs (0.5 mg/mL) in $ZnSO_4$ 2M	-1.18 ; -0.81	i_c = -0.27 (-1.17); i_a = 0.10 (-0.86)
CTN-CDs (0.5 mg/mL) in $ZnSO_4$ 2M	-1.11 ; -0.73	i_c = -1.46 (-1.2); i_a = 1.59 (-0.76)
CRB-CDs (0.5 mg/mL) in $ZnSO_4$ 2M	-1.12 ; -0.73	i_c = -0.56 (-1.2); i_a = 0.63 (-0.77)

The strongest current suppression was observed for the citric acid-derived N-CQDs, followed by a quite comparable effect for the biowaste-derived CRB-CDs. This suggested that both the model material and the crab-derived one strongly interacts with zinc, likely limiting the overall ion flux towards the electrode due to migration kinetics modulation or formation of a self-assembled protective interphase, which regulate diffusion and hinder fast nucleation. The chitin-derived CTN-CDs showed only a small influence on the measured current. This moderate reduction in peak current, compared to the blank, suggested only a partial modulation of Zn^{2+} flux, allowing relatively fast zinc deposition, in great accordance with the plating experiments observation.

In addition to such behaviour, changes in shape and position of the redox peaks associated with Zn^{2+} were also observed. Within the electrolytes containing CDs additives the two peaks appeared slightly broadened, with their maximum/minimum shifting away from their centre. An increased separation between the oxidation and reduction peak potentials was also noted, somehow indicating an altered reversibility of the electrochemical process.

Overall, these results are consistent with the structural observations from TEM and previous characterisation, which highlight the well-defined and surface groups-rich CRB-CDs material as the best candidate in representing a sustainable additive for AZIBs.

UV-Vis absorption spectroscopy

Changes also happen in the optical properties of the dots once added to the Zinc-based electrolyte. For instance, in **Figure 4.27** is possible to see a comparison between the fluorescent profile of the N-CQDs model material dispersed in milli-Q water or in 2M $ZnSO_4$ aqueous solution (concentration 0.5 mg/mL).

In both cases, the spectral profiles exhibited the absorption peaks attributable to the characteristic electronic transitions of the material. Whilst the absorption peak at 243 nm stands firm when changing solvent, a slight redshift of the main peak responsible for the fluorescence can be observed, moving from 353 nm to 360 nm when the interaction between the nanoparticles and the Zn^{2+} ions in solution as a chance to occur, potentially indicating an alteration in the local electronic environment of the nanoparticles.

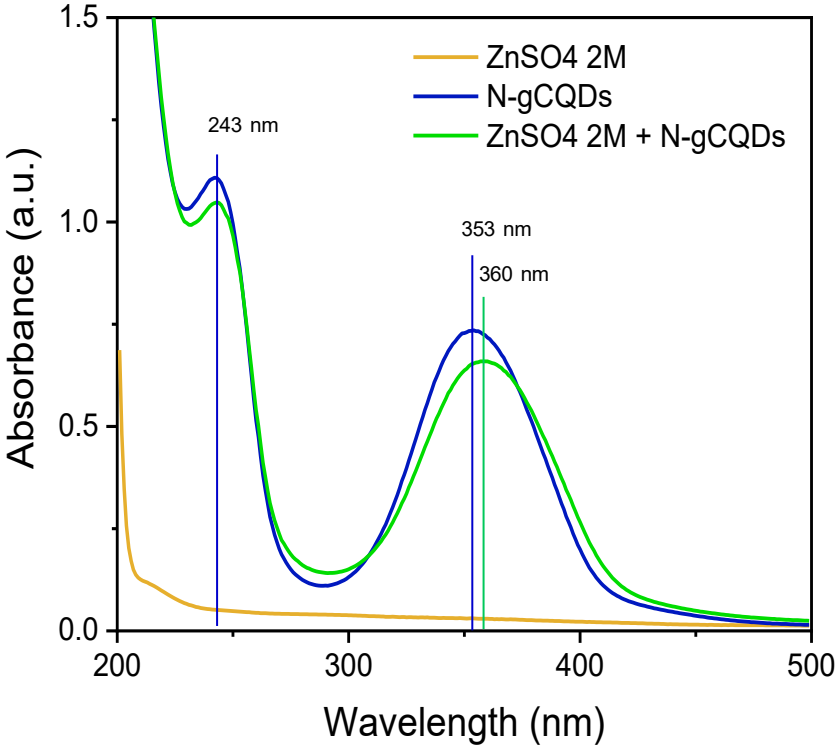

Figure 4.27. UV-Visible absorption spectra of N-CQDs in water (blue), bare 2M $ZnSO_4$ (yellow), and N-CQDs in 2M $ZnSO_4$ solution (green).

These observations suggest that the presence of the additives significantly influence the electrochemical characteristics of the system, likely by interacting with either the zinc ions in solution or the electrode surface. Therefore, our bio-sourced nanomaterials, thanks to the presence of defects and a variety of functional groups decorating their surface, might be able to replace some water molecules within the hydration shell of the Zn^{2+} solvated form, affecting the metal ions mobility towards the electrode surface. This behaviour has been previously reported in the literature and already discussed in Section 4.1, where several studies supported by DFT calculations have been reported to show that zincophilic carbon-based nanomaterials exhibit the ability to strongly interact with Zn^{2+}, likely modifying its solvation shell and promoting a more controlled and less disruptive charge transfer.[72]

Electrode surfaces characterisation

Scanning Electron Microscopy

SEM characterisation was performed to compare roughness and morphology of the deposited zinc layer, confirming a correlation between the use of CDs-based additives and the size/arrangement of the crystals obtained on the electrode surface (**Figures 4.28A-D**).

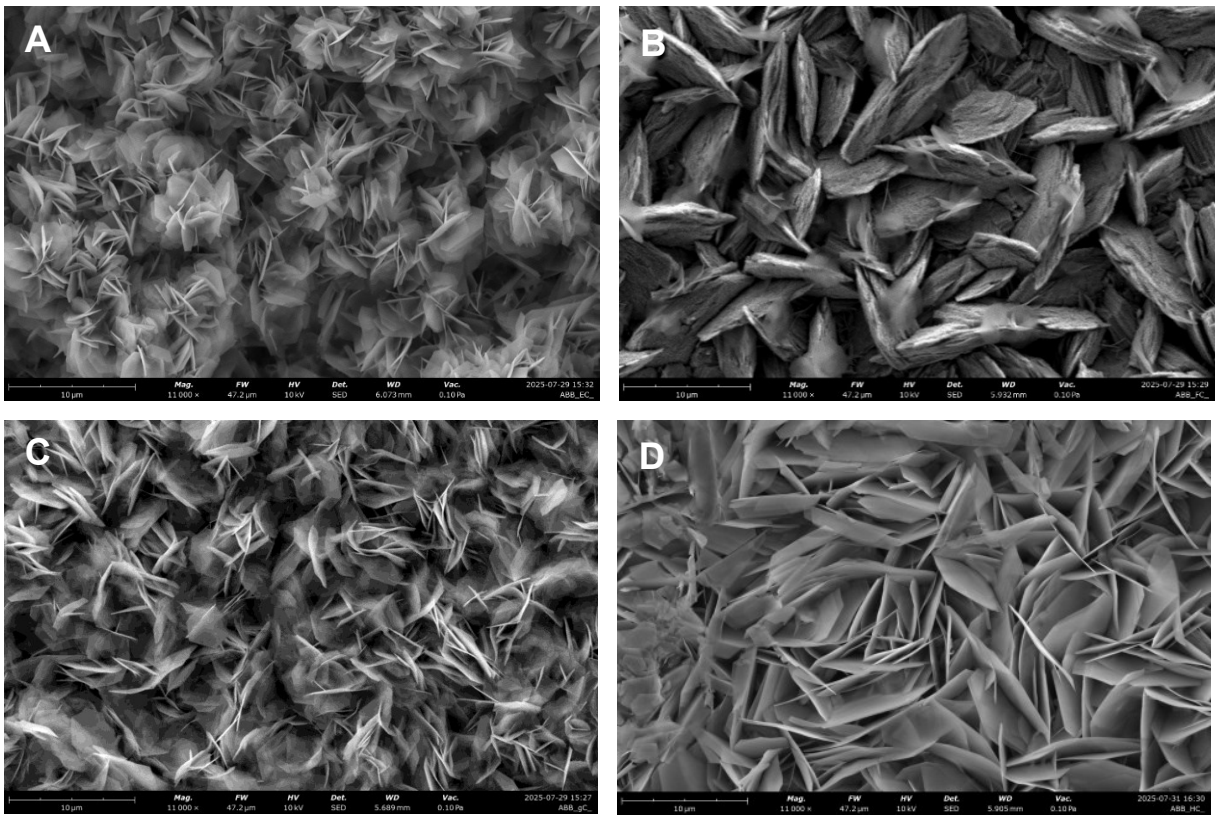

Figure 4.28. SEM images of zinc deposited with **A:** bare 2M $ZnSO_4$, **B:** CTN-CDs-$ZnSO_4$, **C:** N-CQDs-$ZnSO_4$, and **D:** CRB-CDs-$ZnSO_4$ electrolytes.

The SEM image in **Figure 4.28A** displays the surface morphology of the control test, in which zinc plating was carried out using bare 2M $ZnSO_4$ solution as an electrolyte.

SEM images reported in **Figure 4.28B-D** display the zinc-plated surfaces from the experiments carried out using the modified N-CDs-$ZnSO_4$, CTN-CDs-$ZnSO_4$ and CRB-CDs-$ZnSO_4$ electrolytes, respectively. This analysis outline again a behaviour consistent with the plating experiments and previous characterisation, showing that both the model material and the crab-derived one can deeply interact with the zinc deposition process, with the latter giving the best performance in terms of small crystal size and preferential distribution pattern mainly along the (100) plane, while the chitin-derived material is the most similar to the

control test. Nonetheless, across all analysed surfaces, the deposited crystals appear consistent in both type and size within each sample, meaning that each additive has an own behaviour potentially related to the physicochemical features related to electronical structure and surface functionalities.

The extensive characterisation carried out on both the nanomaterials (N-CQDs, CTN-CDs, and CRB-CDs) and their corresponding modified electrolytes (N-CQDs-$ZnSO_4$, CTN-CDs-$ZnSO_4$, and CRB-CDs-$ZnSO_4$) supported the understanding of the regulation mechanisms of the synthesised CDs and allowed correlating their physicochemical properties with their ability to modulate zinc plating. FT-IR and XPS analyses revealed a wide variety of surface functional groups (-OH, -CO, -COO^-/COOH, -CONH, -C=N-) decorating the outer shell of the CDs. The model material exhibited both oxygen- and nitrogen-based functionalities, while the chitin- and crab-derived samples were predominantly enriched in oxygen-based groups, as the nitrogen-doping strategy proved less effective. Nevertheless, the presence of electronegative heteroatoms, either oxygen or nitrogen, conferred all the nanodots active sites able to promote the interaction with Zn^{2+}, with the crab-derived material presenting the highest abundance of carboxylate and hydroxyl moieties. These functional groups together with a well-defined nanostructured crystalline domain allow to say that the sustainable crab-dots represent a valid alternative to conventional AZIBs additives. The plating experiments in asymmetric Zn||Cu-In cells visually corroborate these findings: both N-CQDs-$ZnSO_4$ and CRB-CDs-$ZnSO_4$ proved effective in regulating zinc distribution and nucleation, with the crab-derived material delivering the most stable and reversible plating/stripping performance, thanks to their ability to strongly interact with Zn^{2+}.

4.2.2 Conclusions

Overall, zinc dendrite formation is governed by a complex interplay of diffusion mechanisms and deposition kinetics, influenced by intrinsic electrode properties, electrolyte configuration, and the current density applied.[62] It has been demonstrated that a non-uniform electric field distribution on the electrode-electrolyte interphase is one of the primary factors promoting dendrite growth, leading to the irregular distribution of Zn^{2+} during the plating process.[66] Therefore, the progressive formation of surface asperities further amplifies local electric field inhomogeneities, triggering the so-called tip effect and directing zinc nucleation along preferential pathways, ultimately resulting in dendritic growth.

In this work, the synthesis and application of three different CDs-based additives – derived from citric acid, chitin, and directly from chitinous biowaste, respectively – were presented as surface-stabilising agents to promote uniform and controlled zinc deposition. Owing to their moderate electrical conductivity and the abundance of functional groups (-OH, -COOH, -C=O, $-NH_2$, -(C=O)NHR, as identified by FT-IR and XPS analyses) decorating their surface, our bio-sourced nanomaterials proved effective in regulating zinc plating, enabling dendrite-free deposition. In particular, the crab-derived CRB-CDs-$ZnSO_4$ electrolyte exhibited highly reversible behaviour in plating/stripping experiments, especially when combined with an indium coating that suppress HER at the electrode surface under high current density (20 mA/cm^2). However, Indium is recognised as a relatively rare and expensive metal, features that restrict the scalability perspectives of the processes in which it is involved,[96,97] and therefore the indium-CDs combination does not represent a definitive solution at this stage.

Further research efforts will be directed to deepen the characterisation of these nanomaterials to establish a stronger correlation between their physicochemical features and electrochemical performance. Moreover, taking inspiration from recent studies reported in literature – where, e.g., Cl-doped hydrophobic CDs proved effective in decreasing water activity by forming a repulsive dynamic adaptive interphase[74] – further engineering of the nanomaterials will be explored, especially in terms of co-doping strategies. This could improve their ability to suppress parasitic reactions on the electrode surface, even without the addition of external HER mitigating agents.

4.2.3 Experimental Section

Synthesis of the model N-CQDs

The citric acid-based carbon nanodots used as a model material were synthesised adjusting an already known procedure described in literature.[35] A solution obtained from 9.00 g of citric acid and 1.45 g of diethylenetriamine in 90 mL of Milli-Q water was sealed into an autoclave and heated at 180 °C for 24 h, yielding to a dark brown mixture that was then neutralised with NaOH 1 M filtered on filter paper and dried to powder to obtain 5.40 g of crude product (52 wt.% yield). 2.00 g of the so obtained crude product were then redissolved in 25 mL of milli-Q water and purified through a 15 cm of 1 kDa MWCO dialysis tubing against 1 L of Milli-Q water for 48-72 hours, changing water multiple (6-7) times until clear and no fluorescence was detected out of the bag. The retained solution was then freeze dried to powder to obtain 0.262 mg of pure product (13 wt.% yield on crude), labelled N-CQDs.

Synthesis of the chitin-derived carbon dots (CTN-CDs)

The vibrational ball mill used for the mechanochemical pretreatment arranges four Zirconia jars (50 mL volume), each one equipped with a Zirconia grinding ball (1.5 cm diameter) and loaded with 0.5 g of raw commercial chitin (purchased from Sigma-Aldrich). Milling procedure: 15 min milling at 25 Hz (≈1500 rpm) + 15 min break (to avoid overheating), repeated 7 times.[87] The chitin-derived carbon nanodots were synthesised loading 1.500 g of raw or milled chitin and 40 mL of Milli-Q water into a batch reactor of 45 mL of total volume, sealed and heated at 220 °C for the selected reaction time (20 min - 24 h). The mixture was then filtered under suction, and the solid residue was recovered and dried overnight in a vacuum oven at 60 °C, then weighed to determine the solubilised chitin by difference. The filtered solution was added of 10 mL of NaOH 0.1 M to prevent the carbon nanoparticles from aggregation, then purified by a 0.22 µm syringe filter to remove eventual macro residues and subsequently dialysed through a 1 kDa MWCO dialysis bag against 1 L of milli-Q water for 48-72 hours, changing water multiple (6-7) times until clear. The solution retained inside the bag was then freeze dried to powder and labelled CTN-CDs.

Synthesis of the crab-derived carbon dots (CRB-CDs)

Spanner crab (Ranina ranina) shells were collected from the local Fish Market in Sydney, rinsed with water and dried overnight in a vacuum oven at 60 °C before use. The same

mechanochemical pretreatment described for the synthesis of the chitin-derived carbon nanoparticles was employed for the crab shells. The crab-derived dots were synthesised loading 1.500 g of milled crab shell and 40 mL of milli-Q water into a batch reactor of 45 mL of total volume, sealed and heated at 220 °C for 24 h. The mixture was then filtered under suction, recovering and drying overnight the solid residue in a vacuum oven at 60 °C, while the filtered solution was added of 2 mL of NaOH 0.1 M to stabilise the nanoparticles, then purified by a 0.22 µm syringe filter to remove eventual macro residues and subsequently dialysed through a 1 kDa MWCO dialysis bag against 1 L of milli-Q water for 48-72 hours, changing water multiple (6-7) times until clear. The solution retained inside the bag was then freeze dried to powder to obtain 45-50 mg of pure product and labelled CRB-CDs.

Characterisation of the nanomaterials

^{1}H- and ^{13}C-NMR experiments were carried out on a Bruker AVIII NMR Spectrometer (400 MHz) using D_2O as solvent and 10 mg of acetonitrile or acetone as internal standard. To prepare the sample, 20 mg of material were weighted and dissolved into 1 mL D_2O.

PXRD measurements were conducted using a Rigaku MiniFlex Benchtop powder X-ray diffractometer, with a Cu-Kα anode as X-ray generator (40 kV, 15 mA), registering the spectra within a range of 5-50 degrees.

Atomic Force Microscopy (AFM) analyses of all the three materials were performed on a Bruker NanoWizard ULTRA Speed 3 AFM, using a soft AFM cantilever with a force constant of 3 N/m in tapping mode. All the analysed samples were prepared by drop-casting 20 µL of a 0.01 mg/mL aqueous solution of the selected nanomaterial on a mica thin disc as support. Subsequently, the drop-casted mica was freeze dried for few hours to allow a more homogeneous distribution of the nanoparticles and directly analysed under the AFM microscope.

Fourier Transform-Infrared Spectroscopy (FT-IR) were recorded on a Bruker LUMOS FTIR Microscope within a range of 700-4000 cm^{-1} for both chitin samples and nanomaterials.

UV-Visible absorption spectra were recorded within a range of wavelength of 200-800 nm using a PerkinElmer Lambda 365 UV-Visible spectrophotometer, while photoluminescence (PL) spectra were recorded using xxx, exciting at 355 nm.

Cyclic voltammetry (CV) measurements were performed using a 3 mm glassy carbon as WE, a Pt/Titanium electrode as CE and an Ag/AgCl sat. as RE on an EC-Lab SP-300

Biologic potentiostat. Analysis of the modified electrolytes were carried out on freshly prepared solution of nanomaterial (0.5 mg/mL) dissolved in 2M $ZnSO_4$, in comparison to bare 2M $ZnSO_4$ solution. EC-Lab V11.61 software was employed for data curation.

Photoelectron Spectroscopy (XPS) measurements were carried out on a ThermoScientific K-Alpha+ Surface Analysis.

Preparation of the electrolyte

The electrolytes used for the Zn-plating test were prepared by dissolving 0.5 mg/mL of the selected sample – either the synthesised N-CQDs, CTN-CDs or CRB-CDs – into a 2M $ZnSO_4$ solution. The mixture was then ultrasonicated for 10 minutes and filtered through a 0.22 µm syringe filter to remove eventual undissolved residues. The resulting electrolytes were labelled N-gCQDs-$ZnSO_4$, CTN-CDs-$ZnSO_4$ and CRB-CDs-$ZnSO_4$, respectively, and were tested in comparison to a plain 2 M $ZnSO_4$ electrolyte as control test in the Zn-plating experiments.

Plating experiments

Two different kinds of Zn-plating experiments were conducted within this work. To visually reconstruct the dendrite suppression effect, both the plain and the CDs-based electrolytes were tested through a series of edge plating experiments. In this case, an asymmetric Zn||Cu transparent cell was customised folding the two foil electrodes onto two glass slides, held together at 7-8 mm of distance with two other glass slides (as showed in **Figure 4.17**). The cell was then filled with 0.6 mL of the selected electrolyte and a constant current density of 10 mA/cm^2 was applied for 4 h of plating and 4 h of stripping, recording a video of the process with a microscopy camera. The subsequent asymmetric Zn||Cu-In cell configuration was tested under similar conditions but increasing the current density up to 20 mA/cm^2. The CDs-based electrolytes were also tested on a transparent 3D-printed cell using 12 mm round shaped Zn and Cu electrodes (**Figure 2.25B**). Once assembled, the cell was filled with 1 mL of the selected electrolyte and a constant current density of 4 mA/cm^2 was applied for 1 hour of plating. The cell was subsequently disassembled; the two electrodes were gently washed with Milli-Q water, and their surface was analysed to evaluate the Zinc layer roughness through SEM.

Bibliography

1. Xu, X. *et al.* Electrophoretic Analysis and Purification of Fluorescent Single-Walled Carbon Nanotube Fragments. *J. Am. Chem. Soc.* **126**, 12736–12737 (2004).

2. Wang, B. & Lu, S. The light of carbon dots: From mechanism to applications. *Matter* **5**, 110–149 (2022).

3. Zhu, S. *et al.* The photoluminescence mechanism in carbon dots (graphene quantum dots, carbon nanodots, and polymer dots): current state and future perspective. *Nano Res.* **8**, 355–381 (2015).

4. Liu, M. Optical Properties of Carbon Dots: A Review. *Nanoarchitectonics* **1**, 1–12 (2020).

5. Fu, Q., Sun, S., Lu, K. *et al.* Boron-doped carbon dots: Doping strategies, performance effects, and applications. *Chin. Chem. Lett.* **35**, 109136 (2024).

6. Miao, S. *et al.* Hetero-atom-doped carbon dots: Doping strategies, properties and applications. *Nano Today* **33**, 100879 (2020).

7. Liu, H. *et al.* A review of carbon dots in synthesis strategy. *Coord. Chem. Rev.* **498**, 215468 (2024).

8. Hoang, N. M. *et al.* Experimental synthesis of dual-emission carbon dots: The role of reaction temperature. *Inorg. Chem. Commun.* **148**, 110301 (2023).

9. Qu, D. & Sun, Z. The formation mechanism and fluorophores of carbon dots synthesized *via* a bottom-up route. *Mater. Chem. Front.* **4**, 400–420 (2020).

10. Zhang, M., Long, X., Ma, Y. & Wu, S. Re-discussion on the essence of the ultra-bright fluorescent carbon dots synthesized by citric acid and ethylenediamine. *Opt. Mater.* **135**, 113311 (2023).

11. Duan, P., Zhi, B., Coburn, L., *et al.* A molecular fluorophore in citric acid/ethylenediamine carbon dots identified and quantified by multinuclear solid-state nuclear magnetic resonance. *Magn. Reson. Chem.* **58**, 1130–1138 (2020).

12. Zhu, S., Zhao, X., Song, Y., Lu, S. & Yang, B. Beyond bottom-up carbon nanodots: Citric-acid derived organic molecules. *Nano Today* **11**, 128–132 (2016).

13. Robertson, H. A. The innervation of the salivary gland of the moth, Manduca sexta: evidence that dopamine is the transmitter. *J. Exp. Biol.* **63**, 413–419 (1975).

14. Zhang, W. *et al.* Supramolecular interactions via hydrogen bonding contributing to citric-acid derived carbon dots with high quantum yield and sensitive photoluminescence. *RSC Adv.* **7**, 20345–20353 (2017).

15. Schneider, J. *et al.* Molecular Fluorescence in Citric Acid-Based Carbon Dots. *J. Phys. Chem. C* **121**, 2014–2022 (2017).

16. Mandal, S. & Das, P. Are carbon dots worth the tremendous attention it is getting: Challenges and opportunities. *Appl. Mater. Today* **26**, 101331 (2022).

17. Sharma, S. *et al.* Sustainable applications of biowaste-derived carbon dots in eco-friendly technological advancements: A review. *Mater. Sci. Eng. B* **305**, 117414 (2024).

18. Atchudan, R. *et al.* Hydrophilic nitrogen-doped carbon dots from biowaste using dwarf banana peel for environmental and biological applications. *Fuel* **275**, 117821 (2020).

19. Ozyurt, D., Kobaisi, M. A., Hocking, R. K. & Fox, B. Properties, synthesis, and applications of carbon dots: A review. *Carbon Trends* **12**, 100276 (2023).

20. Xia, C., Zhu, S., Feng, T., Yang, M. & Yang, B. Evolution and Synthesis of Carbon Dots: From Carbon Dots to Carbonized Polymer Dots. *Adv. Sci.* **6**, 1901316 (2019).

21. Tuerhong, M., Xu, Y. & Yin, X.-B. Review on Carbon Dots and Their Applications. *Chin. J. Anal. Chem.* **45**, 139–150 (2017).

22. Yao, Y. *et al.* Carbon dots based photocatalysis for environmental applications. *J. Environ. Chem. Eng.* **10**, 107336 (2022).

23. Yu, H. *et al.* Smart Utilization of Carbon Dots in Semiconductor Photocatalysis. *Adv. Mater.* **28**, 9454–9477 (2016).

24. Xu, D., Lin, Q. & Chang, H. Recent Advances and Sensing Applications of Carbon Dots. *Small Methods* **4**, 1900387 (2020).

25. Kaurav, H. *et al.* Progress in drug delivery and diagnostic applications of carbon dots: a systematic review. *Front. Chem.* **11**, 1227843 (2023).

26. Calabrese, G. *et al.* Carbon Dots: An Innovative Tool for Drug Delivery in Brain Tumors. *Int. J. Mol. Sci.* **22**, 11783 (2021).

27. Wang, B. *et al.* Carbon Dots in Bioimaging, Biosensing and Therapeutics: A Comprehensive Review. *Small Sci.* **2**, 2200012 (2022).

28. Karagianni, A., Tsierkezos, N. G., Prato, M., Terrones, M. & Kordatos, K. V. Application of carbon-based quantum dots in photodynamic therapy. *Carbon* **203**, 273–310 (2023).

29. Singh, P. *et al.* Assessing the biomass-based carbon dots and their composites for photocatalytic treatment of wastewater. *J. Clean. Prod.* **413**, 137474 (2023).

30. Feng, T. *et al.* Recent Advances in Energy Conversion Applications of Carbon Dots: From Optoelectronic Devices to Electrocatalysis. *Small* **16**, 2001295 (2020).

31. Li, J., Zhao, X. & Gong, X. The Emerging Star of Carbon Luminescent Materials: Exploring the Mysteries of the Nanolight of Carbon Dots for Optoelectronic Applications. *Small* **20**, 2400107 (2024).

32. Vu Nu, T. T. *et al.* Green synthesis of microalgae-based carbon dots for decoration of TiO2 nanoparticles in enhancement of organic dye photodegradation. *Environ. Res.* **206**, 112631 (2022).

33. Akbar, K., Moretti, E. & Vomiero, A. Carbon Dots for Photocatalytic Degradation of Aqueous Pollutants: Recent Advancements. *Adv. Opt. Mater.* **9**, 2100532 (2021).

34. Hamadamin, A. *et al.* Nitrogen-doped Carbon Dots as Biobased Catalysts for Visible Light Driven 1,2-Functionalization of Olefins through an Atom Transfer Radical Addition Process. *ChemCatChem* **15**, e202300708 (2023).

35. Cailotto, S. *et al.* Design of Carbon Dots for Metal-free Photoredox Catalysis. *ACS Appl. Mater. Interfaces* **10**, 40560–40567 (2018).

36. Benazzi, V. *et al.* Biobased carbon dots as photoreductants – an investigation by using triarylsulfonium salts. *Beilstein J. Org. Chem.* **21**, 1024–1030 (2025).

37. Campalani, C. *et al.* Carbon dots as green photocatalysts for atom transfer radical polymerization of methacrylates. *Catal. Today* **418**, 114039 (2023).

38. Campalani, C., Causin, V., Selva, M. & Perosa, A. Fish-Waste-Derived Gelatin and Carbon Dots for Biobased UV-Blocking Films. *ACS Appl. Mater. Interfaces* **14**, 35148–35156 (2022).

39. Emanuele, A. *et al.* Precursor-Dependent Photocatalytic Activity of Carbon Dots. *Molecules* **25**, 101 (2019).

40. Cailotto, S. *et al.* Carbon dots as photocatalysts for organic synthesis: metal-free methylene–oxygen-bond photocleavage. *Green Chem.* **22**, 1145–1149 (2020).

41. Campalani, C. *et al.* Biobased Carbon Dots: From Fish Scales to Photocatalysis. *Nanomaterials* **11**, 524 (2021).

42. Cailotto, S. *et al.* N-Doped Carbon Dot Hydrogels from Brewing Waste for Photocatalytic Wastewater Treatment. *ACS Omega* **7**, 4052–4061 (2022).

43. Bertuol, I. *et al.* Metal-free graphitic carbon nitride/carbon-dots composites: unveiling mechanochemical synthesis opportunities. *Sustain. Energy Fuels* **9**, 2031–2044 (2025).

44. Zhai, Y. *et al.* Carbon Dots as New Building Blocks for Electrochemical Energy Storage and Electrocatalysis. *Adv. Energy Mater.* **12**, 2103426 (2022).

45. Chen, C., Li, N. W. & Yu, L. Recent advances in the surface modification strategies towards 3D carbon-based hosts for dendrite-free Li/Na/Zn metal anodes. *EnergyChem* **6**, 100117 (2024).

46. Yan, W. *et al.* Rethinking Chinese supply resilience of critical metals in lithium-ion batteries. *J. Clean. Prod.* **256**, 120719 (2020).

47. Tang, B., Shan, L., Liang, S. & Zhou, J. Issues and opportunities facing aqueous zinc-ion batteries. *Energy Environ. Sci.* **12**, 3288–3304 (2019).

48. Ruan, P., Liang, S., Lu, B., Fan, H. J. & Zhou, J. Design Strategies for High-Energy-Density Aqueous Zinc Batteries. *Angew. Chem.* **134**, e202200598 (2022).

49. Zhang, N. *et al.* Direct Self-Assembly of MXene on Zn Anodes for Dendrite-Free Aqueous Zinc-Ion Batteries. *Angew. Chem.* **133**, 2897–2901 (2021).

50. Foroozan, T. *et al.* Non-Dendritic Zn Electrodeposition Enabled by Zincophilic Graphene Substrates. *ACS Appl. Mater. Interfaces* **11**, 44077–44089 (2019).

51. Hieu, L. T., So, S., Kim, I. T. & Hur, J. Zn anode with flexible β-PVDF coating for aqueous Zn-ion batteries with long cycle life. *Chem. Eng. J.* **411**, 128584 (2021).

52. Yang, X. *et al.* Interfacial Manipulation via In Situ Grown ZnSe Cultivator toward Highly Reversible Zn Metal Anodes. *Adv. Mater.* **33**, 2105951 (2021).

53. Wang, W. *et al.* Organic Acid Etching Strategy for Dendrite Suppression in Aqueous Zinc-Ion Batteries. *Adv. Energy Mater.* **12**, 2102797 (2022).

54. Zeng, X. *et al.* Electrolyte Design for In Situ Construction of Highly Zn^{2+} -Conductive Solid Electrolyte Interphase to Enable High-Performance Aqueous Zn-Ion Batteries under Practical Conditions. *Adv. Mater.* **33**, 2007416 (2021).

55. Sun, P. *et al.* Simultaneous Regulation on Solvation Shell and Electrode Interface for Dendrite-Free Zn Ion Batteries Achieved by a Low-Cost Glucose Additive. *Angew. Chem.* **133**, 18395–18403 (2021).

56. Ming, F. *et al.* Co-Solvent Electrolyte Engineering for Stable Anode-Free Zinc Metal Batteries. *J. Am. Chem. Soc.* **144**, 7160–7170 (2022).

57. Hao, J. *et al.* Boosting Zinc Electrode Reversibility in Aqueous Electrolytes by Using Low-Cost Antisolvents. *Angew. Chem. Int. Ed.* **60**, 7366–7375 (2021).

58. Zhang, L. *et al.* $ZnCl_2$ “Water-in-Salt” Electrolyte Transforms the Performance of Vanadium Oxide as a Zn Battery Cathode. *Adv. Funct. Mater.* **29**, 1902653 (2019).

59. Zhang, W. *et al.* Self-repairing interphase reconstructed in each cycle for highly reversible aqueous zinc batteries. *Nat. Commun.* **13**, 5348 (2022).

60. Mhin, B. J., Lee, S., Cho, S. J., Lee, K. & Kim, K. S. Zn(H2O)2+6 is very stable among aqua-Zn(II) ions. *Chem. Phys. Lett.* **197**, 77–80 (1992).

61. Li, M. *et al.* Comprehensive understanding of the roles of water molecules in aqueous Zn-ion batteries: from electrolytes to electrode materials. *Energy Environ. Sci.* **14**, 3796–3839 (2021).

62. Zhang, H. *et al.* Unraveling the Mechanisms of Aqueous Zinc Ion Batteries via First-Principles Calculations. *ACS Energy Lett.* **9**, 4761–4784 (2024).

63. Chen, T. *et al.* Functional Nanomaterials with Tip Effect: Synthesis and Applications in Electrocatalysis. *CCS Chem.* 1–23 (2025) doi:10.31635/ccschem.025.202506115.

64. Tao, Z. *et al.* Regulating “Tip Effect” and Zn^{2+} -Deposition Kinetics by In Situ Constructing Interphase for Low Voltage Hysteresis and Dendrite-Free Zn Anode. *Small Methods* **8**, 2400463 (2024).

65. Song, T. *et al.* N-Doped and Sulfonated Carbon Dots as a Multifunctional Additive to Realize Highly Reversible Aqueous Zinc-Ion Batteries. *Small* **19**, 2205558 (2023).

66. Zhang, H. *et al.* High-Yield Carbon Dots Interlayer for Ultra-Stable Zinc Batteries. *Adv. Energy Mater.* **12**, 2200665 (2022).

67. Lee, W. J., Lim, J. & Kim, S. O. Nitrogen Dopants in Carbon Nanomaterials: Defects or a New Opportunity? *Small Methods* **1**, 1600014 (2017).

68. Martindale, B. C. M. *et al.* Enhancing Light Absorption and Charge Transfer Efficiency in Carbon Dots through Graphitization and Core Nitrogen Doping. *Angew. Chem. Int. Ed.* **56**, 6459–6463 (2017).

69. Yi, M. *et al.* Recent Developments of Carbon Dots for Advanced Zinc-Based Batteries: A Review. *Adv. Funct. Mater.* **34**, 2400001 (2024).

70. Zhang, H. *et al.* Graphene quantum dots enable dendrite-free zinc ion battery. *Nano Energy* **92**, 106752 (2022).

71. Han, W. *et al.* Toward highly reversible aqueous zinc-ion batteries: nanoscale-regulated zinc nucleation via graphene quantum dots functionalized with multiple functional groups. *Chem. Eng. J.* **452**, 139090 (2023).

72. Wu, J. *et al.* Regulation of the Electrochemical Plating/Stripping Process for Zn: Multifunctional Effects of N, S-Codoped Carbon Dots. *J. Phys. Chem. Lett.* **13**, 11883–11891 (2022).

73. Zhang, H. *et al.* Interfacial reconstruction via electronegative sulfonated carbon dots in hybrid electrolyte for ultra-durable zinc battery. *Chem. Eng. J.* **461**, 142105 (2023).

74. Wang, H. *et al.* Bifunctional Dynamic Adaptive Interphase Reconfiguration for Zinc Deposition Modulation and Side Reaction Suppression in Aqueous Zinc Ion Batteries. *ACS Nano* **17**, 11946–11956 (2023).

75. Han, Y. *et al.* Building block effect induces horizontally oriented bottom Zn(002) deposition for a highly stable zinc anode. *Energy Storage Mater.* **62**, 102928 (2023).

76. Xu, Z. *et al.* Durable modulation of Zn(002) plane deposition *via* reproducible zincophilic carbon quantum dots towards low N/P ratio zinc-ion batteries. *Mater. Horiz.* **10**, 3680–3693 (2023).

77. Wang, F. *et al.* Mitigating the interfacial concentration gradient by negatively charged quantum dots toward dendrite-free Zn anodes. *Energy Storage Mater.* **58**, 215–221 (2023).

78. Jiang, H. *et al.* Defect-rich and ultrathin N doped carbon nanosheets as advanced trifunctional metal-free electrocatalysts for the ORR, OER and HER. *Energy Environ. Sci.* **12**, 322–333 (2019).

79. Polidoro, D., Perosa, A., Selva, M. & Rodríguez-Padrón, D. Metal-Free Carbonaceous Catalytic Materials: Biomass Feedstocks for a Greener Future. *ChemCatChem* **15**, e202300415 (2023).

80. Li, J. *et al.* Dual-doped carbon hollow nanospheres achieve boosted pseudocapacitive energy storage for aqueous zinc ion hybrid capacitors. *Energy Storage Mater.* **42**, 705–714 (2021).

81. Pykal, M. *et al.* Thermodynamics and kinetics of early stages of carbon dot formation: a case of citric acid and ethylenediamine reaction. *Nanoscale* **17**, 7780–7789 (2025).

82. Ru, Y., Waterhouse, G. I. N. & Lu, S. Aggregation in carbon dots: Special Issue: Emerging Investigators. *Aggregate* **3**, e296 (2022).

83. Roy, J. C. *et al.* Solubility of Chitin: Solvents, Solution Behaviors and Their Related Mechanisms. in *Solubility of Polysaccharides* (ed. Xu, Z.) (InTech, 2017). doi:10.5772/intechopen.71385.

84. Yang, W., Wang, H., Zhou, J. & Wu, S. Hydrolysis kinetics and mechanism of chitin in subcritical water. *J. Supercrit. Fluids* **135**, 254–262 (2018).

85. Sakanishi, K., Ikeyama, N., Sakaki, T., Shibata, M. & Miki, T. Comparison of the Hydrothermal Decomposition Reactivities of Chitin and Cellulose. *Ind. Eng. Chem. Res.* **38**, 2177–2181 (1999).

86. Sasaki, M., Fang, Z., Fukushima, Y., Adschiri, T. & Arai, K. Dissolution and Hydrolysis of Cellulose in Subcritical and Supercritical Water. *Ind. Eng. Chem. Res.* **39**, 2883–2890 (2000).

87. Aida, T. M. *et al.* Dissolution of mechanically milled chitin in high temperature water. *Carbohydr. Polym.* **106**, 172–178 (2014).

88. Zhang, W. *et al.* Superfine grinding induced amorphization and increased solubility of α-chitin. *Carbohydr. Polym.* **237**, 116145 (2020).

89. Mogilevskaya, E. L., Akopova, T. A., Zelenetskii, A. N. & Ozerin, A. N. The crystal structure of chitin and chitosan. *Polym. Sci. Ser. A* **48**, 116–123 (2006).

90. Dweltz, N. E. The structure of chitin. *Biochim. Biophys. Acta* **44**, 416–435 (1960).

91. Carlström, D. THE CRYSTAL STRUCTURE OF α-CHITIN (P OLY - *N* -ACETYL-D-G LUCOSAMINE). *J. Cell Biol.* **3**, 669–683 (1957).

92. Saito, Y. *et al.* Structural Aspects of the Swelling of β Chitin in HCl and its Conversion into α Chitin. *Macromolecules* **30**, 3867–3873 (1997).

93. Campalani, C. *et al.* Green extraction of chitin from hard spider crab shells. *Carbohydr. Polym.* **345**, 122565 (2024).

94. Xiao, P. *et al.* An anticorrosive zinc metal anode with ultra-long cycle life over one year. *Energy Environ. Sci.* **15**, 1638–1646 (2022).

95. Belgacem, M. N. & Gandini, A. 25. Chitin and Chitosan: Major Sources, Properties and Applications. in *Monomers, polymers and composites from renewable resources* (Elsevier, Amsterdam Boston, 2008).

96. McCulloch, I., Chabinyc, M., Brabec, C., Nielsen, C. B. & Watkins, S. E. Sustainability considerations for organic electronic products. *Nat. Mater.* **22**, 1304–1310 (2023).

97. Alfantazi, A. M. & Moskalyk, R. R. Processing of indium: a review. *Miner. Eng.* **16**, 687–694 (2003).

Concluding remarks and future perspectives

This doctoral research Thesis has focused on the development of diverse strategies for the upgrading of biowaste and bio-sourced chemicals through sustainable approaches. The investigated methodologies range from multiphase catalysis and green extraction of marine-derived biopolymers to hydrothermal valorisation routes for the production of advanced functional materials. All these strategies share a common thread of sustainability and a clear orientation towards circular resource management.

As discussed in Chapter 2, the gamechanger of MPS is the possibility of confining the catalyst within a phase, an ionic liquid in our case, different from that where the reaction occurs. This configuration allowed for highly selective (>99%) conversion of BnOH into its partially oxidised derivative, PhCHO. Another key point of this study is that a very high selectivity (>99%) was maintained for five successive catalytic cycles when employing a benign molybdenum-based catalyst supported on biobased carbon (Mo/C). The relevance of this study particularly relies on a scalability perspective where MPS are increasingly recognised for their ability to streamline standard operating procedures, eliminating steps and reducing solvent use, process time, costs, and more importantly environmental impact.

Chapter 3 illustrated the optimisation of a green extraction protocol for the isolation of an important biocompatible compound, chitin. Developing green extraction routes for biowaste valorisation is crucial for two main reasons: i) it helps mitigating the burden of waste management by reintroducing waste streams into the economic loop as new resources, and ii) allows the replacement of hazardous substances with eco-compatible reagents minimising the environmental impact of the processes. Our one-pot approach for processing hard chitinous matrix (i.e. Spider crab shells) proved effective in achieving efficient demineralisation, deproteinisation, and decolourisation, ultimately yielding final chitin with physiochemical properties comparable, or even superior, to its commercial counterpart, and opening promising perspectives for future process scale-up. A parameter analysis according to the CHEM21 guidelines also provided a comprehensive overview of the actual sustainability of our green extraction method, highlighting areas for improvement on which it will be necessary to focus on the next future to ensure the sustainability of the protocol.

Finally, in Chapter 4 a complementary valorisation route was presented, this time converting marine biowaste (Australian crab shells) into nitrogen-doped carbon nanomaterials to be employed as functional additives in aqueous zinc-ion batteries (AZIBs). Compared to analogous materials synthesised from small organic precursors (citric acid and

diethylenetriamine) or biopolymer as chitin, the crab-derived nanomaterials exhibited superior performance in mitigating zinc dendrite formation, leading to enhanced stability during plating/stripping cycles and emerging as sustainable alternatives to conventional additives. A complete characterisation of the materials, electrolytes, and electrodes obtained from plating experiments revealed important correlations between structural/surface properties and electrochemical behaviour, with the presence of abundant oxygen-containing functional groups and graphene-like crystalline domains enabling effective coordination with Zn^{2+} effectively improving zinc deposition behaviour and overall battery performance.

Overall, the research presented in this thesis aims to provide tangible tools for narrowing the gap between the theoretical framework of sustainability and its practical implementation, which often remains challenged by technological, economic, and social barriers. The development of simple, cost-effective and cleaner alternatives to current fossil fuels-based processes remains a pressing and evolving topic. Establishing robust correlations between the sustainable methodologies investigated (i.e. MPS and hydrothermal extractive/synthetic protocols) and the final process outcomes (i.e. selectivity of the chemical transformations, products quality, effective functionality) represents a crucial step towards bridging scientific research and industrial application, as well as the central focus of this doctoral Thesis.

Several challenges remain open and will guide future efforts. These include improving the reactivity of molybdenum catalysts to lower the energetic demand of the oxidation reaction, enhancing the deproteinisation efficiency during chitin extraction from biowaste matrices, and conducting life cycle testing for a more comprehensive long-term behaviour of the crab-derived additives for AZIBs. Overcoming these issues will be essential to further enhance the sustainability, scalability, and technological relevance of this work, ultimately contributing to a more circular and resource-resilient chemical economy.

Summary of activities

Alongside laboratory work, data collection, and bibliographic research, significant efforts of the PhD activity were devoted to scientific dissemination and tutoring. Teaching support was provided for several undergraduate courses within the Department of Molecular Sciences and Nanosystems at Ca' Foscari University of Venice, including *Organic Chemistry II and Laboratory* (December 2023), *Inorganic Chemistry and Laboratory* (May 2023), and *Eco-Friendly Organic Synthesis and Laboratory* (March 2023), for a total of 90 hours. Research results were disseminated at national and international scientific events, specifically through few poster presentations at: the *Circular Bio-based Europe Joint Undertaking* (Venice, 2023), *EUROPACAT 2023* (Prague, Czech Republic, 2023), and the *6thEuChemS Conference on Green and Sustainable Chemistry* (Salerno, Italy, 2023). Further oral presentations were delivered at the *Progress Evaluation Meeting* at the University of Sydney (November 2024), the *International Summer School on Organic Synthesis, ISOS Corbella 2025* (Gargnano, June 2025), and the *XII GCCS Workshop on Green Chemistry–Chimica Sostenibile* (Bologna, July 2025). Additionally, a research seminar entitled *From Seafood to Sustainable Energy: Chitin-based CDs for Zn Batteries* was presented during the research group retreat held in the Blue Mountains (Sydney, February 2025).

Appendix Section

Characterization of Hydroxylammonium acetate (HA)

^{1}H-NMR and ^{13}C-NMR analyses

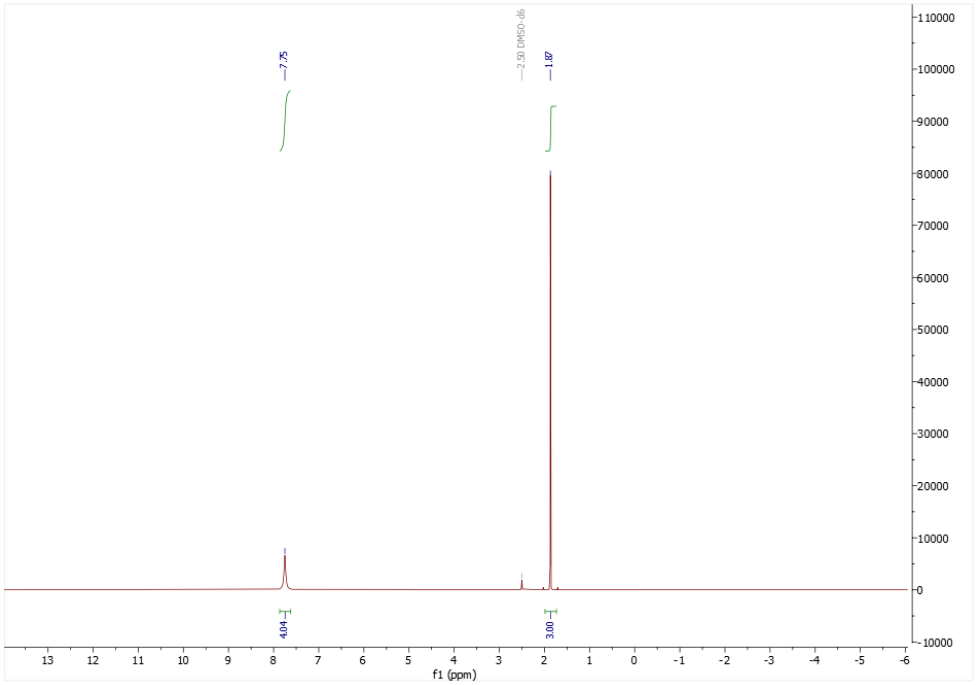

Figure A1. ^{1}H-NMR spectrum of hydroxylammonium acetate in DMSO-d_6.

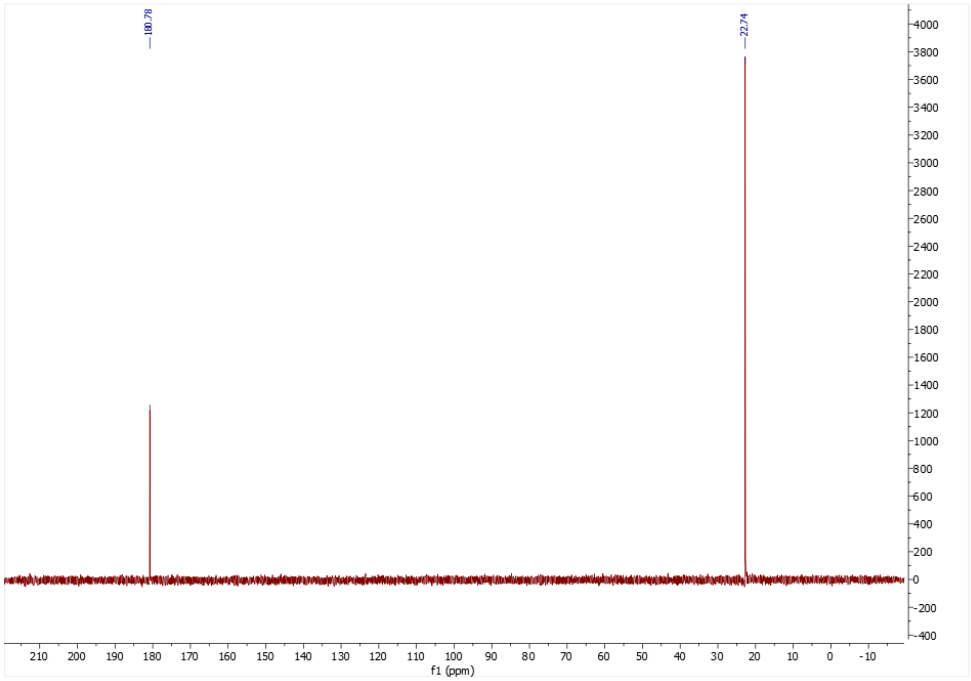

Figure A2. ^{13}C-NMR spectrum of hydroxylammonium acetate in D_2O.

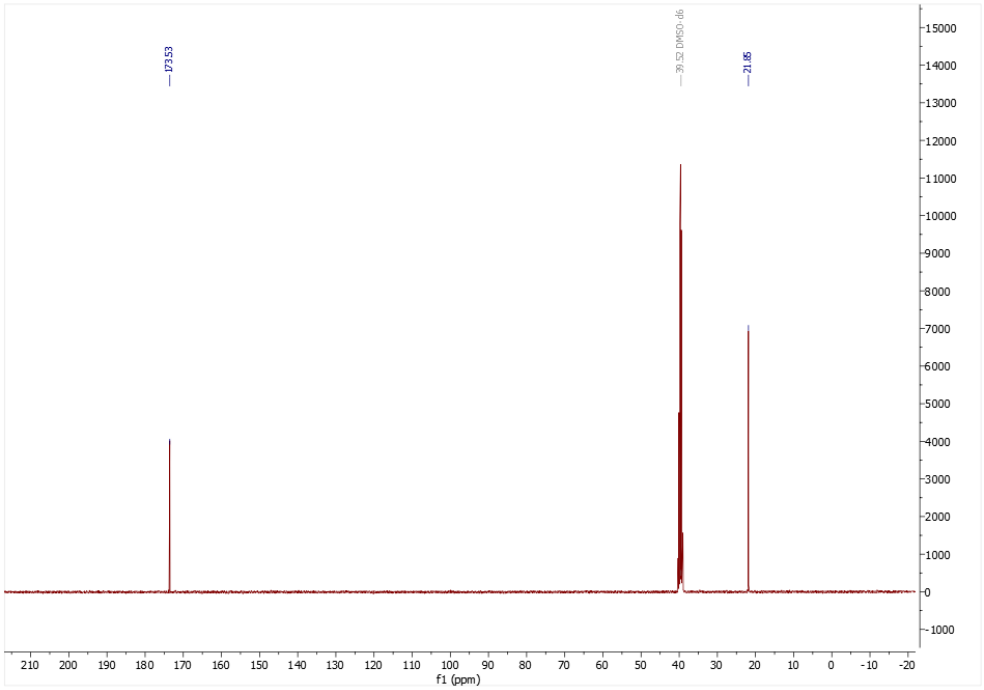

Figure A3. ^{13}C-NMR spectrum of hydroxylammonium acetate in DMSO-d_6.

Characterization of chitin pulped with ammonium acetate (AA)

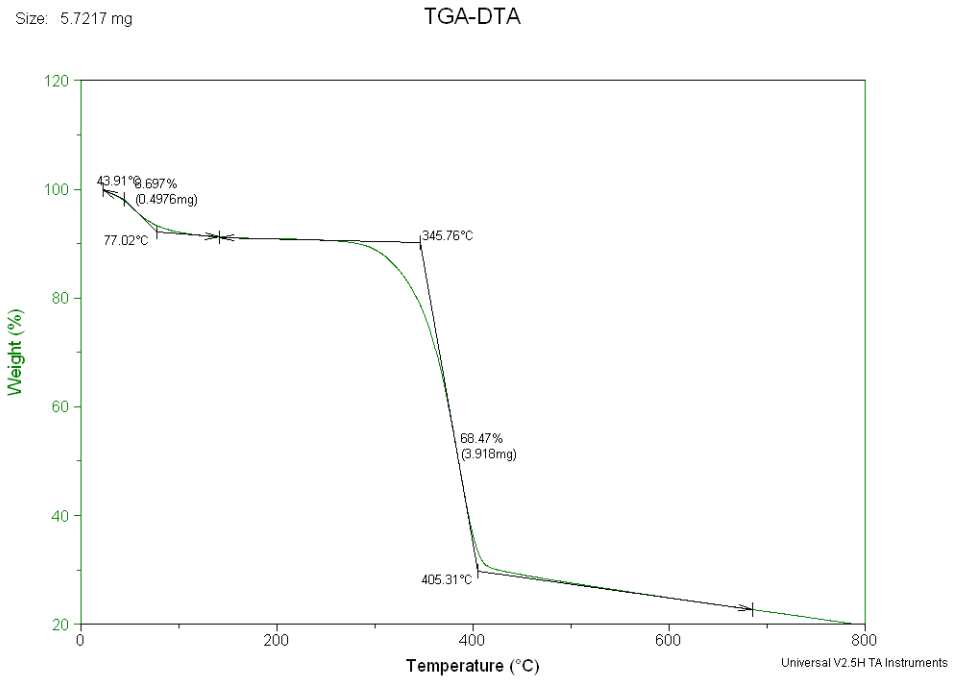

Figure A4. TGA curve of chitin pulped with AA solid salt (at 130 °C) in the range 25°C-800°C in nitrogen atmosphere.

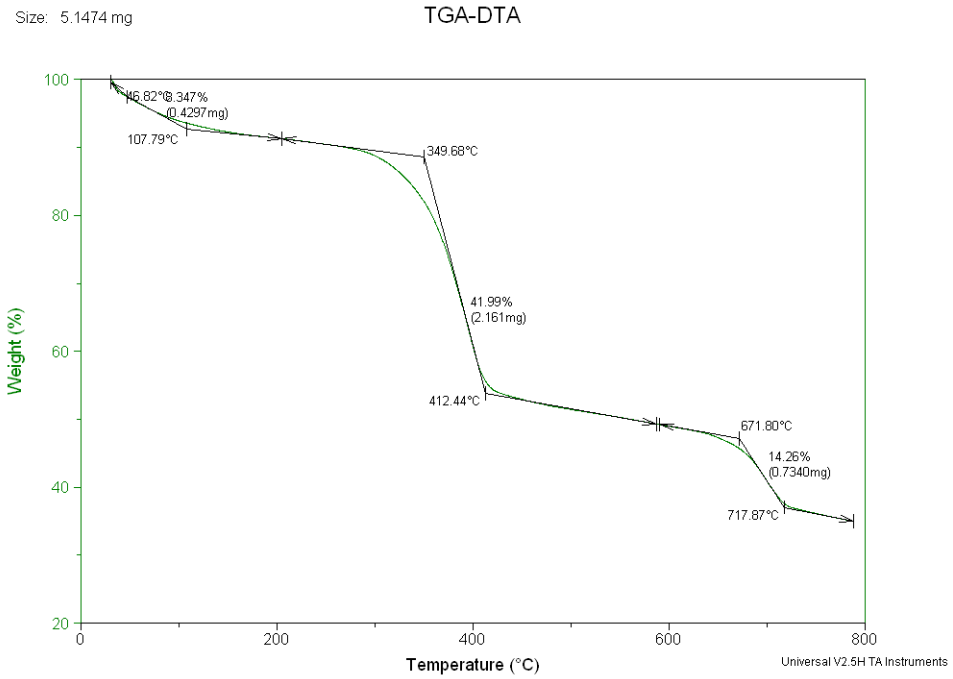

Figure A5. TGA curve of chitin pulped with AA prepared *in situ* in batch condition (at 100 °C) by sequential addition of acid prior to base in the range 25°C-800°C in nitrogen atmosphere.

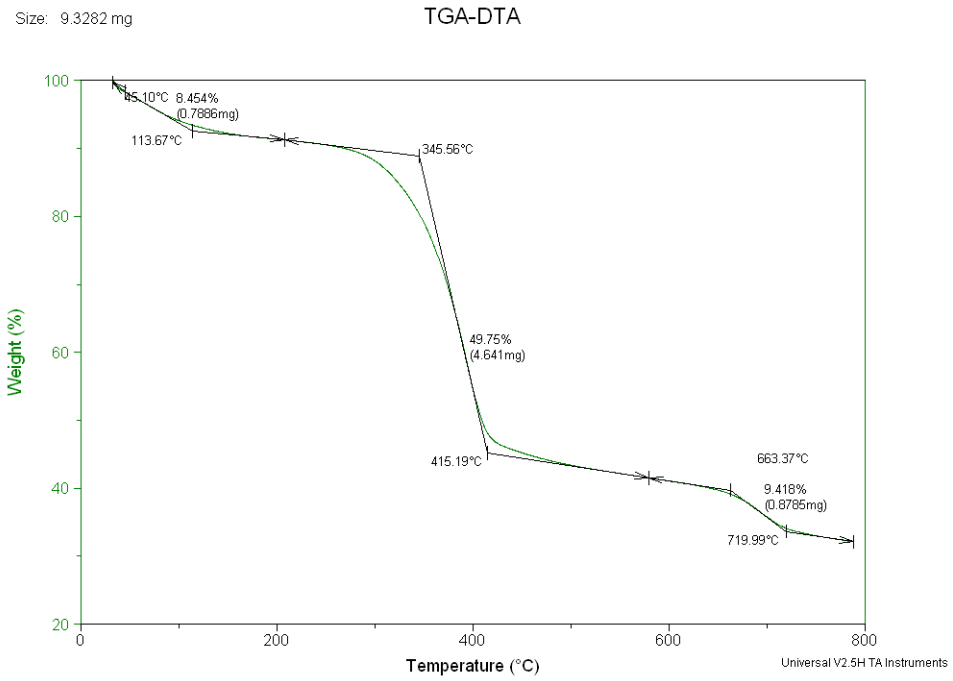

Figure A6. TGA curve of chitin pulped with AA prepared *in situ* in batch condition (at 100 °C) by sequential addition of base prior to acid in the range 25°C-800°C in nitrogen atmosphere.

Characterization of chitin pulped with ammonium formate (AF)

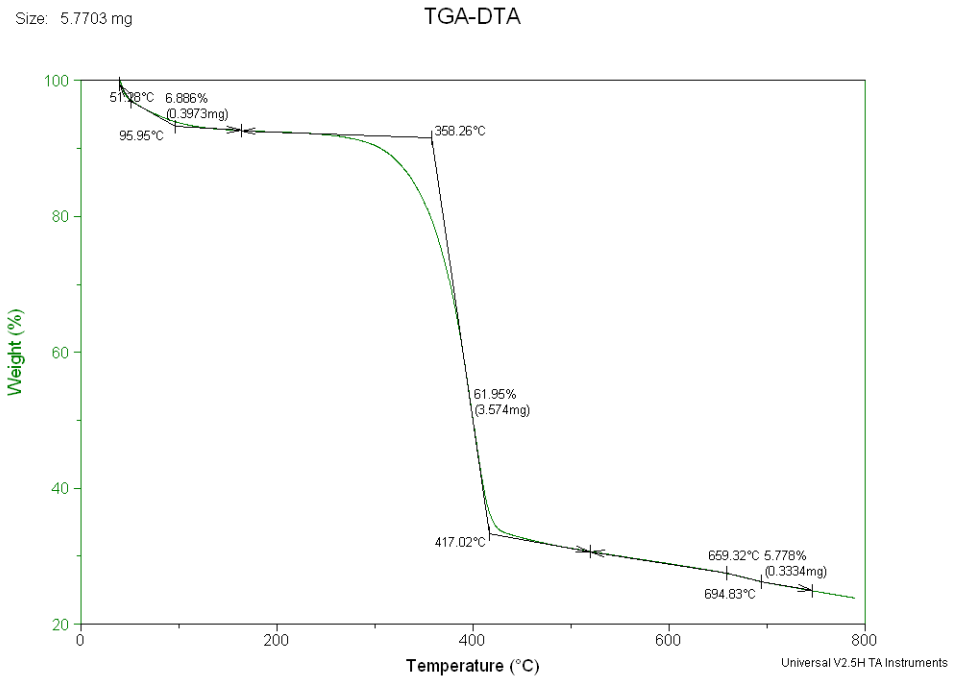

Figure A7. TGA curve of chitin pulped with AF solid salt (at 130 °C) in the range 25°C-800°C in nitrogen atmosphere.

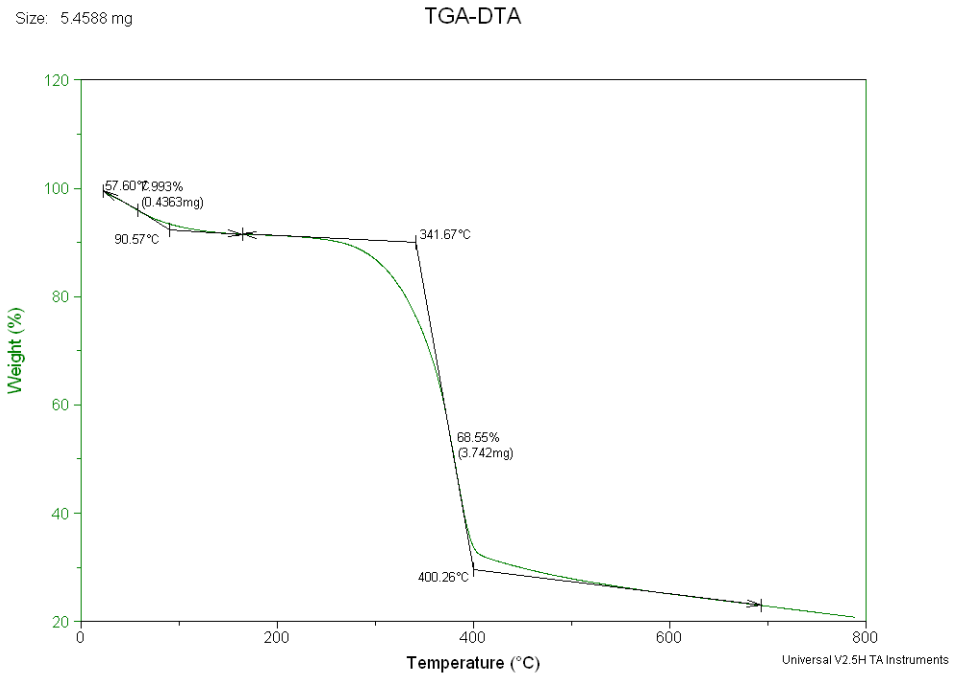

Figure A8. TGA curve of chitin pulped with AF prepared *in situ* in batch condition (at 100 °C) by sequential addition of acid prior to base in the range 25°C-800°C in nitrogen atmosphere.

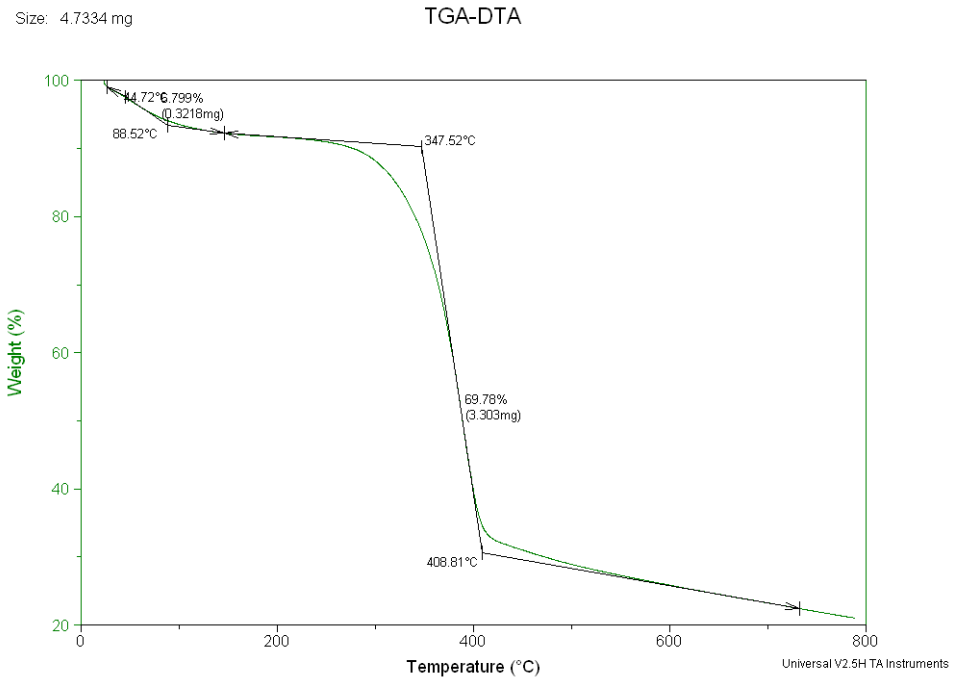

Figure A9. TGA curve of chitin pulped with AF prepared *in situ* in batch condition (at 100 °C) by sequential addition of base prior to acid in the range 25°C-800°C in nitrogen atmosphere.

Characterization of chitin pulped with hydroxylammonium acetate (HA)

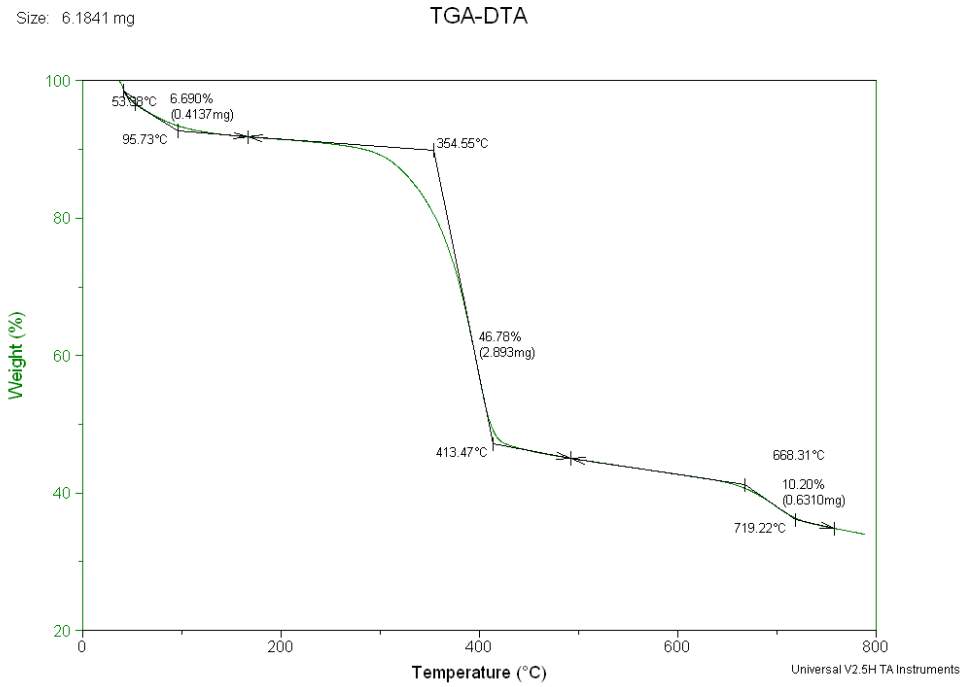

Figure A10. TGA curve of chitin pulped with HA solid salt (at 130 °C) in the range 25°C-800°C in nitrogen atmosphere.

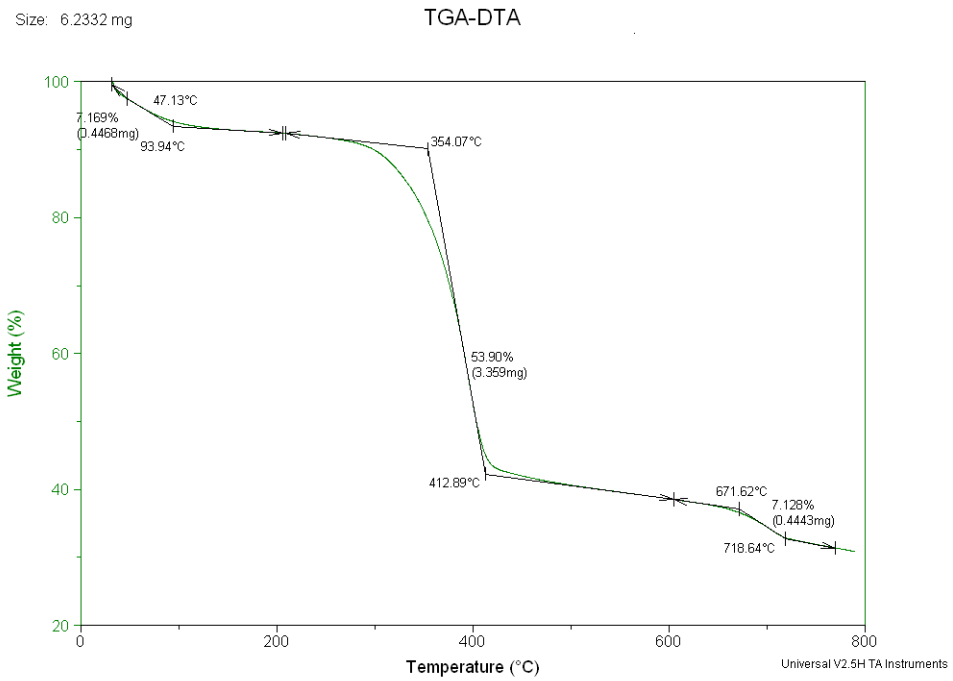

Figure A11. TGA curve of chitin pulped with HA prepared *in situ* (at 100 °C) by sequential addition of acid prior to base in the range 25°C-800°C in nitrogen atmosphere.

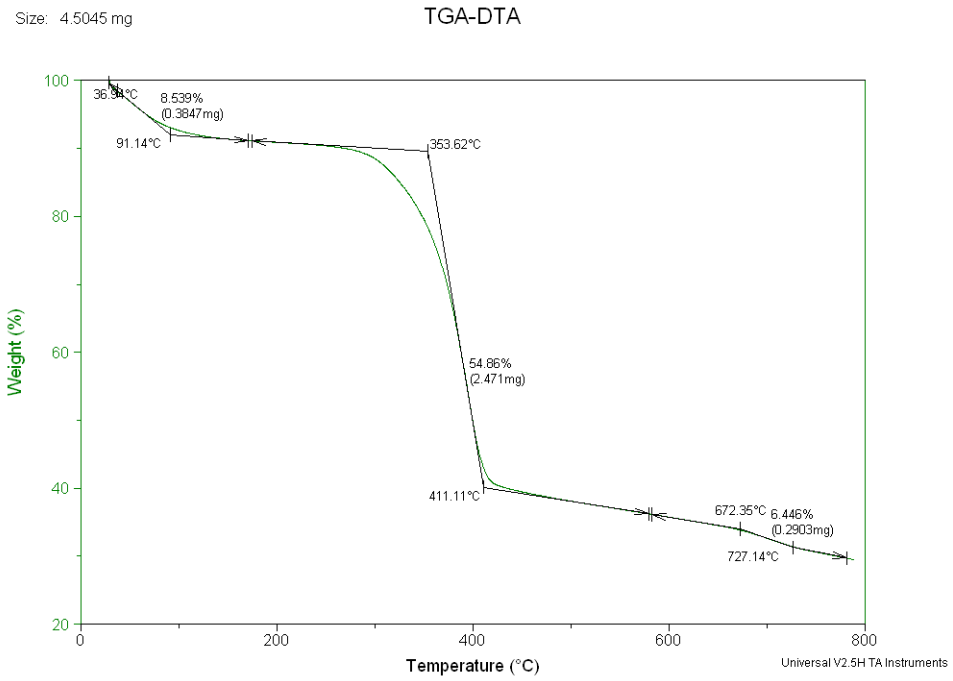

Figure A12. TGA curve of chitin pulped with HA prepared *in situ* (at 100 °C) by sequential addition of base prior to acid in the range 25°C-800°C in nitrogen atmosphere.

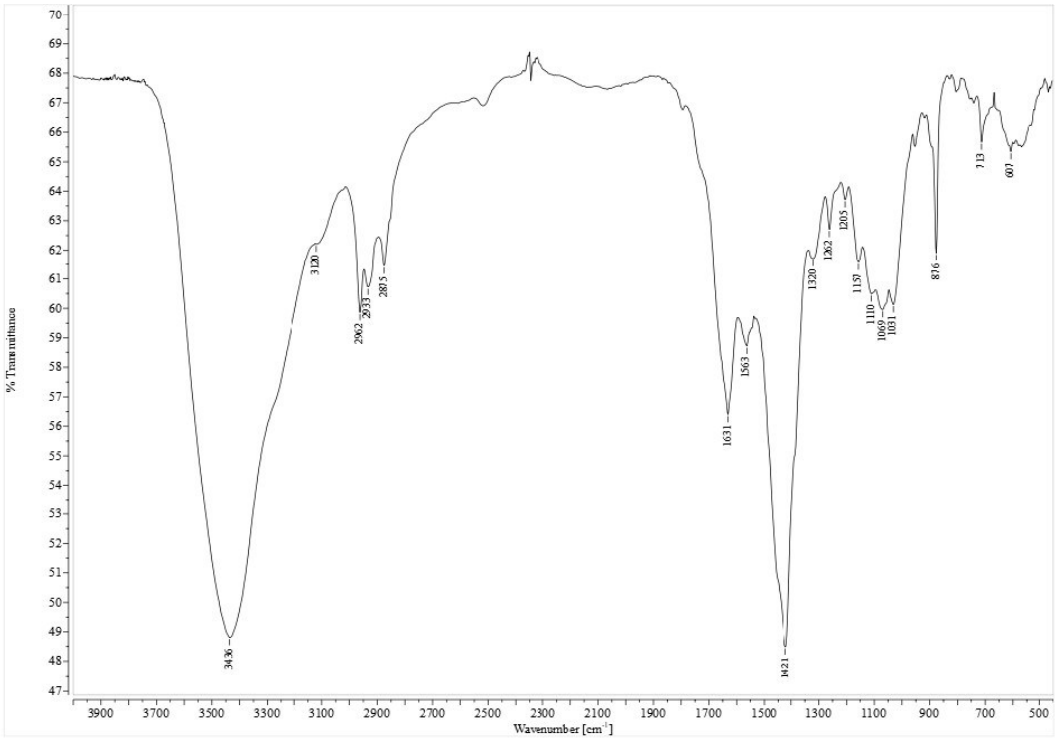

Figure A13. FT-IR spectrum of chitin pulped with HA *in situ* at 100 °C (1 mg) in KBr pellet (100 mg).

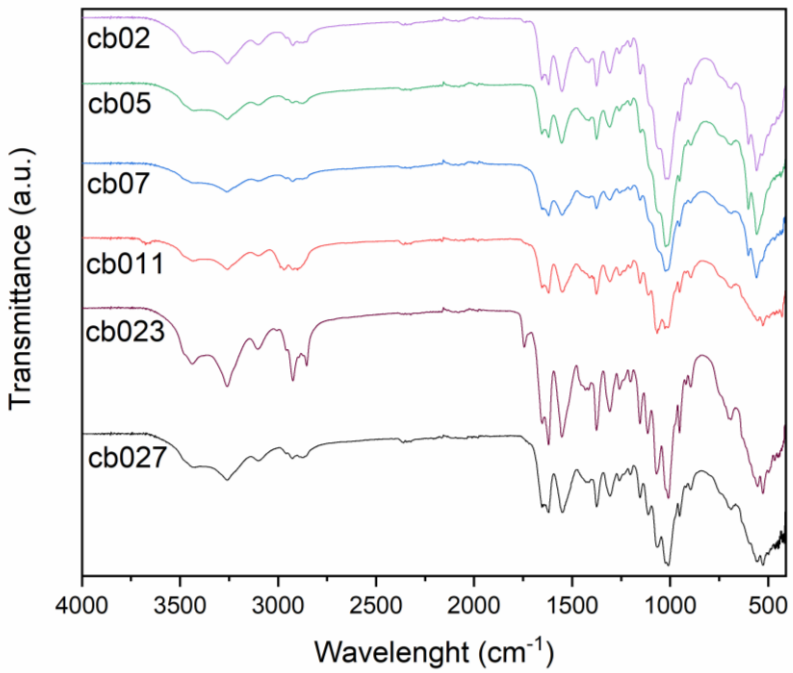

Figure A14. FT-IR spectrum of pulped chitin samples (1 mg) in KBr pellet (100 mg). CB02: 100˚C, 24 h, 10 wt.%; CB05: 100˚C, 24 h, 7 wt.%; CB07: 100˚C, 24 h, 5 wt.%; CB011; 100˚C, 24 h, 20 wt.%; CB023: 150˚C, 4 h, 10 wt.%; CB027: 140˚C, 2 h, 10 wt.%

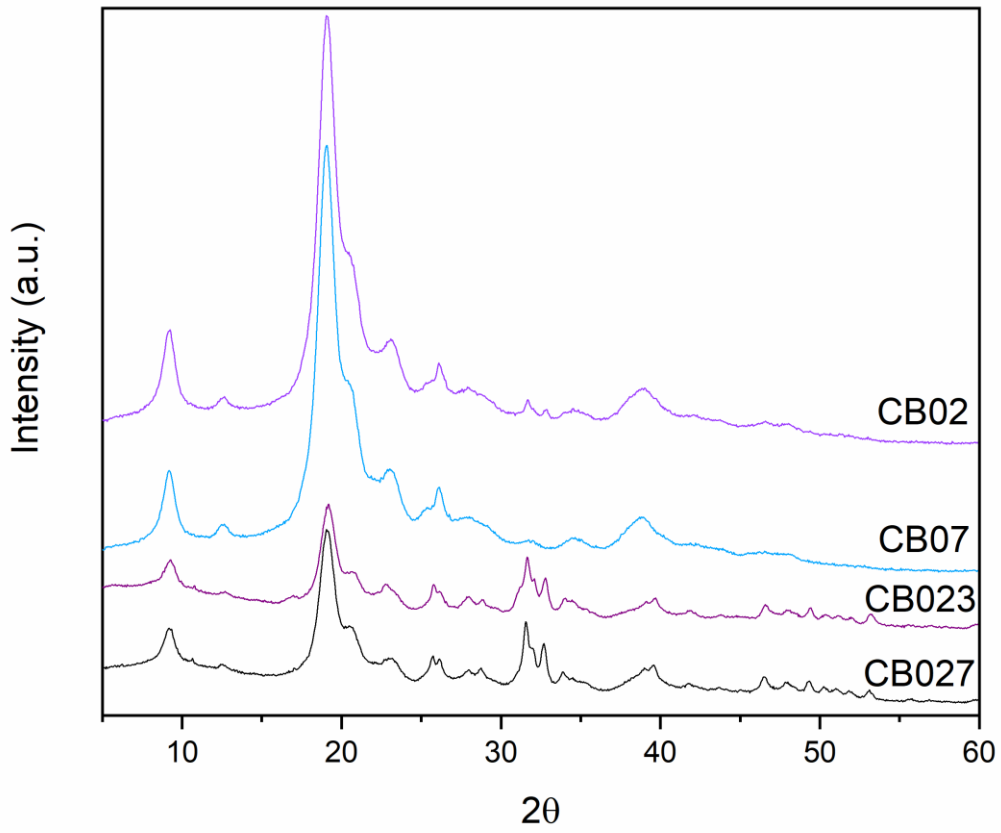

Figure A15. XRD patterns of the pulped chitin samples. CB02: 100˚C, 24 h, 10 wt.%; CB07: 100˚C, 24 h, 5 wt.%; CB023: 150˚C, 4 h, 10 wt.%; CB027: 140˚C, 2 h, 10 wt.%

GPC analysis

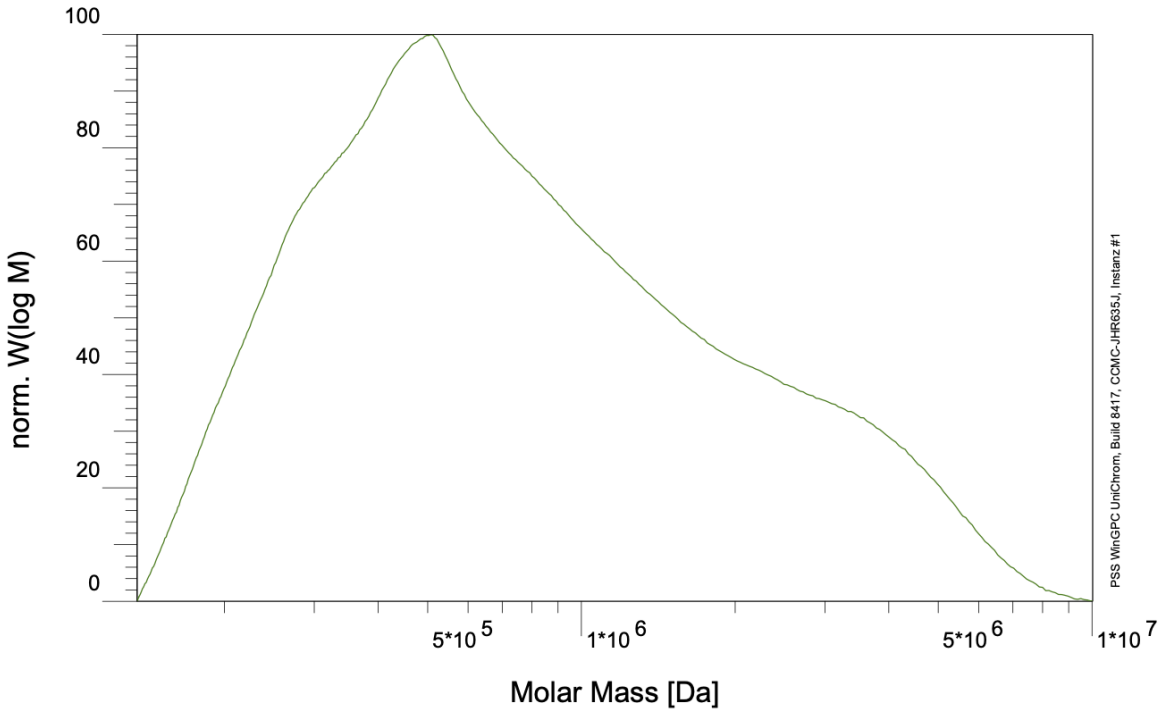

Probe :	Vial 5: CB-07 (Calmanti) - 1		
Integration von :	Dienstag 27.06.23 16:04:58		11.139 ml
Integration bis :	Dienstag 27.06.23 16:12:00		14.688 ml
Kalibration :	C:\Calib\N-LiCl-PS-29-06-2023.CAL	**Eluent :**	NMP-LiCl-5 w%
MHK - A (Kal.):	0.000E+0	**MHK - K (Kal.):**	1.000E+0 ml/g
Int.Stand.-K :	23.390 ml	**Int.Stand.-M :**	23.185 ml
Pumpe :	PSS SECcurity	**Flussrate :**	0.500 ml/min
Konzentration :	1.016 g/l	**Injektvolumen :**	100.000 ul
Säule 1 :	PSS GRAM VS	**Temperatur :**	70.000 °C
Säule 2 :	PSS GRAM 7µm, 100A	**Temperatur :**	70.000 °C
Säule 3 :	PSS GRAM 7mm, 1000A	**Temperatur :**	70.000 °C
Detektor 1 :	PSS SECcurity UV	**Versatz :**	0.000 ml
Detektor 2 :	PSS SECcurity RI	**Versatz :**	0.146 ml
Operateur :	Grä.	**Messintervall :**	1.000 sec

PSS SECcurity RI

Mn :	5.5125e5	g/mol
Mw :	1.1936e6	g/mol
Mz :	2.5681e6	g/mol
Mv :	0.000000	g/mol
D :	2.1652e0	
[n]:	0.000000	ml/g
Vp :	1.3095e1	ml
Mp :	5.1184e5	g/mol
FI :	1.042e-2	ml*V
< 134904	0.00	
w% :	100.00	
> 10028647	0.00	

Figure A16. GPC report for the sample of entry 1, table 2 (100 °C, 24 h, loading 5 wt.%)

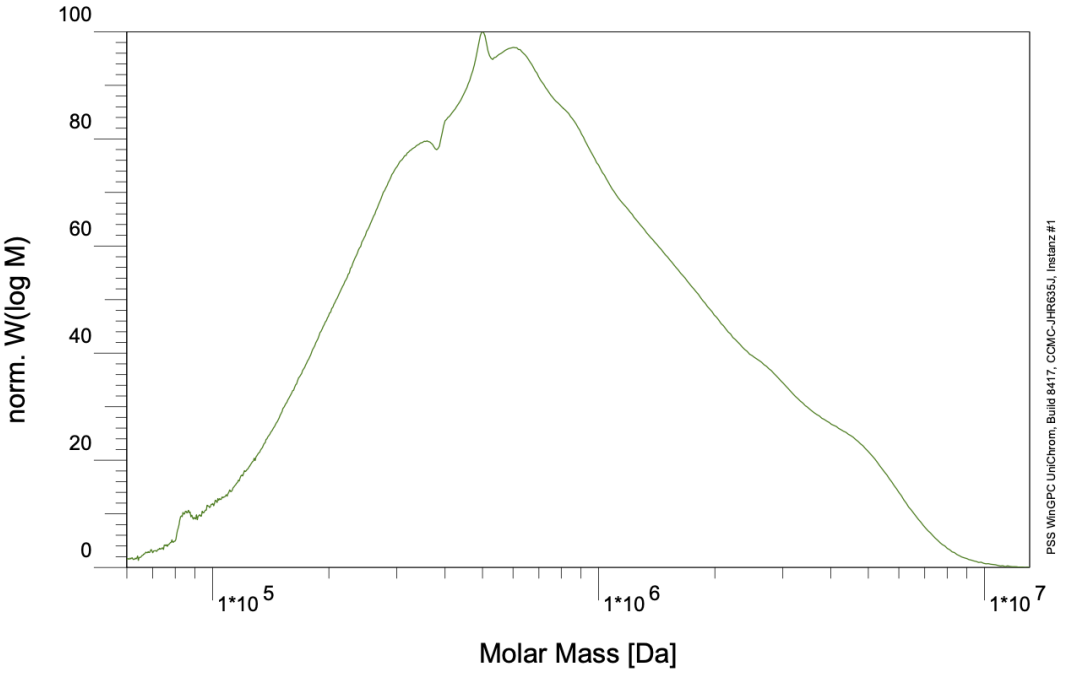

Probe :	Vial 4: CB-02 (Calmanti) - 1		
Integration von :	Dienstag 27.06.23 15:07:58		10.983 ml
Integration bis :	Dienstag 27.06.23 15:18:06		16.102 ml
Kalibration :	C:\Calib\N-LiCl-PS-29-06-2023.CAL	**Eluent :**	NMP-LiCl-5 w%
MHK - A (Kal.):	0.000E+0	**MHK - K (Kal.):**	1.000E+0 ml/g
Int.Stand.-K :	23.390 ml	**Int.Stand.-M :**	23.183 ml
Pumpe :	PSS SECcurity	**Flussrate :**	0.500 ml/min
Konzentration :	1.013 g/l	**Injektvolumen :**	100.000 ul
Säule 1 :	PSS GRAM VS	**Temperatur :**	70.000 °C
Säule 2 :	PSS GRAM 7µm, 100A	**Temperatur :**	70.000 °C
Säule 3 :	PSS GRAM 7mm, 1000A	**Temperatur :**	70.000 °C
Detektor 1 :	PSS SECcurity UV	**Versatz :**	0.000 ml
Detektor 2 :	PSS SECcurity RI	**Versatz :**	0.146 ml
Operateur :	Grä.	**Messintervall :**	1.000 sec

PSS SECcurity RI

Mn :	4.5719e5	g/mol
Mw :	1.1441e6	g/mol
Mz :	2.6328e6	g/mol
Mv :	0.000000	g/mol
D :	2.5026e0	
[n]:	0.000000	ml/g
Vp :	1.2918e1	ml
Mp :	6.2586e5	g/mol
Fl :	1.290e-2	ml*V
< 59902	0.00	
w% :	100.00	
> 13088367	0.00	

Figure A17. GPC report for the sample of entry 2, table 2 (100 °C, 24 h, loading 10 wt.%)

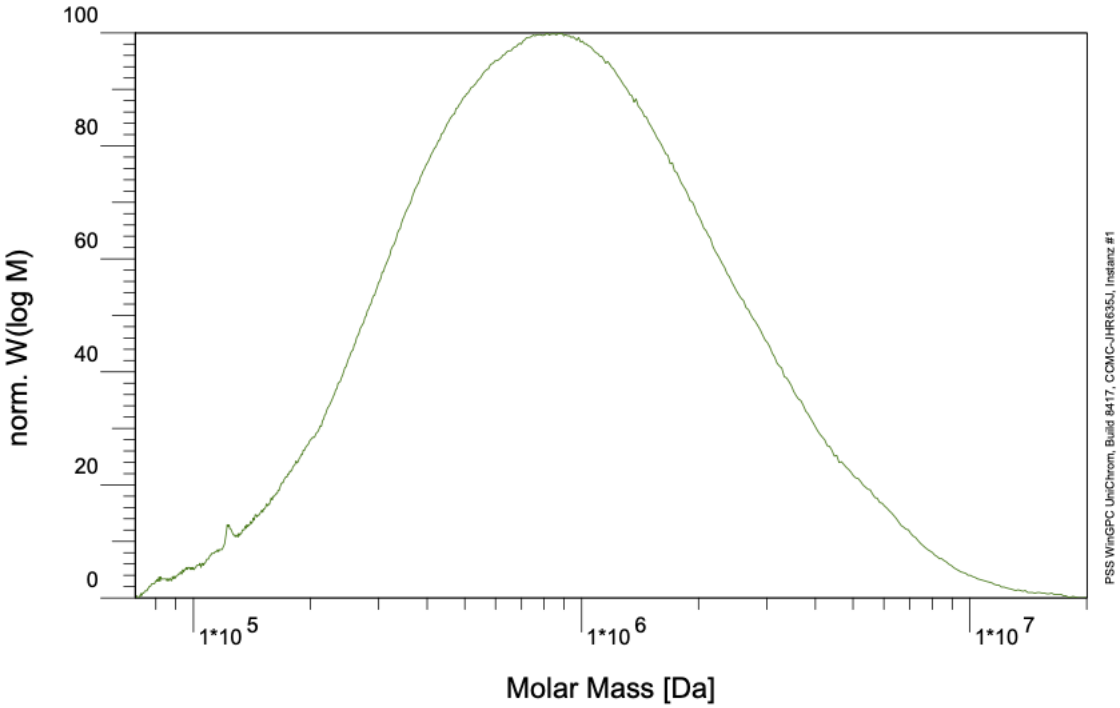

Probe :	Vial 2: CB-11 (Calmanti) - 1		
Integration von :	Freitag 30.06.23 08:24:26		10.735 ml
Integration bis :	Freitag 30.06.23 08:34:37		15.791 ml
Kalibration :	C:\Calib\N-LiCl-PS-29-06-2023_A.CAL	**Eluent :**	NMP-LiCl-5 w%
MHK - A (Kal.):	0.000E+0	**MHK - K (Kal.):**	1.000E+0 ml/g
Int.Stand.-K :	23.390 ml	**Int.Stand.-M :**	23.571 ml
Pumpe :	PSS SECcurity	**Flussrate :**	0.500 ml/min
Konzentration :	1.008 g/l	**Injektvolumen :**	100.000 ul
Säule 1 :	PSS GRAM VS	**Temperatur :**	70.000 °C
Säule 2 :	PSS GRAM 7µm, 100A	**Temperatur :**	70.000 °C
Säule 3 :	PSS GRAM 7mm, 1000A	**Temperatur :**	70.000 °C
Detektor 1 :	PSS SECcurity UV	**Versatz :**	0.000 ml
Detektor 2 :	PSS SECcurity RI	**Versatz :**	0.146 ml
Operateur :	Grä.	**Messintervall :**	1.000 sec

PSS SECcurity RI

Mn :	6.0495e5	g/mol
Mw :	1.4053e6	g/mol
Mz :	3.1703e6	g/mol
Mv :	0.000000	g/mol
D :	2.3230e0	
[n]:	0.000000	ml/g
Vp :	1.2437e1	ml
Mp :	1.1666e6	g/mol
FI :	5.653e-3	ml*V
< 70728	0.00	
w% :	100.00	
> 20035290	0.00	

Figure A18. GPC report for the sample of entry 3, table 2 (100 °C, 24 h, loading 20 wt.%)

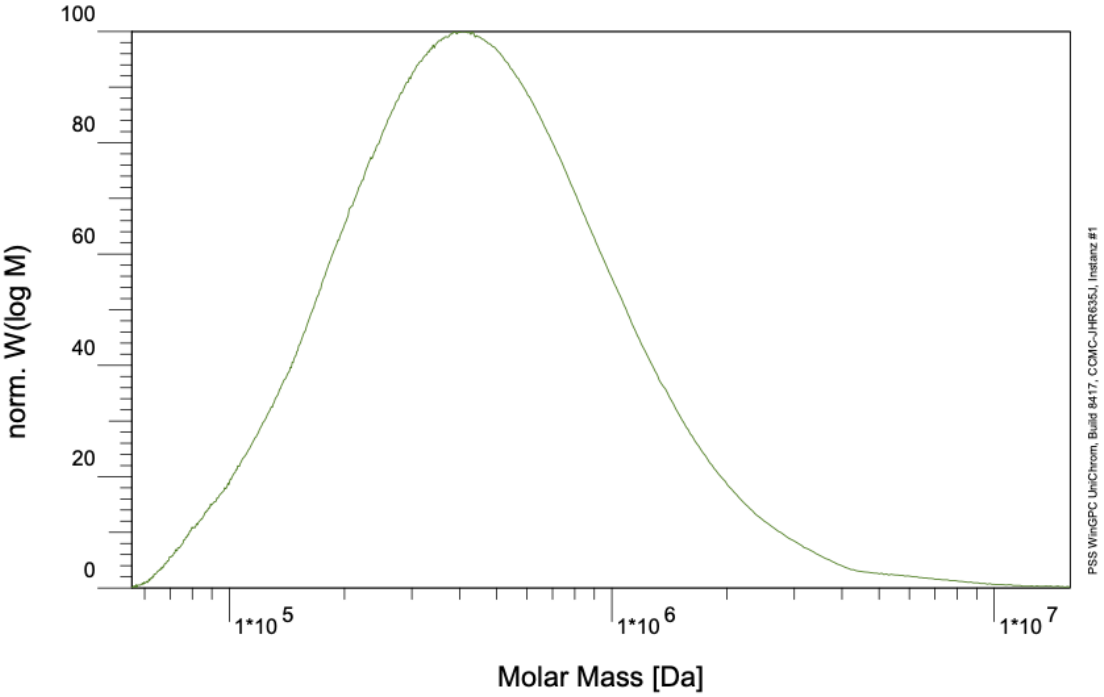

Probe :	Vial 4: CB-24 (Calmanti) - 1		
Integration von :	Freitag 30.06.23 10:28:03		10.873 ml
Integration bis :	Freitag 30.06.23 10:38:53		16.247 ml
Kalibration :	C:\Calib\N-LiCl-PS-29-06-2023_A.CAL	**Eluent :**	NMP-LiCl-5 w%
MHK - A (Kal.):	0.000E+0	**MHK - K (Kal.):**	1.000E+0 ml/g
Int.Stand.-K :	23.390 ml	**Int.Stand.-M :**	23.589 ml
Pumpe :	PSS SECcurity	**Flussrate :**	0.500 ml/min
Konzentration :	1.009 g/l	**Injektvolumen :**	100.000 ul
Säule 1 :	PSS GRAM VS	**Temperatur :**	70.000 °C
Säule 2 :	PSS GRAM 7µm, 100A	**Temperatur :**	70.000 °C
Säule 3 :	PSS GRAM 7mm, 1000A	**Temperatur :**	70.000 °C
Detektor 1 :	PSS SECcurity UV	**Versatz :**	0.000 ml
Detektor 2 :	PSS SECcurity RI	**Versatz :**	0.146 ml
Operateur :	Grä.	**Messintervall :**	1.000 sec

PSS SECcurity RI

Mn :	3.3313e5	g/mol
Mw :	6.6636e5	g/mol
Mz :	1.7080e6	g/mol
Mv :	0.000000	g/mol
D :	2.0003e0	
[n]:	0.000000	ml/g
Vp :	1.3098e1	ml
Mp :	5.1022e5	g/mol
FI :	9.649e-3	ml*V
< 55510	0.00	
w% :	100.00	
> 15804838	0.00	

Figure A19. GPC report for the sample of entry 4, table 2 (150 °C, 2 h, loading 20 wt.%)

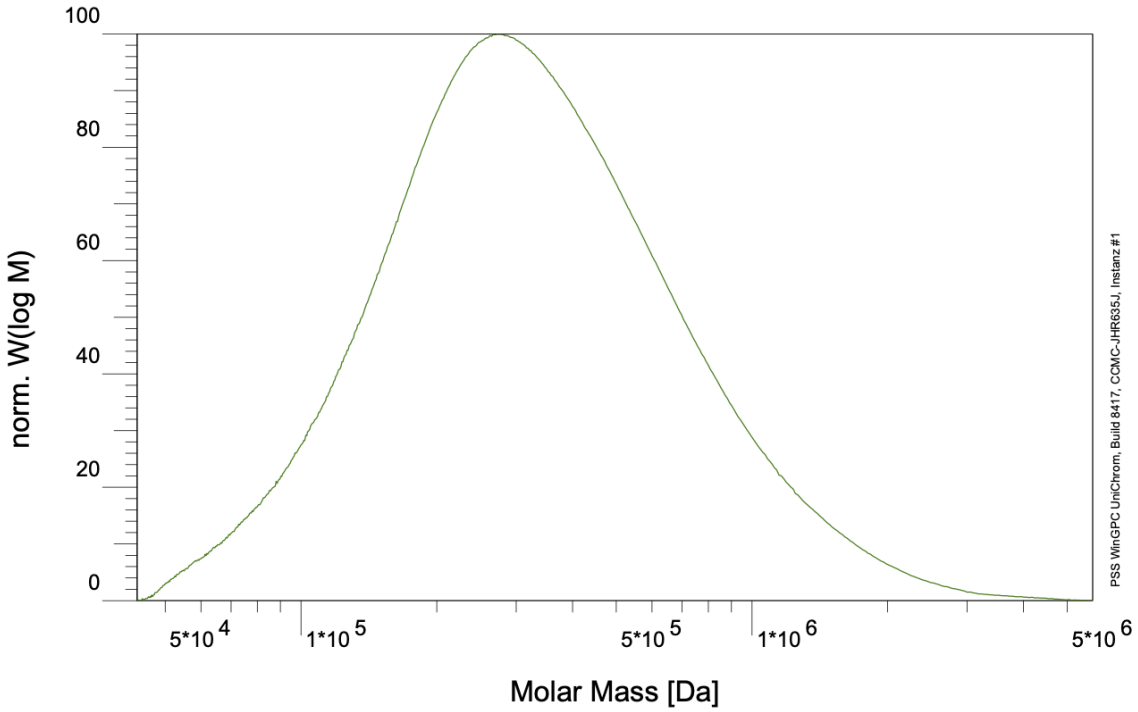

Probe :	Vial 6: CB-22 (Calmanti) - 1		
Integration von :	Dienstag 27.06.23 17:07:16		11.469 ml
Integration bis :	Dienstag 27.06.23 17:17:41		16.724 ml
Kalibration :	C:\Calib\N-LiCl-PS-29-06-2023.CAL	**Eluent :**	NMP-LiCl-5 w%
MHK - A (Kal.):	0.000E+0	**MHK - K (Kal.):**	1.000E+0 ml/g
Int.Stand.-K :	23.390 ml	**Int.Stand.-M :**	23.169 ml
Pumpe :	PSS SECcurity	**Flussrate :**	0.500 ml/min
Konzentration :	1.015 g/l	**Injektvolumen :**	100.000 ul
Säule 1 :	PSS GRAM VS	**Temperatur :**	70.000 °C
Säule 2 :	PSS GRAM 7µm, 100A	**Temperatur :**	70.000 °C
Säule 3 :	PSS GRAM 7mm, 1000A	**Temperatur :**	70.000 °C
Detektor 1 :	PSS SECcurity UV	**Versatz :**	0.000 ml
Detektor 2 :	PSS SECcurity RI	**Versatz :**	0.146 ml
Operateur :	Grä.	**Messintervall :**	1.000 sec

PSS SECcurity RI

Mn :	2.4881e5	g/mol
Mw :	4.3025e5	g/mol
Mz :	7.9624e5	g/mol
Mv :	0.000000	g/mol
D :	1.7292e0	
[n]:	0.000000	ml/g
Vp :	1.3526e1	ml
Mp :	3.3121e5	g/mol
Fl :	1.275e-2	ml*V
< 43308	0.00	
w% :	100.00	
> 5695162	0.00	

Figure A20. GPC report for the sample of entry 5, table 2 (150 °C, 3 h, loading 20 wt.%)

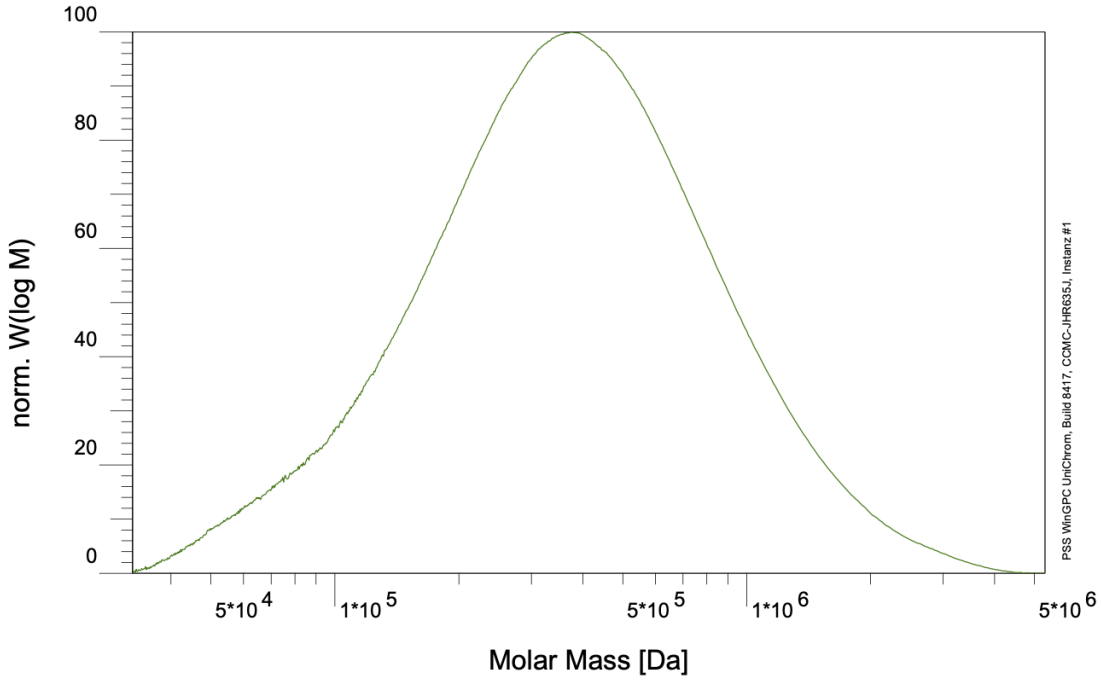

Probe :	Vial 3: CB-23_turbid ! (Calmanti) - 1		
Integration von :	Freitag 30.06.23 09:27:40		11.511 ml
Integration bis :	Freitag 30.06.23 09:39:19		17.292 ml
Kalibration :	C:\Calib\N-LiCl-PS-29-06-2023_A.CAL	**Eluent :**	NMP-LiCl-5 w%
MHK - A (Kal.):	0.000E+0	**MHK - K (Kal.):**	1.000E+0 ml/g
Int.Stand.-K :	23.390 ml	**Int.Stand.-M :**	23.579 ml
Pumpe :	PSS SECcurity	**Flussrate :**	0.500 ml/min
Konzentration :	1.017 g/l	**Injektvolumen :**	100.000 ul
Säule 1 :	PSS GRAM VS	**Temperatur :**	70.000 °C
Säule 2 :	PSS GRAM 7µm, 100A	**Temperatur :**	70.000 °C
Säule 3 :	PSS GRAM 7mm, 1000A	**Temperatur :**	70.000 °C
Detektor 1 :	PSS SECcurity UV	**Versatz :**	0.000 ml
Detektor 2 :	PSS SECcurity RI	**Versatz :**	0.146 ml
Operateur :	Grä.	**Messintervall :**	1.000 sec

PSS SECcurity RI

Mn :	2.6003e5	g/mol
Mw :	5.0488e5	g/mol
Mz :	9.2314e5	g/mol
Mv :	0.000000	g/mol
D :	1.9416e0	
[n]:	0.000000	ml/g
Vp :	1.3202e1	ml
Mp :	4.5661e5	g/mol
FI :	1.100e-2	ml*V
< 32250	0.00	
w% :	100.00	
> 5303574	0.00	

Figure A21. GPC report for the sample of entry 6, table 2 (150 °C, 4 h, loading 20 wt.%)

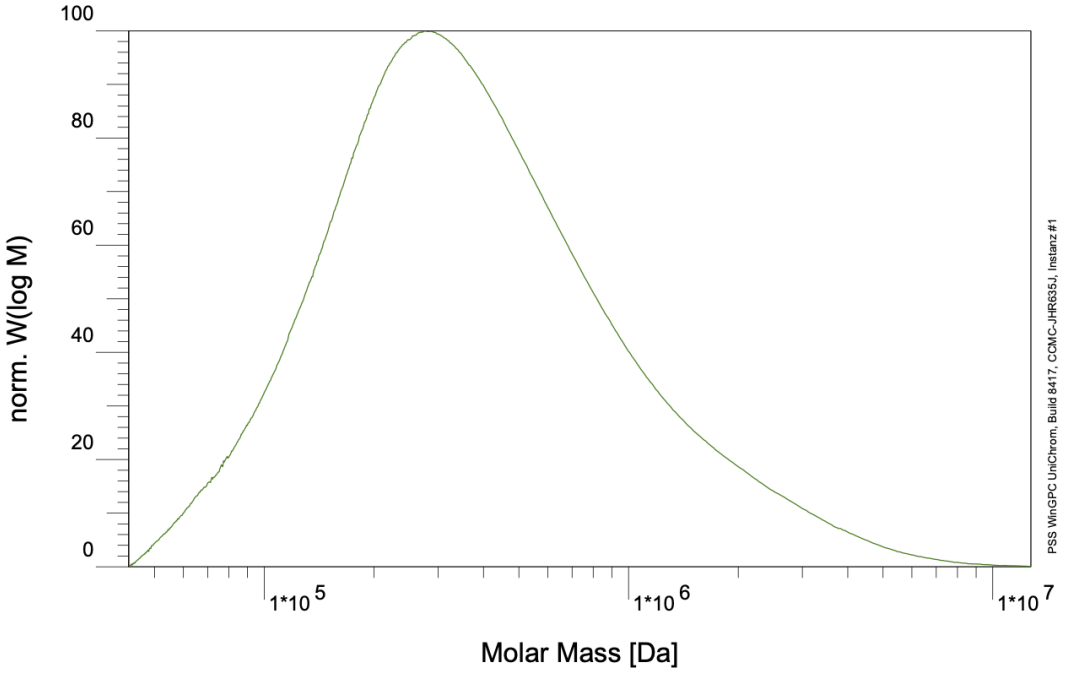

Probe :	Vial 3: Chitin_TCI (Calmanti) - 1		
Integration von :	Dienstag 27.06.23 14:11:20		11.000 ml
Integration bis :	Dienstag 27.06.23 14:22:46		16.763 ml
Kalibration :	C:\Calib\N-LiCl-PS-29-06-2023.CAL	**Eluent :**	NMP-LiCl-5 w%
MHK - A (Kal.):	0.000E+0	**MHK - K (Kal.):**	1.000E+0 ml/g
Int.Stand.-K :	23.390 ml	**Int.Stand.-M :**	23.188 ml
Pumpe :	PSS SECcurity	**Flussrate :**	0.500 ml/min
Konzentration :	1.019 g/l	**Injektvolumen :**	100.000 ul
Säule 1 :	PSS GRAM VS	**Temperatur :**	70.000 °C
Säule 2 :	PSS GRAM 7µm, 100A	**Temperatur :**	70.000 °C
Säule 3 :	PSS GRAM 7mm, 1000A	**Temperatur :**	70.000 °C
Detektor 1 :	PSS SECcurity UV	**Versatz :**	0.000 ml
Detektor 2 :	PSS SECcurity RI	**Versatz :**	0.146 ml
Operateur :	Grä.	**Messintervall :**	1.000 sec

PSS SECcurity RI

Mn :	2.6189e5	g/mol
Mw :	5.9990e5	g/mol
Mz :	1.6631e6	g/mol
Mv :	0.000000	g/mol
D :	2.2907e0	
[n]:	0.000000	ml/g
Vp :	1.3475e1	ml
Mp :	3.4746e5	g/mol
FI :	1.740e-2	ml*V
< 42456	0.00	
w% :	100.00	
> 12728180	0.00	

Figure A22. GPC report for the sample of entry 7, table 2 (commercial chitin from TCI chemicals)

Atomic Force Microscopy characterisation of the nanomaterials

The three nanomaterials were characterised by AFM to investigate their morphology, size and shape (see below **Figure A23**).

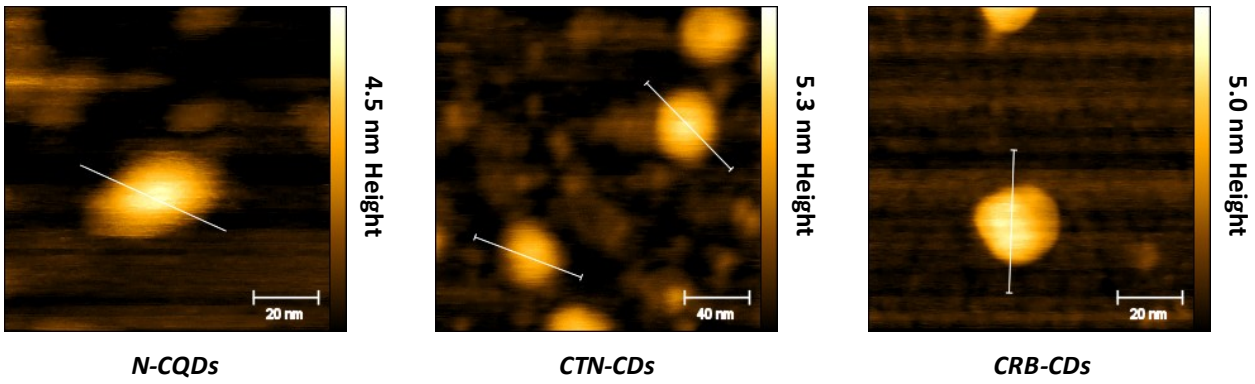

Figure A23. AFM images of the N-CQDs, CTN-CDs, and CRB-CDs nanomaterials.

AFM analyses revealed the presence of nanoparticles with lateral dimension in the range of 35-45 nm and heights between 4.5-5.5 nm, values significantly larger than those expected for CDs (typically in the range of 5-10 nm), potentially ascribable to the formation of aggregates during sample preparation and solvent evaporation. However, the apparent overestimation of the particle size could also be partially influenced by the tip convolution effect, typically affecting lateral dimensions in AFM measurement.

Preliminary Transmission Electron Microscopy characterisation of the nanomaterials

Preliminary TEM analyses confirmed the presence of aggregates. In the case of the chitin-derived CTN-CDs (**Figure A24, left**) this large lump appeared amorphous and irregular, likely associated with chitinous residues of relatively large dimensions (40-50 nm). Conversely, the crab-derived CRB-CDs (**Figure A24, right**) exhibited a more defined aggregate structure, approximately 50-60 nm in size, clearly composed of smaller nanodots.

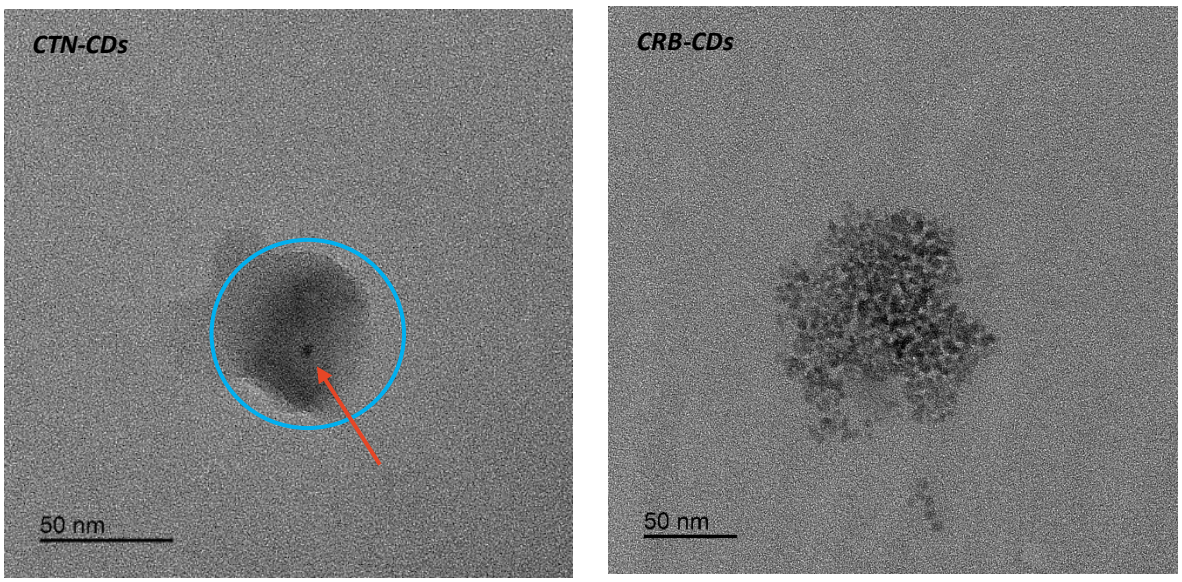

Figure A24. First series of TEM images of large aggregates of CTN-CDs and CRB-CDs materials.

Surface roughness profiles of the nanomaterials

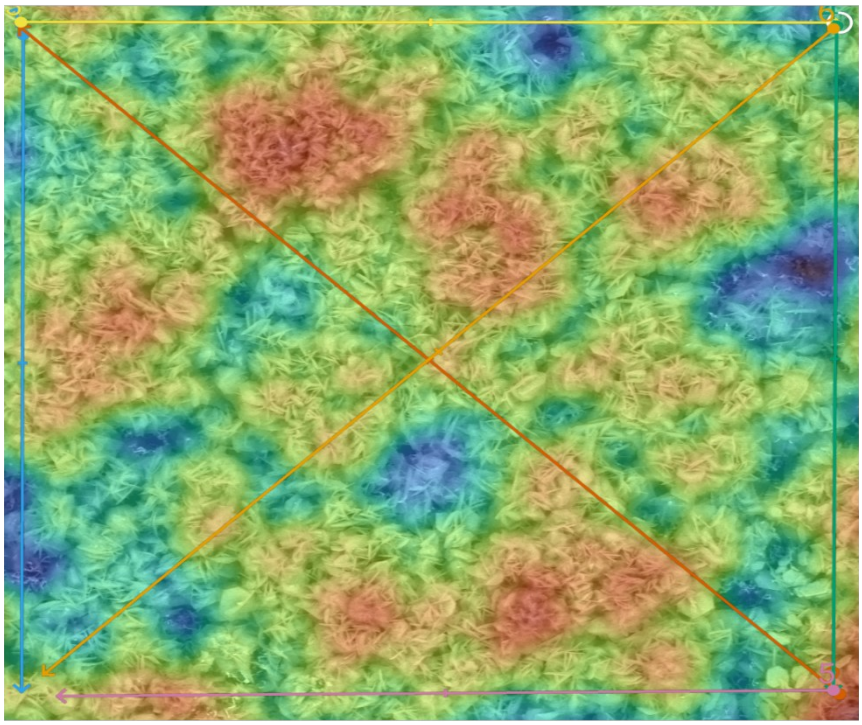

Figure A25. Roughness profile of the control test. Sa: 778.36 nm. Field of view: 108.13 µm; λs: 223.61 nm; λc: 282.84 µm.

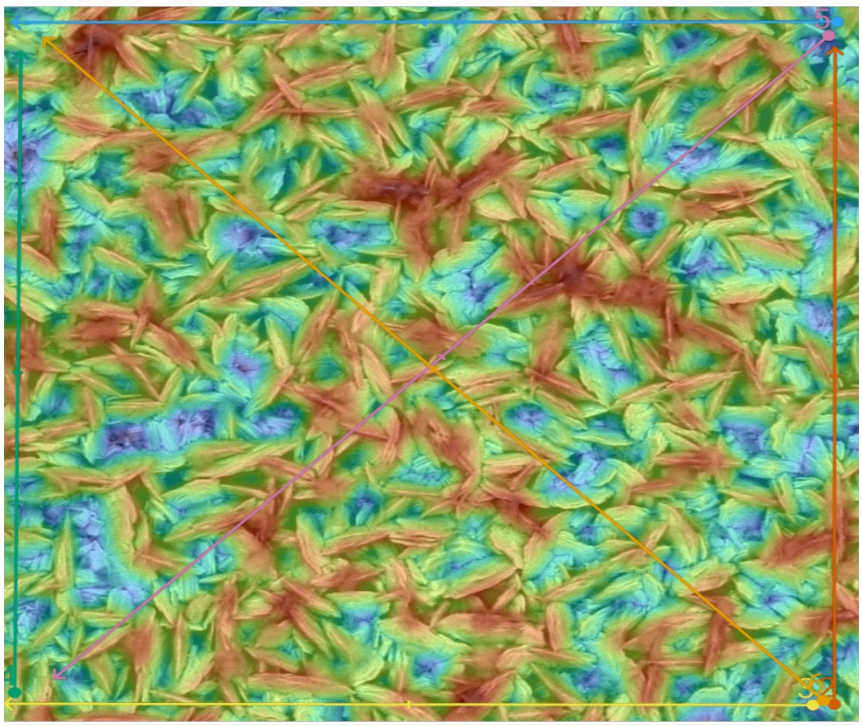

Figure A26. Roughness profile of the plating experiment with the N-CQDs additive. Sa: 390.20 nm. Field of view: 108.13 µm; λs: 223.61 nm; λc: 282.84 µm.

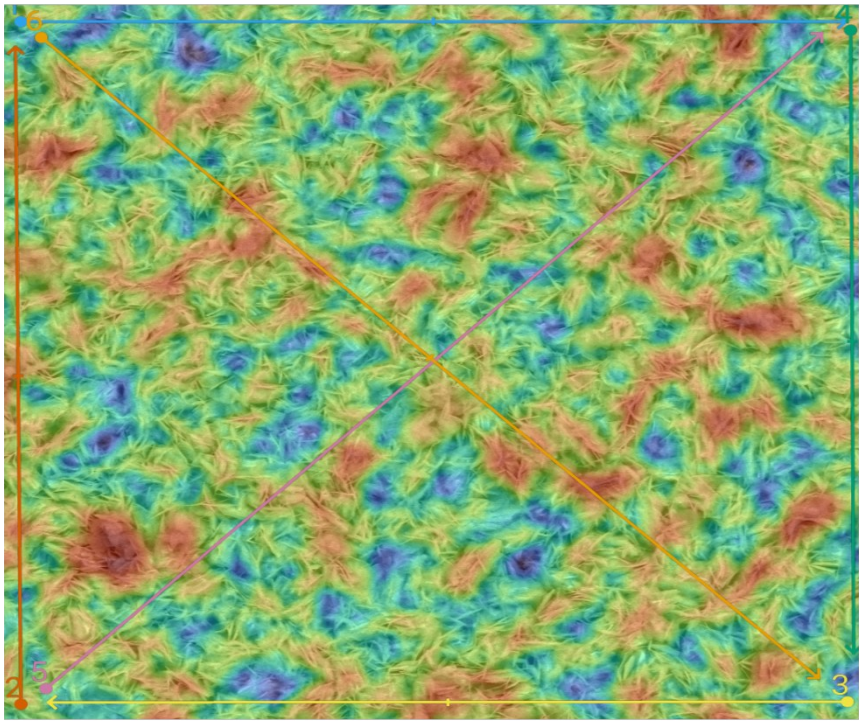

Figure A27. Roughness profile of the plating experiment with the CTN-CDs additive. Sa: 267.94 nm. Field of view: 120.14 µm; λs: 223.61 nm; λc: 282.84 µm.

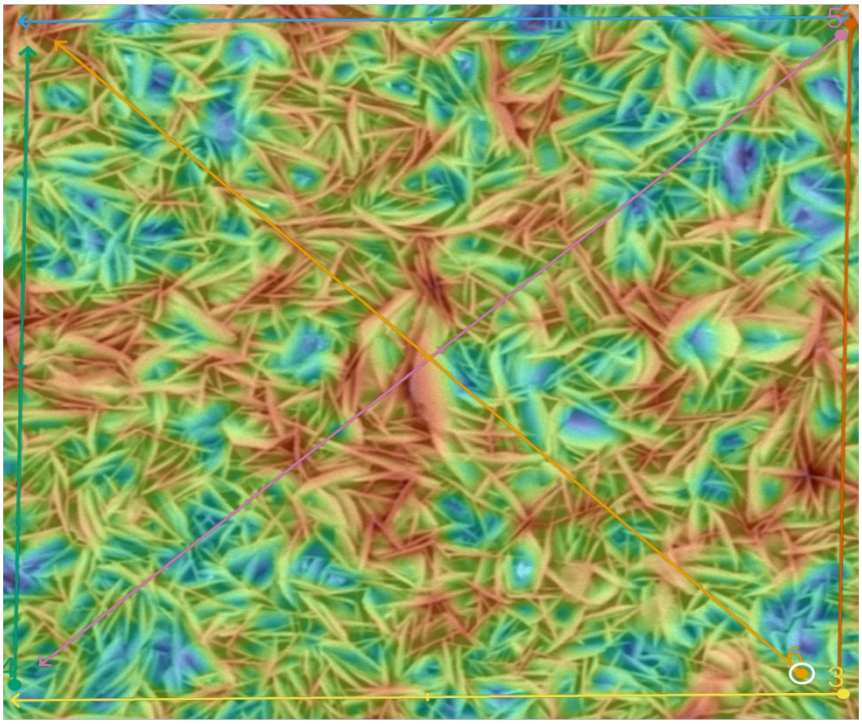

Figure A28. Roughness profile of the plating experiment with the CRB-CDs additive. Sa: 292.66 nm. Field of view: 108.13 µm; λs: 223.61 nm; λc: 282.84 µm.